THE UNIVERSITY *of* EDINBURGH

The Development of SmartProbes for the Optical Imaging of Pulmonary Inflammation

Gavin Peter Birch

Doctorate of Philosophy

The University of Edinburgh

2019

Lay summary

Interrogating disease with human lung optical imaging could improve the outcomes of clinical trials, provide early validation of lead candidates within drug discovery programmes, whilst also offering diagnostic capabilities. Optical molecular imaging using smart fluorescent probes (SmartProbes) provides a safe and affordable technique to analyse multiple lung pathologies and diseases, such as fibrosis and chronic obstructive pulmonary disease (COPD). The aim of this project was to develop families of SmartProbes and validate their biological utility.

Macrophages are a key inflammatory cell in the lung. The ability to image these cells gives an understanding of macrophage biology, along with their interactions with other host-cells in the lung. SmartProbes were targeted to macrophages via receptors that they express highly, notably the folate receptor and macrophage mannose receptor. The synthesis of SmartProbes targeting these markers and their biological evaluation, is reported.

Epithelial cells line the surface of the lung and can become damaged during a number of lung diseases. Certain diseases involve a process known as senescence, this is a process of cellular aging and its role is to indicate the need for repair. To visualise these processes, activity-based SmartProbes that can sensitively detect esterases and beta-galactosidase were synthesised. Esterase probes were evaluated in enzyme and cellular assays. A beta-galactosidase probe (XD-βGal) was able to detect senescent epithelial cells.

Abstract

The prospect of an optical biopsy to interrogate disease within the human lung offers the ability to improve the outcomes of clinical trials, provide early validation within drug discovery programmes, while also offering diagnostic capabilities. Optical molecular imaging using smart fluorescent probes offers a safe and affordable technique to allow the analysis of multiple lung pathologies and diseases such as fibrosis and chronic obstructive pulmonary disease (COPD). The aim of this project was to develop a number of families of SmartProbes and validate their biological utility.

Macrophages are a valuable imaging target due to their key role in maintaining homeostasis and responding to inflammatory stimuli in the lung. Imaging these cells will allow us to dynamically observe macrophage biology and the multitude of host cell interactions within the lung. SmartProbes were targeted to macrophages via the cell specific markers - the macrophage mannose and folate receptors. The synthesis of SmartProbes targeting the folate receptor, including the application of new solid phase methodology to simplify the synthesis of these probes, is reported. *In vitro* studies were carried out in cancer cells and primary human monocyte-derived macrophages. An anti-MMR nanobody that targets the mannose receptor was fluorescently labelled to give a near-infrared SmartProbe. Its specificity and selectivity was assessed with primary immune cells and *ex vivo* clinical lung samples.

The epithelial barrier is a layer of cells that line the lung and undergoes remodelling during diseases such as COPD and idiopathic pulmonary fibrosis (IPF). Hence,

methods to visualise epithelial integrity were sought. SmartProbes that were pro-fluorophores for beta-galactosidase were synthesised. Beta-galactosidase probes were applied in epithelial cell models and murine tissue, allowing the detection of senescence associated beta-galactosidase (SA-βGal) positive senescent cells in 3D tissue samples.

Declaration of authorship

I declare that this thesis is an original report of my research, has been written by me and has not been submitted for any previous degree. The experimental work is almost entirely my own work. Any contributions from colleagues carried out in collaboration are explicitly referenced in the text. References have been provided to all supporting literature and resources, including the published work of others.

Parts of the presented work have been published as:

- **G.P Birch**, T. Campbell, M. Bradley and K. Dhaliwal, Optical molecular imaging of inflammatory cells in interventional medicine – an emerging strategy, *Front. Oncol.*, accepted.

Parts of this work are in preparation for publication:

- G.P. Birch, A. Lilienkampf, K. Dhaliwal, M. Bradley, FolateTag: solid phase synthesis of fluorophore-folate conjugates for imaging the tumour microenvironment, in preparation.

Signed:

Dated: 06 June 2020

Table of Contents

Acknowledgments

I am especially grateful to Mark and Kev for providing the opportunity to work on such a vibrant research topic, and for their support and encouragement. You taught me that developing as a person was just as important as developing as a multidisplinary scientist. For their friendship and support throughout this project thank you to Vikki, Paul, Dan, Alessia, Antonio, Assel, Muhammed and Katjana. For their help and expertise I thank Christophe Portal, Steve Jenkins, Pieter Louwe and Richard O'Connor. I am also grateful to Malcolm Begg, Gus Amour and Dave Hassell from GSK for their supervision and hosting me for three months; embedding a chemist with immunology experts was a rewarding experience and focused me on understanding the true value of this project.

For supporting this interdisciplinary project, I have to thank many people from the Bradley/ Dhaliwal groups and Proteus (past and present) that I have been able to work alongside. In alphabetical order, Alicia, Ahsan, Anne, Beth, Emma, Jess, Jin, Jingjing, Kevin, Maria, Matt, Matteo, Mike, Mirek, Mithun, Nestor, Philip, Shelagh, Thane, Tom S, Tushar, Yichuan. For their technical support, the members of the MS facility, Alan Taylor, Faye Cruickshank and Logan Mackay; members of the NMR facility Juraj Bella and Lorna Murray; Chemistry Stores and the specialist staff in QMRI; Rolly Wiegand, Shonna Johnston.

A special thanks to Hannah, my parents and grandparents for supporting and encouraging me during another four years of further education.

Abbreviations

δ	Chemical shift in ppm
λ	Wavelength
τ	Fluorescence lifetime
Φ	Quantum yield
a.u.	Arbitrary units
COPD	Chronic obstructive pulmonary disease
Cy	Cyanine (3,5,7)
DCC	N,N'-Dicyclohexylcarbodiimide
DCM	Dichloromethane
DIPEA	N,N-Diisopropylethylamine (Hünig's base)
DMEM	Dulbecco's Modified Eagle's Medium
DMSO	Dimethylsulfoxide
ELSD	Evaporative light scattering detector
ESI	Electrospray ionisation
FBS	Fetal bovine serum
FDA	Food and Drug Administration
Fmoc	9-fluorenylmethyl carbamate
FR(-α/-β)	Folate receptor (alpha/beta)
FRET	Förster resonance energy transfer
HPLC	High performance liquid chromatography
HRMS	High resolution mass spectrometry
IMS-MS	Ion-mobility spectrometry–mass spectrometry
LC-MS	Liquid chromatography mass spectrometry
MALDI-TOF MS	Matrix-assisted laser desorption/ionization-time of flight mass spectrometry
MDM	Monocyte-derived macrophage
MeCN	Acetonitrile
MMR	Macrophage mannose receptor
Mφ	Macrophage
MS	Mass spectrometry

MW	Molecular weight
m/z	Mass-to-charge ratio
NHS	N-Hydroxysuccinimide
NIR	Near infrared
NMR	Nuclear magnetic resonance
PBS	Phosphate buffered saline
PEG	Poly(ethylene glycol)
PET	Positron emission tomography
pH	*Potentiahydrogenii*
RFU	Relative fluorescent units
RP-HPLC	Reverse phase high performance liquid chromatography
RPMI	Roswell Park Memorial Institute Medium
rt	Room temperature
TEA	Triethylamine
TFA	Trifluoroacetic acid
tlc	Thin layer chromatography
t_R	Retention time
UV-Vis	Ultraviolet-Visible

1. Molecular imaging in the lung

Medical imaging techniques such as magnetic resonance imaging (MRI) and X-ray computed tomography (CT) are widely used within healthcare systems, along with the nuclear imaging techniques of positron emission tomography (PET) and single-photon emission computed tomography (SPECT).[2] These imaging techniques provide predominately structural information about a patient, however they have limitations such as cost and the use of radioactive materials (PET and SPECT). Thus, the development of new imaging techniques that are safer, cheaper and offer molecular information would be beneficial for the diagnosis of disease. One such modality, optical molecular imaging, is capable of giving cellular level resolution images, allowing the interrogation of biological events at a molecular level.[3]

At this point it is worth considering the specific definition of molecular imaging since it is the focus of this thesis. It is defined as "the visualisation of *in vivo* biological processes at a molecular level using optical probes".[4] Molecular imaging has a wide scope of biomedical applications and has already been applied in cardiology and oncology, and inflammatory diseases.[5-7] For example, fluorescein is used in ophthalmology for assessing the vascular structure of the eye,[8] while indocyanine green (ICG) is used as a tracer of liver function and vasculature in the eye, heart and liver.[3, 9]

1.1. Optical imaging

Optical molecular imaging relies on the emission of light in the form of fluorescence and is a high resolution method to generate molecular level of information. Absorption of light by a fluorophore gives a singlet excited state (S_1) which can relax through several pathways including fluorescence ($S_1 \rightarrow S_0 + h\nu$), phosphorescence ($S_1 \rightarrow T_1 \rightarrow S_0$) and non-radiative decay. This can be described by a Jablonski diagram (**Figure 1.1**). The absorption maxima and emission maxima are characteristic of each fluorophore.

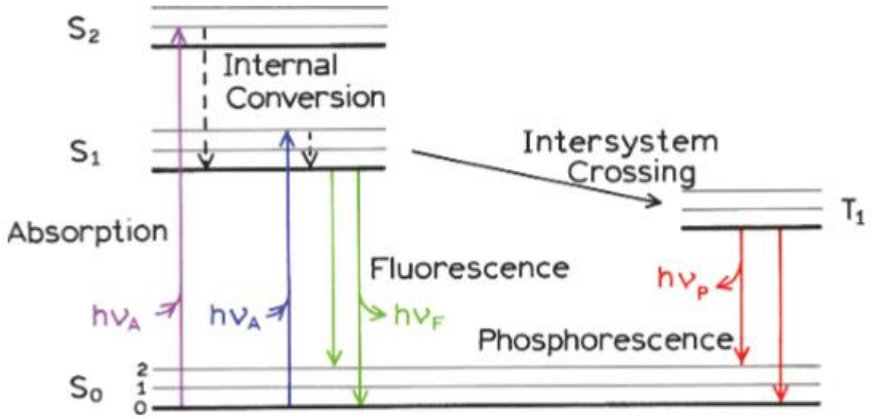

Figure 1.1. A Jablonski diagram showing the ground (S_0), first (S_1), and second (S_2) excited electronic states and the transitions between states as vertical lines. Internal conversion involves rapid relaxation of higher vibrational states to S_1 in ~10^{-12} s. Return to the ground state results in fluorescence emission, or alternatively conversion to the T_1 state followed by emission as phosphorescence. Reprinted by permission from Springer Nature: Principles of Fluorescence Spectroscopy (J.R. Lakowicz), copyright (2006).[10]

Optical molecular imaging technology is available at a much lower cost than other imaging techniques such as PET that requires sophisticated imaging equipment and on-site radioisotope production due to their short half-lives. Unlike PET, optical molecular imaging does not carry the same safety concerns of ionising radiation.[3] One

major drawback of optical imaging is the low penetration depth of visible light (several millimetres) that makes detection of a fluorescent signal through tissue almost impossible.[3] Excitation wavelengths towards the UV region (below 400 nm) are unsuitable for biomedical applications as they can cause tissue damage, whilst visible excitation light is scattered in tissue. This has led to researchers describing an '*in vivo* imaging window' in the far-red and near-infrared region (650-900 nm), due to the greater tissue penetration depths.[11] Furthermore, a particular problem with lung imaging is that a mixture of intrinsic molecules all exhibit green autofluorescence (**Figure 1.2**).[1] Thus, the NIR spectrum is increasingly exploited due to the relative lack of autofluorescence at these wavelengths.[12]

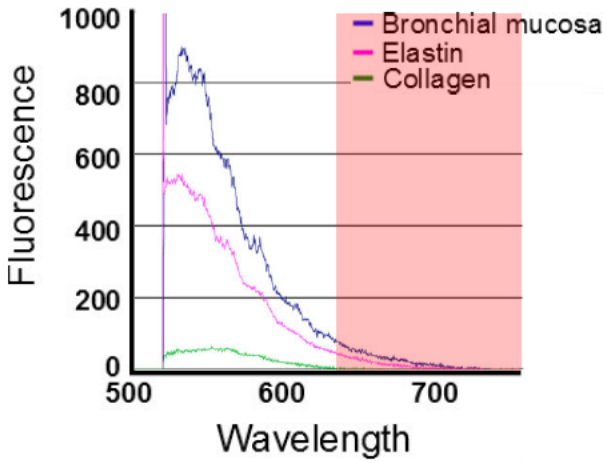

Figure 1.2. Autofluorescence spectra of bronchial mucosa, elastin and collagen when excited at 488 nm and measured using an optical endomicroscopy system. Lower autofluorescence is seen in the near infrared region of 650-900nm making this the optimal region for *in vivo* applications. Adapted from Thiberville.[1]

1.2. *In vivo* fluorescence imaging

Widefield fluorescence and endomicroscopy systems are the major technologies that have been used clinically to detect optical molecular agents. Recently, fluorescence

guided surgery is becoming possible for tumour resection.[13] Complete tumour removal is difficult with conventional microscopy as visually determining tumour-free margin is problematic. With fluorescence guided surgery, surgeons were able to assess the extent of excision in real-time using a fluorescent label that 'lights up' the tumour (see **Figure 1.3**).

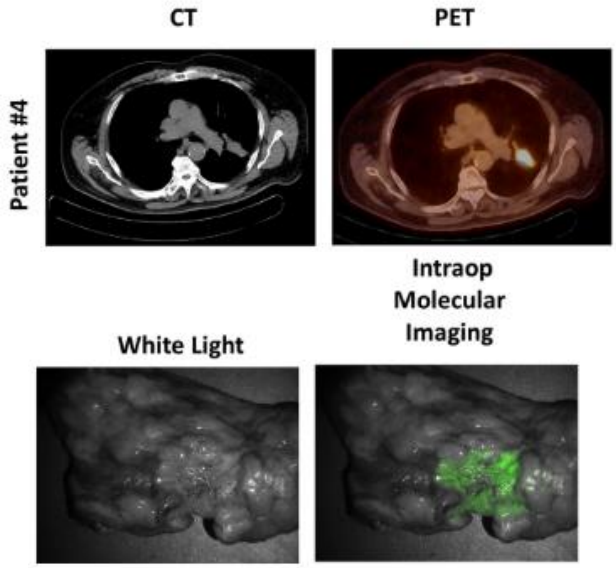

Figure 1.3. A demonstration of the power of molecular imaging for the detection of lung adenocarcinomas using the FITC-folate probe. A patient was diagnosed with lung adenocarcinoma by CT, PET and optical molecular imaging using the Artemis Fluorescence Imaging System. Intraoperative imaging provides clear identification of cancer cells stained with a fluorescent agent. Reprinted from Okusanya et al.[14], Copyright (2015), with permission from Elsevier.

Optical endomicroscopy via an optical fibre imaging bundle can give microscopic analysis and has the capability to explore a variety of cavities. More recently, imaging fibre endomicroscopy has been used in the lung for the *in vivo* detection of bacteria,[15] as well as in the GI tract to show changes due to colorectal polyps.[16] There are a number of optical endomicroscopy platforms from clinical to developmental systems

(as demonstrated in **Figure 1.4**),[1, 15] although standardisation is a key challenge to producing useful diagnostic information.[17]

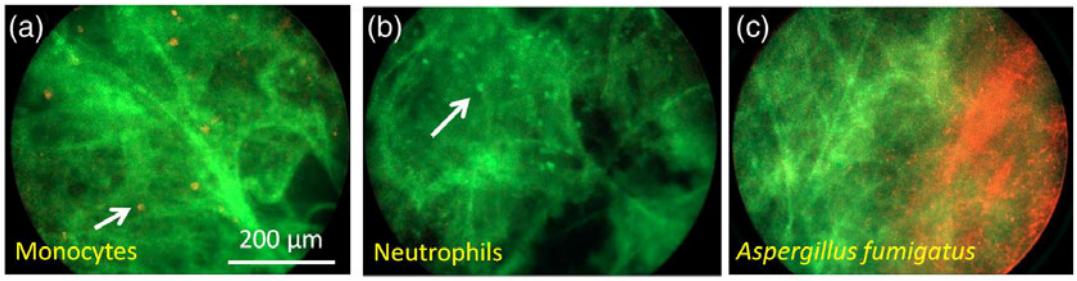

Figure 1.4. An example of optical endomicroscopy of multiple targets in *ex vivo* lung tissue including (a) monocytes, (b) neutrophils, and (c) fungus (*Aspergillus fumigatus*) by a Proteus system. Copyright Krstajić et al.[15] Reproduced under a Creative Commons Attribution 3.0 Unported License.

The Proteus team in Edinburgh has a current focus on improving molecular imaging technologies in the human lung. These new technologies have the power to impact the drug discovery progress by enriching assay outputs, accelerating development and enabling better drug response metrics in clinical trials.

1.3. Design of Smartprobes

A recent focus in the field of optical imaging are so-called "Smartprobes", agents that should only fluoresce after activation and engagement with a target.[18] These fluorescent molecules have been tuned to give a variety of different properties and to allow visualisation of targets of interest. A plethora of Smartprobes have been designed that target disease relevant targets, such as c-Met expression[19], proteases[20], receptor expression, glutathione[21], hypochlorous acid[22] and reactive oxygen species.[23] An in depth review of peptide optical probes for the clinical imaging of specific targets

in the areas of cancer, inflammation and infection was carried out by Staderini in 2018.[24]

1.3.1. NIR dyes

The existing toolbox of fluorescent dyes is vast but focused on a number of "core" fluorophore scaffolds; these typically cover emission wavelengths from 300 to 900 nm, a range of photophysical properties and chemical functionalities.[25] However, common problems with fluorophores in a medical imaging setting is their poor aqueous solubility or high levels of aggregation, while existing Food and Drug Administration (FDA) approved NIR fluorophores are limited (**Figure 1.5**). Synthetic chemistry can be used to modulate the fluorescent properties of fluorophores towards the ideal properties of; emission towards the red or infrared region (600-900 nm), bright, high quantum yield, high photostability, solubility and a scalable method of synthesis.

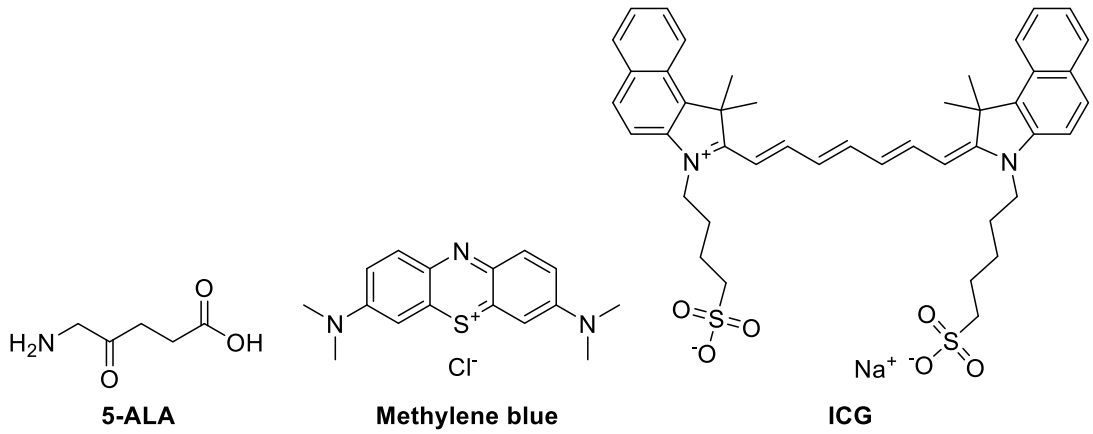

Figure 1.5. Near-infrared dyes or precursors currently used in clinical applications. 5-aminolevulinic acid (5-ALA) via biosynthesis of the fluorescent protoporphyrin XI (λ_{em} = 632 nm), methylene blue (λ_{em} = 700 nm), indocyanine green (ICG) (λ_{em} = 835 nm).

One suitable class of NIR dyes having most desired properties are the cyanines. Their naming is based on the number of carbons in the polymethine chain, n = 3, 5, 7, being tri- (cyanine 3), penta- (cyanine 5) or heptamethine (cyanine 7) cyanine's respectively.[26]

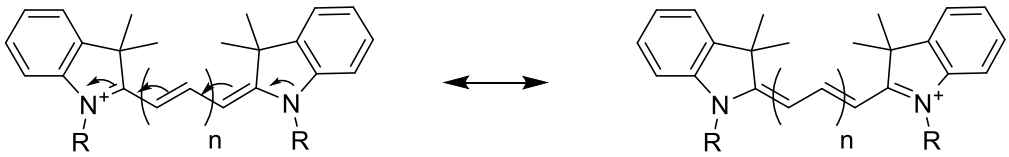

Figure 1.6. The structure of cyanine dyes comprises two heterocyclic groups connected by a methine chain, usually with an odd number of carbons. Varying the structure from n = 3, 5 or 7 methines changes their emission properties from the visible to the near infrared, allowing the molecule to be tuned to the desired wavelength. The backbone of cyanine dyes allows delocalisation of electrons along the polymethine chain to give their fluorescent properties.

A clear limitation of commercially available NIR dyes is their propensity for nonspecific binding, uptake and retention, due to their hydrophobicity.[27] To some extent, it is necessary to optimise the choice of fluorophore as this can have a significant effect on a probes biodistribution.[27] The highly sulfonated Cy5** dye was previously developed by GE Healthcare to avoid these problems (**Figure 1.7**). This dye is known to have high water solubility and fast renal clearance.[19] Due to the penta-sulfonated nature of the dye, it would be advantageous over existing commercial Cy5 dyes due to the increased aqueous solubility and reduced potential for dye aggregation.[28]

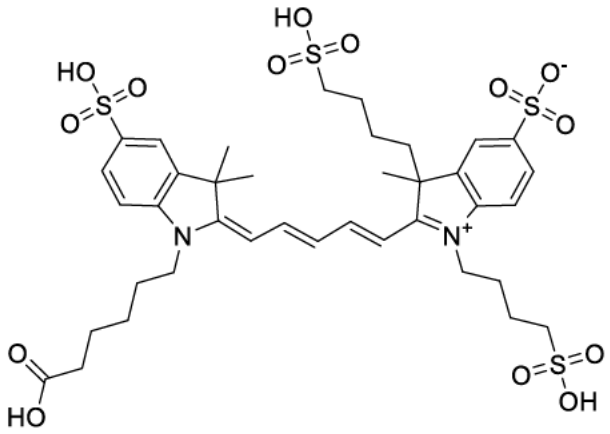

Figure 1.7. Structure of the Cy5** fluorophore developed by GE Healthcare.[19]

1.3.2. Always-on Smartprobes

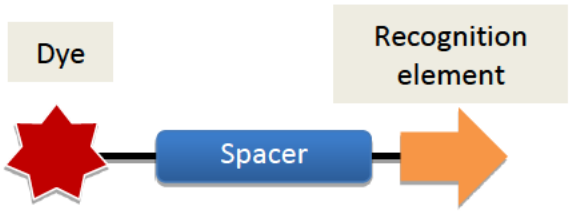

Figure 1.8. Structural elements of an 'always-on' Smartprobe.

Optical molecular imaging probes typically consist of three main components: a recognition (or targeting) moiety, a fluorescent dye and a spacer. The recognition moiety is responsible for forming an interaction with a biological target (e.g. enzyme active site or cell surface receptor). For example, antibodies, antimicrobials and peptides have all previously been used for recognition of specific cell types.[11, 29] As discussed, the dye generates a fluorescent signal upon excitation that can be detected at the desired emission wavelength. A spacer may be used for ease of chemical synthesis, to help with the physicochemical properties of the probe such as solubility or cell penetrating abilities, or to physically separate the dye and recognition element. Often all these elements are optimised to produce a probe with the ideal properties. A

common problem of 'Always-on' probes is low target-to-background ratios which requires specificity to minimise off-target labelling.[18]

1.3.3. Activity-based Smartprobes

Two phenomena that are important for activity-based fluorophores are Förster resonance energy transfer (FRET) and photoinduced electron transfer (PeT).

1.3.3.1. Förster resonance energy transfer

FRET describes the interaction of electronic excited states between two neighbouring chromophores within 10-100 Å proximity. This is a non-radiative process that occurs when the excited state of Dye A relaxes to a neighbouring Dye B that causes quenching, with the energy transferred between the fluorophores.[30] For example, a FRET system can be created by placing a donor fluorophore (Dye A) and an acceptor/quencher (Dye B) in close proximity, linked by a peptide (**Figure 1.9**). Cleavage of the peptide releases the quencher from the FRET system and fluorescence is regained.

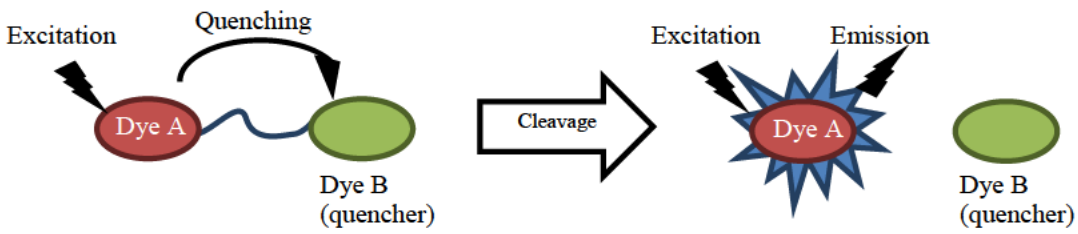

Figure 1.9. Cleavage of the linker between two dyes forms a FRET system and results in de-quenching in a FRET system and "turning on" of fluorescence.

1.3.3.2. Photoinduced electron transfer

In a photoinduced electron transfer (PeT) system excitation of a fluorophore (donor) permits electron transfer from the acceptor partner, rather than electronic relaxation that leads to fluorescence. This occurs provided the oxidation potential of the acceptor is smaller than the donor and the PeT process results in quenching. In the presence of an analyte that changes the oxidation potential of the acceptor group, PeT becomes energetically unfavourable resulting in dequenching.[31]

A related mechanism is intramolecular charge transfer (ICT) which can occur in a molecule with both donor and acceptor moieties. In an excited state, electron transfer occurs from one part of the molecule to another.[10] This has been exploited in molecules by masking the electron donating group with a chemical moiety to change the fluorescent emission.

1.4. Macrophages

Macrophages (from the Greek: big eater) are an immune cell. Along with other leukocytes, macrophages are found throughout the body and play a key role in both the initiation and resolution of inflammation. Their roles include phagocytosis of debris and foreign material, signalling and activation of the immune system through cytokine and chemokine release. Defects in macrophage function can also lead to certain pathologies.[32] A major area of biomedical research is furthering the understanding of macrophage functions in health and disease.

Macrophage functions are known to be specialised to tissues in which they reside. In the lung, alveolar macrophages are adapted to the challenging environment they face; varying oxygen concentrations, contact with toxic inhaled particles and environmental antigens.[32] Alveolar macrophages are long lived and approximately 40% are replaced in a year. Compared to airway macrophages, alveolar macrophages show decreased phagocytic ability until activated and they produce specific cytokines.[32]

Macrophages are differentiated from monocytes and this process is regulated by a number of growth factors (**Figure 1.10**).[33] To study macrophage biology, different models have been used. Peritoneal or bone marrow derived macrophages can be isolated from mice, however there are limitations in comparing mice and human cells, since features of the immune system are species specific.[34] Human macrophage cell lines can also be used such as U937 and THP-1, however these are derived from cancerous tissues. An alternative method is to isolate peripheral blood mononuclear cells (PBMCs) from whole blood. After the lysis of red blood cells, a monocyte population can be purified from other immune cells by cell separation with magnetically tagged antibodies.[35, 36] Subsequently these cells can be stimulated *in vitro* with growth factors to generate macrophages that have different phenotypes.

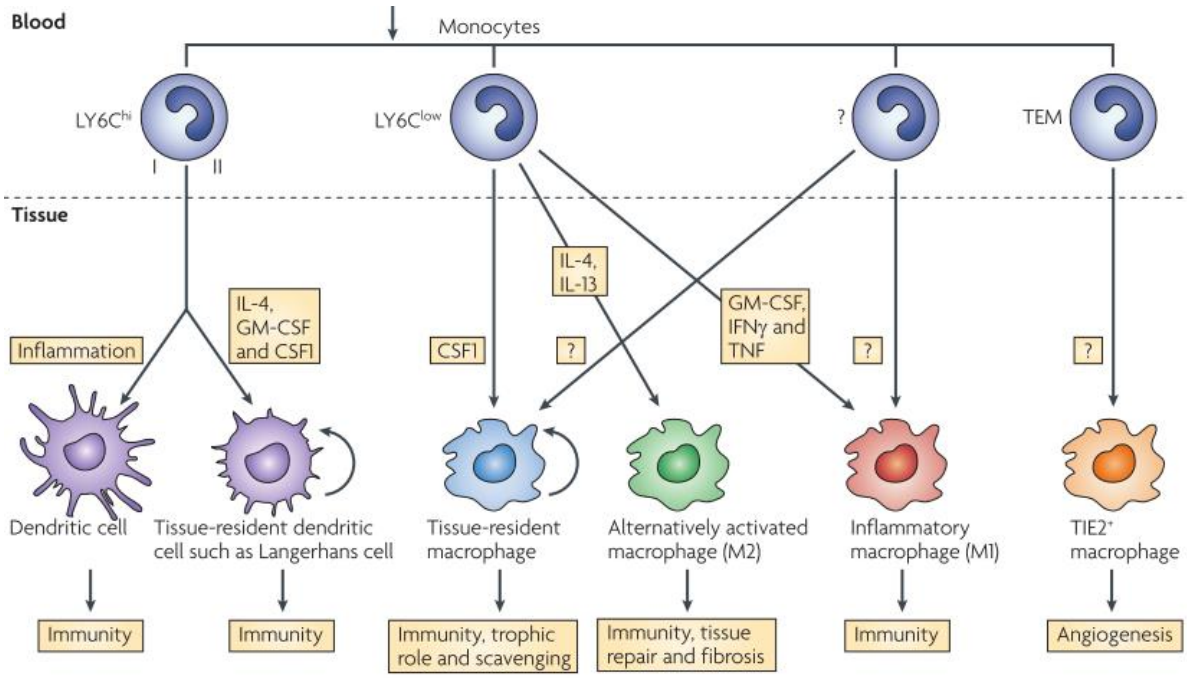

Figure 1.10. Mononuclear phagocyte lineage. Monocytes develop in bone marrow from pluripotent stem cells. Subpopulations of monocytes (including Ly6C^{hi} and Ly6C^{low}) develop depending on the stimuli shown in yellow boxes. Alternatively activated macrophage differentiate through interleukin-13 (IL-13) and IL-4; inflammatory macrophages develop under the influence of GM-CSF, interferon-γ (IFN-γ) and tumour necrosis factor (TNF); Angiopoietin-1 receptor (TIE2)-expressing monocytes (TEMs) give rise to TIE2+ macrophages. The rigid lineage diagrams and growth factor assignments depicted here are for illustrative purposes only. Adapted by permission Springer Nature: *Nature Reviews Immunology*, Pollard.[33] Copyright 2009 Nature Publishing Group.

1.4.1. Macrophage activation

Macrophages respond to different signals triggering activation. This results in a change in cell phenotype which have been broadly classified as M1 and M2 states. M1 macrophages have commonly been referred to as 'classically activated' or 'pro-inflammatory', with the M2 phenotype as 'alternatively activated' or 'anti-inflammatory' (**Figure 1.11**). Although it is now understood that macrophages do not always fit into these strict classifications and have 'plasticity' - the ability to move between phenotypes.[32] These phenotypes have different functions and in disease states

such as chronic obstructive pulmonary disease (COPD) a bias towards the M2 phenotype has been reported.[37] The ability to image and characterise alveolar macrophage activity in the native lung remains a challenge. However, the capability to do this with optical imaging techniques would help us to understand the functions of alveolar macrophages in disease.

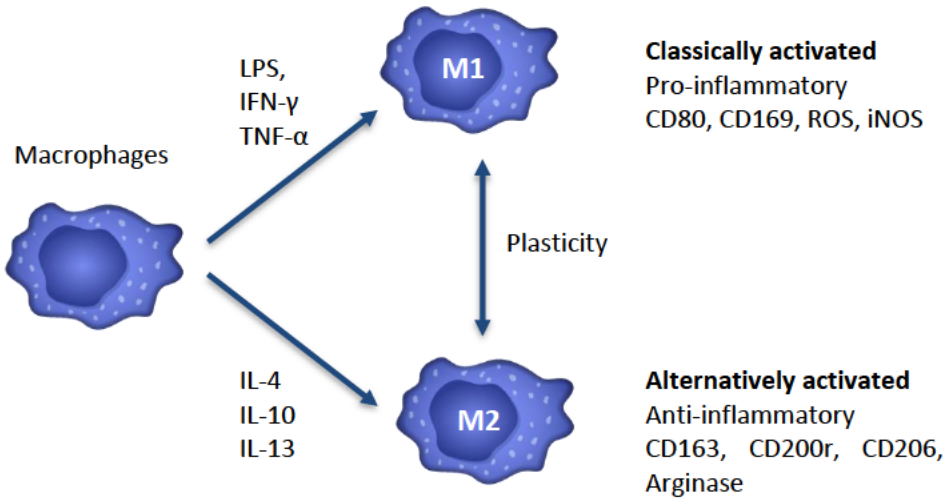

Figure 1.11. Understanding different macrophage polarisation states that can be caused by different stimuli. Examples of common markers for the M1 and M2 states are given.

A number of existing imaging agents have been reported to track macrophage activity including those targeted to matrix metalloproteinases, reactive oxygen/nitrogen species, phagocytosis or cathepsins.[38] Although these agents are excellent for monitoring the inflammatory response, they are likely not specific to macrophages over other host immune cells. An important step remains, the translation of these imaging agents into clinically useful probes. Future work will be required to develop further macrophage imaging agents and validate their specificity, before leading to their human translation.

1.5. Aims

There is a practical need to develop new chemical probes to aid the diagnosis of chronic conditions affecting the lung. This thesis aims to address this through the synthesis of novel Smartprobes targeting processes relevant to pulmonary inflammation and validating their use in biological studies, with the aim to progress these for clinical use. Three sets of probes were investigated in this project.

In order to visualise alveolar macrophages, Smartprobes were synthesised to target macrophages via cell-surface receptors. The folate receptor was targeted using folic acid-fluorophore conjugates and their use validated by *in vitro* studies with cancer cells and human macrophages. The macrophage mannose receptor (MMR) was targeted with an MMR specific nanobody that was fluorescently labelled to give a near-infrared probe for identifying macrophages and was tested with primary macrophages.

To track the damage caused to the epithelial barrier by acute lung conditions, biomarkers of epithelial cell damage were investigated. Near-infrared beta-galactosidase probes were evaluated to detect senescent cells that expressed senescence-associated beta-galactosidase (SA-βGal). These activatable probes were validated *in vitro* and murine tissue slices.

2. Folate receptor probes

Folic acid is an essential nutrient classified as vitamin B9 and was discovered in 1941 by Esmond Snell. Snell first isolated the compound from spinach and named it after the Latin for 'leaf', *folium*. Metabolism of folic acid provides multiple forms that participate in the one carbon metabolism pathway. These folates are key for the biochemical conversion of homocysteine into methionine, deoxyuridylate (dUMP) to thymidylate (dTMP) and *de novo* purine biosynthesis. Folic acid thus plays a crucial role in DNA synthesis and it is an essential nutrient in a human diet since it cannot be synthesised in the body. Interfering with the folate metabolic pathway has been a druggable target for several decades, especially as antimicrobials and in cancers where folate is needed to support cell growth. This led to the development of a number of licensed drugs (often called antifolates), among those is the chemotherapy drug methotrexate which inhibits dihydrofolate reductase (DHFR).[39]

2.1. Folate receptors

The folate receptor gene family has four isoforms FR-α, FR-β, FR-γ and FR-δ. The most studied are FR-α which is expressed in epithelial tissues and FR-β which is restricted to myeloid lineage cells; both isoforms are glycosylphosphatidylinositol (GPI) anchored receptors. The restricted expression of FR-α and FR-β to these tissues makes folate imaging conjugates useful for their visualisation in cancers and inflammatory diseases.[40]

Over the years a number of different folate targeting imaging agents have been developed, taking advantage of the high affinity of folate derivatives for their receptor targets.[41-46] However, many have not been translated further. Recently, a demonstration of the capabilities of folate targeting during fluorescence guided surgery of cancer was described by Mahalingam et al.[47] OTL38 is an NIR labelled folate which accumulates in cancer tissue, has a high target affinity and enables the visualisation of cancer tissue using image-guided surgery (**Figure 2.1** and see **Figure 2.2** for the structure of OTL38). This agent allows the surgeon to see tumour nodules to help improve surgical resection. OTL38 has completed Phase I and II clinical trials for ovarian and lung cancers and is now in Phase III trials for the detection of FR^+ ovarian cancer (NCT03180307).

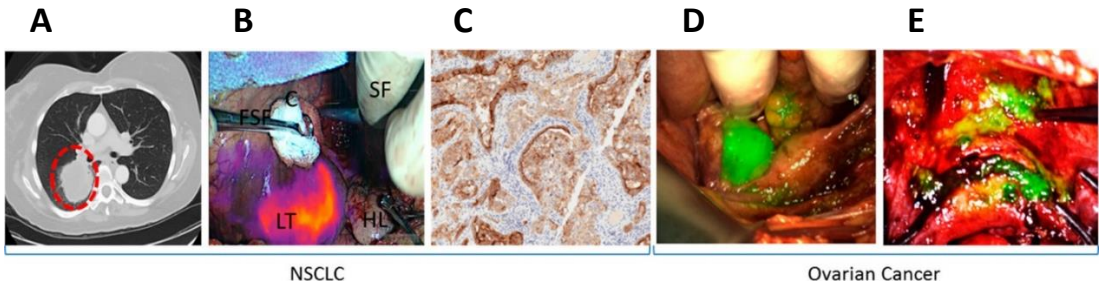

Figure 2.1. Clinical uses of OTL38 showing **A)** Preoperative CT image of pulmonary tumor nodal, **B)** overlay of fluorescence image over white light image of pulmonary tumor nodal, and **C)** immunohistochemical (IHC) staining of resected pulmonary tumor nodal indicating tumor is FRα+. Representative fluorescence images over white light images of primary and metastatic ovarian tumors in **D)** uterine adnexa and **E)** uterus and bladder peritoneum. Note: LT = lung tumor, HL = healthy lung, FSF = Foerster sponge forceps, SF = surgeons fingers, and C = cotton. Adapted with permission from Mahalingam et al.[47] Copyright 2018 American Chemical Society.

2.1.1. Folate conjugates for molecular imaging

The previous studies demonstrate that conjugates of folic acid are applicable for the imaging of FR^+ cells and these maintain high binding affinity to folate receptors. Folate-FITC and OTL38 are the most widely used conjugates for folate imaging with fluorescence emission in the green and near infrared regions of the spectrum, respectively.

The aim was therefore to develop a collection of folate conjugates that could be evaluated with FR-positive cells. It would be assessed if these imaging agents could provide information on the polarisation state of macrophages within the inflamed lung.

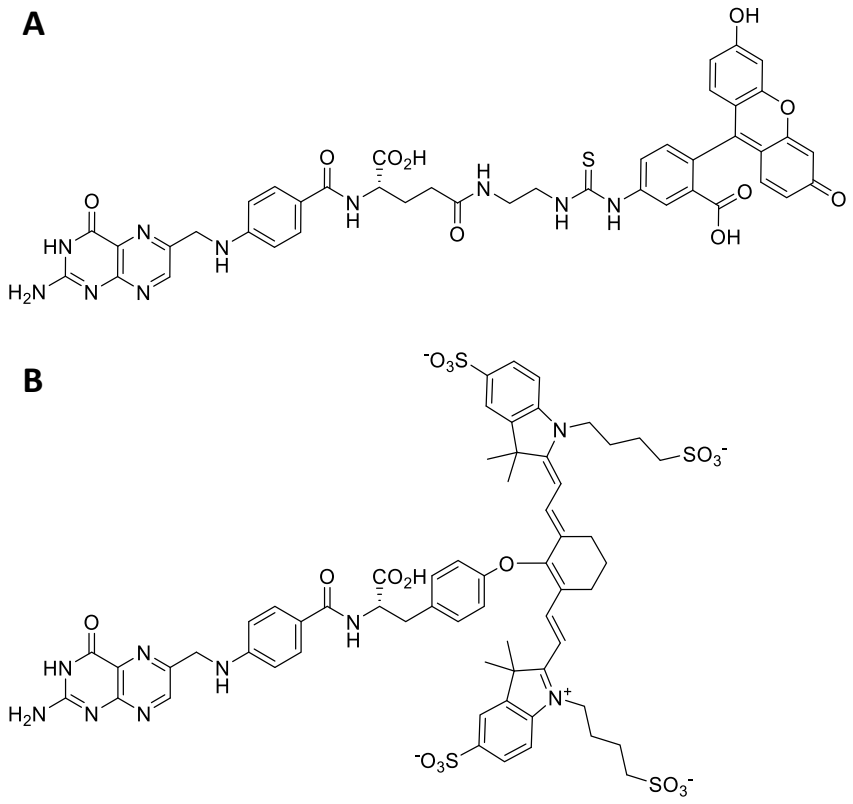

Figure 2.2. Chemical structures of **A)** Folate-FITC and **B)** OTL38.

2.1.2. FR-beta

FR-β has become an investigational tool for targeting myeloid cells since the discovery by Nakashima-Matsushita et al. of its expression on a subset of activated macrophages and placental cells.[48] It is characterised by having a high affinity for folic acid (K_d = 10^{-10} M).[40] Since then, FR-β has been reported on monocytes and macrophages in a number of different diseases.[49-51] The reason for the overexpression of this receptor in these cells types is not currently known. It is also known to be present on $CD34^+$ bone marrow cells[52] and neutrophils,[53] however in these cells the receptor is non-functional and does not bind folates. This could be due to a post-translational modification in these cell types that disrupts its ligand binding ability.

A summary table of evidence of FR-β expression (**Table 1**) shows the complex nature of this biomarker, based on data from a number of different *in vitro* and *in vivo* models; including studies showing folate mediated uptake in rheumatoid arthritis, osteoarthritis and tumour associated macrophages.[48, 54, 55] In the lung human tissue samples from patients with idiopathic pulmonary fibrosis, chronic obstructive pulmonary disease and nonspecific interstitial pneumonia all show an increase of FR-β expressing macrophages. Currently, uptake of folate conjugates by pulmonary macrophages has only been demonstrated *in vivo* in a mouse model.[49]

Table 1: Evidence of the expression of FRβ in immune cells from human and animal samples relevant to certain diseases and the phenotypic markers co-expressed on the FR-β positive cells.

Cell type	Host species	Activation	Phenotypic markers present	Ref.
Peritoneal Mφ	Mouse	Bacteria/ thioglycolate	CD80, CD86, Ly-6C/G	[50]
Synovial Mφ	Human rheumatoid arthritics	N/A	CD14	[48]
Peripheral blood monocytes	Human	None/ naive	$CD16^{-}$ $CD14^{+}$	[56]
Lung Mφ	Mouse	Ovalbumin	CD206, Arg1	[51]
Tumour-associated Mφ	Human melanoma	M-CSF	CD14, CD68 and CD163	[54]
Myeloid leukaemia	Human	N/A[a]	CD33, CD13, and CD11b	[53]

[a] Samples were taken from patients with various leukaemia's

Xia investigated the presence of the folate receptor on activated macrophages from arthritic patients.[50] Fluorescence imaging was used to show that the folate receptor was a valid marker for activated macrophages, while non-activated macrophages did not express the folate receptor. After characterising that bacteria-recruited murine macrophages expressed FR and that these were activated (upregulation of Ly-6C/G, CD80 and CD86), folate-FITC was incubated with the synovial fluid of patients with diagnosed rheumatoid arthritis. A subset of the $CD11b^{+}$ macrophages were found to uptake folate-FITC, and competition experiments showed that this uptake could be inhibited with free folic acid - showing FR specificity. Finally, a technetium-

radiolabelled folate (FolateScan: EC20) was utilised to perform single-photon emission computed tomography (SPECT) imaging of human inflamed joints in a Phase II trial (NCT00588393).

In murine models of asthma, Shen showed that *ex vivo* lung macrophages with an M2 phenotype (arginase^{+}, CD206^{+}) bound the green fluorescent probe, folate-Oregon Green. SPECT/CT imaging of ^{99m}Tc-EC20 showed uptake in ovalbumin induced asthmatic lungs, while there was no uptake in the lungs of healthy mice (**Figure 2.3**).[51]

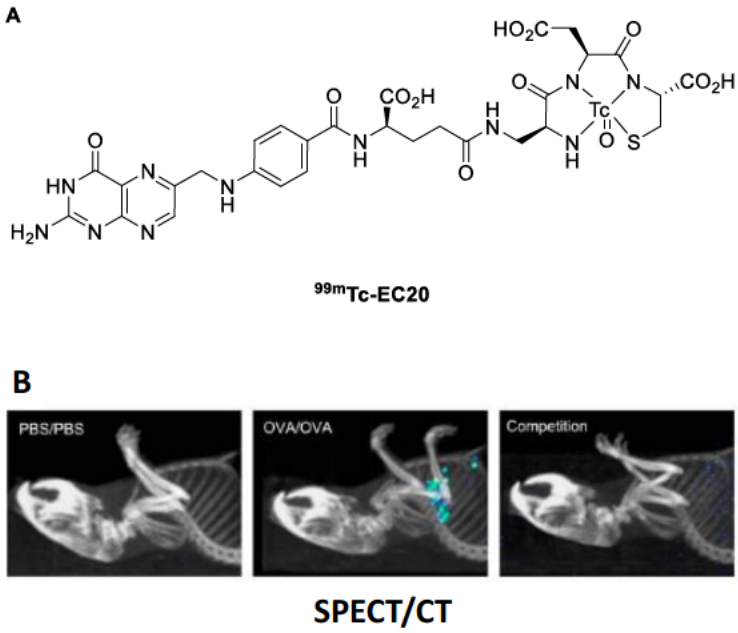

Figure 2.3. A) Chemical structure of EC20 – a folate radiolabel. **B)** SPECT/CT images ^{99m}Tc-EC20 uptake in the lung of OVA-induced asthmatic mice, competition experiment with ^{99m}Tc-EC20 plus 100-fold excess folate-glucosamine. Adapted with permission from Shen et al. Copyright American Chemical Society.[51]

Recent work by Poh showed that a folate liposome could act as a specific method of targeting FR^{+} immune cells, specifically in mouse models of colitis and atherosclerosis.[57] This study used fluorescent DiD (a carbocyanine membrane dye) liposomes labelled with folate, called Fol-liposome-DiD, as a demonstration of the

ability to deliver payloads via the folate receptor which could then accumulate in inflamed tissues. Atherosclerotic mice (ApoE-/- mice fed a high fat 'Western diet') were injected via the tail vein with 2 mg/kg of NT-liposome-DiD or Fol-liposome-DiD, respectively. Fluorescence imaging showed selective uptake of Fol-liposomes in atherosclerotic mice (**Figure 2.4**).

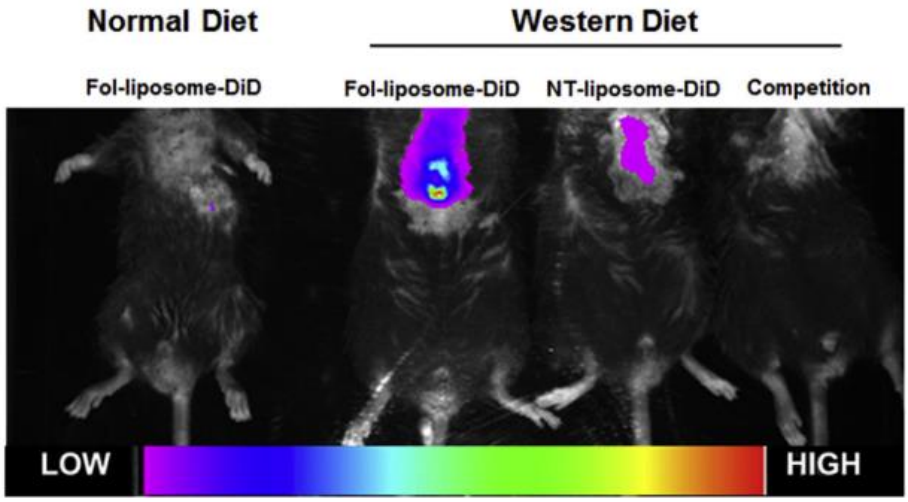

Figure 2.4. Representative images of fluorescent liposomes in an atherosclerosis mouse model (ApoE-/-). Mice were injected via tail vein with 2 mg/kg Fol-liposome-DiD, NT-liposome-DiD, or Fol-liposome-DiD + unlabelled Fol-liposome (competition). 12 hours after injection, fluorescence images were acquired on a Kodak imaging station (λ_{ex} = 635nm, λ_{em} = 700nm). Adapted from Poh et al.,[57] with permission from Elsevier.

Han applied a Cy5 labelled folate probe to an lipopolysaccharide (LPS) murine model of acute lung inflammation.[49] Healthy and inflamed mice were dosed with the Cy5 probe and representative fluorescence imaging is shown in **Figure 2.5**. Flow cytometry was used to show that FRβ^+ interstitial macrophages and monocytes were responsible for probe uptake. The authors concluded that these cells had characteristics of macrophages with an M1 phenotype.

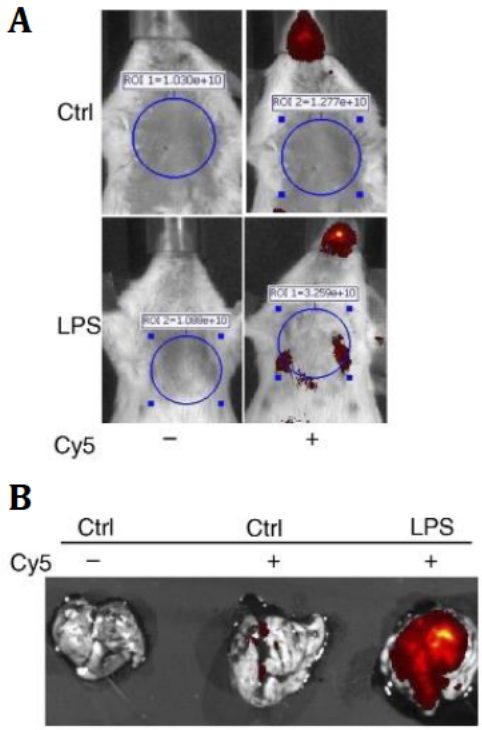

Figure 2.5. Cy5 folate probe uptake demonstrated in an LPS induced inflammation model. **A)** Representative fluorescent imaging (IVIS 200, Xenogen Corp.) showing fluorescence background (no probe) in ctrl and fluorescence at 1 hour after injection of probe. **B)** Ex vivo imaging of probe showing lung fluorescence at 48 hours after PBS (ctrl) or LPS administration. Adapted from Han et al,[49] with permission from the American Thoracic Society (ATS).

In 2009, Puig-Kröger et al. reported FRβ as a marker of M2 phenotype macrophages and its presence on tumour-associated macrophages (TAMs).[54] In vitro, FRβ was expressed selectively on blood monocyte derived macrophages generated in the presence of monocyte colony stimulating factor (M-CSF) and not granulocyte macrophage colony-stimulating factor (GM-CSF). These are generally thought of as M2 and M1 polarisation stimuli, respectively. Furthermore, TAMs isolated from the pleural fluid of breast adenocarcinoma tissue expressed FOLR2 mRNA (the gene encoding for FRβ) and by flow cytometry it was shown these cells bind folate-FITC (**Figure 2.6**).

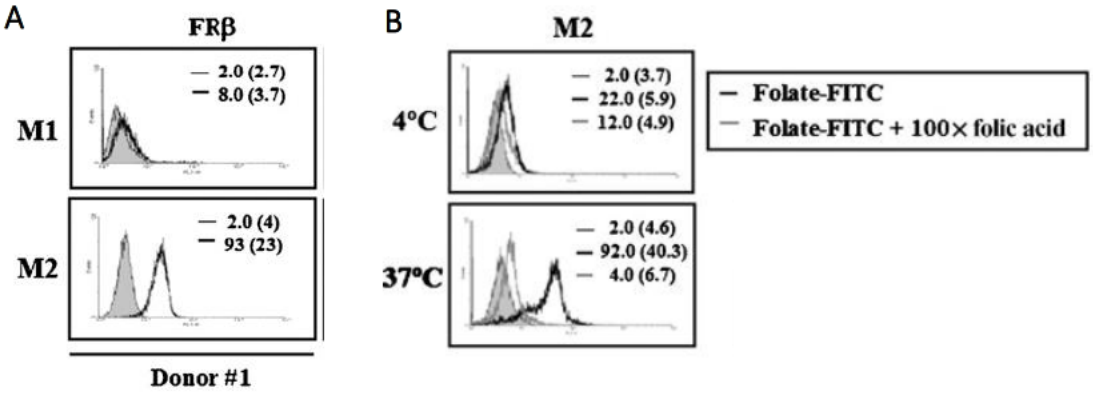

Figure 2.6. A) Cell surface expression of FRβ on M1 and M2 macrophages, determined by flow cytometry using a polyclonal antiserum against human FRβ (empty histogram) and control antiserum (filled histogram). **B)** Binding (4°C) and internalization (37°C) of folate-FITC by M2 macrophages, in the absence (empty histograms, black line) or the presence (empty histograms, gray line) of a 100 mol/L excess of folic acid. The percentage of marker-positive cells and the mean fluorescence intensity (in parentheses) are indicated in flow cytometry experiments. Adapted from Puig-Kröger et al.,[54] with permission from AACR.

In summary, macrophage expression of the folate receptor has been revealed in several different disease relevant models and it doesn't seem to fit clearly into simple M1/M2 activation states, which is a limitation of these simplified categorisations. However, given that folate conjugates appear to accumulate at sites of inflammation in preclinical models, imaging FR positive cells could provide valuable information towards understanding the immune response in lung diseases.

2.2. Synthesis and characterisation

Originally, two molecules were synthesised for folate receptor targeting – labelled with either a green or a far-red emitting fluorophore. Firstly, FITC-Folate (**1**) was

synthesised as a tool compound from a reported procedure.[41] A folic acid analogue with an ethylenediamine spacer was synthesised in high and was conjugated to the single isomer of fluorescein-5-isothiocyanate (5-FITC) through a thiourea bond (**Scheme 2.1**). The product was purified by RP-HPLC and lyophilised, giving a 30% yield.

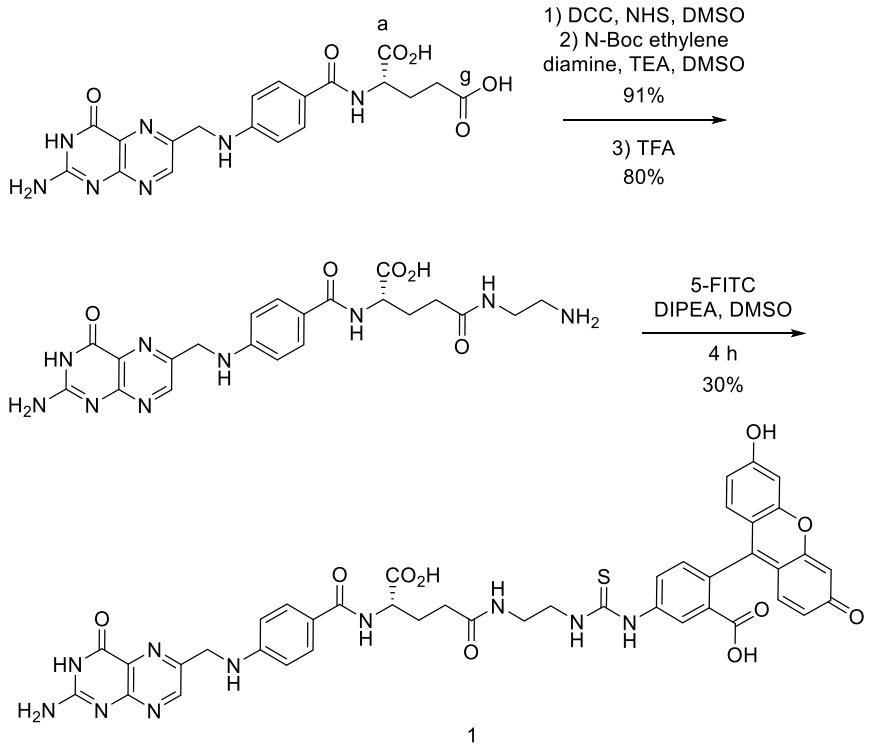

Scheme 2.1. Synthesis of FITC-Folate (**1**). An ethylenediamine spacer was selectively added to the γ carboxylic acid group (highlighted) of folic acid. Following Boc deprotection under acid conditions (TFA), the free amine was conjugated to the fluorophore via a thiourea moiety.

To synthesise a far-red analogue, we decided to conjugate a Cy5 dye to folate. A far-red fluorophore would be more suitable for *in vivo* imaging applications given the known problems of green autofluorescence from tissues, however there are limited examples of far-red folate conjugates.[7, 44] The Cy5** fluorophore was chosen as it had been demonstrated in a recent clinical study to have suitable solubility, stability,

brightness and clearance when used *in vivo*.[19] Using the amine functionalised folic acid previously prepared, the Cy5** folate conjugate was synthesised by reaction with Cy5**-NHS that was formed in situ (**Scheme 2.2**). This required purification by RP-HPLC giving the probe Cy5**-Folate (**3**).

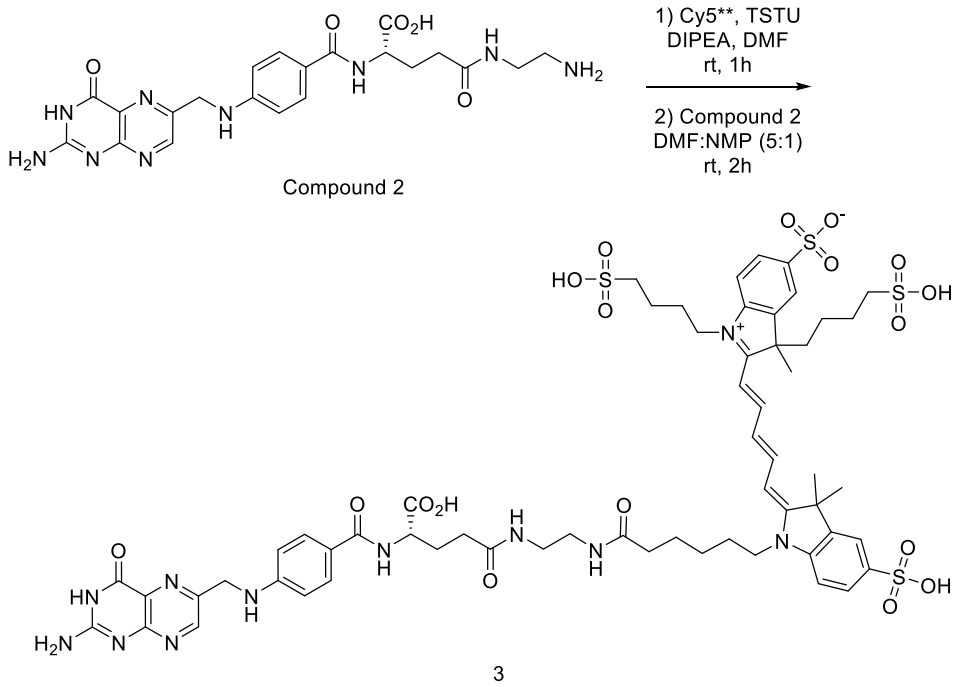

Scheme 2.2. Synthesis of Cy5**-Folate (**3**). Cy5**-NHS was formed in situ with the activating agent TSTU (*N,N,N′,N′*-Tetramethyl-O-(N-succinimidyl)uronium tetrafluoroborate) and immediately allowed to react with Compound 2.

Attempts to modify the ethylenediamine spacer with a longer PEGylated spacer gave reaction mixtures from which it was difficult to isolate the product. Additionally, poor final yields and tedious RP-HPLC purification required after the solution synthesis led to an alternative synthetic route being sought. Existing routes involve the functionalisation of folic acid to bear an alkyne group for click chemistry[58] or its hydrolysis to give pteroic acid.[59] However, these require further synthetic steps and purifications, while the ideal procedure would not require extensive modification of the fluorophore or folic acid.

2.2.1. FolateTag: generating folate receptor targeting probes

In order to generate a library of folate compounds, a standard Fmoc solid phase synthesis was developed on a polystyrene resin with a Rink-Amide linker. The following building blocks were coupled under standard DIC and Oxyma coupling conditions: Fmoc-Lys(Dde)-OH, Fmoc-PEG_2-OH; then the deprotected terminal amine was reacted with a folate NHS ester. The reactive folate NHS ester was synthesised using conditions reported by Trindade, that result in higher regioselectivity for the gamma-conjugate over the alpha-conjugate in the final product due to formation of the cyclic anhydride.[58] In the last step, the Dde protecting group was removed by hydrazine to give a deprotected amine that could be used for fluorophore conjugation (**Scheme 2.3**).

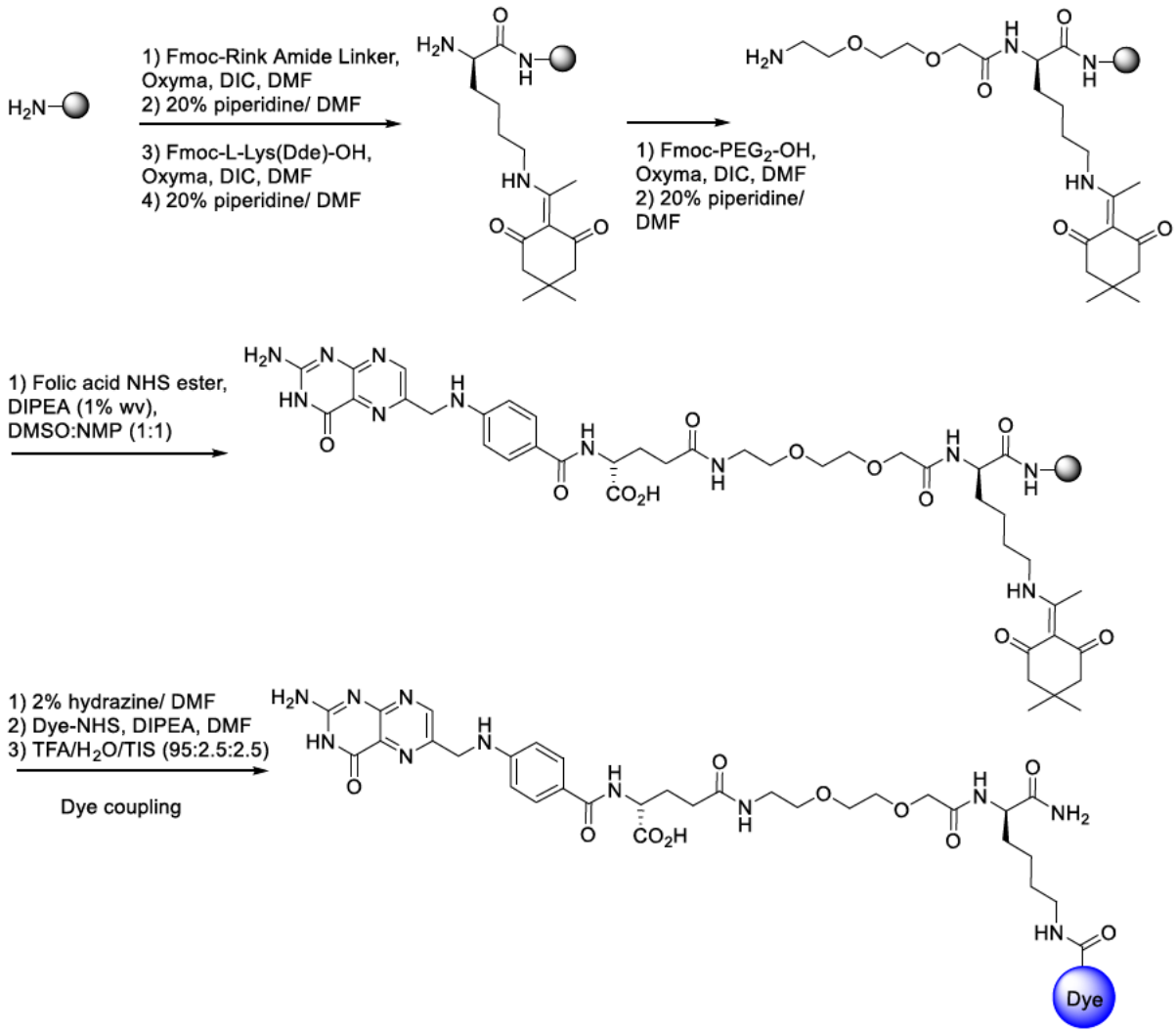

Scheme 2.3. Solid phase synthesis of the FolateTag resin for the generation of fluorophore-folate conjugates.

Next, the following fluorophores were conjugated to the FolateTag resin. 6-carboxyfluorescein, a green emitting fluorophore; nitrobenzoxadiazole, a solvatochromic green fluorophore; Merocyanine-SO, an orange emitting solvatochromic fluorophore; and Cy5**, the far red fluorophore previously used in the first generation analogue (**Figure 2.7**). These fluorophores were chosen to represent a diverse mix of chemical structures, fluorescent properties and 'always-on' versus 'solvatochromic' fluorophores.

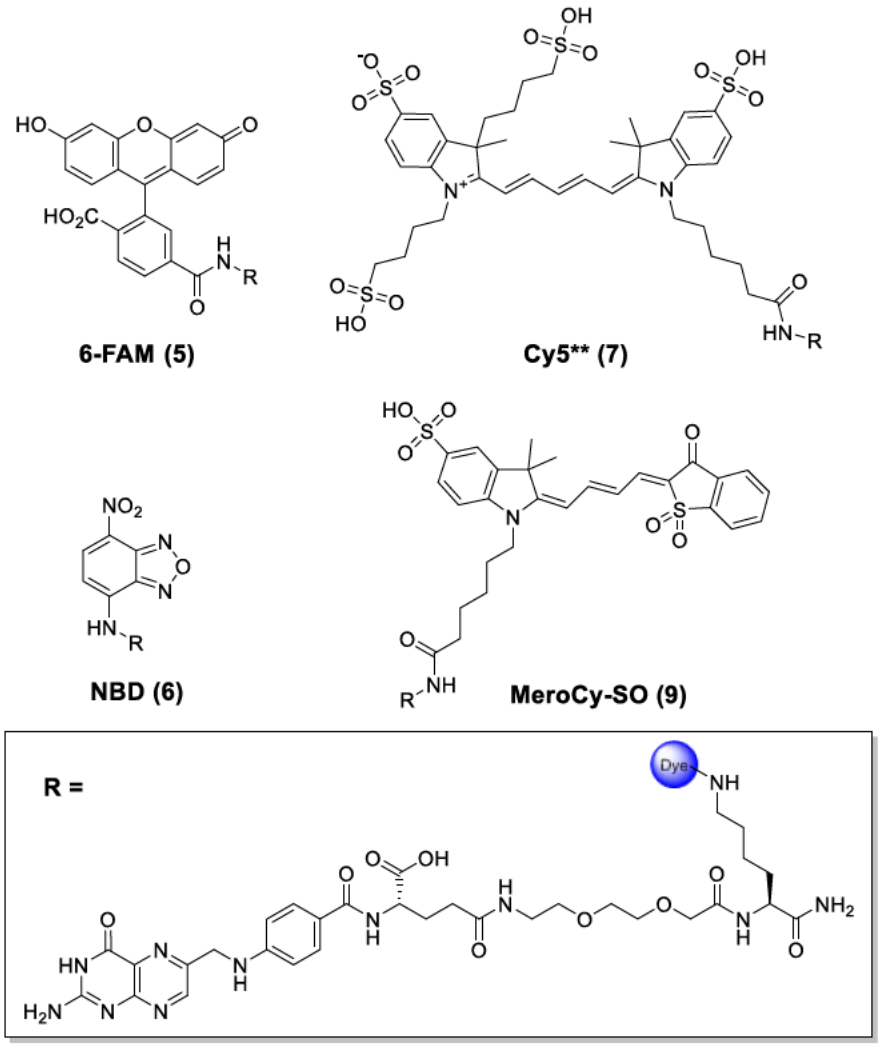

Figure 2.7: The range of fluorophores that were conjugated with the FolateTag resin (inset) included 6-carboxyfluorescein (6-FAM), Cy5**, nitrobenzoxadiazole (NBD) and a merocyanine (MeroCy-SO). The compound code of the probe is bracketed.

2.2.2. Optical properties

After the purification and characterisation of the pure compounds by HPLC and MALDI-TOF MS, their optical properties were measured. UV-Vis spectroscopy was used to show that the absorption spectra were comparable to the parent fluorophores after conjugation to folate (**Figure 2.8**). This class of compound has good aqueous solubility and all stock solutions were prepared in PBS buffer (pH 7.4).

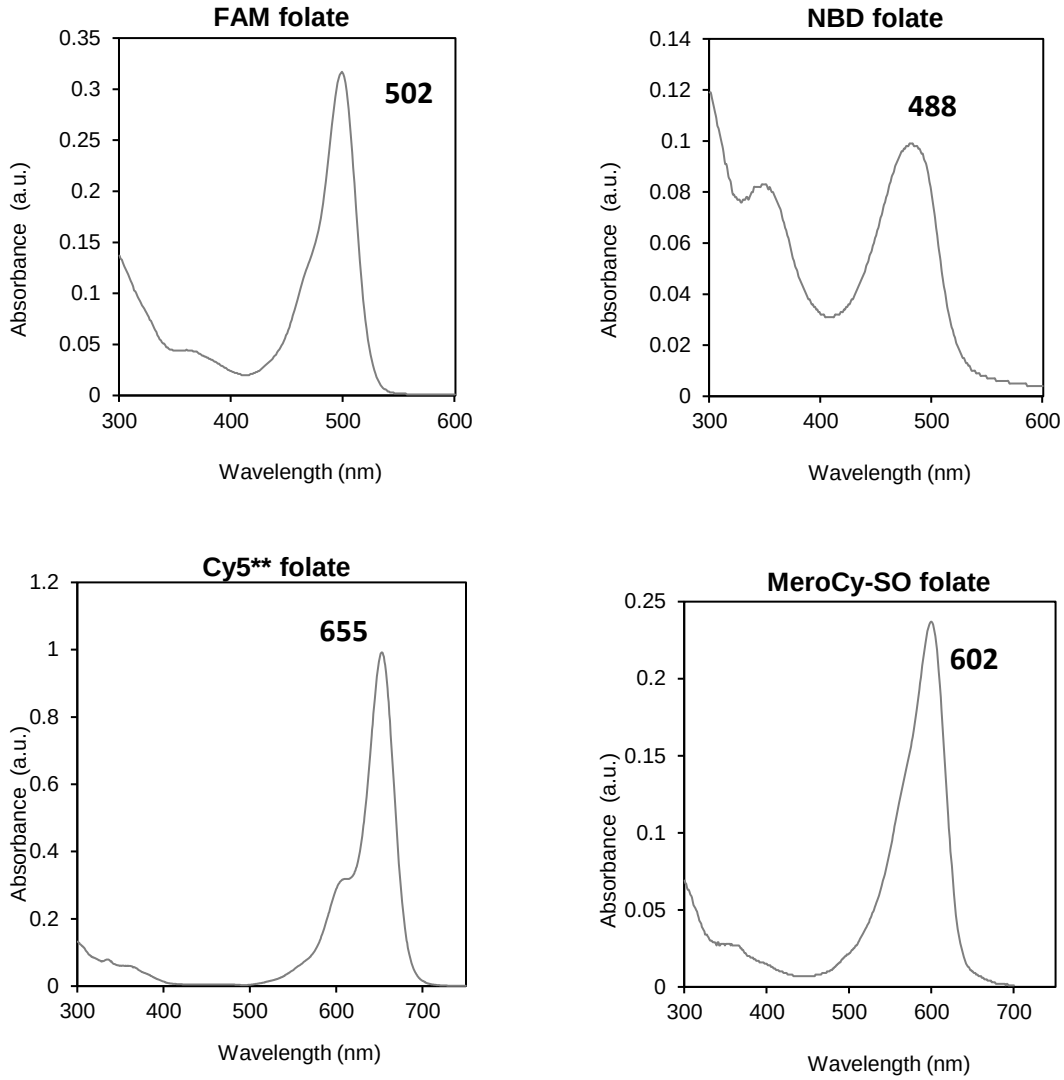

Figure 2.8: Absorption spectra of folate-fluorophore conjugates were recorded using a Shimadzu UV1800 spectrophotometer. Samples were prepared in PBS pH 7.4. The absorption maxima are given for each conjugate (in nm).

Next, the fluorescence spectra were measured. These compare closely to the parent fluorophores showing that attachment to FolateTag had caused no change in fluorescent properties (**Figure 2.9**).

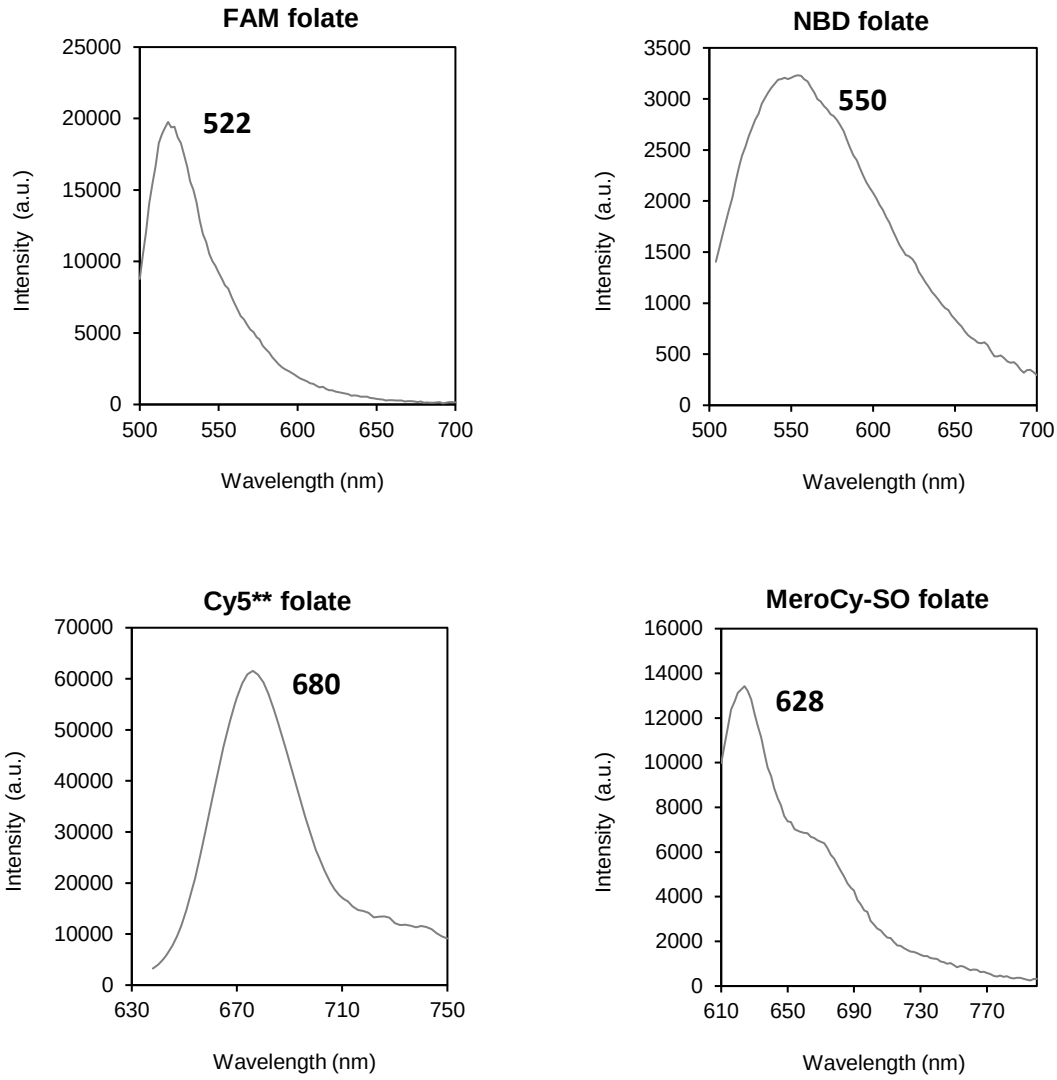

Figure 2.9: Fluorescence spectra were recorded in PBS solution at room temperature using a Horiba FluoroMax fluorometer. The emission maxima are given for each conjugate (in nm). Excitation energies: FAM folate:497 nm, NBD folate: 459 nm, Cy5** folate: 652 nm, MeroCy-SO folate: 582 nm. Spectra were processed with SpectraGryph.

2.3. FR^+ cancer cell targeting

Initial evaluation of the probes was carried out with the KB cell line (ATCC CCL17, human cervical carcinoma, subclone of the HeLa line). KB are known to overexpress FR at higher levels than other immortalised cancer cell lines (HeLa, SKOV3) and

therefore provide a good model for testing target interaction of these probes. Previous experience in our group with folate-targeted agents showed it was necessary to use folic acid depleted media (FF-RPMI) for cell culture, up to 2 weeks prior to experiments. This agrees with reported methods by other researchers, providing cells with functional levels of folate receptor expression that are not saturated.[60, 61] Cell survival is maintained by the minimal level of folic acid present in FBS, which is at more physiologically relevant levels in this media (FF-RPMI) compared to the 2 µM in conventional RPMI.[61] After establishing KB and A549 cultures (as a negative FR-α control), these were cultured over 2 weeks in folate deficient RPMI media. However, as these immortalised cancer cells are presumably adapted to excess folate supplementation, over 2 weeks cell proliferation noticeably decreased.

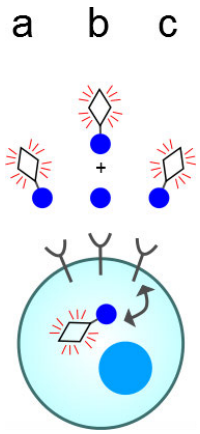

Figure 2.10. FR cell targeting and modes of action, **A)** Folate probe binding, **B)** Folate probe in the presence of 1000x folic acid, **C)** Folate probe binding and receptor mediated internalisation active at 37 °C.

Each compound was assessed by flow cytometry and live cell confocal microscopy for FR receptor-mediated labelling and endocytosis (**Figure 2.10**). Confocal microscopy was performed in a controlled environment (37 ^{o}C temperature, 5 % CO_2) and cells were incubated with nucleus and plasma membrane stains according to manufacturer's

instructions, washed with PBS, then incubated with the folate probe for 15 min at 37 ^{o}C and subsequently washed with PBS once. A Leica SP5 confocal system was used with laser lines 405 nm, 488 nm, 633 nm and tuneable detectors set at 435-460 nm (for Hoechst), 500-550 nm (for fluorescein), 640-750 nm (for Cy5). For all microscopy studies, except with a Cy5 probe, cells were co-stained with CellMask™ DeepRed (Invitrogen) to highlight the plasma membrane. The CellMask™ stains are amphipathic dyes that have a lipophilic component which interacts with the cell membrane and a hydrophilic dye which localises to the plasma membrane. However, long incubation times caused this stain to be endocytosed resulting in additional intracellular staining. The results are summarised below for each probe.

FITC-folate

FITC-folate (**1**) gave strong cell membrane staining of all KB cells, as expected from existing data on this compound. There was no off-target labelling upon A549 cells with **1**.

KB A549

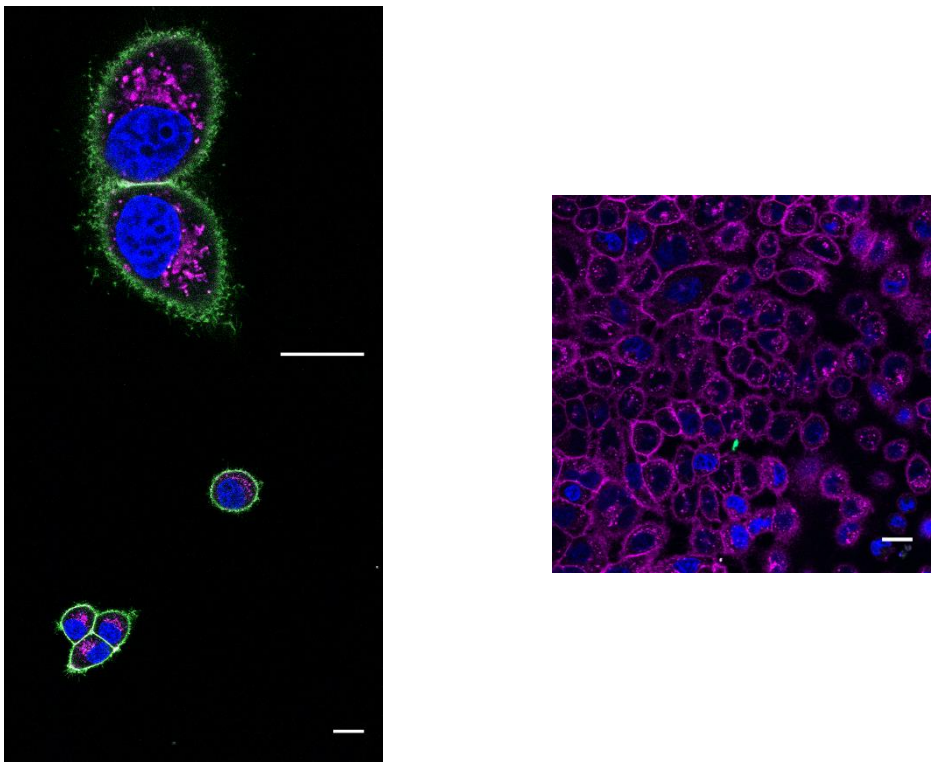

Figure 2.11. Confocal imaging of KB (left, enhanced size) and A549 control cells incubated with 0.5 µM of probe **1**. Legend: Probe **1** (green), nuclei (blue) and CellMask DeepRed (magneta). Scale = 20 µm

Cy5-folate**

The Cy5** analogue (**3**) from the initial series of compounds showed bright membrane localisation on all cells, similar to the FITC analogue. No labelling was seen on A549 control cells.

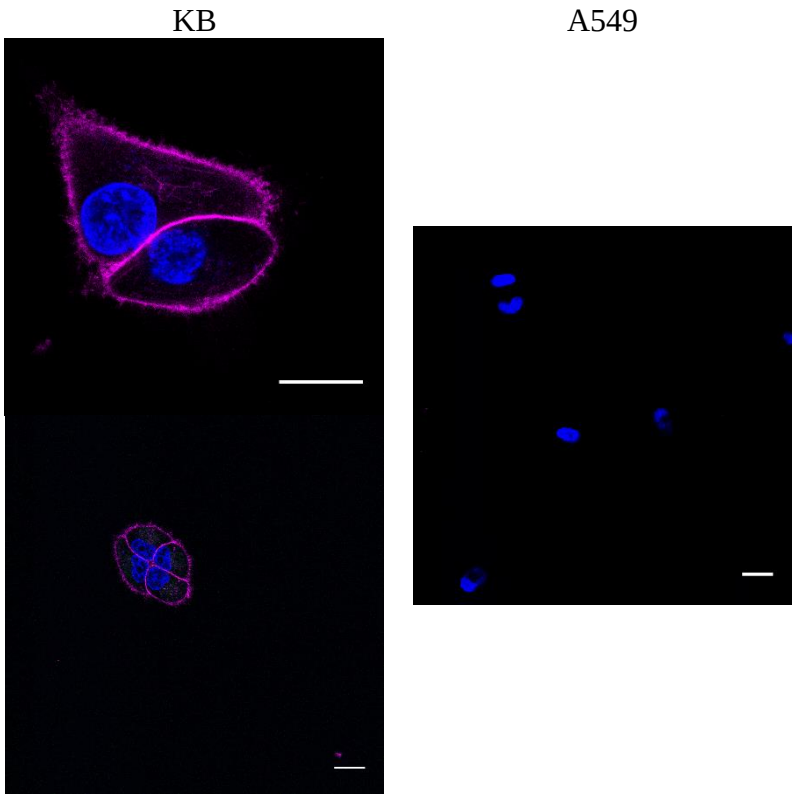

Figure 2.12. Confocal imaging of KB and A549 cells incubated with 1 µM of probe **3**. Legend: Probe **3** (magenta) and nuclei (blue). Scale = 20 µm

FAM folate

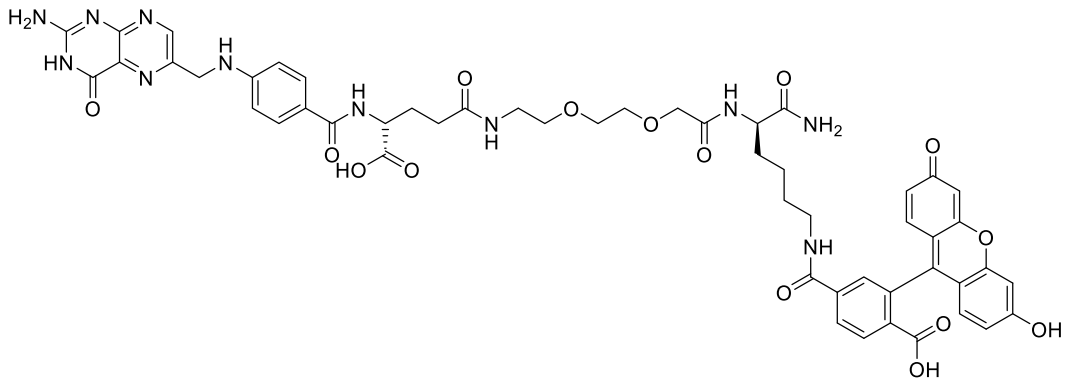

Figure 2.13. Chemical structure of the FAM-Folate probe (**5**).

With the PEGylated FAM-Folate probe (**5**), this was highly specific to the cell membrane of KB cells. Although the intensity was not as bright as the FITC fluorophore with **5**.

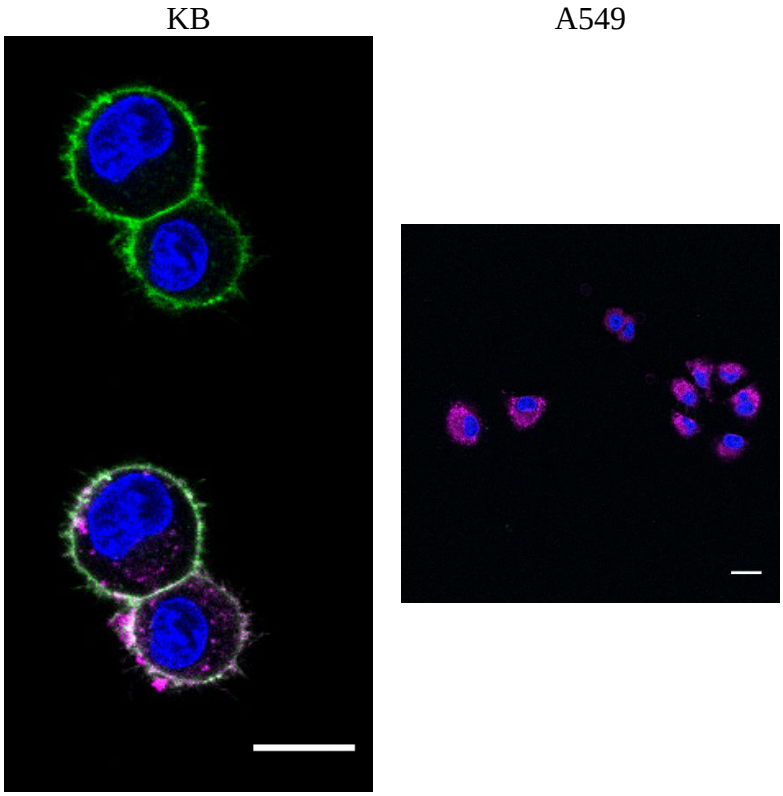

Figure 2.14. Confocal imaging of KB and A549 control cells incubated with 1 µM of probe **5**. Merge of probe and membrane stain on KB cells shown bottom left. Legend: Probe **5** (green), nuclei (blue) and CellMask DeepRed (magneta). Scale = 20 µm.

NBD folate

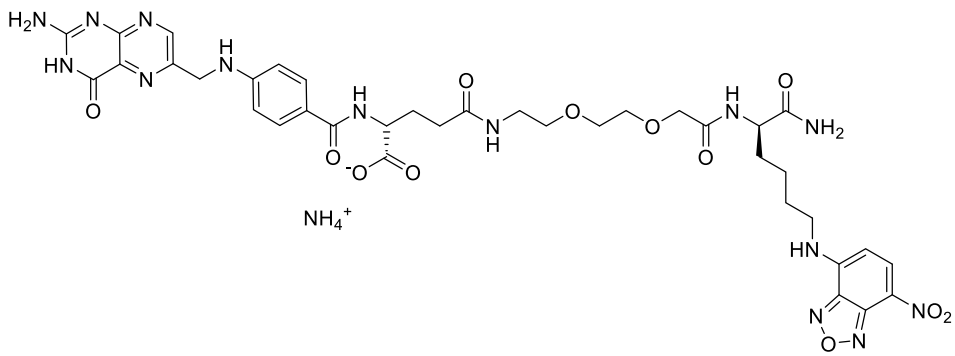

Figure 2.15. Chemical structure of the NBD-Folate probe (**6**).

Confocal imaging with the NBD-Folate probe (**6**) showed very weak staining, presumably due to **6** not localising in hydrophobic environments which are necessary to switch on the fluorophore. Instead localised intracellular staining was seen. Additionally, there was some colocalisation of **6** with the membrane stain. The membrane stain was endocytosed over time, meaning it could be in endosomes or recycling endosomes.

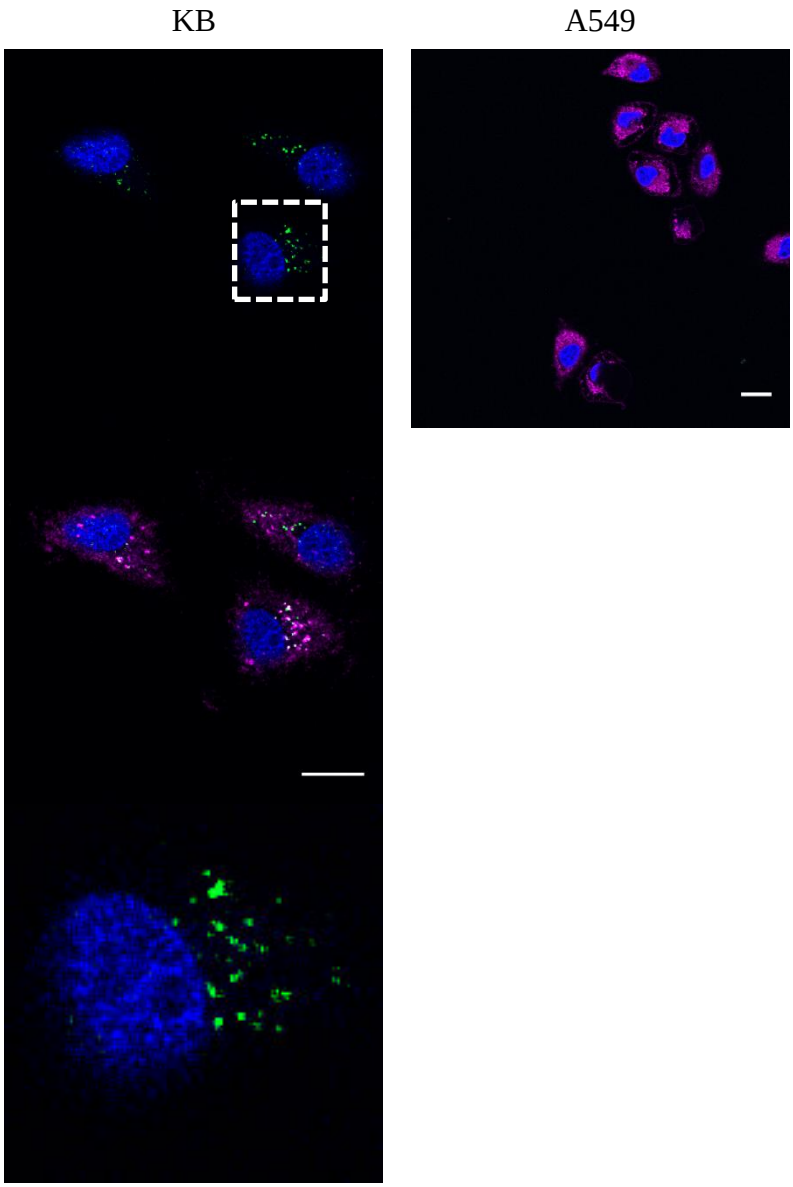

Figure 2.16. Confocal imaging of KB (**6** and merge image shown separately) and A549 control cells incubated with 1 μM of probe **6**. The NBD staining of the cell highlighted is shown separately for clarity (below). Legend: Probe **6** (green), nuclei (blue) and CellMask DeepRed (magneta). Scale = 20 μm

Cy5 folate (7)**

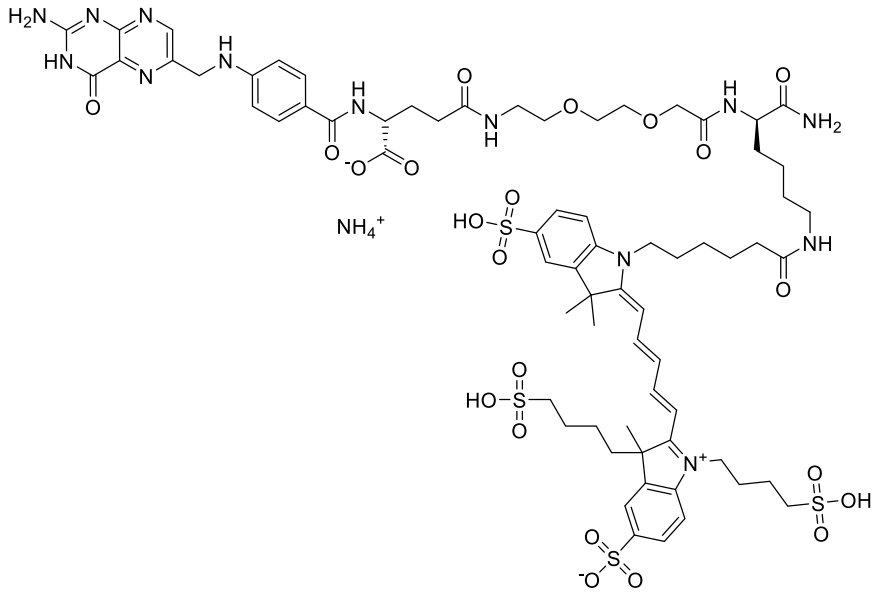

Figure 2.17. Chemical structure of the Cy5**-Folate probe (**7**).

Confocal imaging with KB cells showed bright membrane staining with **7** and it did not stain A549 cells.

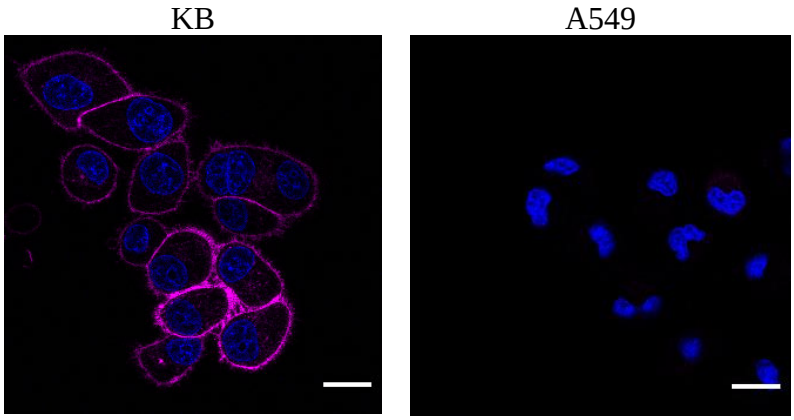

Figure 2.18. Confocal imaging of KB and A549 control cells incubated with 0.5 µM of probe **7**. Legend: Probe **7** (magenta) and nuclei (blue). Scale = 20 µm

MeroCySO-folate

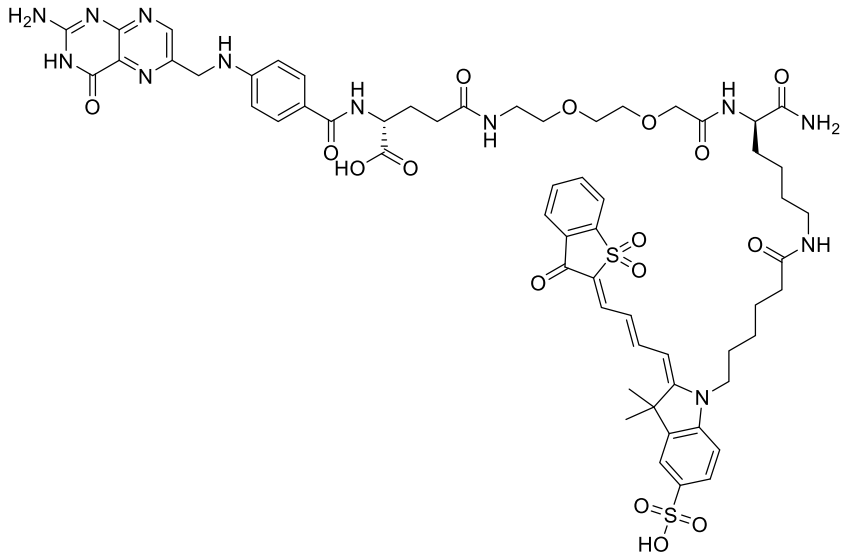

Figure 2.19. Chemical structure of the MeroCySO-Folate probe (**9**).

Confocal imaging was performed with **9**, however labelling of KB cells was weak even with increased laser power (**Figure 2.20**, red staining). There was weak intensity cell membrane labelling, as seen by the localisation with the green plasma membrane staining. Labelling of A549 cells was not seen (not shown).

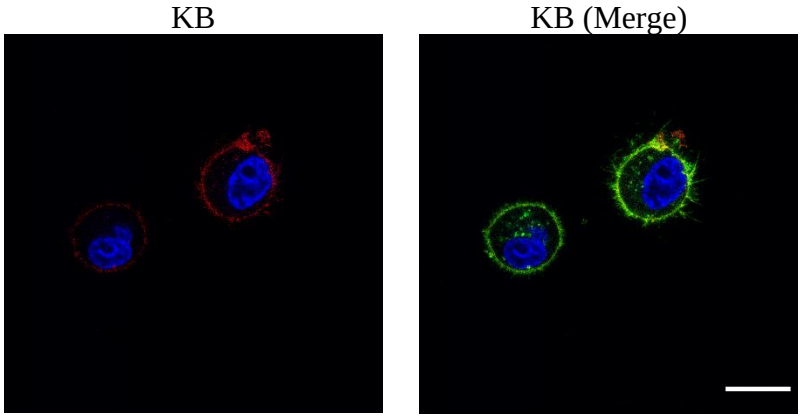

Figure 2.20. Confocal imaging of KB cells incubated with 1 µM of probe **9**. Left: Nuclei and Probe **9** channels, Right: Merge. Legend: Probe **9** (red), nuclei (blue), and CellMask Green (green). Scale = 20 µm

2.3.1. Flow cytometry

Using flow cytometry these observations were quantified by looking at; optimal incubation times, the concentrations required to saturate folate receptors and determination of specificity by blocking probe binding with 1000x molar excess of folic acid. **Figure 2.21** shows the results of these experiments.

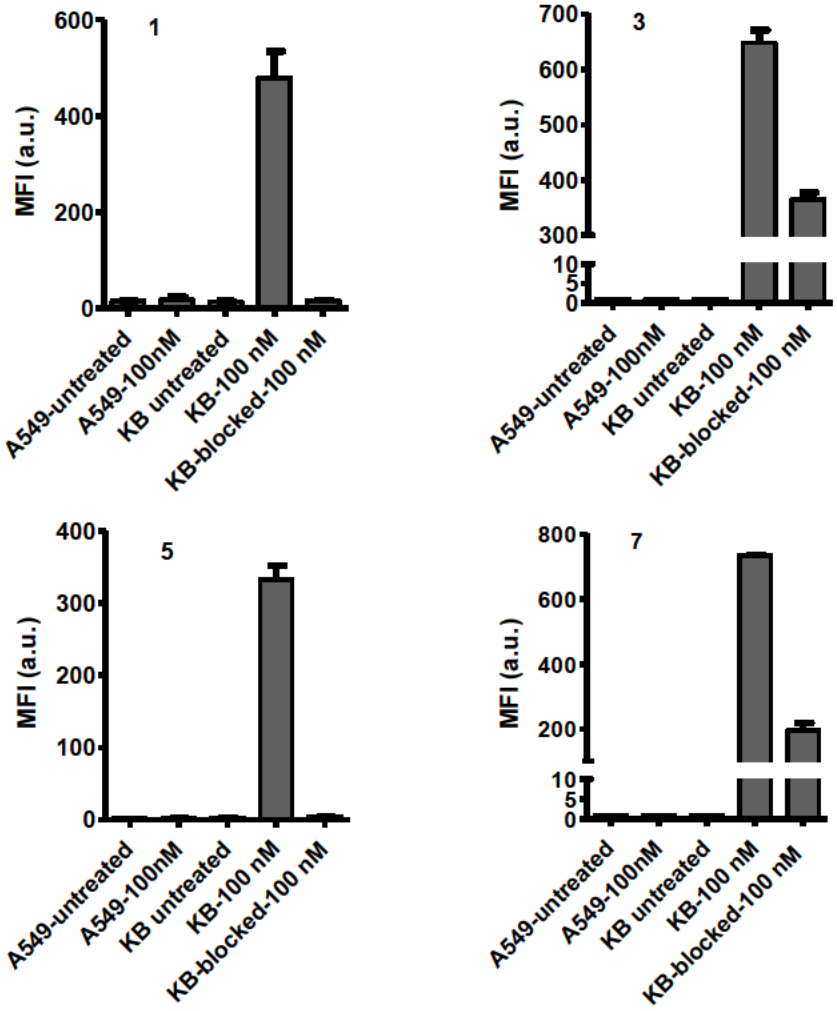

Figure 2.21. Flow cytometry of KB and A549 cells with 100 nM fluorescein (**1, 5**) and 100 nM Cy5** probes (**3, 7**), showing selectivity for KB cells and the ability to block the binding of these probes with 1000x excess folic acid. All experiments were performed with 100 nM probe and an incubation time of 30 minutes, as this was the saturating conditions for FITC-folate. Flow cytometry was performed with a BD FACScan and CellQuest software and gated for live cells based on FSC/SSC profiles. Excitation: 488 nm, emission filter: 525/20 nm for probes **1** and **5**; excitation: 633 nm, emission filter: 666/27 nm for probes **3** and **7**. N=3, MFI + SEM.

Both fluorescein probes (**1, 5**) performed similarly. With KB cells, the compound saturated available receptors at 100 nM and no uptake was seen on A549s under the same conditions. Blocking with excess folic acid reduced the mean fluorescence intensity (MFI) to background levels, suggesting the binding was receptor dependent. With the Cy5** probes (**3, 7**), KB cells were also saturated by 100 nM of probe and no uptake was seen on A549 cells, demonstrating folate targeting. For probes (**3, 7**) some binding occurred after blocking, with a signal reduction for **3**, however this could be due to the recycling nature of the receptor.

Flow cytometry showed a fluorescence increase in the presence of NBD-Folate (**6**), however it was not used further due to the relatively low signal over background (**Figure 2.22**). Flow cytometry was not performed with **9** due to the inability to excite the MeroCySO fluorophore with the FACScan flow cytometer.

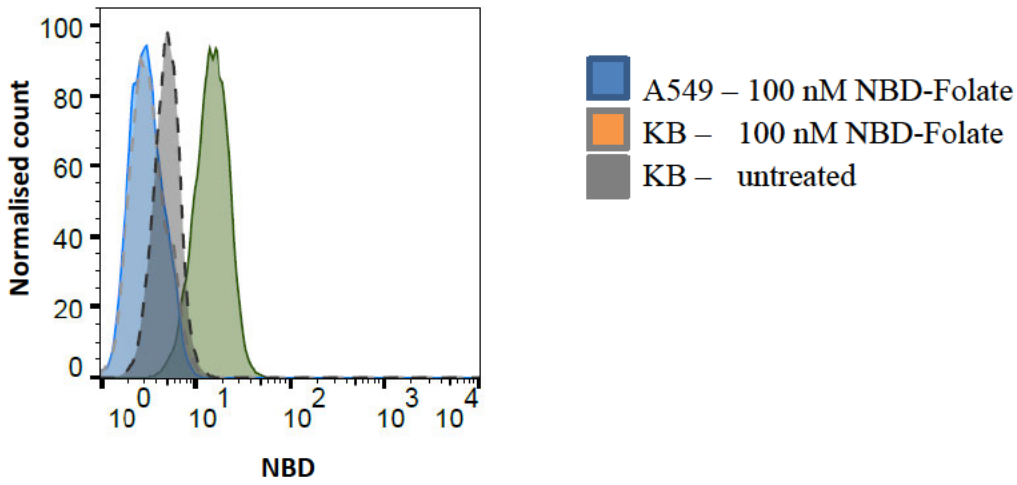

Figure 2.22. Representative flow cytometry histogram of KB and A549 cells, showing a modest increase in NBD fluorescence when KB cells are incubated with probe **6** (100 nM). Flow cytometry was performed with a BD FACScan and CellQuest software and gated for live cells based on FSC/SSC profiles. Excitation: 488 nm, emission filter: 525/20 nm.

2.3.2. Relative binding affinities

Binding saturation by flow cytometry was measured for serial dilutions of the fluorescein and Cy5** conjugates (**1, 3, 5, 7**) to KB cells. This data was then processed to generate binding isotherms (**Figure 2.23**).

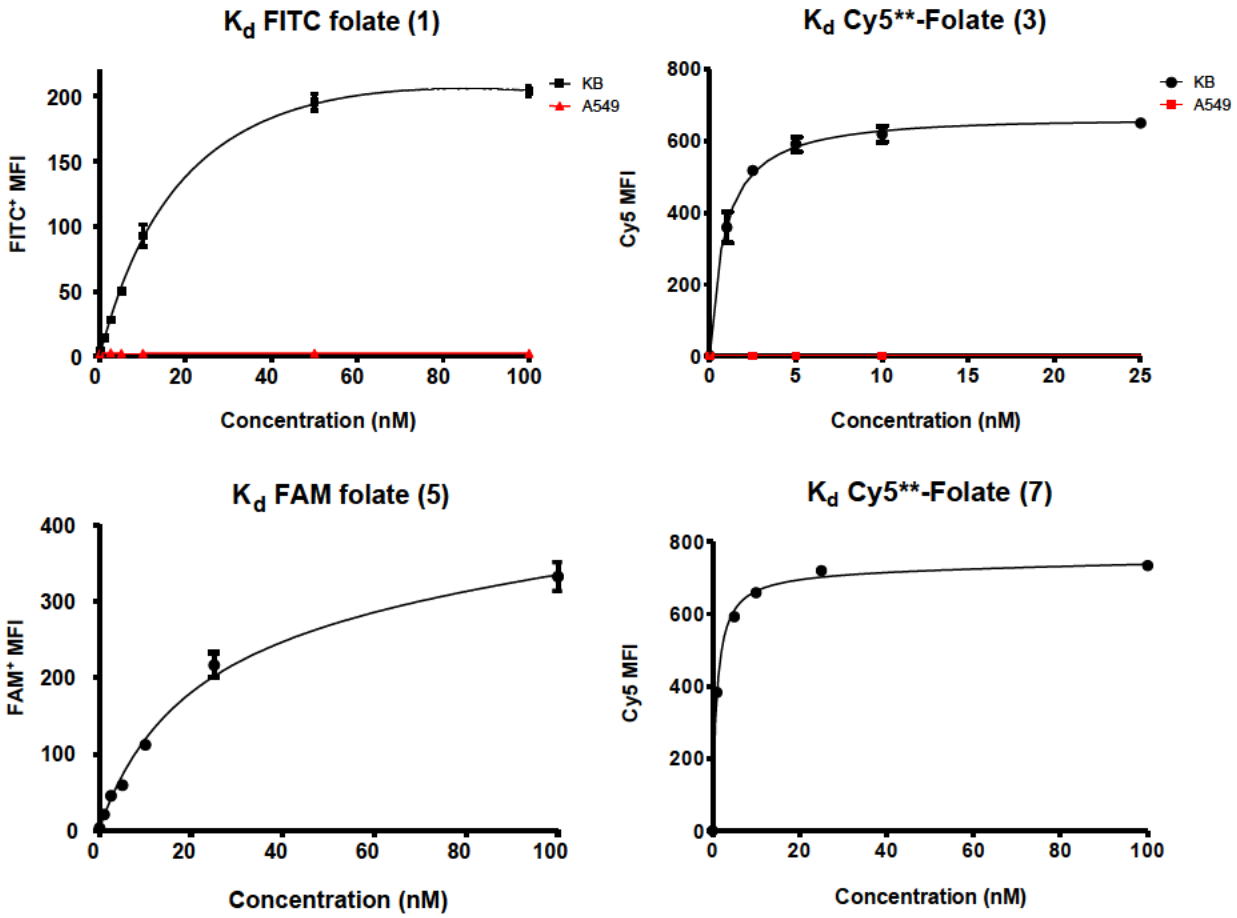

Figure 2.23. Binding curves were measured by flow cytometry of KB or A549 cells incubated with serial dilutions of each probe (1 to 100 nM) for 15 min at 37 °C. Flow cytometry was performed with a BD FACScan and CellQuest software and gated for live cells based on FSC/SSC profiles. Excitation: 488 nm, emission filter: 525/20 nm for probes **1** and **5**; excitation: 633 nm, emission filter: 666/27 nm for probes **3** and **7**. Curves were fitted by non-linear regression using GraphPad Prism. N=3, MFI + SEM.

Conjugate	Affinity (nM)
1	26 ± 1.1
3	0.9 ± 0.1
5	20 ± 6.0
7	0.9 ± 0.1

Table 2: Relative affinity (concentration of 50% saturation) was derived for each conjugate from the non-linear regression of binding curves generated in **Figure 2.23**.

From fitting non-linear regression curves, the affinity of each probe could be determined. The K_D was determined from the concentration of ligand at which half of the receptors are occupied (**Table 2**). Every folate conjugate assessed has a binding affinity in the low nanomolar range, with the Cy5 conjugates having higher affinity under these assay conditions. This shows that the large fluorophore moiety does not interfere with the FRα binding affinity. There was not a large difference in affinity between the shorter linker and PEG_2 linker (e.g. 26 nM (**1**) and 20 nM (**5**)).

2.3.3. Cellular cytotoxicity

Cytotoxicity of each probe to KB cells was assessed using the CellTitreGlo 2.0 assay (Promega) which measures ATP activity that can be directly related to cell viability. As expected, very little cytotoxicity was seen at the compound concentrations of 50 nM to 500 nM for all compounds. The highest concentration used was five-fold higher than that used in most functional experiments. In addition, the Pierce LDH (lactase dehydrogenase) assay was used to measure possible cytotoxicity based on membrane damage by cytotoxic compounds. If cell membranes were damaged then more LDH would be released, suggesting higher cytotoxicity of the compound. In the LDH assay, there was some LDH release at the highest concentration particularly for **6**, suggesting the cell membranes had been partly compromised.

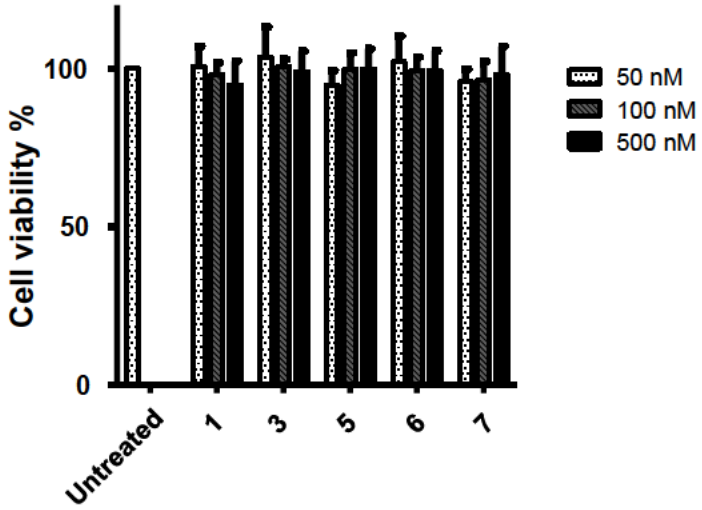

Figure 2.24: CellTitreGlo 2.0 cytotoxicity assay shows no decrease in viability after incubation with 50, 100 and 500 nM concentrations of probes for 2 hours. Data was normalised to the untreated control. N=3

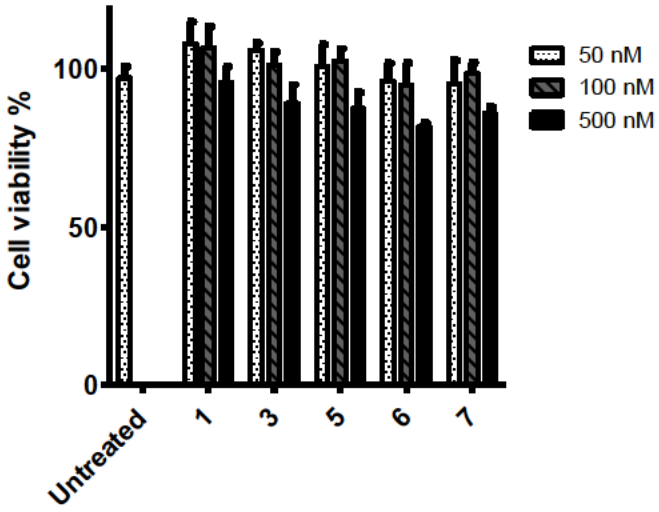

Figure 2.25. LDH cell viability assay after incubation with 50, 100 and 500 nM concentrations of probes for 2 hours, relative to the untreated control. N=3

2.3.4. Primary lung cancer phenotyping

To validate the clinical applicability of the probes the labelling properties towards digested human lung tissue were explored. We chose to focus on lung adenocarcinoma over squamous cell carcinoma samples, due to reports that these cancers had higher

levels of FR-α expression (10^3 to 10^4 receptor/cell).[14, 62] Also, normal lung tissue was assessed as a comparison. We selected the best performing FAM and Cy5 probes (**5** and **7**) to be evaluated in a multiparameter flow cytometry assay which aims to identify the different cell types present in a primary tissue digest (**Figure 2.26**, carried out by Richard O'Connor at the QMRI). In normal lung samples, the probe preferentially labelled $EpCAM^+$ epithelial cells. No significant staining was seen on $CD45^+$ cells which could be expected as the majority of cells in this population are T cells and lymphocytes that do not express folate receptors.[49-51] However, when the $CD45^+$ population was gated for macrophages that do express folate receptors, some binding was apparent. The high expression of folate receptors in normal lung tissues has been reported before, however, the quality of adenocarcinoma tumour digest was poor, meaning these samples had too few cells to analyse.[63]

The labelling of normal lung tissue could be a problem for the identification of tumour cells in a clinical setting. However, previously developed folate conjugates have been reported to not accumulate in the lung. This could be because the folate receptor is expressed on the apical membrane which is not exposed to folate image agents delivered through the bloodstream in clinical studies. Also, in our experiment it is possible that tissue digestion could change the receptor expression. Further work is

required to understand the cell types that are labelled by this probe with primary cells and whether this could be applicable for in vivo lung cancer diagnosis.

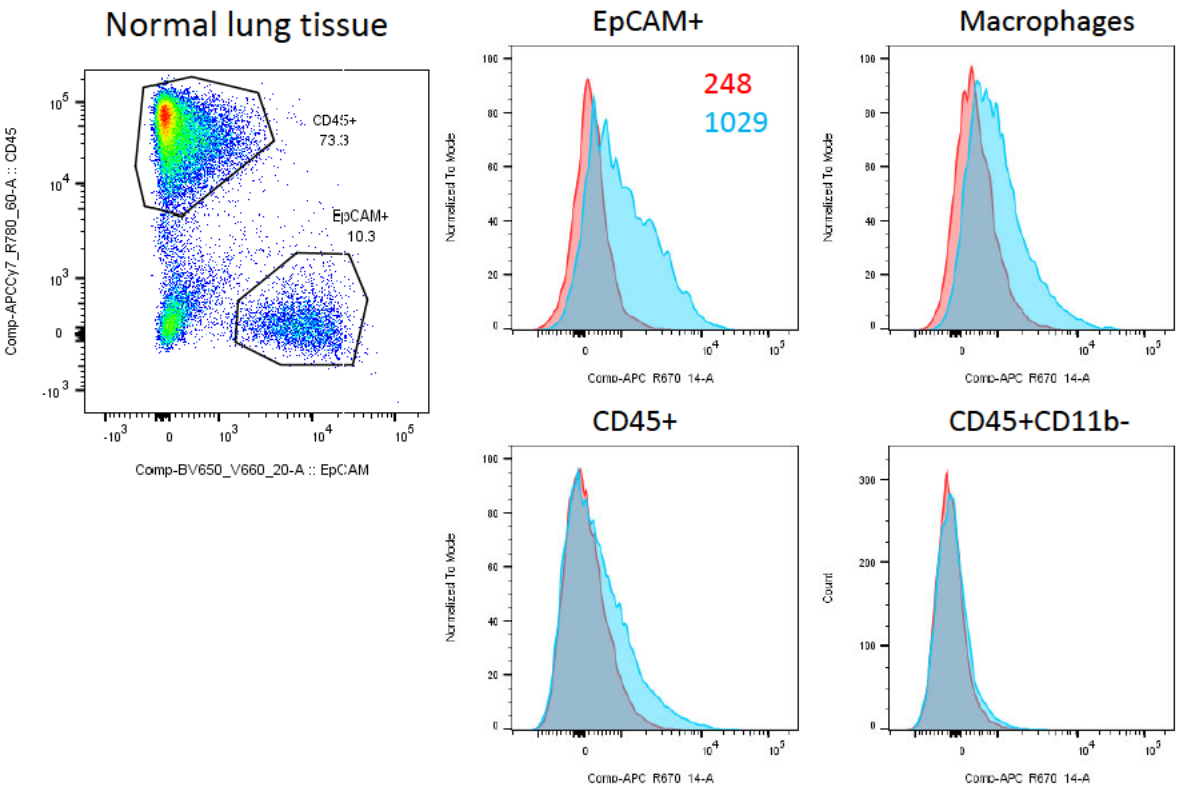

Figure 2.26. Representative flow cytometry of lung tissue digests. **A)** Gating strategy to separate CD45 and EpCAM cells. **B)** Histograms of binding on subsets of cells showing untreated (red) and Cy5**Folate **7** (100 nM) probe treatment (blue) groups. MFI is given for EpCAM+ cells (top left). Data from Richard O'Connor.

2.3.5. Cancer cell summary

Using a folate-deficient cancer cell model, compounds were specifically targeted to the folate receptors overexpressed on KB cells. This was demonstrated thoroughly with confocal microscopy and flow cytometry studies. Microscopy clearly showed the preference of folate targeted compounds for KB cells. All compounds appear to saturate available binding sites at 100 nM within an incubation time of 30 minutes. Receptor binding could be knocked down by pre-incubation with folic acid, a known

high affinity ligand for folate receptors, to show that binding was due to interaction with the folate receptor. Further evidence of folate specific binding was shown with FR negative A549 cells that do not uptake the conjugates.

While under the ideal conditions of our *in vitro* assays these compounds are straight forward to assess, it was more difficult to apply in primary lung cancer tissue digests.

2.4. FR^+ macrophage targeting

In collaboration with Tom Speight, we had tried to reproduce work that showed that monocyte derived macrophages were capable of binding folate conjugates.[64] In addition, monocytes themselves should uptake folate conjugates as previously shown.[56] Macrophages, monocytes, lymphocytes and neutrophils were obtained from the buffy coat of healthy blood donors as described in Chapter 1.

Our initial results by flow cytometry suggested low amounts of binding occurred to the folate receptor, as the overall change in fluorescence was small. Secondly, there was not a significant amount of binding to macrophages and lymphocytes compared to the non-targeted Cy5 dye that used as a control condition (**Figure 2.27**). It appeared that non-receptor mediated events dominated in the case of monocytes, as we were unable to compete probe binding to this cell type (**Figure 2.27C**). It is worth noting, in this experiment a concentration of 1 μM Cy5**-Folate probe was used, as we believed this would be enough to saturate any available receptors. In this experiment, differentiation of macrophages was carried out with autologous serum and this may lead to different phenotypic markers compared to the reported studies of folate receptor

beta expression. Also, there are mixed opinions on how well *in vitro* MDM culture can represent pulmonary macrophages, with different expression of common markers shown between MDM and AM populations in healthy donors[65] and COPD patients.[66]

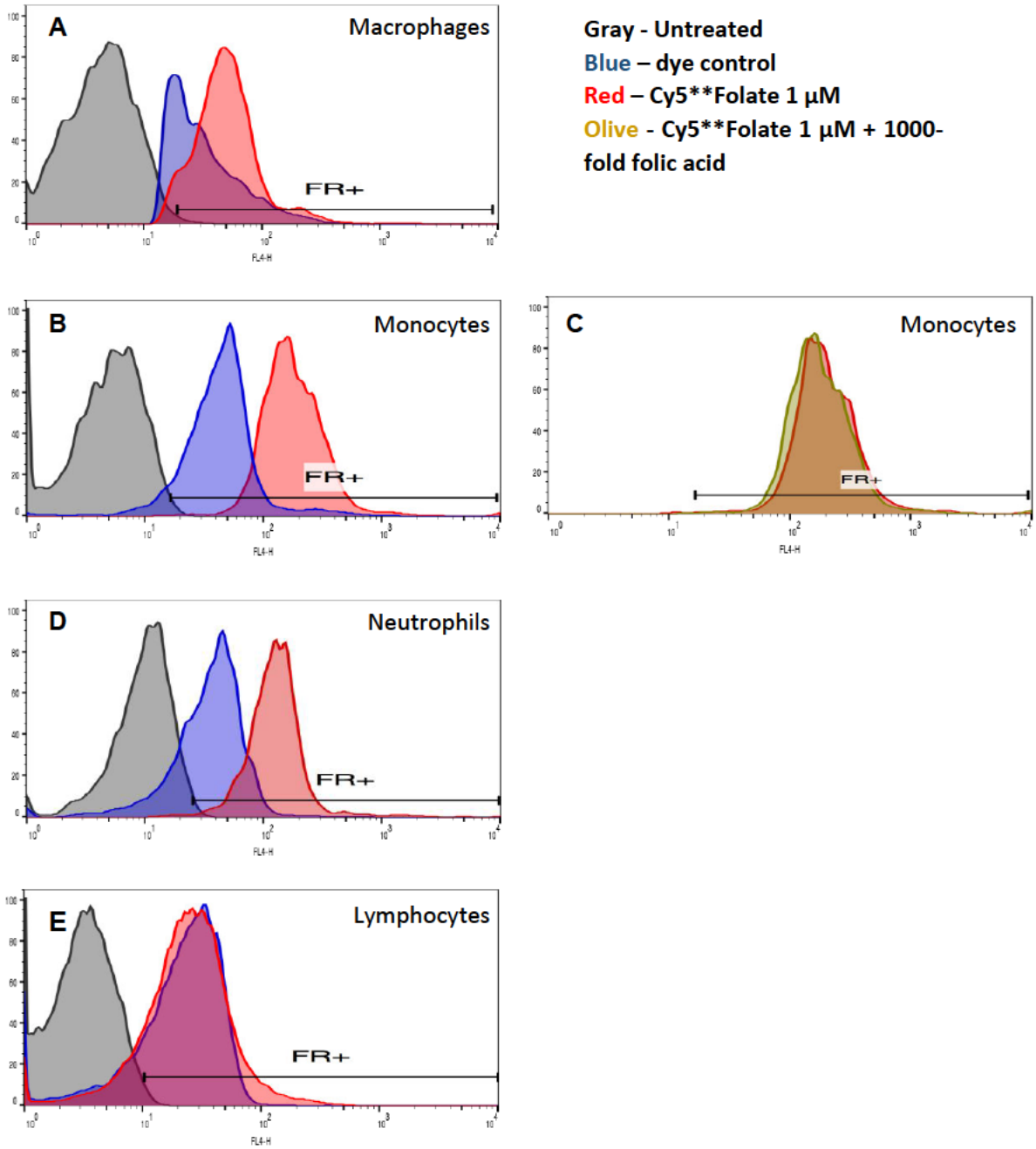

Figure 2.27. Representative flow cytometry history showing initial profiling of Cy5**-Folate (**3**) (1 µM incubated in RPMI for 30 minutes at 37 °C) to **A)** macrophages, **B)** monocytes, **D)** neutrophils and **E)** lymphocytes isolated from healthy volunteers. **C)** Binding to monocytes could not be competitively inhibited with 1000-fold unlabelled folic acid. Data obtained by Tom Speight.

As this model was not initially useful, a macrophage cell line was used to represent alveolar macrophages, with the advantage that cells could be generated without needing blood donors.

2.4.1. NR8383 expression of FR-β

To demonstrate the folate receptor was a valid target for visualising alveolar macrophages, the NR8383 rat alveolar macrophage cell line was used. There were several reasons for choosing this particular cell line. They are one of the few immortalised alveolar macrophage cell lines, along with other commonly used macrophage lines such as RAW264.7 murine leukaemia monocyte derived macrophages, U937 human lymphocytes and THP-1 human leukaemia monocytes which can be differentiated to macrophage-like cells. Although this line is derived from rats, the advantage of NR8383 cells is they adequately represent the features of human alveolar macrophages.[67] Additionally, NR8383 cells are known to respond in a functional manner to common stimuli (e.g. lipopolysaccharide, interferon-gamma, interleukin-4) to produce activated macrophages that release inflammatory cytokines, such as tumour necrosis factor (TNF-α).[67, 68] Initially, the level of FR-β expression in this cell line was determined as it had not previously been shown to express FR-β.

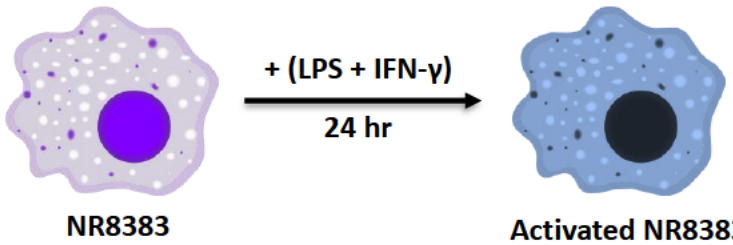

Figure 2.28. Stimulation conditions used to generate activated NR8383 cells.

We also wanted to determine whether FR-β expression was upregulated under classical activation conditions with lipopolysaccharide (LPS) and interferon-gamma (IFN-γ).

There were several challenges to detecting this target; there is no well-validated anti-rat folate receptor-β antibody and it was unclear which cell lines express high levels of this receptor (for use as a positive control). Instead, a number of groups have produced custom antibodies or transfected cell models.[53, 69] Initially, validation work was performed to determine if NR8383 cells expressed FR-β on the cell surface with flow cytometry, and to check the levels of protein expression by Western blot.

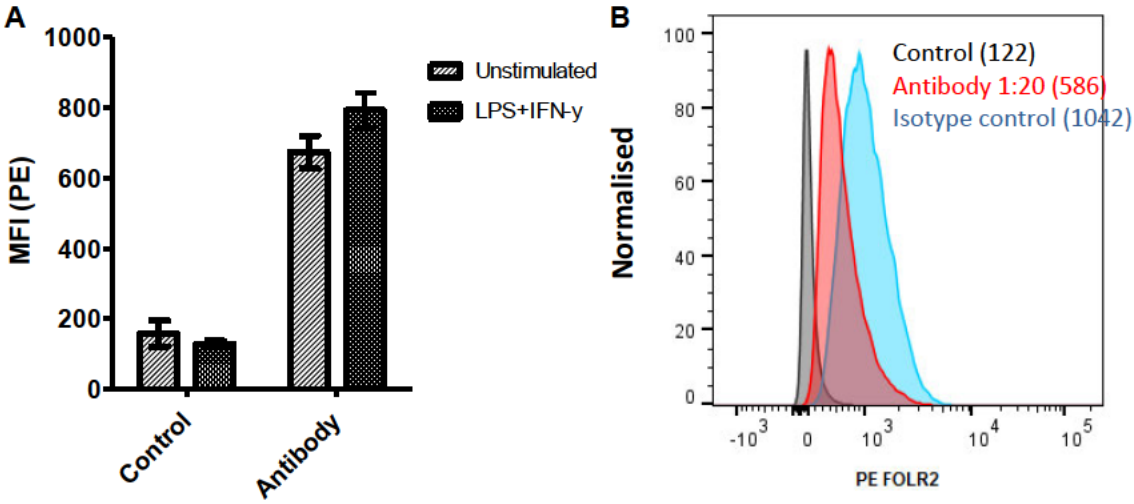

Figure 2.29. Validation of FOLR2 (FR-β) expression was determined by flow cytometry. **A)** Mean fluorescence intensity from the flow cytometry of antibody stained NR8383 cells and cells plus stimuli. N=3. **B)** Representative histogram of antibody staining showing this is comparable to the level of an isotype control. MFI in brackets.

By flow cytometry, a weak increase in fluorescence was seen compared to control upon incubation of the FR-β antibody (**Figure 2.29**). Stimulation was performed with both lipopolysaccharide (LPS) and interferon-gamma (IFN-γ) for 24 hours, seen as a pro-inflammatory stimulus,[68] and it was expected that this might increase the receptor

cell surface expression. However, after antibody staining the fluorescence signal (MFI) was lower than the unstimulated population. Compared to an isotype control, neither antibody signal showed a significant level of fluorescent increase/binding, suggesting that the binding seen was non-specific and/or the receptor was not highly expressed.

In order to confirm the findings and given the lack of validation data for the PE-FOLR2 antibody used for flow cytometry, a Western blot was carried out with another antibody. Cell lysates from NR8383 and A549 cells (a negative control for FR-β) were prepared using a lysing buffer (RIPA buffer with protease inhibitor cocktail). Total protein concentration in the lysate was quantified using the Bio Rad DC colorimetric assay. Immunoblotting with an anti-FOLR2 antibody was carried out with a range of antibody dilutions (1:500 – 1:2000) and total protein concentrations, however no band corresponding to the target protein (~37 kDa) was seen for either cell type (**Figure 2.30**). This suggested that under the conditions tested NR8383 cells did not express a detectable level of folate receptor beta.

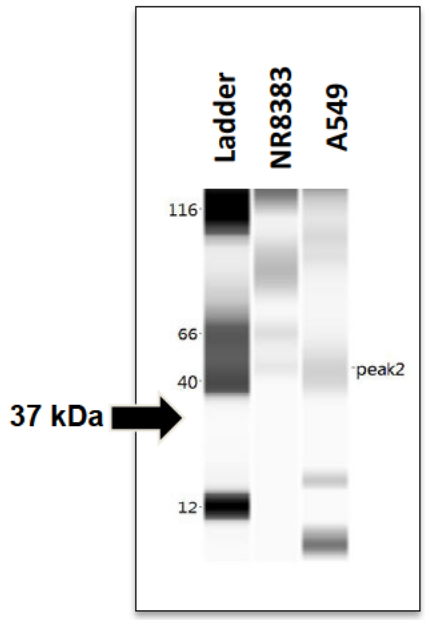

Figure 2.31. FOLR2 (FR-β) expression determined by Western blot. Western blots of lysates of NR8383 and A549 cells were probed with a rabbit polyclonal FR-β antibody, HRP-labelled goat anti-rabbit IgG secondary and bands detected by an ECL substrate. The FOLR2 protein is reported as having a band at ~37 kDa by the supplier.

2.4.2. Probe labelling on NR8383

Since it was possible that neither antibody may be specific for the target – given the lack of validation data – binding experiments were performed with fluorescent probes to see if these were capable of binding to the macrophages. These experiments should show that binding to this cell line was receptor-mediated– rather than mediated by macrophage phagocytosis, pinocytosis or a similar phenomenon. By microscopy, Cy5**Folate (**7**) bound to a number of macrophages, although with faint staining (**Figure 2.31**). By flow cytometry, NR8383 cells bind **7**, however this does not reach a saturation point, probably due to non-specific processes. Further evidence that this

was non-specific was seen in the competition experiment, where addition of 100x excess folic acid with 1 μM Cy5**-Folate was unable to block binding (**Figure 2.32**).

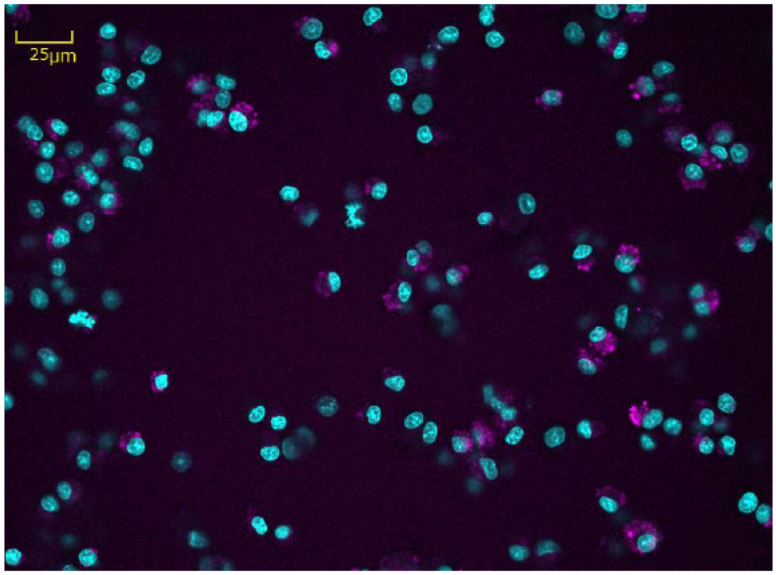

Figure 2.32. NR8383 cells stained with Hoechst 33528 and Cy5**-Folate **7** (250 nM, 30 minutes). Hoechst – cyan, Cy5 – magenta. Scale = 25 μm.

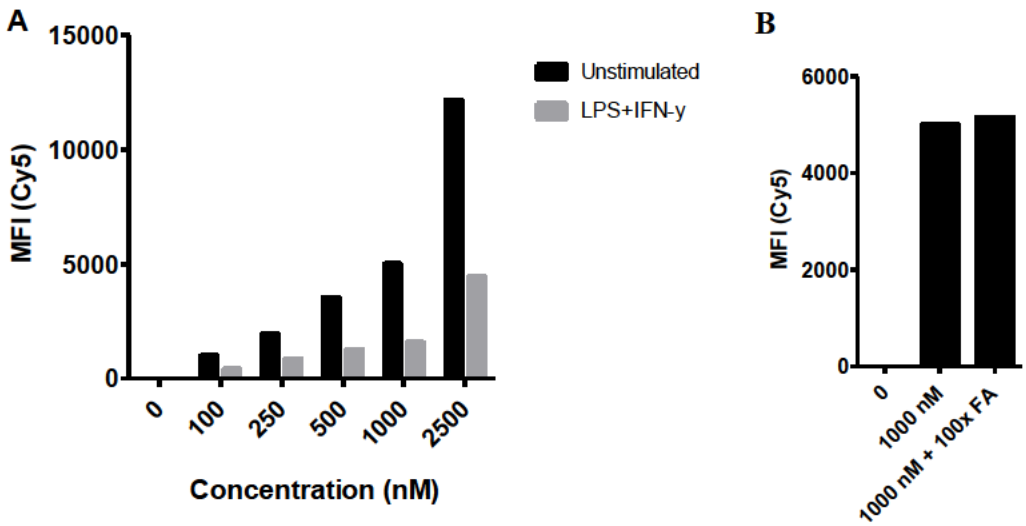

Figure 2.33. Flow cytometry data of **7** binding to NR8383 macrophages. **A)** Titration of the probe over increasing concentrations (0 to 2.5 μM) shows increasing MFI values, while the intensity is weaker with the LPS+IFN-γ stimuli. **B)** MFI values for **7** and an inhibiting condition (1000 nM + 100x FA) compared to control (no probe) shows the probe signal is not inhibited.

In conclusion, NR8383 cells were established as an *in vitro* model of alveolar macrophages, however in the experiments carried out they did not express significant levels of FR-β to permit functional studies. NR8383 cells were able to bind both the FITC and Cy5 probe, however this probably occurred due to non-specific mechanisms.

2.4.3. Human macrophage labelling

Having understood that nonspecific binding to macrophages was an issue with such class of probes, particularly at micromolar concentrations, we went back to investigate a human macrophage model. Looking at the literature, Puig-Kröger reported that monocyte colony stimulating factor (M-CSF) regulated FR-β expression. They showed that MDMs polarised with M-CSF (categorised M2 macrophages) selectively expressed FR-β, while GM-CSF polarised cells did not.[54, 69] The aim was to replicate their experiments by culturing monocytes in the presence of 100 μg/mL M-CSF for 7 days. This differed to the culture method with autologous serum used previously.

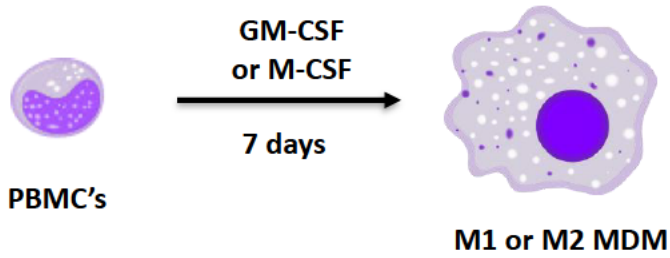

Figure 2.34. Differentiation protocol of peripheral blood mononuclear cells to M1 or M2-like monocyte-derived macrophages

Human $CD14^+$ peripheral monocytes were isolated from the blood of healthy volunteers. These were differentiated with either GM-CSF or M-CSF to give macrophages that should represent the M1/M2 phenotypes. The probe labelling experiments with NR8383 were repeated for these cells with flow cytometry, with a

range of concentrations used to determine target binding specificity. The focus was on Cy5**-Folate **7**, as it would be more applicable in the lung due to its far-red emission.

Flow cytometry macrophage assays were performed with Cy5**-Folate (**Figure 2.35**). Incubation of serial dilutions of **7**, with and without receptor blocking, were measured and the fluorescence intensity plotted as an isotherm. With the M2 MDMs it was possible to detect cells which bound **7**, although this was a heterogeneous population representing 77% of total cells when stained with 50 nM of **7**. The sensitivity of the probe in this assay was also highlighted by the ability to detect FR^+ cells with 50 nM of probe.

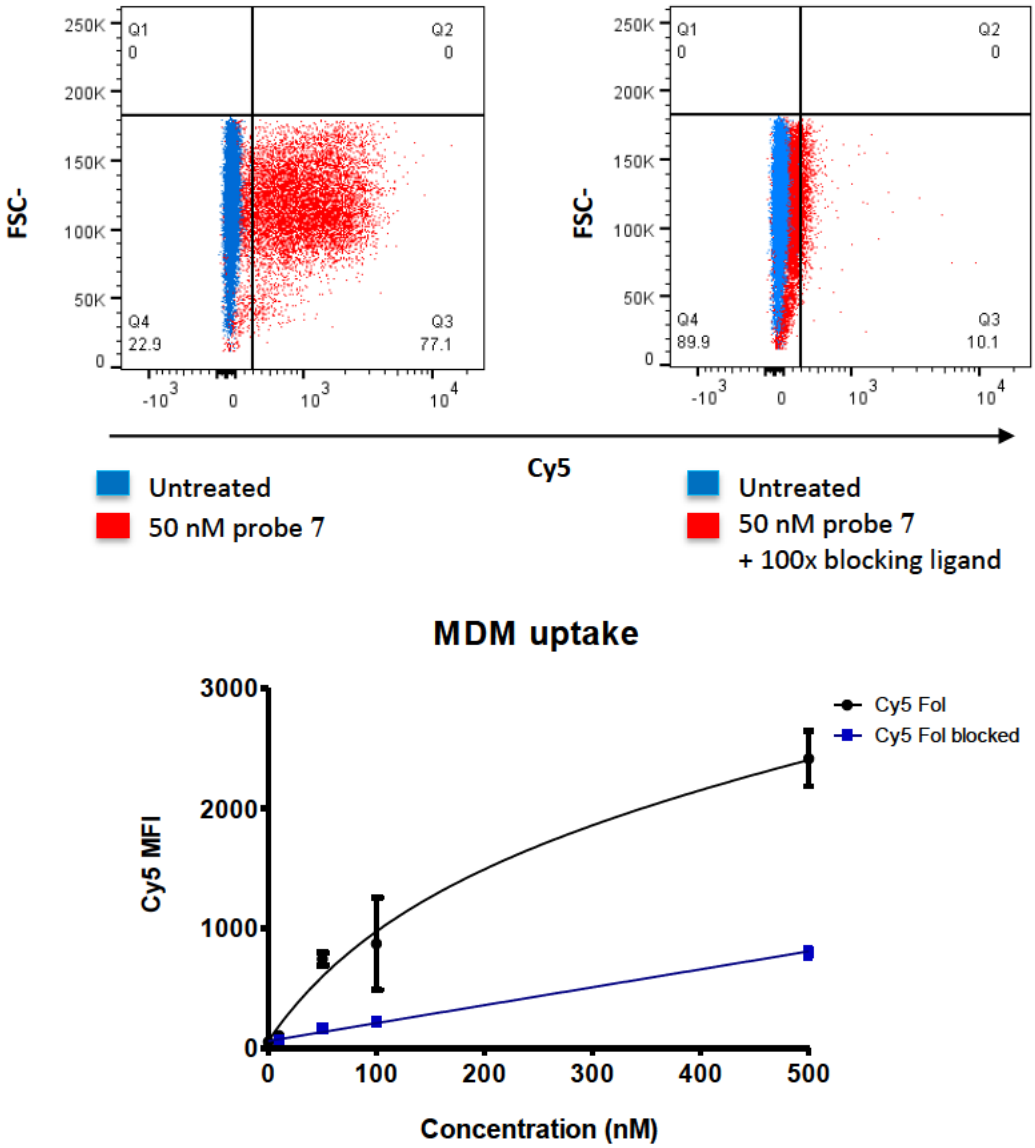

Figure 2.35. Flow cytometry data of probe binding. A range of concentrations of Cy5**-Folate were incubated for 30 min with M-CSF MDM's. **A)** Representative scatter plot with 50 nM probe shown as Cy5 signal against FSC of live MDMs. **B)** Efficient blocking of receptor binding with 100x folic acid to block folate receptor mediated binding. **C)** Mean fluorescence intensity by cytometry of 7 as a binding isotherm. Binding and inhibited binding of concentrations of 7 to M2 polarised MDMs, fitted with a non-linear regression curve. N=2.

The binding curve showed that at lower concentrations the fluorescent signal could be blocked. Once the receptors reached saturation then nonspecific background fluorescence was seen, resulting from labelling not due to the receptor.

Fluorescence microscopy was used to show the localisation of the probe. In the previous experiments we had only investigated M-CSF stimulated MDM, neglecting the GM-CSF treated phenotype that may also bind the probe. In the imaging experiment both GM-CSF and M-CSF cells were compared to see if there was a preference for either macrophage phenotype (**Figure 2.36** and **Figure 2.37**).

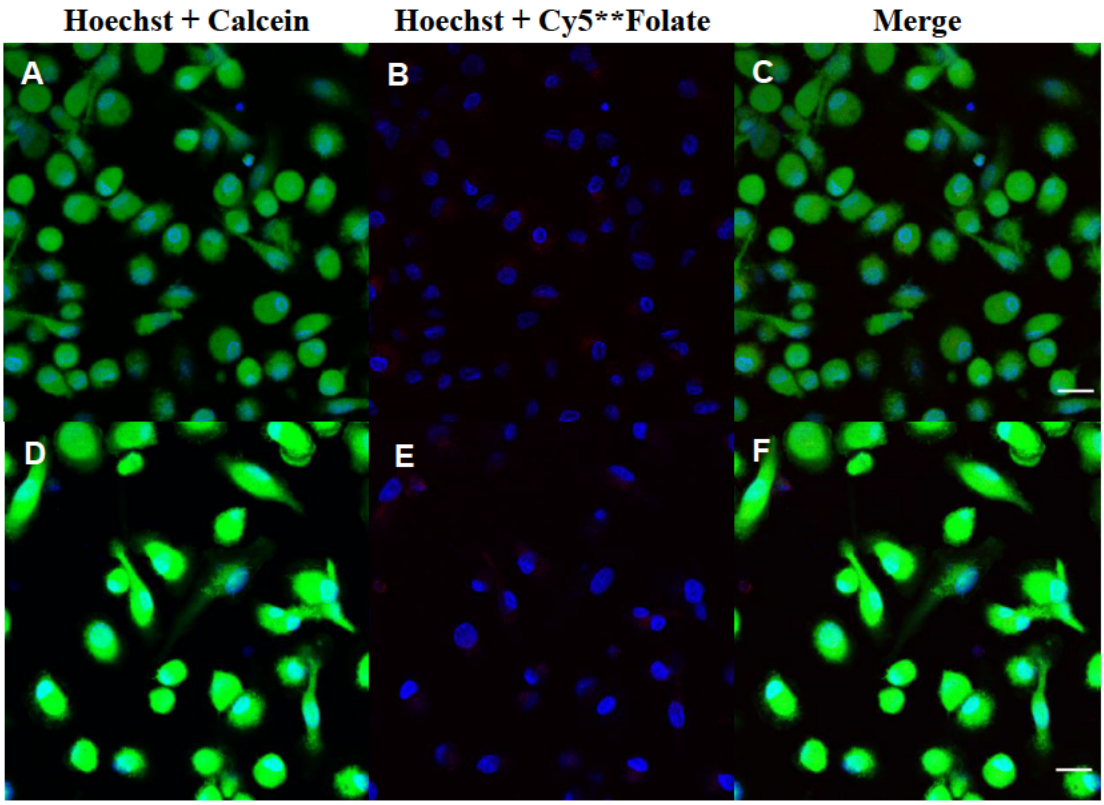

Figure 2.36. Confocal microscopy of M1 MDMs showing no labelling of (**A–C**) Cy5**-Folate (250 nM) and (**D–F**) Cy5**-Folate (250 nM) + 100x FA, nucleus labelling with Hoechst 33342 (1 µg/mL), for 30 minutes. Hoechst – blue, Calcein – green and Cy5 – red. Scale = 20 µm.

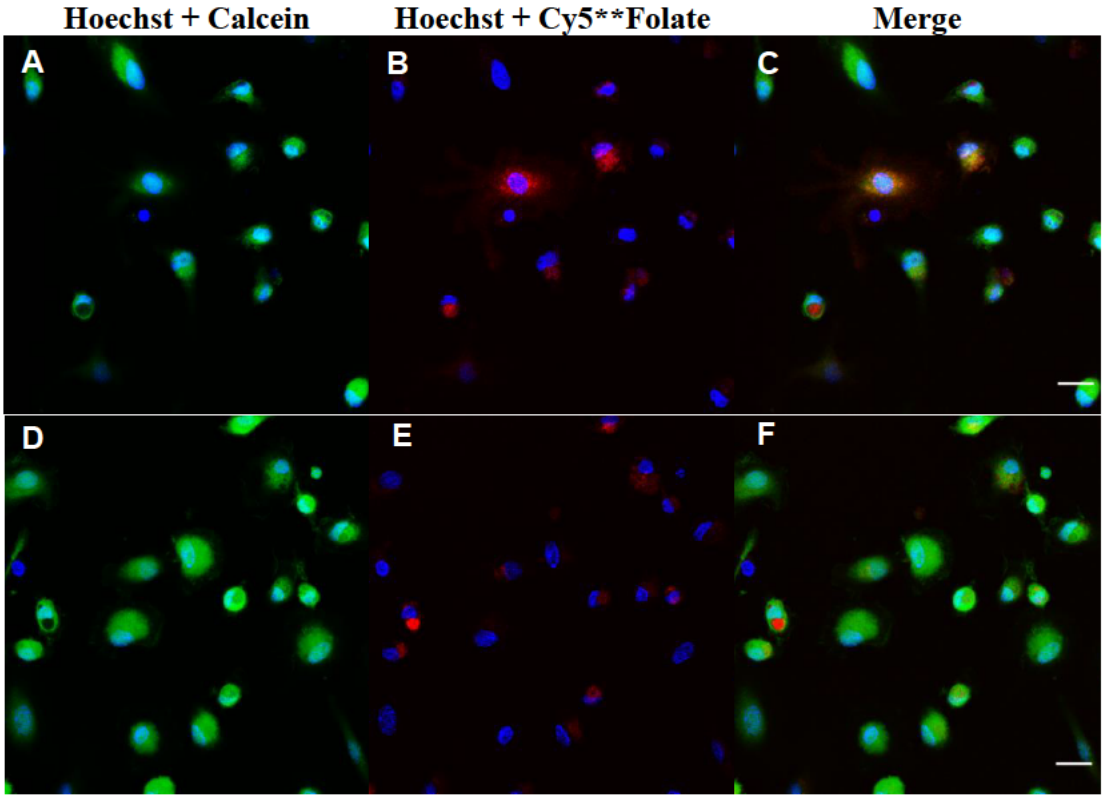

Figure 2.37. Confocal microscopy of M2 MDMs showing the labelling of (**A–C**) Cy5**-Folate (250 nM) and (**D–F**) Cy5**-Folate (250 nM) + 100x FA, nucleus labelling with Hoechst 33342 (1 µg/mL), for 30 minutes. Hoechst – blue, Calcein – green and Cy5 – red. Scale = 20 µm.

Using the probe at a higher concentration (250 nM), the GM-CSF group showed no accumulation of probe, but there was labelling in a high number of cells in the M-CSF group. Compared to FRα, FRβ is known to be mostly present intracellularly in macrophages which explains seeing cytoplasmic rather than membrane staining. Interestingly, this uptake appears to be concentrated in a cytoplasmic compartment (possibly either a phagosome or vacuole) in some cells (example in **Figure 2.38**). We did not study this suspected event any further. Some off-target labelling was seen in the blocked M-CSF condition (**Figure 2.37E**). This could be expected as a higher concentration of probe was necessary for microscopy and may lead to non-specific accumulation, yet this is only a feature of M-CSF macrophages demonstrating the

phenotyping ability of this probe. Importantly, this *in vitro* experiment only represents two populations of cells that would be found in the lung and so further imaging would be necessary on inflammatory cells present in the human lung.

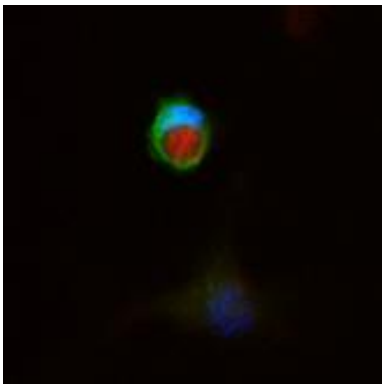

Figure 2.38. Zoomed image of the apparent cytoplasmic concentration of Cy5**-Folate shown in **Figure 2.37C**.

Additionally, GM-CSF or M-CSF are not always seen as activation stimuli of macrophages but generate a resting state. Further stimulation might be necessary to generate macrophages representing classical and alternative activation states – with microbial LPS and/or IFN-γ (a T helper 1 cytokine), or IL-4 and IL-13 (T helper 2 cytokines).[71] In a pilot experiment to look at the response of M-CSF macrophages to stimuli, cells from one donor were polarised with M-CSF and then stimulated further with either LPS (100 ng/mL) or IL-4 (20 ng/mL), for 24 hours respectively. Each well was stained with either Cy5**-Folate or PerkinElmer FolateSense (a commercial probe for folate receptors). Microscopy and automated image analysis was performed on the CellInsight system (ThermoFisher). An analysis algorithm was used to calculate the average intensity of fluorescent probe in each cell (**Figure 2.39**). The data shows some correlation with the findings of Puig-Kröger that IL-4 increases FOLR2 mRNA levels, while LPS does not greatly decrease cell surface levels of FRβ. Although in our case this experiment shows no significance due to the small sample size.

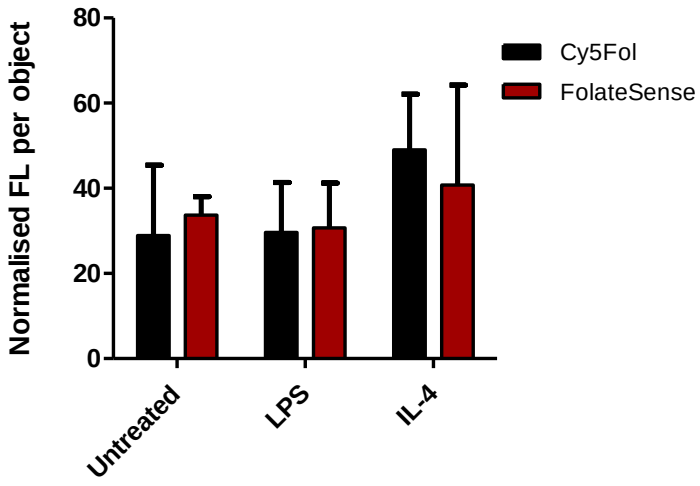

Figure 2.39. Image analysis of the M-CSF macrophage stimuli panel with the Cy5**-Folate and FolateSense probes (100 nM **7** and 25 nmol FolateSense). The nucleus was labelled with 1 µg/mL Hoechst 33342 for segmentation. Data represents the average intensity per object detected from at least 3 wells per condition. N=3, mean ± SD.

2.4.4. Folate mediated internalisation

As imaging data suggested that the uptake of the probe was rapid and it was mostly internalised, we looked at the dynamics of labelling over time. Timelapse imaging of M2 MDMs was used to show whether only a population of cells uptake the probe, as seen by flow cytometry. This would reveal any morphological differences of the cells that were responsible for probe uptake. With an environmentally controlled confocal microscope, cells were dosed with 250 nM Cy5**-Folate and observed over 15 hours (**Figure 2.40**). A difference with the previous imaging experiment was that the media contains the fluorescent probe continuously, rather than it being removed after 30 minutes. After 30 minutes the fluorescent signal was accumulated in cells in the top left region. However, further signals were seen within other cells throughout the

imaging (highlighted with arrows). This experiment shows that the dynamics of FR-positive macrophages can be observed using this probe.

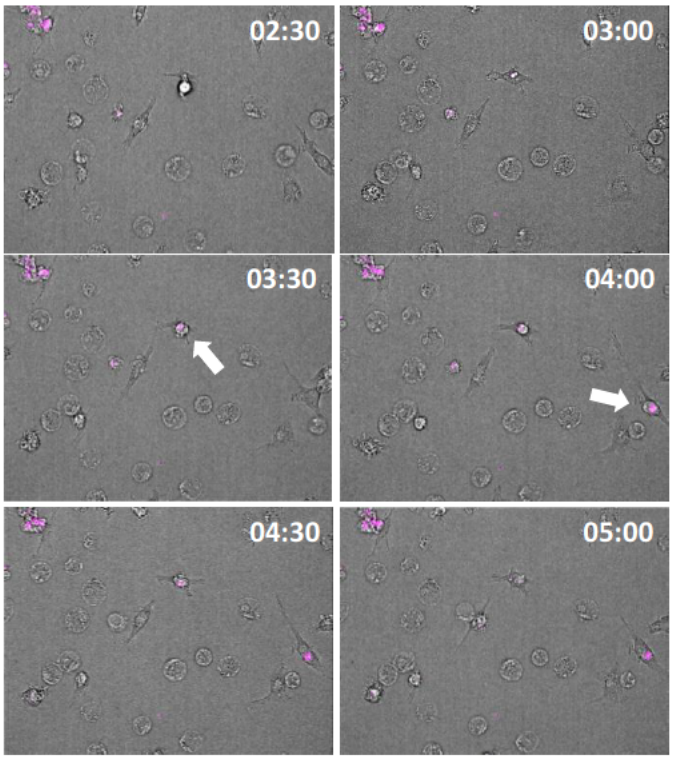

Figure 2.40. Clips from a segment of a timelapse video showing the uptake of Cy5**-Folate by M2 MDMs, taken every 30 minutes for 15 hours (time format HH:MM). The video file can be found in the Appendix. Brightfield images with Cy5 channel (magenta) overlaid, no further staining was used to avoid toxicity.

2.4.5. Primary BAL macrophages

Bronchoalveolar lavage samples were taken from COPD patients and analysed by flow cytometry to see the labelling on alveolar macrophages. A problem when analysing these samples was that most donors were smokers and as a result many macrophages were highly autofluorescent. Due to this, it was not possible to detect a folate probe

signal over the autofluorescence of these cells (autofluorescent component was strong in the Cy5 channel by flow cytometry).

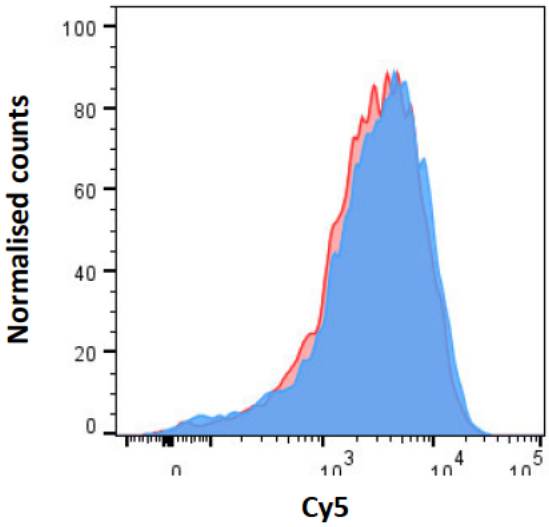

Figure 2.41. Representative flow cytometry histogram of primary BAL cells from the COPD clinic. BAL cells were incubated with Cy5**-Folate (100 nM) for 30 minutes, then washed. Untreated and autofluorescent cells are shown in red, staining after incubation with Cy5**-Folate **7** is shown in blue. Data collected in collaboration with Tom Speight.

2.4.6. Murine macrophages

In addition, we profiled the probes characteristics on peritoneal cells taken from a murine model [in collaboration with Pieter Louwe and Steven Jenkins]. Recent transcriptomic data within the Jenkins group showed that Folr2, the gene that encodes FR-β expression, was present on a population of monocyte-derived peritoneal macrophages and that this subset of cells was enriched and then persists following inflammation. This data suggests that recently monocyte-derived macrophages express FR-β, this could mean that alveolar macrophages (as a long-lived resident macrophage population) have different folate receptor expression due to their different cell lineage.

In the lung it may be more suitable to study interstitial macrophages – a population recruited from peripheral monocytes following lung injury.

Initially, aged mice were investigated for FR-β (FOLR2) expression by flow cytometry. Using an established flow cytometry assay, peritoneal cells were retrieved from mice and then immunophenotyped, with macrophages determined by their $CD11b^{+}$ status. The population of monocyte-derived macrophages were selected based on their marker status as $F4/80^{high}$ and MHC class II^{low}; with the remaining smaller population of $F4/80^{low}$/ MHC class II^{high} macrophages being resident macrophages. In the $F4/80^{high}$/ MHC class II^{low} population, a percentage of cells were FR-β positive. When Cy5**-Folate was applied in this flow cytometry assay, a clear correlation between FR-β antibody and Cy5**-Folate positive cells was seen (**Figure 2.40A**).

Competitive binding experiments used previously (labelled 'Probe +FA') also showed the probe was specific to the FR-β^{+} subset, while a small percentage of FR-β^{-} cells also bound the probe. The experiment was reproduced with five mice, giving significant changes between the control and probe ($p \leq 0.0001$), and probe +FA ($p \leq 0.0001$) (**Figure 2.40B**).

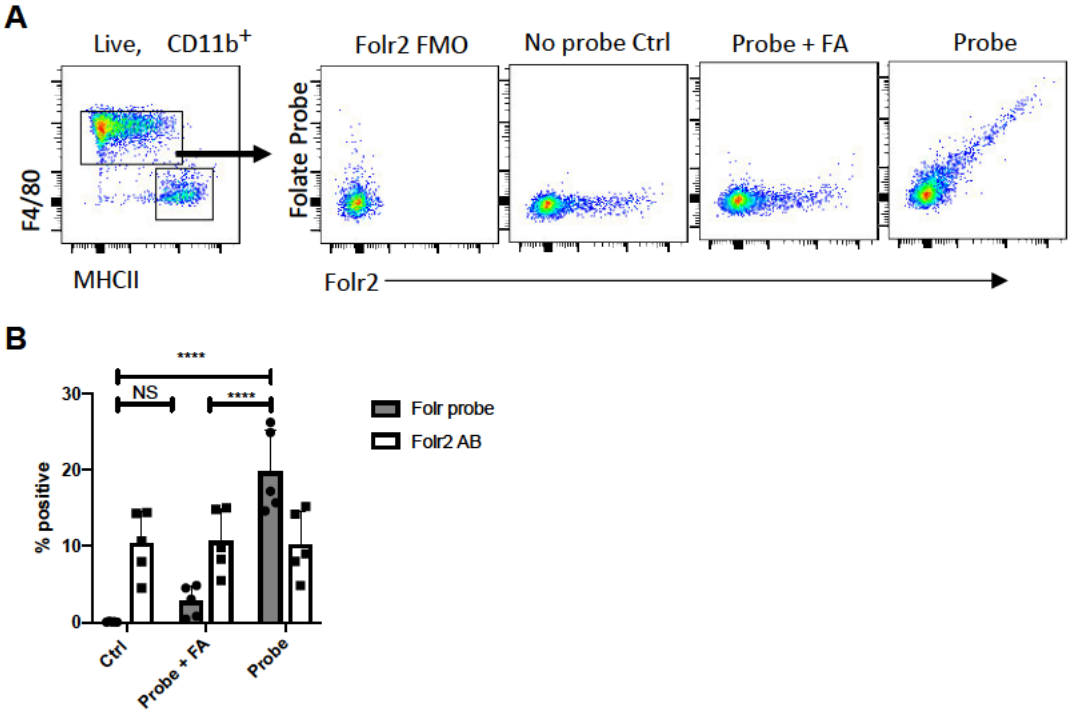

Figure 2.42. A) Representative flow cytometry data showing the gating of $CD11b^{+}$/ $F4/80^{high}$/ MHC class II^{low} macrophages. Plots of folate probe against Folr2 antibody showing the staining in each condition. **B)** Quantification of % cells in the sample positive for antibody (clear) or probe (gray) in the control, probe+FA (competition) or probe groups. (Mean ± SEM, N=5). Data collected by Pieter Louwe.

The flow cytometry results were further validated by confocal microscopy one day after collection. Cells were allowed to adhere to coated coverglass slides for 2 hours at 37°C before media was removed and the adherent cells (predominantly macrophages) were cultured in RPMI 1640 medium overnight. The imaging protocol aimed to replicate the conditions used for flow cytometry. Bright Cy5 fluorescence was seen on a number of cells and these were deemed to be FR^{+} cells by the lack of staining in the competition experiment (**Figure 2.43**). There was some autofluorescence, at a much lower fluorescence intensity, as seen in the control condition (**Figure 2.43D**).

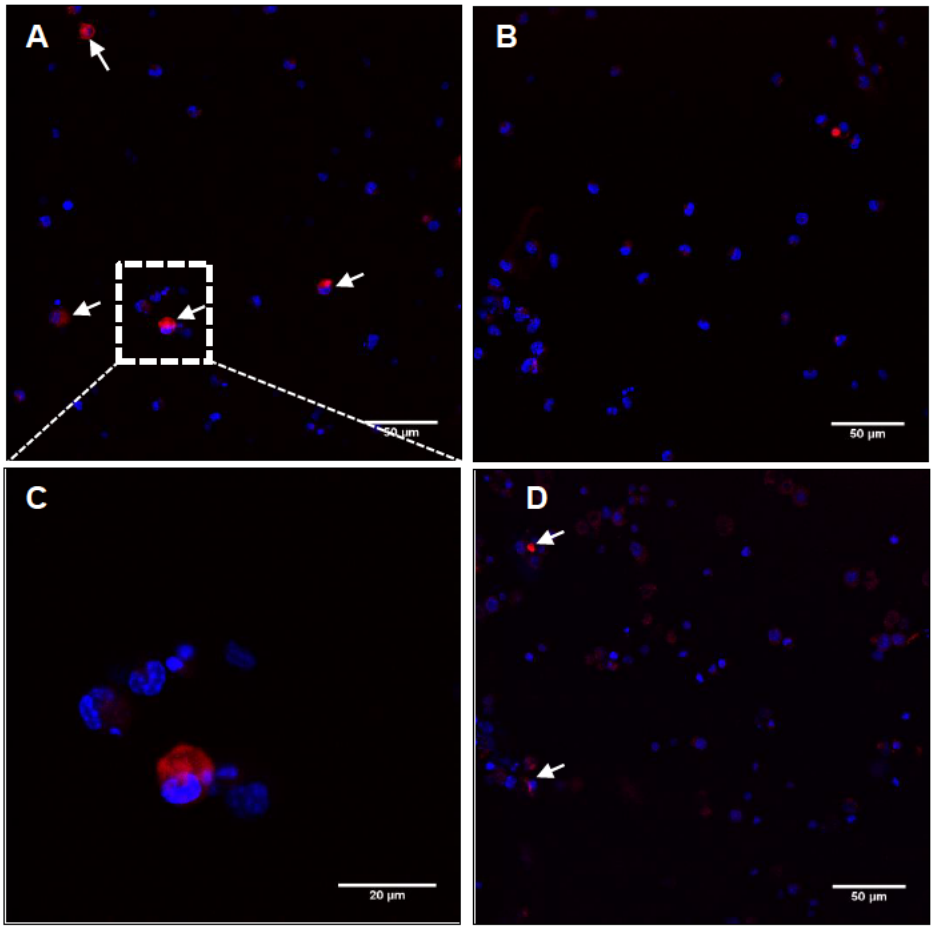

Figure 2.43. Confocal fluorescence microscopy of peritoneal cells incubated with **A)** Cy5**-Folate (250 nM) with arrows highlighting the brightest subset of cells, **B)** Cy5**-Folate (250 nM) + 100x FA, **C)** higher magnification image of region of interest highlighted in **A**, **D)** untreated cells (no probe) showing autofluorescence in a subpopulation of cells. Scale = 50 µm (20 µm for **C**).

2.5. Summary

After testing a number of biological models for assessing folate targeting, we used KB cells as a model for FR-α and monocyte-derived macrophages as a model for FR-β. Our findings support the hypothesis that FR-β is a marker of monocyte-derived macrophages and is not present in resident macrophages (such as AMs). Importantly, the pharmacology of our folate probes was assessed with NR8383 alveolar macrophages and human monocyte derived macrophages. NR8383 cells did not

express significant levels of FR-β. Together this data shows that an optimal concentration of probe needs to be determined to avoid binding through non-specific processes. Probe **7** (50 nM) can detect FR-β^+ M2 macrophages in a flow cytometry assay. Additionally, **7** shows selectivity to an M2 phenotype of macrophage over M1 macrophages, showing the probe could be useful for the detection of tumour associated macrophages in the tumour microenvironment. This probe was also able to detect folate receptor beta positive macrophages in peritoneal macrophages, showing it could be valuable for macrophage imaging outside of the lung.

2.6. Further work

The next steps for the use of folate Smartprobes include imaging in a whole lung model. Due to the challenges of generating a FR positive population in vitro, it is difficult to say how these results would translate into an *in vivo* setting. While the results show folate receptor expression is upregulated in the presence of the cytokine M-CSF, without further evaluation it is not possible to say if this represents a macrophage phenotype. Additionally, there is differential expression across the populations of monocyte-derived macrophages tested, which may bring challenges to determining the relevance of this marker in disease.

The use of primary murine cells highlighted that in aged mice a small population of peritoneal macrophages are FR-β positive and these can bind folate conjugates. Similarly, it would be expected that an inflammatory stimulus (such as LPS or zymosan) would increase the number of F4/80$^+$ macrophages found in this model. The future direction of this work is to optically image mice following intraperitoneal

injection of the compound, to show that the accumulation of probe can be detected in the peritoneal cavity. Additionally, carrying out an *in vivo* mouse inflammation model would help to determine the function of FR+ macrophages in the peritoneal cavity. The immune cell populations from healthy and inflamed mice could be observed by flow cytometry and the relative levels of FR-β positive cells between groups compared. After this, using genetically engineered mice to knockout FR+ macrophages could hypothetically be a method to understand the importance of these cells in the inflamed peritoneum.

3. Macrophage nanobody probe

The macrophage mannose receptor (MMR), also known as CD206, is a carbohydrate binding receptor expressed by certain populations of macrophages and dendritic cells.[2] Its roles include the clearance of endogenous molecules (by internalisation and degradation in lysosomes), promoting antigen presentation, modulation of activation and trafficking. It has a number of endogenous ligands including myeloperoxidase, tissue plasminogen activator, thyroglobulin and hepatocyte growth factor β-chain, and is characterised by two carbohydrate binding domains. These recognise sulfated and mannosylated sugars, and a number of C-type lectin like domains (CTLDs), which bind carbohydrates with terminal mannose, fucose or *N*-acetylglucosamine (GlcNAc) units.[2] MMR is a member of an receptor family that endocytose their ligands and it is the only member of this family to have a cysteine rich (CR) domain that binds sulfated galactose or *N*-acetylgalactosamine (GalNAc) through a recognition motif on a sulfated *N*-acetylgalactosamine terminated sequence.[72] MMR plays a role in collagen internalisation in macrophages, through recognition of collagens I – IV by its fibronectin type II domain (FNII), which also recognises exogenous molecules such as microbial particles from bacteria, fungi and viruses.[2]

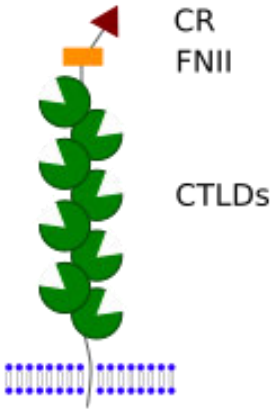

Figure 3.1. Representation of the mannose receptor showing the structural properties with three types of extracellular domains. CR, cysteine rich domain; FNII, fibronectin type II domain and CTLDs, C-type lectin like domains.

In a cellular context, the mannose receptor recycles constantly between the plasma membrane and early endosomal compartments, with most of the receptor being intracellular.[73, 74] MR mediated endocytosis is clathrin-dependent, a form of vesicular transport that involves internalisation and receptor recycling. Clathrin proteins are responsible for polymerising around the budding cytosolic face of the membrane, initiated by the accumulation of so called 'adapter proteins', while endosomal acidification induces ligand release and subsequent receptor recycling. The mannose receptor is not involved in phagocytosis, as over expression in mouse macrophages did not affect the uptake of particulate ligands.[75] Actin polymerisation (commonly inhibited by cytochalasin D) may be required for mannose receptor recycling, as shown by studies where receptor expression was modulated by cytochalasin D.[76] This suggests inhibitors commonly used for distinguishing phagocytosis may affect MMR function. The mannose receptor also has a role in signalling and modulating activation through toll-like receptors (TLR) and Fragment, crystallisable receptors (FcR), which

needs to be considered as ligating this receptor could lead to cross-linking of the MR and FcRs.[77]

As explained in Chapter 1 macrophages can be polarised by environmental stimuli. *In vitro*, MMR expression is increased in human macrophages undergoing M2-like activation (e.g. treatment with IL-4, IL-13 or IL-10).[32] *In vivo*, major histocompatibility complex (MHC) class II low, M2-like TAMs are present in lung and breast carcinoma's and MMR's are upregulated on these TAMs,[78] making them angiogenic, immunosuppressive and tumour promoting. Additionally, macrophages in the tumour environment are known to contribute to cancer progression and poor prognosis in many human tumours.[79, 80] Mannose receptors have also been used as a biomarker of M2 polarised macrophages in COPD patients, with increased MMR^+ alveolar macrophages correlating with smoking and COPD severity.[81] Due to the relevance of this receptor in the pathologies discussed, methods to image MMR^+ macrophages would be a valuable diagnostic tool.

3.1. MMR targeted imaging agents

A number of different approaches have been taken to designing probes against $CD206^+$ macrophages, from antibodies to a more recent report of a target-binding peptide. The Manocept agents developed by Navidea Biopharmaceuticals are glucose polymers appended with mannose and are imaging agents targeting the lectin domain of CD206. One of these agents called γ-Tilmanocept has been FDA approved which is an ^{99m}Tc-labeled radiolabelled tracer for the imaging of sentinel lymph nodes.[82] A similar strategy was applied by Kim who developed a near-infrared MMR targeting polymer

and utilised using NIR optical coherence tomography to visualise carotid atheroma plaques.[83] However, mannose derivatives are not specific to CD206 and can be recognised by other mannose receptors such as DC-SIGN on dendritic cells.[84] Therefore, there is a desire to develop different ligands that are more specific to CD206 which are suitable for use in the clinic. Recent developments have included nanobody ligands and MMR-targeted peptides.[85, 86]

3.1.1. Nanobodies as imaging probes

In 1993, Muyldermans et al. reported the first nanobodies, also known as single domain antibodies (sdAb). These contain only variable domain heavy chains (V_HH domain, ~15 kDa) and are isolated from the serum of immunised camelids.[87] Nanobodies have since been developed as imaging tracers (radionuclide, optical and ultrasound) against a number of targets in oncology and inflammation[88-91] due to their high affinities, small size and good physicochemical properties.[92] They represent an alternative to monoclonal antibodies (mAb) because of their comparable antigen affinities, while their small size (~15 kDa) avoids the long circulation times that hinder the applications of mAbs for imaging (**Figure 3.2**). Additionally nanobodies have low immunogenicity due to sharing high identity with the human type 3 and 4 VH domain families and have been humanized.[93] These features are being exploited in drug discovery, with a number of nanobodies in clinical development for diverse targets.[94] As imaging agents, they promise to play an important role in the diagnosis of various pathologies.

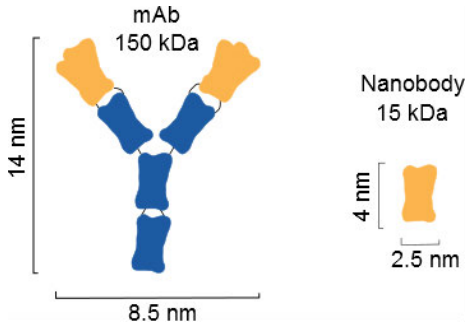

Figure 3.2. Size comparison of a mAb and nanobody (sdAb).

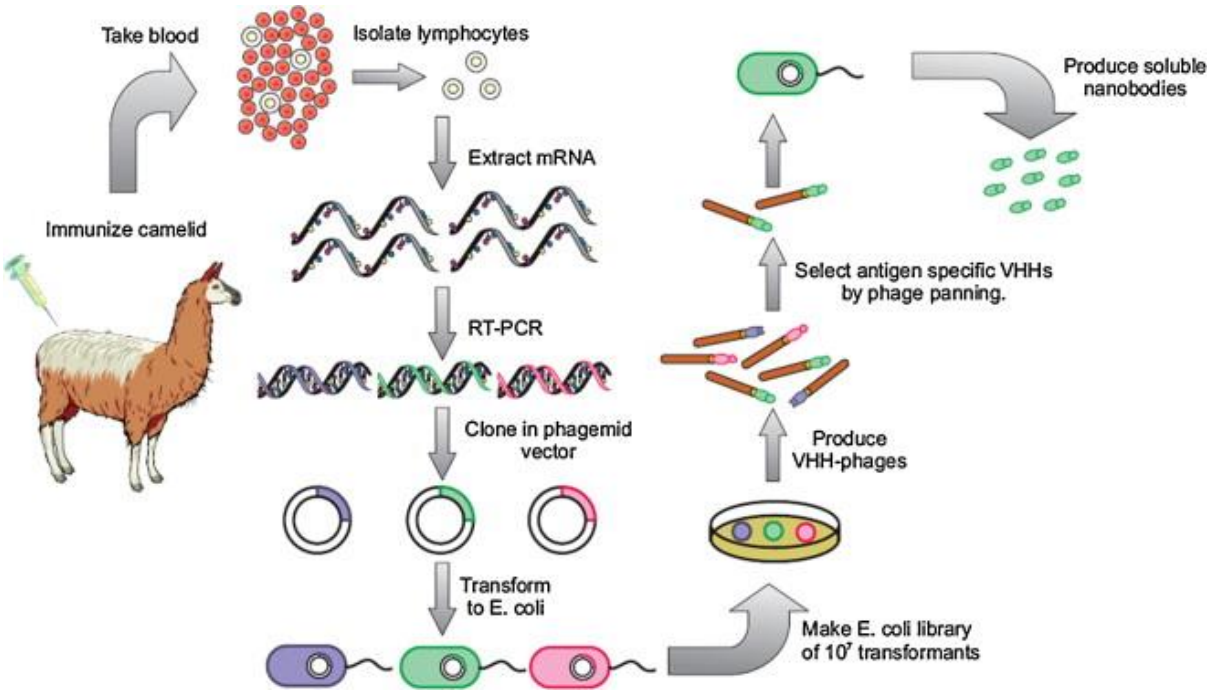

Figure 3.3. Overview of the *in vivo* phage display of nanobodies. After immunisation of a camelid, cDNA is isolated from the animal's lymphocytes. The cDNA is introduced into a phagemid and used for panning against the antigen of interest. Positive clones are expressed in a desired format. Reproduced from Schoonooghe.[95] Copyright 2012, with permission from Elsevier.

The *in vivo* phage display of nanobodies (**Figure 3.3**) was carried out by immunising camelids (in this case an alpaca) with human MMR. After immunisation, blood was taken from the animal and mRNA extracted from peripheral blood lymphocytes. The gene sequences for the variable domains were PCR amplified, ligated into a phagemid vector that codes for a HA with a His tag to allow purification of the nanobody. Phage

display is carried out by transforming the vector into a host cell such as *E.coli*. With the variable domain of heavy chain antibodies (V_HH) library obtained, the desired V_HHs were obtained by panning. The V_HH library was expressed on phage and enriched by selection with antigen coated plates. In a second round of biopanning, bound phage particles were used to infect *E.coli* and subsequently the periplasmic extract of each clone was tested for target affinity in a human MMR ELISA. The desired nanobody could then be produced, commonly in *E.coli*. The complementarity determining regions (CDRs) of nanobodies play a role in maintaining their stability and binding affinity.[96]

3.1.2. MMR nanobody

Nanobodies represent the most advanced agents for CD206 targeting that have shown promise as molecular imaging agents.[97] Movahedi produced a ^{99m}Tc-labelled nanobody against MMR with an affinity of 2 nM determined by SPR and validated its use for SPECT/micro-CT imaging of tumour-associated macrophages (TAMs) in preclinical models.[91] SPECT/CT imaging in tumour-bearing mice showed uptake of the nanobody which was significantly higher than uptake of the control nanobody with analysis of the dissected tissue confirming these findings.

This nanobody was further developed by Blykers as an ^{18}F-PET tracer for the detection of macrophages in tumour stroma.[85] TAMs with upregulated CD206 were found to be tumour promoting. *In vitro* studies with ^{18}F-benzoic acid labelled nanobody (anti-MMR 3.49) showed it had high affinity for human MMR (K_D = 1.8 nM), while *in vivo* biodistribution studies showed rapid renal clearance and specific retention in the

tumour and MMR-expressing tissue. In a small animal PET imaging study, the nanobody was specifically recognised by MMR in 3LL-R tumour bearing mice, when compared with the uptake in MMR-deficient mice. (**Figure 3.4**)

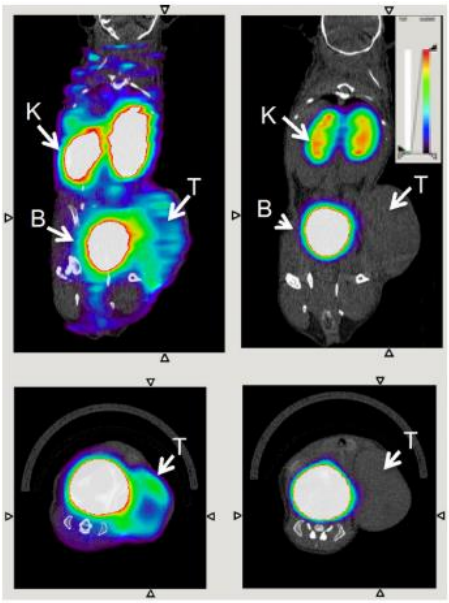

Figure 3.4. Transverse and coronal PET/CT images of WT (left) vs. MMR-deficient (right) 3LL-R tumor–bearing mice scanned 3 h after injection of ^{18}F-benzoic acid labelled-anti MMR 3.49. Arrows point to the tumour (T), kidney (K), and bladder (B). Adapted with permission from Blykers et al. Copyright 2015 Society of Nuclear Medicine and Molecular Imaging.[85]

This ligand shows promise as a radiopharmaceutical due to its ideal properties and the ease of radiolabelling, while it could also be developed as an optical probe for highlighting M2 macrophages during fluorescence-guided surgery. As noted by Debie et al. the fluorophore chosen and method of conjugation should be carefully considered when developing labelled nanobodies.[98]

3.1.3. Peptide imaging agents

Fluorescent peptides are a widely utilised method for labelling receptors and a number of peptidic agents are under clinical investigation for cancer and bacterial infection

imaging.[24] There are a number of reports of peptides that bind CD206, including a 10-mer peptide RP-182 developed by Riptide Bioscience, however this is not specific as it also binds a number of other receptors.[99] Recently, Scodeller et al. showed that M2-like TAMs could be targeted by a 'FAM-UNO' fluorescent cyclic peptide (sequence: 5(6)-FAM-Ahx-CSPGAKVRC).[86]

3.2. Optical MMR nanobody probe

The work presented is a collaboration between myself, Tom Speight, Edinburgh Molecular Imaging and Vrije Universiteit Brussels. The MMR targeting nanobody (clone 3.49) used in the study by Blykers obtained had the properties below.[85]

Table 3.1. Properties of the batch of nanobody used.

	MW (Da)	ε ($M^{-1}cm^{-1}$)	Concentration (mg/mL)
MMR 3.49	12,682	24,660	3.805

The protein sequence has been published and is given below with the CDRs highlighted in grey.[100] As a random lysine labelling would be carried out, it was important to know there were six lysine residues in the sequence.

QVQLQESGGGLVQPGGSLRLSCAASGFSLDYYAIGWFRQAPGKEREGISCISYKGGSTTYADSVKGRFTIS
KDNAKNTAYLQMNSLKPEDTGIYSCAAGFVCYNYDYWGQGTQVTVSS

Figure 3.5. Peptide sequence of nanobody 3.49.

Blykers used surface plasmon resonance (SPR) to calculate the kinetic and equilibrium properties of the nanobody to recombinant MMR protein (**Table 3.2**). The binding affinity was 1.8 nM, showing that the nanobody expressed had high affinity for its target.

Table 3.2. Binding kinetics of the nanobody to hMMR by Blykers.[85]

	k_a (M^{-1} s^{-1})	k_d (s^{-1})	K_D (nM)
MMR 3.49	4.4 x10^5	8.0 x10^{-4}	1.8

3.2.1. MMR nanobody labelling

Fluorophore labelling of this protein was carried out under mild conditions with the *N*-hydroxysuccinimidyl (NHS) reactive ester of the dye, which reacted with lysine residues forming an amide bonds between the protein and the fluorophores. It was important to test the conjugation conditions due to the limited amount of nanobody. Initially, lysozyme was chosen as a model protein due to its similar size and availability. This protein was successfully labelled with the far-red Cy5** active ester [see data in Chapter 6.4]. Conjugation conditions were optimised for pH and reaction time.

Initial attempts at fluorophore labelling nanobody 3.49 were carried out using this validated procedure. However, labelling with the Cy5** fluorophore gave poor levels of protein labelling. The reason for this is not fully understood as the model protein reactions were successful. Instead when the SulfoCy5 dye was used the levels of protein labelling were much higher, therefore this dye was used. (**Table 3.3**)

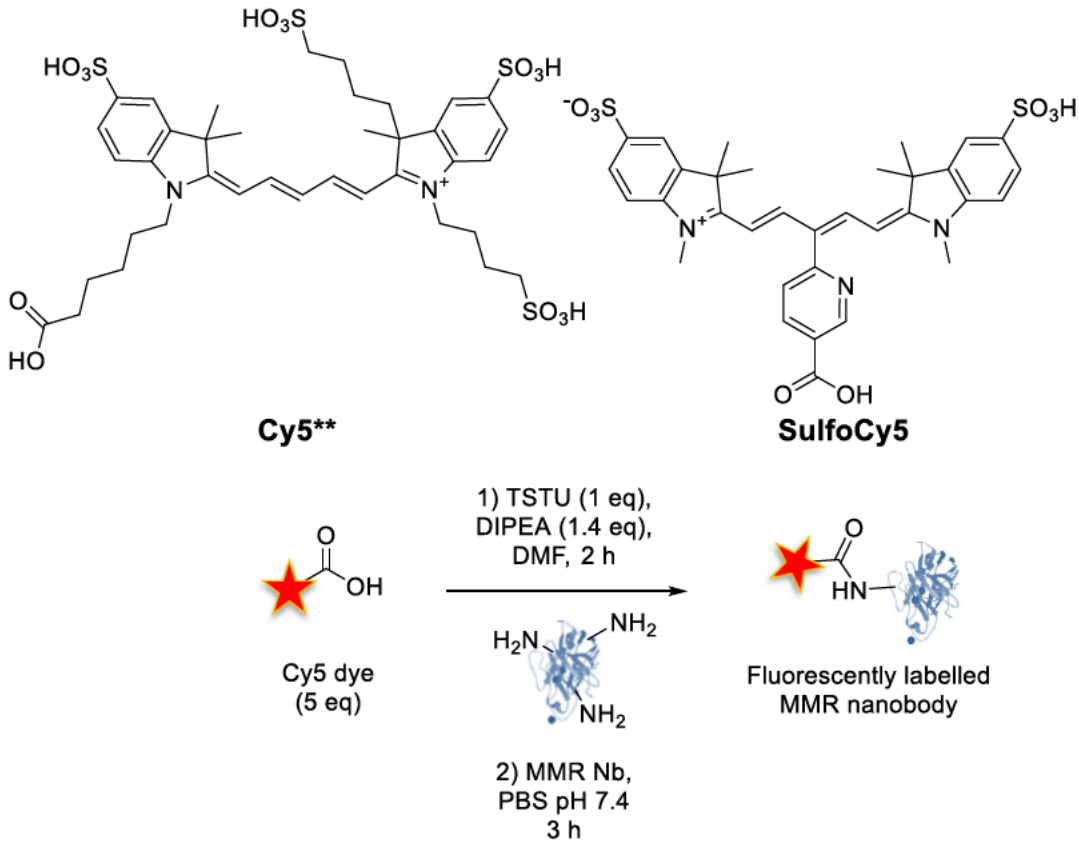

Figure 3.6. The labelling procedure of nanobody 3.49 with Cy5 fluorophores. Successful labelling was observed with SulfoCy5.

Table 3.3. Summary of the methods attempt for the nanobody-fluorophore labelling.

Fluorophore	Code	Purification method	Comment on reaction/purification
Cy5**	Nb-23	PD-10	Mixture of labelled and unlabelled
Cy5**	Nb-24	Centrifugation	Low efficiency of dye labelling
SulfoCy5	Nb-25	Centrifugation	Successfully labelled, no dye contamination
SulfoCy5	Nb-26	Centrifugation	Successfully labelled, no dye contamination

To purify the labelled protein from residual dye both PD-10 gel filtration and spin centrifugation/filtration (Amicon 10 kDa MW cut off-filters) were tested. Spin centrifugation provided better results in terms of removing unconjugated dye

molecules present after the reaction. 'Nb-25' and 'Nb-26' are referred to as **Cy5-Nb** and were used throughout. The optimised reaction conditions are shown above in **Figure 3.6**. Protein conjugations were carried out at Edinburgh Molecular Imaging with Christophe Portal.

3.2.2. Characterisation

The purified **Cy5-Nb** nanobody probe was characterised by RP-HPLC to confirm that there was no remaining dye in the protein sample after purification. Common conditions which can be optimised for HPLC analysis include the column material, solvent and solvent pH. Different HPLC media can be used for the analysis of molecules, for this project we attempted both C4 and polymeric PLRP-S stationary phases (**Figure 3.7**) that can be used in reverse-phase mode. C4 columns are based on alkyl-ligand silanols while PLRP-S media uses copolymers of styrene/divinylbenzene which gives excellent pH stability. Both rely on the interaction of the analyte with the hydrophobic media and elution with a polar solvent.

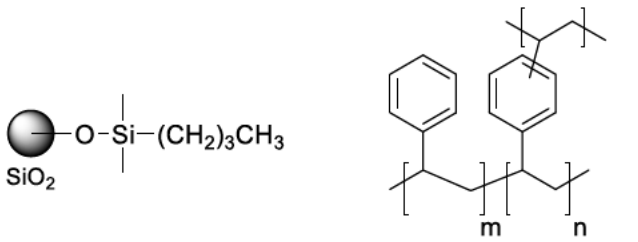

Figure 3.7. Comparison of the functional ligands on C4 and copolymer styrene/divinylbenzene (PS/DVB) column stationary phases.

An HPLC gradient of water and acetonitrile with 0.1% trifluoroacetic acid was created, based on a method previously developed for nanobodies by Blykers.[85] When both columns were compared the C4 showed no separation between unlabelled protein and the product, while the Agilent PLRP-S (styrene/divinylbenzene) 300Å column showed separation. This optimised HPLC method indicated a heterogeneous mixture, as expected by the random nature of lysine labelling (**Figure 3.8**). The HPLC signal for **Cy5-Nb** showed a broader peak than the unlabelled material.

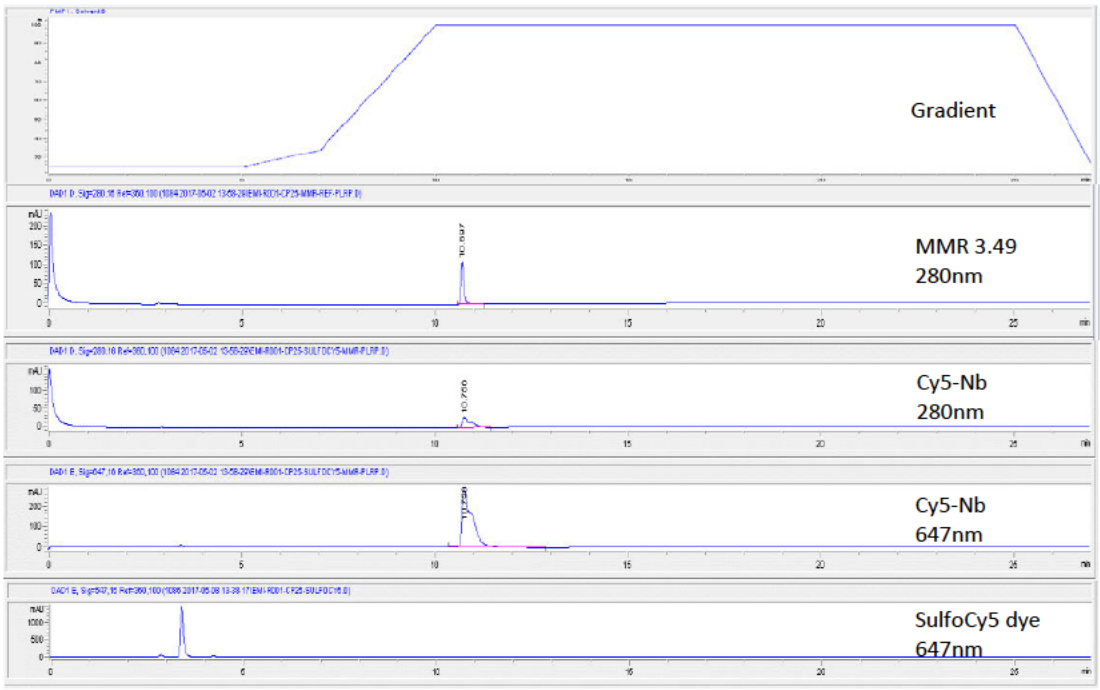

Figure 3.8. HPLC analysis using the polymer-based column (Agilent PLRP-S) showing gradient and chromatograms of the unlabelled **MMR**, **Cy5-Nb** (280 nm and 647 nm) and **SulfoCy5** dye (647 nm).

Several methods to characterise **Cy5-Nb** by mass spectrometry using MALDI-TOF were explored, but overall there was a problem with poor ionisation of the material. With assistance from the SIRCAMS facility, ion-mobility spectrometry-mass spectrometry (IMS-MS) was performed with a Waters Synapt Q-TOF. This is a higher resolution spectrometry technique that analyses molecules after ionisation by both

shape and charge separation. Firstly, the unlabelled nanobody was analysed and at least two oxidation forms were detected (**Figure 3.9**) with the 8+ charge state showing the best ionisation. Based on the molecular ions, this could be oxidation of cysteine, methionine or histidine. **Cy5-Nb** was then analysed and the molecular ion of the dye labelled protein was detected (**Figure 3.10**). This showed the degree of protein labelling as three dyes per protein. The mass spectrum complexity was due to each oxidation state being labelled with different degrees of fluorophores.

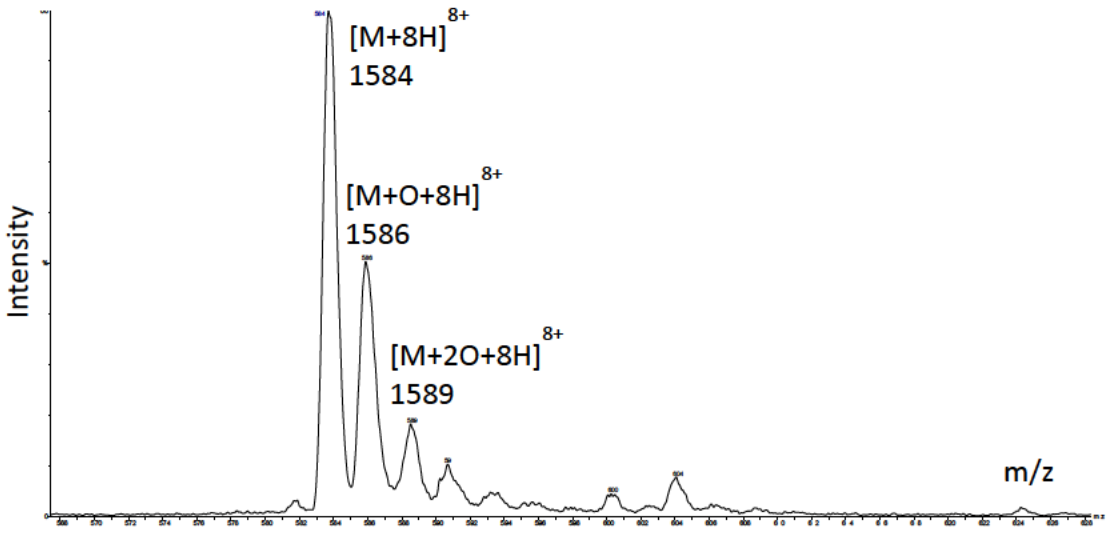

Figure 3.9. Ion mobility MS spectrum of **MMR 3.49** showing the *m/z* of $[M+8H]^{8+}$ and the oxidation states, $[M+O+8H]^{8+}$, $[M+2O+8H]^{8+}$.

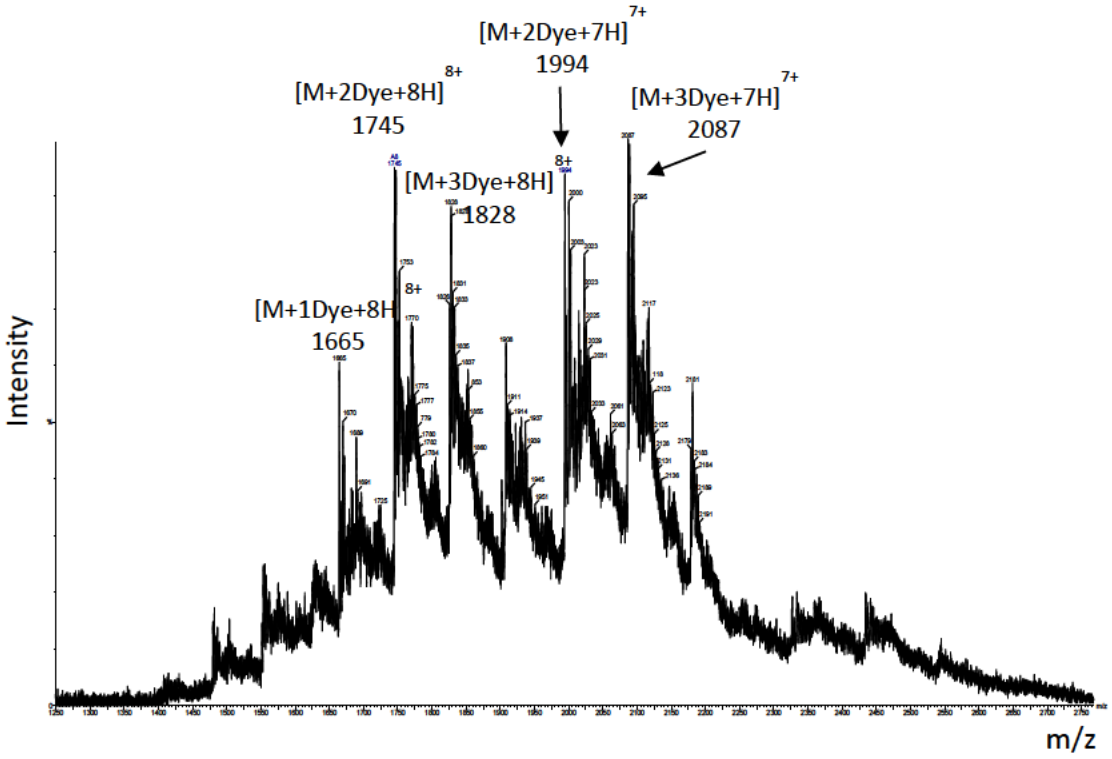

Figure 3.10. Ion mobility MS spectrum of **Cy5-Nb** showing the complex mixture of Cy5 molecules conjugated to the Nb, in the 8+ and 7+ charge states. The modifications with one, two and three dyes are indicated.

By UV-Vis spectroscopy, the absorbance of **Cy5-Nb** at 280 nm (predominately absorbance by tyrosine and tryptophan residues) and 640 nm (Cy5 dye) was measured. Protein concentration of the probe was determined to be 0.46 mM using the equation below. The degree of labelling was calculated to be approximately 4 dyes/ protein by using **Equation 3.2**, although this is an average value due to the heterogeneous nature of lysine labelling.

$$protein\ concentration\ (M) = \frac{[A_{280} - (A_{max} \times CF)] \times dilution\ factor}{\varepsilon}$$

Equation 3.1. Calculation of protein concentration; where CF = correction factor for the dye, ε = molar extinction coefficient of the protein.

$$degree\ of\ labelling\ (dye\ per\ protein) = \frac{A_{max} \times dilution\ factor}{\varepsilon' \times protein\ conc.\ (M)}$$

Equation 3.2. Calculation of degree of labelling, where ε' is molar extinction coefficient of the dye.

SDS PAGE was ran for both the labelled and unlabelled forms of the protein, however standard glycine gels did not have the separating ability to resolve the small size of this protein. Thus a tricine gel was used with 0.5 – 1 μg of protein loaded in each lane in reduced sample buffer, which gave a clearer band for the unlabelled and labelled proteins when visualised with Coomassie staining (**Figure 3.11**). However, the change in position of the band was not clear due to the relatively small change in total protein size after fluorophore labelling.

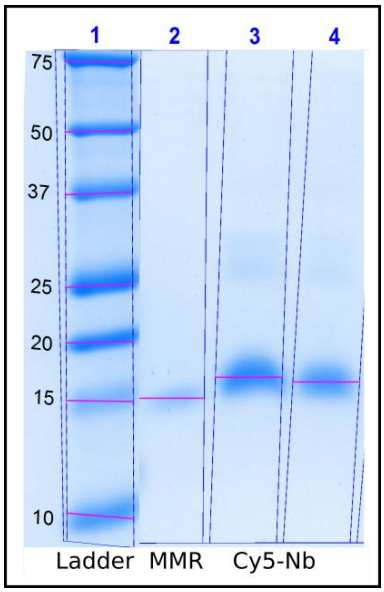

Figure 3.11. SDS-tricine PAGE under reducing conditions (10% separating: 3% stacking gel) visualised with Coomassie staining. The lanes correspond to lane 1 (standards ladder), lane 2 (0.5 μg unlabelled MMR), lane 3 (1 μg labelled MMR, **Cy5-Nb**) and lane 4 (0.5 μg labelled MMR, **Cy5-Nb**) with the pink marker showing the slight increase in MW of lane 3 relative to the 15 kDa standard.

The fluorescence spectrum of **Cy5-Nb** in PBS showed that the nanobody was labelled with the dye and that this labelling had not changed the emission properties of the SulfoCy5 fluorophore (**Figure 3.12**).

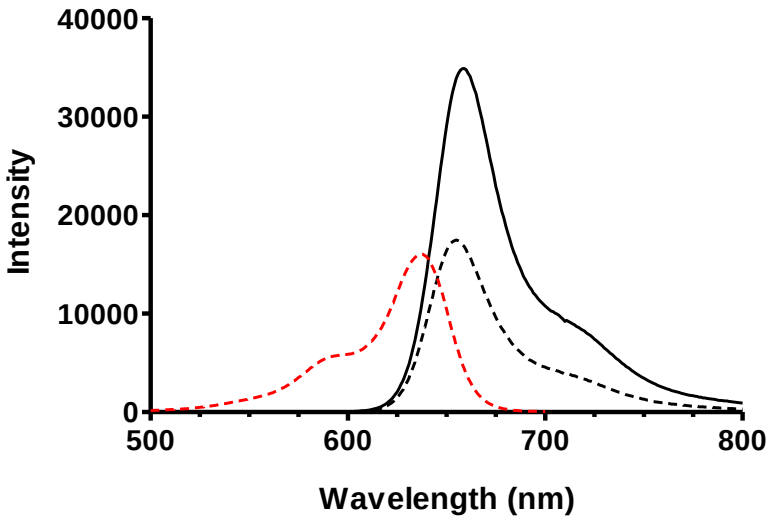

Figure 3.12. Fluorescence spectra of SulfoCy5 dye excitation (dashed red) and emission (dashed black) and **Cy5-Nb** emission (solid black). Solutions were prepared in PBS, 1 µM, excitation = 640 nm.

3.3. Cellular labelling

Biological studies with this probe were performed by Tom Speight with the aim to study the specificity of the probe for macrophages using an established model of human macrophages derived from healthy blood donors. Firstly, expression of CD206 was examined in monocyte-derived macrophages (MDMs) after 6 days in culture. The CD206 receptor was significantly upregulated once monocytes were differentiated to macrophages (**Figure 3.15**). However, in the presence of common polarisation stimuli (LPS, IL-4, M-CSF, dexamethasone) no difference in receptor expression was seen – suggesting CD206 cannot be claimed to represent an M2 macrophage activation marker in this model.

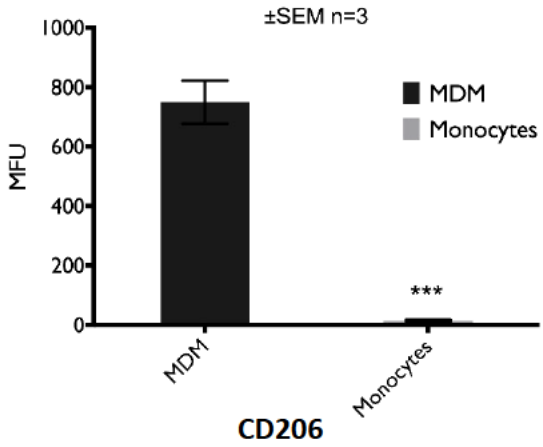

Figure 3.13. Expression of CD206 in monocyte derived macrophages. Quantification of flow cytometry data showing the fluorescence increase representing the change in expression of CD206 following monocyte differentiation, N=3, mean ± SEM. Data from Tom Speight.

Once our model had been characterised as generating macrophages that expressed CD206, the probe was used to label macrophages and this labelling was examined by confocal microscopy (**Figure 3.14**). 50 nM **Cy5-Nb** gave bright cytoplasmic staining after 30 minutes incubation with a good signal/background ratio. No staining was observed on undifferentiated monocytes (day 0) or on a non-macrophage cell line (A549 cells). These imaging studies thus demonstrate the specificity of the probe for macrophages over monocytes and cancer cells that do not express CD206.

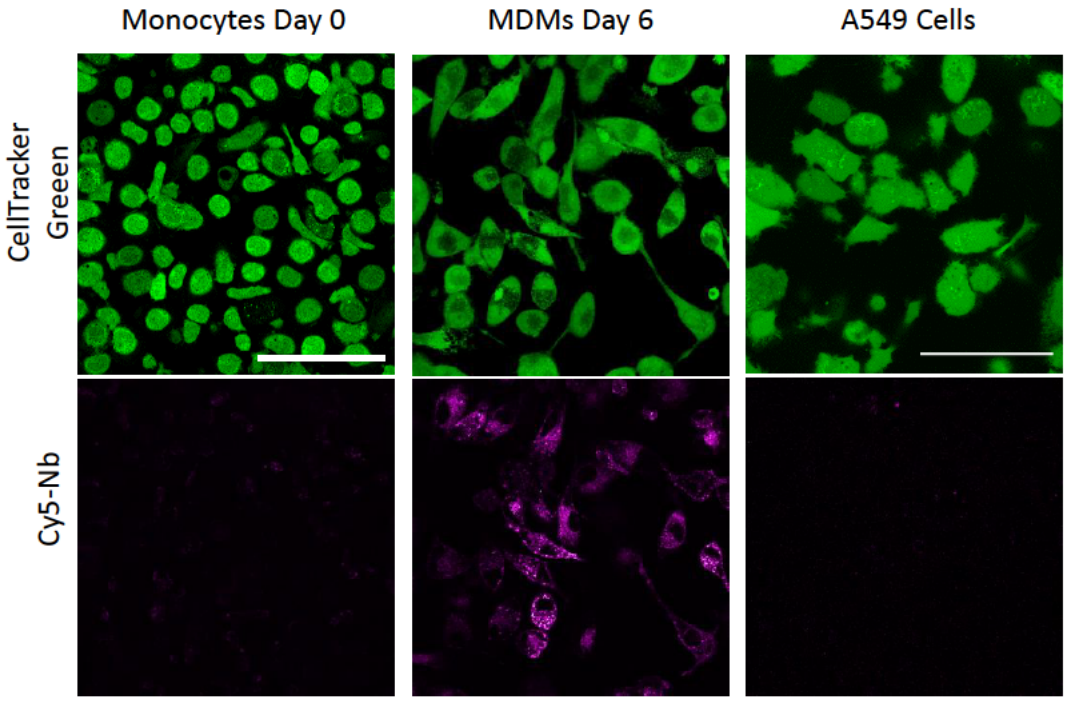

Figure 3.14. Confocal microscopy studies to reveal the specificity of the nanobody for macrophages (MDMs). Imaging was performed with monocytes, MDMs and A549 (epithelial lung cancer) cells and staining was selective to macrophages. Cells were labelled with 50 nM **Cy5-Nb** (shown in magenta) for 30 min and counterstained with CellTracker Green (cytoplasm stain, shown in green). Scale = 100 µm. Data from Tom Speight.

To reveal the localisation of CD206 by another method, MDMs were imaged with a phycoerythrin (PE) labelled anti-CD206 primary antibody (**Figure 3.15**). One limitation was that the PE antibody could not be used in tandem with the probe to show colocalisation due to the overlapping spectra of PE and Cy5 fluorophores. Similar to **Cy5-Nb**, the PE-CD206 antibody showed intracellular staining and agreed with the findings that most of the receptor is intracellular.[73]

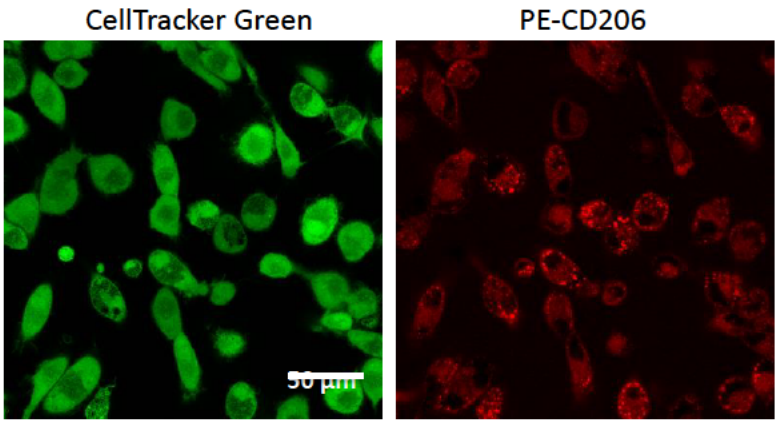

Figure 3.15. Confocal microscopy of the labelling of MDMs by a commercial anti-CD206 PE flow antibody. Cells were labelled with the antibody at 1:20 dilution for 30 min with PE excitation at 543 nm. Cells were labelled with the PE antibody (shown in red) for 30 min and counterstained with CellTrackerGreen (shown in green). Data from Tom Speight.

To further validate the specificity of the probe, the labelling on other human immune cell populations that do not express CD206 was explored. Neutrophils (PMNs) were isolated from the blood of healthy volunteers and were studied by microscopy following staining with the probe (**Figure 3.16**).

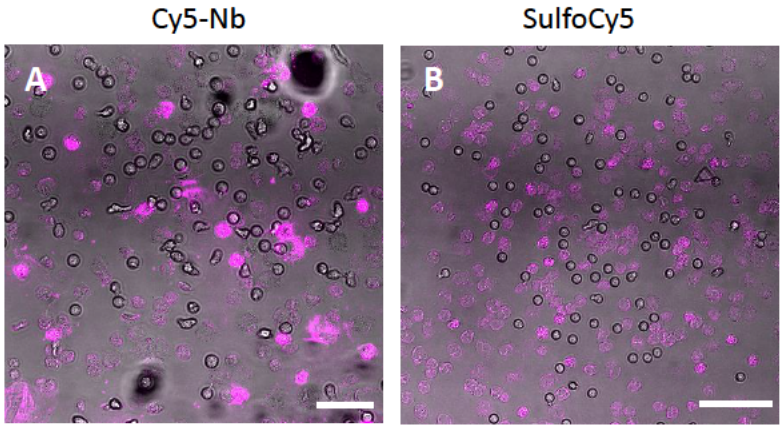

Figure 3.16. Confocal and brightfield microscopy overlaid, showing the neutrophil staining of **A)** 50 nM **Cy5-Nb**, and **B)** 50 nM SulfoCy5 dye. Unattached cells are seen in both images by the brightfield image. Cy5 fluorescence is shown in magenta. Scale = 100 µm. Data from Tom Speight.

With neutrophils **Cy5-Nb** uptake was observed, however there was also uptake of the non-conjugated Cy5 dye. This suggested non-specific uptake was responsible for the labelling and could be explained in a number of ways; neutrophils may recognise the Cy5 dye in some manner, alternatively it could be via phagocytosis and recognition of foreign material by Fc receptors, which a major responsibility of neutrophils in their function as phagocytes.[101] As neutrophils are recruited in the lung by inflammatory stimuli, this off-target binding should be considered for preclinical applications of this probe in inflammatory disease models.

3.3.1. Receptor-mediated internalisation

There are a number of cellular uptake pathways, however mannose receptor uptake is via clathrin-dependent endocytosis.[1] We investigated if **Cy5-Nb** underwent uptake via the same method as it appeared to be internalised within macrophages and this differed to the labelling profile of a commercial PE-conjugated antibody for CD206 (**Figure 3.15**). This difference in labelling could be due to the smaller size of the nanobody allowing more rapid internalisation or an alternative pathway. To our knowledge the endocytic capability of the mannose receptor has not previously been shown with this ligand.

To generate images of the precise localisation of the nanobody within a cell spinning disk microscopy was used. By using multiple pinholes, spinning disk microscopes are able to obtain confocal resolution images at a much faster speed than a confocal scanning system. This is useful for live cell imaging as it gives the ability to observe dynamic events. In this experiment, cells were prelabelled with CellTracker Green and

Cy5-Nb. Cell representations were generated using the "Kinder Egg" model in Imaris (**Figure 3.17**). The 3D images show clearly that the majority of fluorescence signal from **Cy5-Nb** is located intracellularly, agreeing with previous results that the majority of the receptor is intracellular.[73, 74] In the 3D visualisations the probe is also seen throughout the cytoplasmic compartment.

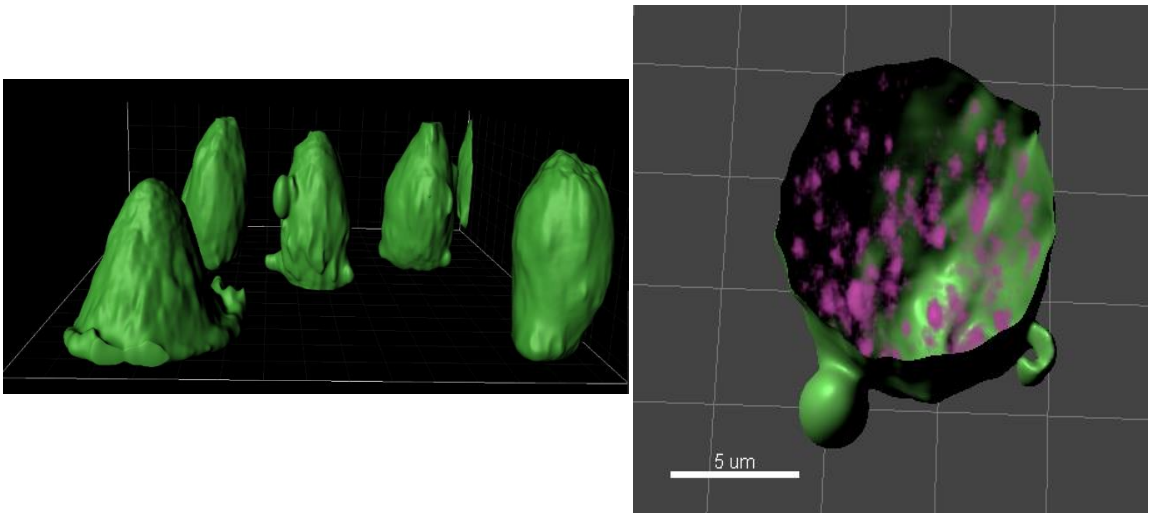

Figure 3.17. 3D visualisation of macrophage labelling generated using **s**pinning disk microscopy and analysed by the Kinder Egg model in Imaris. **Left**: macrophages labelled with CellTracker Green to allow masking of each cell, **Right**: 50 nM **Cy5-Nb** probe fluorescent signal (shown in magenta) in a macrophage. A video file showing the imaging from different fields of view is available in the Appendix. Data from Tom Speight.

Time-lapse confocal imaging was used to evaluate the kinetics of the probe labelling on macrophages and to show how quickly it bound (**Figure 3.18**). As this imaging was carried out without any washing step, it shows the advantage of having a highly specific imaging probe generating a high signal/noise ratio.

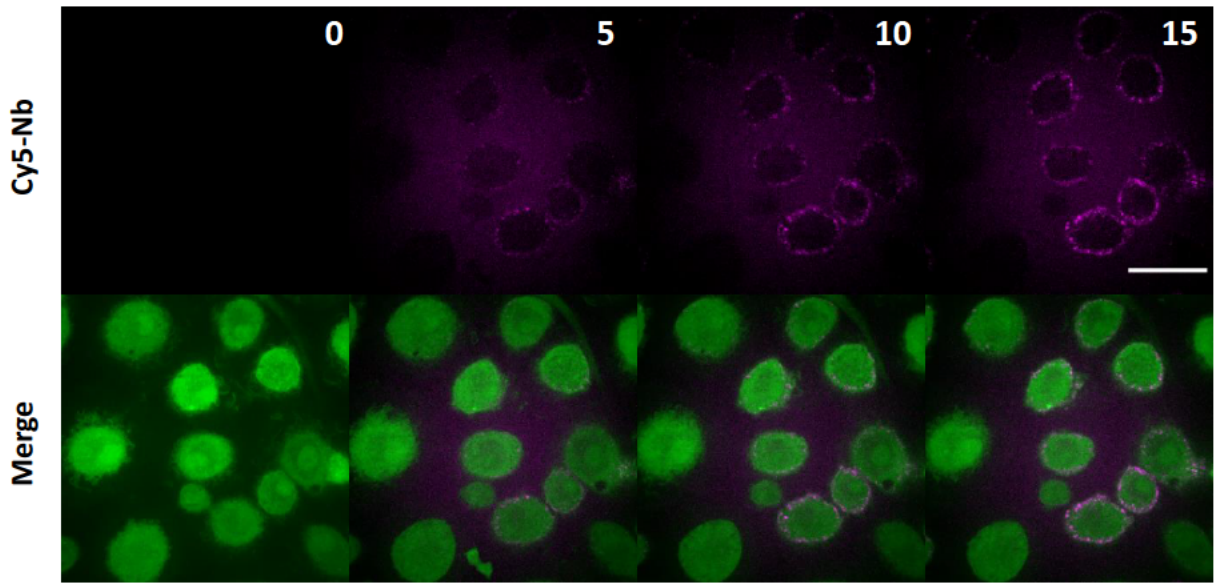

Figure 3.18. Timelapse imaging of MDMs by spinning disk microscopy showing the Cy5 and merged channels at 5-minute intervals. **Cy5-Nb** (100 nM) was added and imaged at room temperature without washing for 15 minutes. The video file showing the full timelapse is available in the Appendix. CellTracker Green (shown in green) and Cy5 (shown in magenta). Scale = 50 µm. Data from Tom Speight.

In an initial attempt to prove the target-specificity, blocking experiments with CD206 ligands were performed. However, attempts to prevent nanobody uptake with either unlabelled nanobody or another CD206 antibody did not reduce the Cy5 fluorescence signal. Instead, the labelled nanobody bound even in the presence of these 'blocking' ligands. Further investigation of the mechanism behind probe internalisation was needed.

3.4. Alternate mechanisms of uptake

Fluorescence imaging was carried out with different concentrations of **Cy5-Nb** at 37°C revealing that probe accumulation was a dose dependant dynamic process (**Figure 3.19**). The line profiles plotted showed an increase in fluorescence pixel intensity

across the selected cells, showing the concentration dependent increase. Additionally, an equivalent concentration of the SulfoCy5 dye was not taken up by macrophages, showing that the fluorophore was not responsible for macrophages binding.

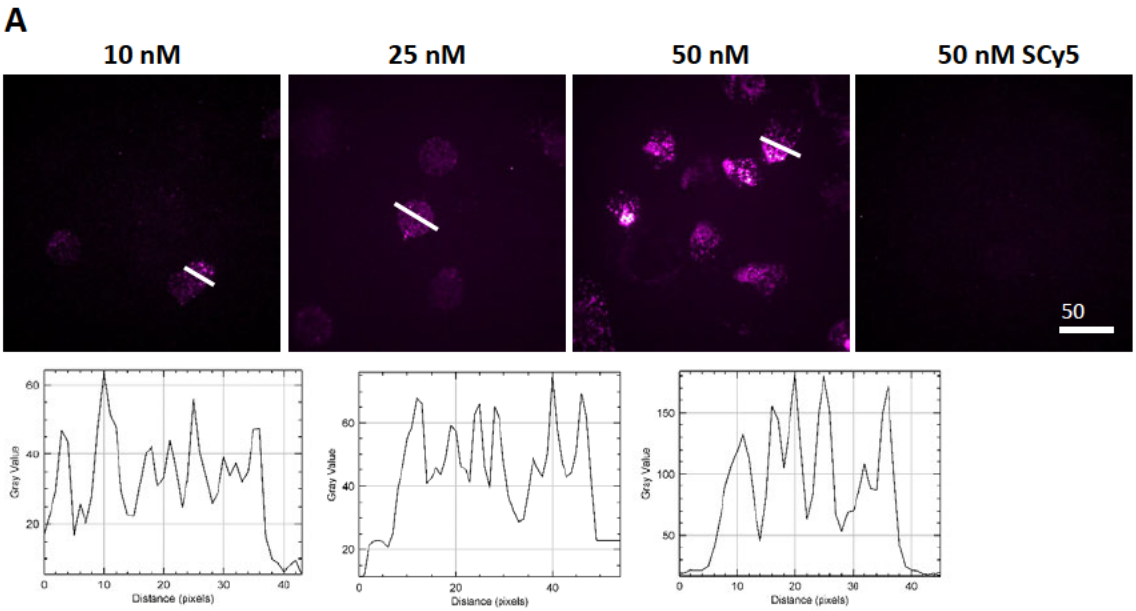

Figure 3.19. A) Confocal imaging of MDMs labelled with 50 nM **SCy5 dye** or increasing concentrations of **Cy5-Nb** (10, 25 and 50 nM) for 30 min. **B)** Quantification of fluorescence intensity from the line profiles, showing the pixel intensities within the cells. Cy5 fluorescence is shown in magenta. Data from Tom Speight.

We investigated alternative mechanisms to receptor-mediated endocytosis to see if **Cy5-Nb** was uptaken by phagocytosis (cell eating) or pinocytosis (cell drinking) (**Figure 3.20**), as it was important to understand if modification of the nanobody had affected the MMR targeting ability of the probe. Chemical inhibitors are known that block different endocytic pathways and have been applied in different studies to reveal the mechanisms of cell uptake. However, a potential weakness is that some of these

compounds have low aqueous solubility and hence require dissolution in organic solvents (DMSO) that can result in cytotoxicity and complicate results.

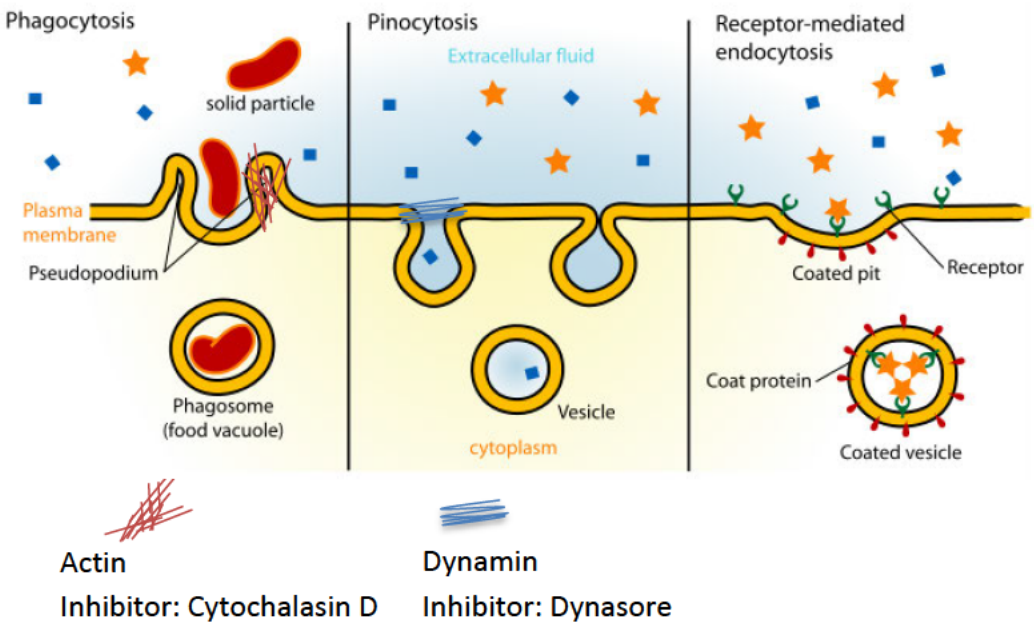

Figure 3.20. Phagocytosis or pinocytosis are alternative, passive mechanisms of uptake that macrophages may use to process **Cy5-Nb**, compared to receptor-mediated endocytosis, and their mechanisms can be studied using chemical inhibitors for actin polymerisation and dynamin.

3.4.1. Energy dependent

Energy dependent pathways are typically prevented by low temperatures as cellular processes slow down when temperatures are lower than physiologically found (37 °C). Therefore lowering the temperature of incubation has an effect on cellular uptake. However, this also slows passive diffusion mechanisms and membrane events due to hardening of the lipid bilayer.[102] To investigate the temperature dependence on **Cy5-Nb** uptake, treatment was performed at 4°C and 37 °C and MDMs assessed by microscopy (**Figure 3.21**). Reducing the temperature of incubation showed no apparent reduction in the intensity of fluorescent staining and the probe was located

intracellularly under both conditions. This suggests that the internalisation mechanism for our probe did not involve an energy dependent process.

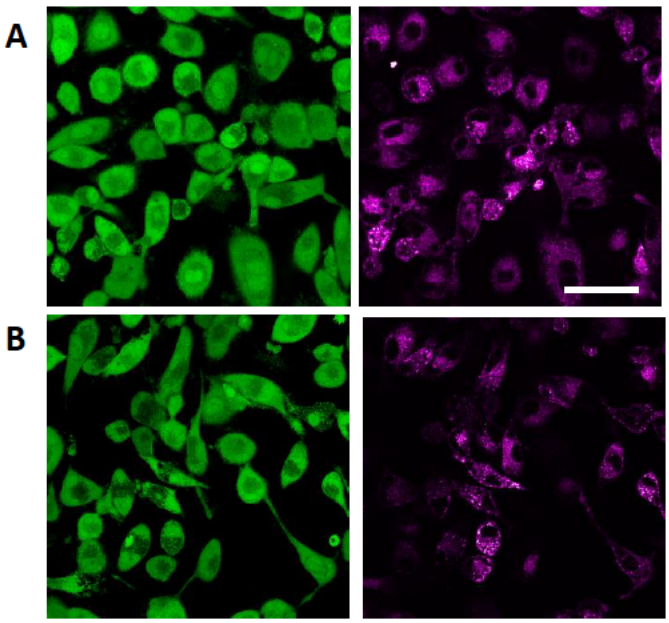

Figure 3.21. Confocal microscopy studies looking at the effect of temperature on probe internalisation. Cells labelled at **A)** 4 °C and **B)** 37 °C, with 50 nM **Cy5-Nb** (shown in magenta) for 30 min and counterstained with CellTrackerGreen (cytoplasm stain, shown in green). Scale = 50 μm. Data from Tom Speight.

3.4.2. Phagocytosis or pinocytosis

Non-targeted endocytosis of our molecule could be possible due to the role of macrophages as professional phagocytes. Chemical inhibition of phagocytosis was investigated with Cytochalasin D that blocks active uptake, and pinocytosis with Dynasore which blocks clathrin-dependent vesicle formation. Cytochalasin D acts as a phagocytosis and macropinocytosis inhibitor by disrupting actin polymerisation and preventing non-specific membrane ruffling.[103] Dynasore is a pan-dynamin inhibitor; dynamins are required for membrane budding during the transition to a vesicle. This inhibitor was originally discovered to halt receptor-mediated endocytosis of fluorescent transferrin.[104]

Imaging MDMs in the presence of the inhibitors and semi-quantification of the mean fluorescence (**Figure 3.22**) showed incubation with Cytochalasin D reduced probe signal resulting in a significant decrease in the fluorescent signal ($p \leq 0.001$), while Dynasore had no significant effect. This suggests that actin polymerisation is required for probe uptake in MDMs, while pinocytosis plays no role.

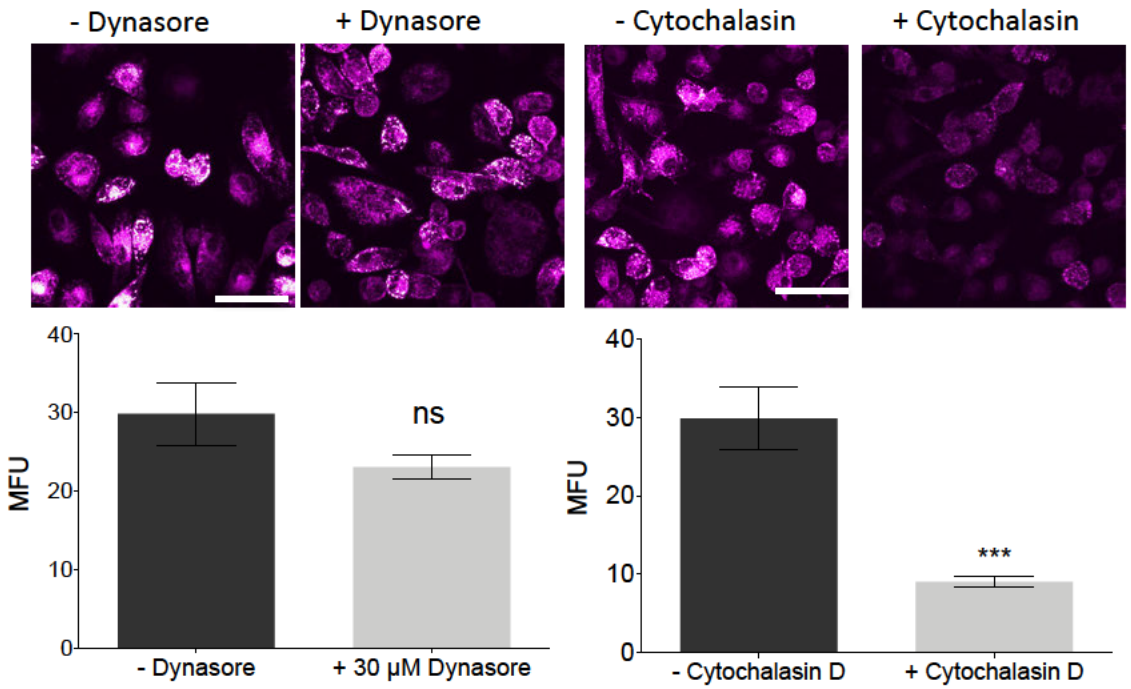

Figure 3.22. Confocal microscopy (above) of probe uptake in the presence of chemical inhibitors Dynasore and Cytochalasin D and quantification of mean fluorescence intensity from these images (below). Cells labelled with 50 nM **Cy5-Nb** for 30 min. N=2, mean ±SEM, 15-20 cells/field of view (FOV), 3 FOV/expt. Scale = 50 µm. Cy5 fluorescence is shown in magenta. Data from Tom Speight.

As previously discussed, actin polymerisation may be required for mannose receptor recycling as discovered by Gazi et al. who showed receptor expression was modulated by cytochalasin D.[76] This could mean inhibition studies with cytochalasin D may be unable to determine if the mechanism is receptor mediated. MR mediated endocytosis

was previously demonstrated as clathrin-dependent, however there are alternative dynamin-independent methods of endocytosis which could explain why the probe signal was not inhibited.

Our inhibition studies did not consider other methods of uptake such as caveolae dependent endocytosis. Caveolae mediated mechanisms could be studied with a tyrosine kinase inhibitor that prevents caveolae formation.[105] These studies would be needed to rule out this mechanism.

3.5. Primary macrophages

We also had the opportunity to test this probe on primary *ex vivo* patient samples. A bronchoalveolar lavage (BAL) from a human lung was taken, consisting of predominantly alveolar macrophages and provided an ideal model for testing macrophage probes. With BAL, a large percentage of cells were labelled by the nanobody probe (**Figure 3.23**), additionally, cells from an IPF patient contained a large number of cells that stained positively for the MMR nanobody.

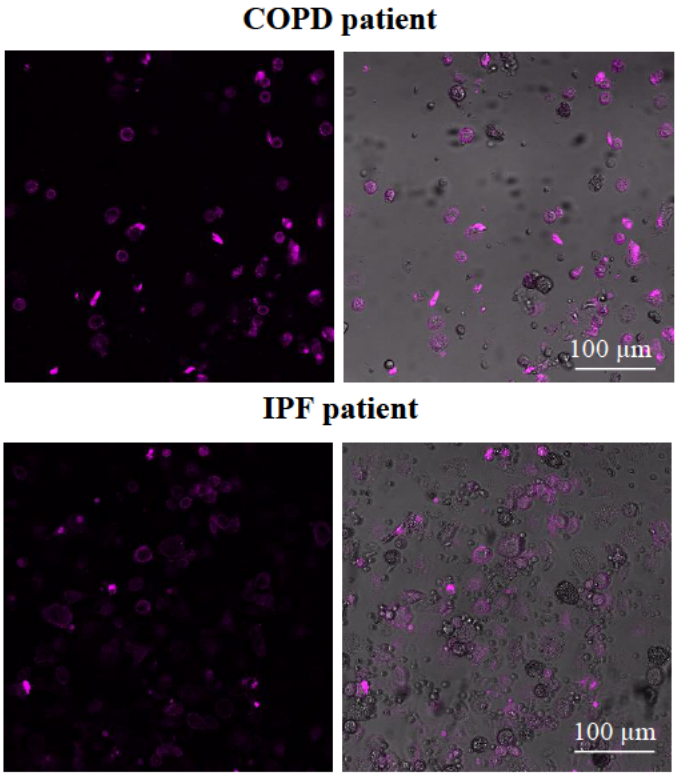

Figure 3.23. Confocal microscopy of lavage cells from COPD and IPF patients. Cells were labelled with 50 nM **Cy5-Nb** for 30 min at 37 °C. Left: Cy5 fluorescence shown in magenta. Right: Merge of Cy5 and brightfield image. Data from Tom Speight.

3.6. Conclusions

A far-red nanobody imaging agent that targets the MMR receptor of macrophages was developed. The probe was evaluated with MDM's that overexpressed CD206. Imaging studies demonstrated that the probe has high affinity, specificity to macrophages and accumulated intracellularly after a short incubation time (20 minutes). It was unclear whether this internalisation is due to receptor mediated endocytosis as competition experiments with numerous conditions could not explain the mechanism. Uptake could not be blocked with unlabelled nanobody or an anti-CD206 mAb. Phagocytosis was a possible mechanism as cytochalasin D inhibited a degree of probe uptake.

Characterisation with BAL clinical isolates from COPD patients showed that **Cy5-Nb** was able to detect a large number of MMR+ cells in these samples, demonstrating the potential application of MMR nanobodies in monitoring inflammatory diseases. The probe is the first example of a fluorescent nanobody specific to macrophages, justifying its further preclinical development.

3.7. Further work

There are several further experiments needed to validate this probe before clinical use. To show applicability to humans, imaging needs to be performed in a whole lung model to show that sufficient probe signal can be detected in such a complex environment. Nanobodies are still in their infancy, in 2019 the first nanobody received FDA approval called Caplacizumab, for the blood clotting disorder acquired thrombotic thrombocytopenic purpura (aTTP).[94] Studies are necessary to understand the potential toxicity and immunogenicity of using a nanobody imaging agent; although Caplacizumab was demonstrated to have low immunogenicity. This understanding would help the field to develop more nanobody imaging agents.

4. Beta-galactosidase probes

4.1. Cellular senescence

Cellular senescence is a process of cellular aging and a state of growth arrest. Its function is to prevent damaged cells proliferating and to indicate the need for tissue repair. Senescence can be induced by telomere shortening, often referred to as replicative senescence, or telomere-independent signalling which is often characterised by DNA damage or oxidative stress and is called stress-induced senescence. Senescent cells accumulate in certain tissues and this is evident in both disease states and aging processes, e.g. osteoarthritis, fibrosis.[106] A model of the main stages of senescence is illustrated in **Figure 4.1**.

Tissue remodelling plays a key role in the pathology of chronic airway diseases, for example idiopathic pulmonary fibrosis (IPF) leads to a progressive loss of lung function and is characterised by a loss of epithelial cells, increased interstitial fibroblasts and evidence of wound healing.[107] In 2014 Tsuji looked at whether cigarette smoke exposure induced cellular senescence of alveolar epithelial cells,[108] and showed cigarette smoke contributed to oxidative stress induced senescence and reduced epithelial proliferation. More recently, serum from COPD patients was found to endow a senescent phenotype on bronchial epithelial cells when cultured *in vitro*.[109] In parallel with the increased understanding of cellular aging, there is growing interest in the discovery of compounds (referred to as senolytics) that can impact pathways that cause these processes. For example, targeting senescent cells has been demonstrated to attenuate lung fibrosis in murine models.[110]

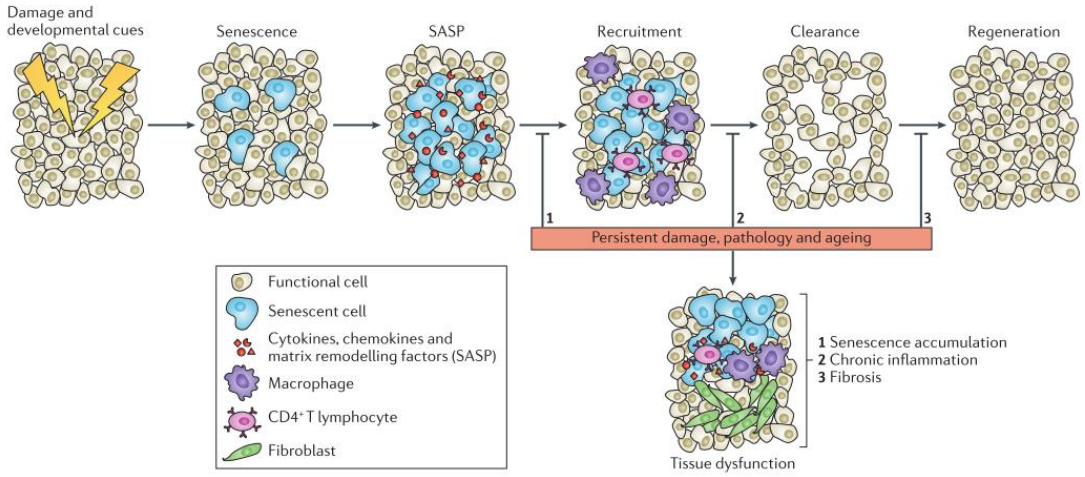

Figure 4.1. A proposed model of senescence. Senescence initiates tissue remodelling by recruiting immune cells through the senescence-associated secretory phenotype (SASP). Immune cells clear senescent cells and progenitor cells regenerate the damaged tissue. The senescence-clearance-regeneration process may be impaired by persistent damage, pathological states or ageing. In these cases, senescent cells are not efficiently cleared and the tissue is not fully regenerated. Instead the damage response leads to scarring and fibrosis. Reproduced by permission from: Nature Reviews Molecular Cell Biology, Muñoz-Espín.[111] Copyright 2014 Springer Nature.

A key feature of senescent cells is their increased beta-galactosidase (β-Gal) enzyme activity. β-Gal is an enzyme responsible for the hydrolysis of lactose to galactose and glucose. Due to its role in energy production, there is a low level of endogenous β-Gal in proliferating cells, however it accumulates in senescent cells.[111] This has been refered to as 'senescence-associated β-galactosidase' (abbreviated: SA-βGal) and is distinguishable from endogenous galactosidase as it is localised in lysosomes. Kurz determined its activity at pH 6.0 was caused by increased lysosomal biogenesis,[112] and in senescent endothelial cells the activity of SA-βGal was three to six times higher than proliferating cells. Other features of senescent cells include changes in morphology, increased lysosomal mass and expression of markers such as $p16^{INK4A}$, p21 and p53.[111, 113]

4.1.1. Alveolar macrophages

Another cell type that expresses β-Gal are alveolar macrophages which are enriched in lysosomal β-galactosidase.[114] The relative concentrations of this enzyme during epithelial cellular senescence is unclear as this has not been reported, however it would be useful to understand as the interactions between leukocytes and the epithelial barrier are a key feature of lung immunology. Recently it was reported by Qiu that M1 activated macrophages, which typically have increased glycolysis, may develop into a senescent state with knocking out guanylate binding protein (Gbp1) in RAW264.7 macrophages associated with significantly higher levels of phosphorylated p53, AMPK and increased β-Gal staining.[115] Despite alveolar macrophages and epithelial cells both expressing β-Gal, an *in vivo* method of detecting senescent cells would be a useful target.

4.2. Beta-galactosidase activity probes

The development of activatable fluorescent probes for senescence has mostly focused on detection of SA-βGal activity. However, historically there has been a wide interest in detecting the accumulation of β-galactosidase in primary ovarian cancers,[116, 117] and its use in molecular biology as a marker of transcriptional regulation.[118] The gold standard test for β-galactosidase is colorimetric 5-bromo-4-chloro-3-indoyl β-galactopyranoside (X-gal) staining, although this requires a lengthy process of cell fixation, overnight staining and manual counting.[113] In contrast, fluorescent probes are more sensitive, their readouts can be readily quantitated and they can be used with live

cells. For these reasons, the detection of SA-βGal is a valuable target for fluorescent probe development.

There are a number of existing compounds to detect the activity of β-galactosidase and the area was recently reviewed by Liu.[119] These probes are often based on the mechanism of β-Gal catalysing the hydrolysis of β-$_D$-galactosides to release fluorescent alcohols or phenols. The most widely known probe is C_{12}FDG (**Figure 4.2**) – a galactosylated hydrophobic fluorescein that is cell permeable and often used for flow cytometric detection of senescent cells.[112] This compound is non-fluorescent until hydrolysis of the galactosyl groups. Commonly, the fluorescent properties of such molecules are quenched by *O*-galactosylation due to intramolecular charge transfer (ICT). This *O*-galactosylation masks the electron donating groups which contribute to fluorescent emission. A number of recent fluorescent probes are summarised below (**Figure 4.2**).

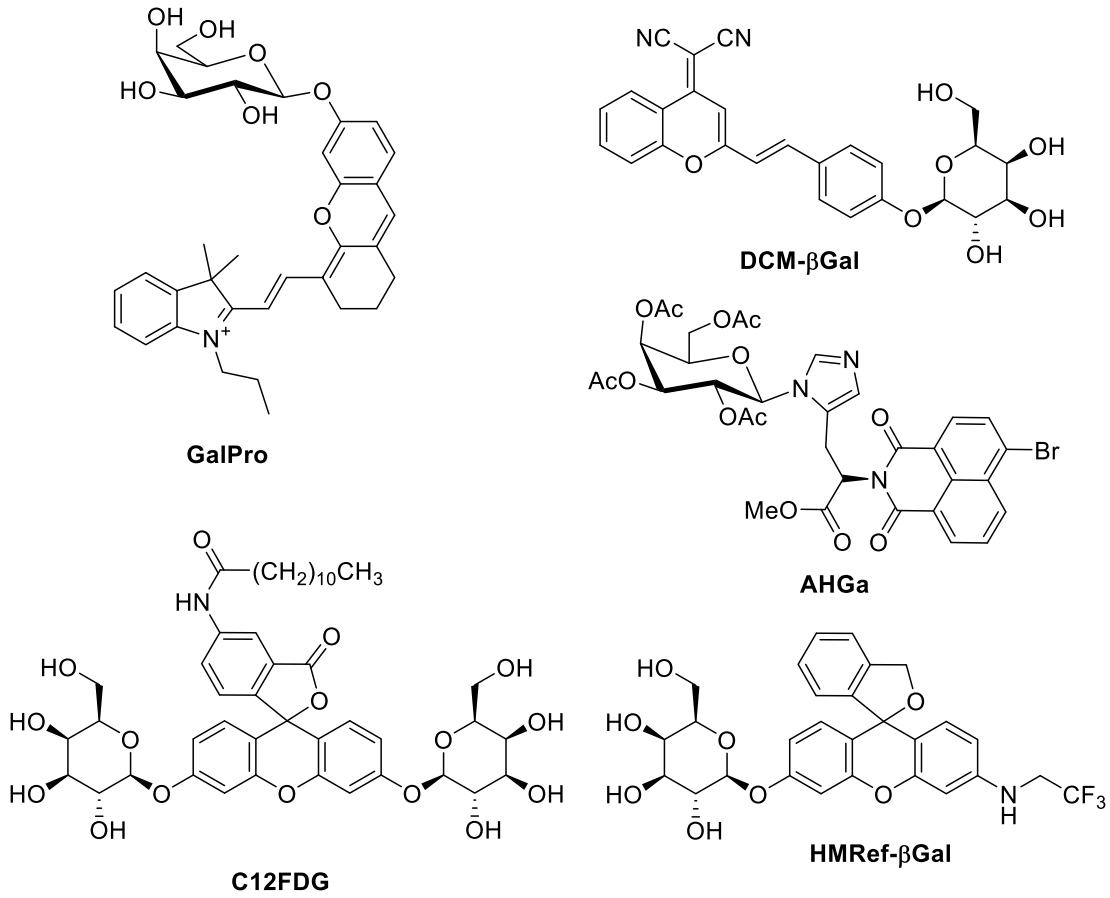

Figure 4.2. Chemical structures of a selection of recently reported fluorescent β-Gal probes including GalPro,[124] C12FDG,[112] DCM-βGal,[120] AHGa[121] and HMRef-βGal.[116]

Gu developed a ratiometric NIR probe (DCM-βgal) using the large Stokes shifted 4-(Dicyanomethylene)-2-methyl-6-(4-dimethylaminostyryl)-4*H*-pyran (DCM) dye which allowed imaging of a colorectal tumour in real-time.[120] Notably this probe required solubilisation with 30% DMSO in PBS, suggesting poor solubility. A napthalimide-based two-photon probe (AHGa) for detecting senescence was designed by Lozano-Torres using a napthalimide-L-histidine scaffold with a hydrolysable *N*-glycosidic bond.[121] This was applied for *in vivo* detection of senescence in mice bearing tumour xenografts that had induced senescence by chemotherapy.

Asanuma synthesised a β-Gal probe based on a xanthene HMRef-βGal.[116] By optimisation of the fluorophore to reduce background interference they developed a probe which had good cell permeability. Upon enzymatic cleavage this probe generates a remarkable 1420-fold fluorescence enhancement due to release of the highly fluorescent rhodol dye (**Scheme 4.1**). HMRef-βGal was able to detect β-Gal activity in ovarian cancer lines and peritoneal metastatic tumours of <1 mm during *in vivo* fluorescence guided surgery.

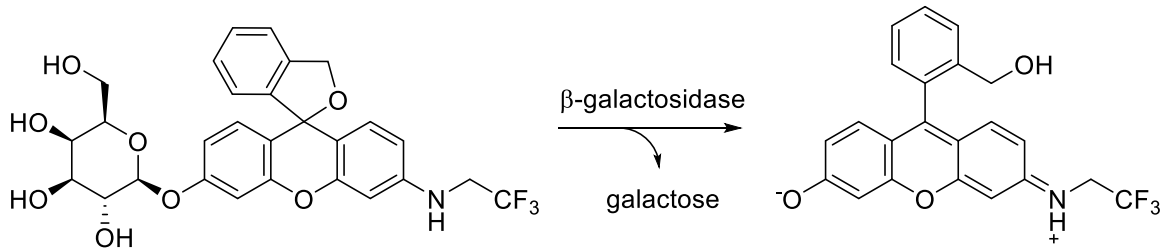

HMRef-βGal **HMRef**

Scheme 4.1. Hydrolysis of the quenched HMRef-βGal probe by β-galactosidase gives the fluorescent product HMRef and galactose as a by-product.

In order to reduce the cellular leakage of HMRef-βGal, Doura synthesised a probe (SPiDER-βGal**)** for the detection of lacZ(+) cells.[122] A weakness of their previously developed HMRef fluorophore was that it tended to diffuse and leak out of cells upon activation. To prevent this, SPiDER-βGal was designed to undergo a reaction with cellular nucleophiles via a quinone methide intermediate after activation by β-galactosidases (**Scheme 4.2**). This probe gave single-cell resolution of enzyme activity in HEK cells expressing the lacZ reporter and in *ex vivo* imaging of wing disks from *Drosophila melanogaster* and brain slices of mice. Although this probe was highly optimised, it was never applied in models of cellular senescence to detect SA-βGal. In

addition, the use of a green fluorophore would be problematic for clinical applications, as discussed in Chapter 1.

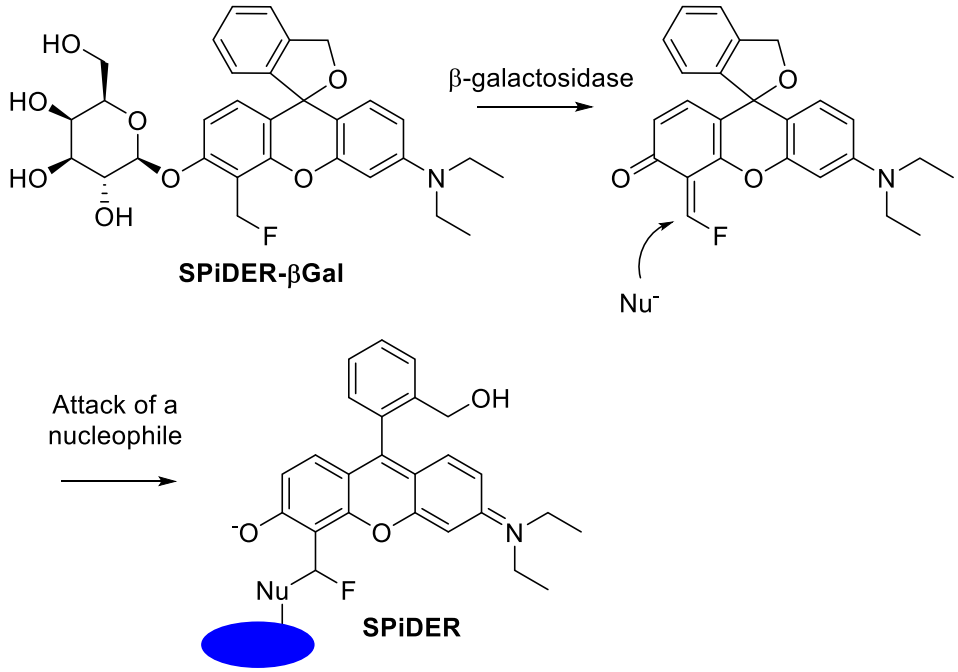

Scheme 4.2. SPiDER-βGal probe showing when the galactoside moiety is cleaved the probe can bind to intracellular proteins (shown in blue) and this occurs along with the activation of fluorescence (SPiDER).

Hemicyanines are a recent development in the class of cyanine fluorophores and have near-infrared emission, moderate quantum yields, good brightness and low photobleaching.[123] They have been used as activatable fluorophores due to the presence of a hydroxyl group within the conjugation structure of the molecule that can be functionalised to give a quenched intramolecular charge transfer (ICT) system (**Scheme 4.3**).[10] Additionally, they were synthesised in a single step from the IR780 cyanine 7 dye. Zhang developed a near infrared probe for β-galactosidase (GalPro) by attaching β-$_D$-galactoside to the NIR hemicyanine fluorophore.[124]

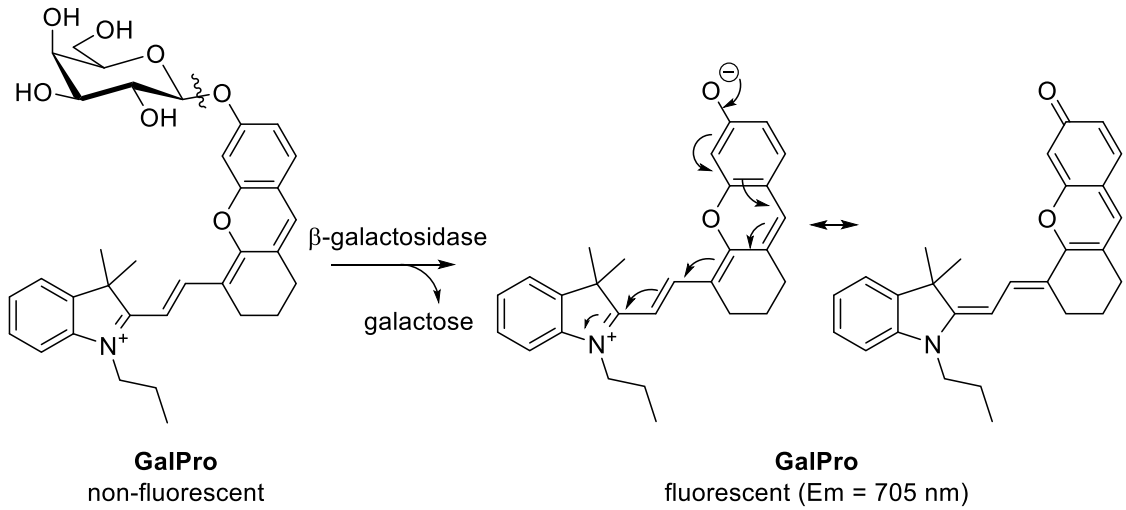

Scheme 4.3. GalPro has a O-galactose moiety that forms a quenched ICT system. After cleavage of the galactose unit by β-galactosidase the fluorescent phenolate is liberated, giving an extended conjugation system within the hemicyanine dye and removal of the ICT system.

GalPro has properties such as NIR emission at 703 nm, a 12.8-fold fluorescence increase upon glycosidic cleavage and a limit of β-Gal detection of 0.057 nM.[124] In comparison to other reported probes (**Table 4.1**), it had a higher catalytic efficiency (k_{cat}/K_m) than the DCM-*β*gal and FDG probes.

Table 4.1. Comparison of reported properties of **Gal-Pro** with other β-Gal fluorescent probes.

Probe name	**Emission maxima for detection (λ_{em})**	**Detection limit**	***K*m (μM)**	**k_{cat}/K_m ($M^{-1}s^{-1}$)**	**Ref.**
DCM-*β*gal	685 nm	1.7 x10^{-4} U/mL	60.1	4.8 x10^5	[120]
SG1	~550 nm	0.25 nM	1.73	4.73 x10^6	[125]
FDG	520 nm	N/A	10.2	1.6 x10^4	[125]
Gal-Pro	703 nm	0.057 nM	3.6	2.2 x10^6	[124]

Although most of the probes generated are capable of sensitively detecting β-galactosidase, only a few have been applied to detect SA-βGal. GalPro was used for the detection of SA-βGal in fibroblasts where premature senescence was induced with hydrogen peroxide, however a limited amount of biological data was reported and this model does not truly represent epithelial cell senescence.

While some of the reported probes can detect cellular senescence, it is not clear whether the models used reflect the complexity of the senescence phenotype *in vivo*. For this project a β-Gal probe was needed that could detect senescent epithelial cells and that had suitable physiochemical properties for *in vivo* lung imaging. Therefore, the ideal properties a β-galactosidase probe would be far-red/NIR emission for low background fluorescence and specifically turned-on by β-galactosidase in senescent epithelial cellular models. Synthesising a galactosidase probe would be a good starting point for investigating SA-βGal.

4.3. Synthesis of hemicyanine probes

Following on from the work of Zhang, two NIR galactosidase activatable probes were synthesised. The commercial cyanine dye IR780 was initially synthesised (**Scheme 4.4**) and then transformed into the hemicyanine dye by retro-Knoevenagel condensation with 1,3-dihydroxybenzene or 4-bromo-1,3-dihydroxybenzene. The mechanism of this reaction is shown in **Scheme 4.5**. The galactosyl moiety was appended in two steps; *O*-galactosylation of the phenol with galactose pentaacetate using caesium carbonate and subsequent deprotection under basic conditions (**Scheme 4.6**).

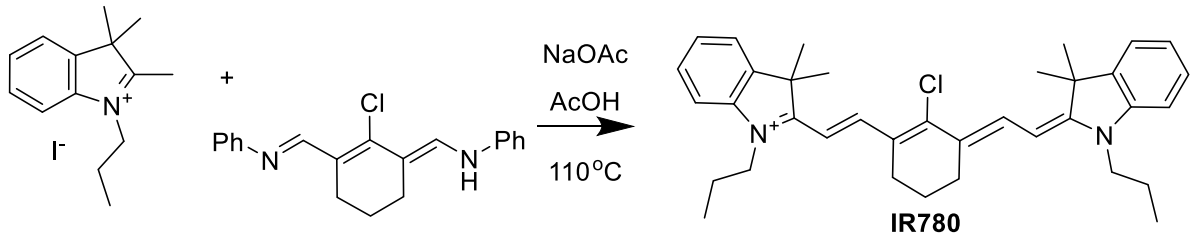

Scheme 4.4. Synthesis of cyanine 7 dye IR780 by condensation of the indolenine salt with the dianil linker.

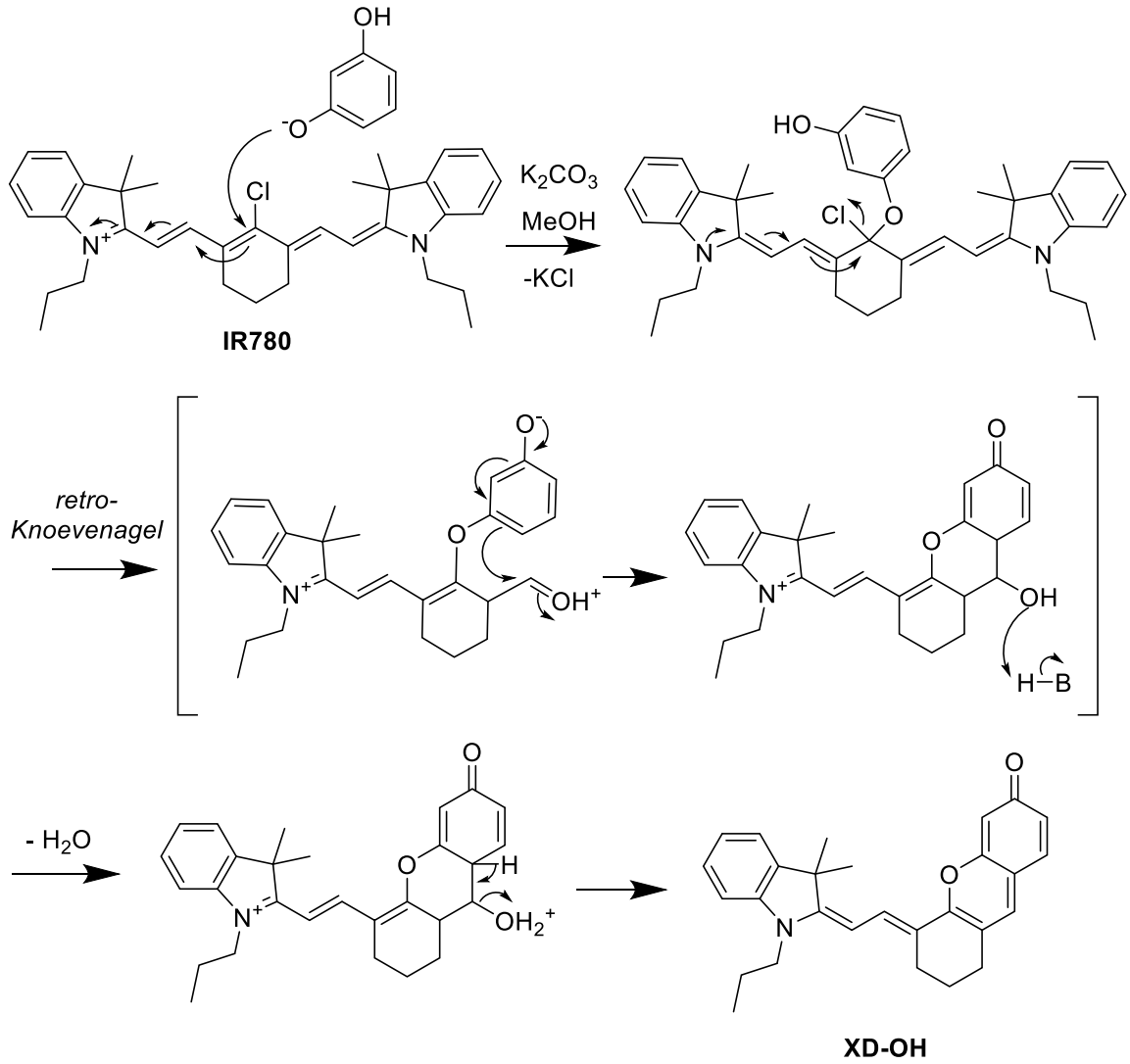

Scheme 4.5. Reaction mechanism for the formation of the hemicyanine dye **XD-OH**. Although the first step is shown as an S_N2' mechanism. IR780 is reacted with 1,3-dihydroxybenzene in the presence of K_2CO_3 as base at 50 °C. The first step is a nucleophilic substitution, followed by the retro-Knoevenagel leading to the elimination of a trimethyl-indole group. This allows for a ring-formation with elimination of water, to give the hemicyanine dye.

The probes were purified by prep-TLC or RP-HPLC as the deprotected sugar is highly polar (see **Table 4.2**). The GalPro compound synthesised by Zhang is referred to as **XD-BGal** in this work. A variant containing a bromine was synthesised in parallel called **XD-Br** and its galactosyl analogue **XD-BrBGal**. The partition coefficients (clogP) were calculated using the molinspiration program to give an idea of the lipophilicity of these probes and whether they would be likely to permeate cell membranes.

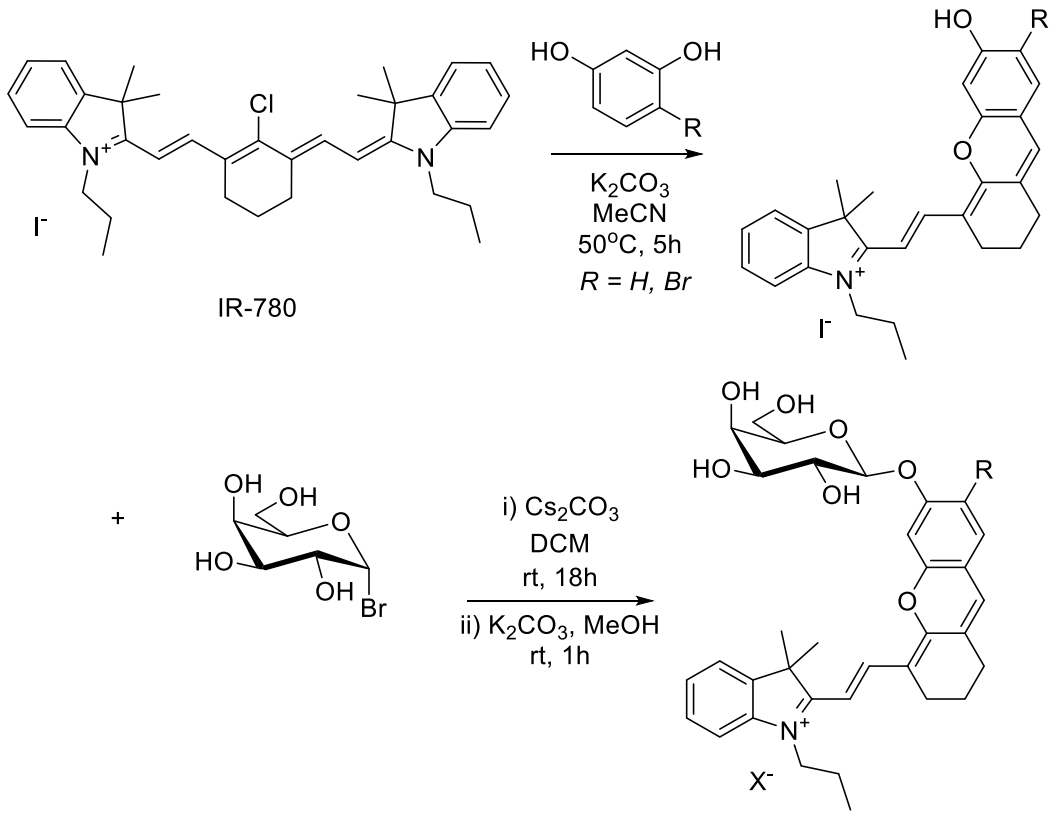

Scheme 4.6. Synthesis of two hemicyanine based fluorophores with a β-galactose unit attached.

Table 4.2. The properties for the four compounds synthesised. clogP was calculated using the molinspiration properties calculator.[151]

Code	Structure	Molecular weight (free base)	clogP
XD-OH	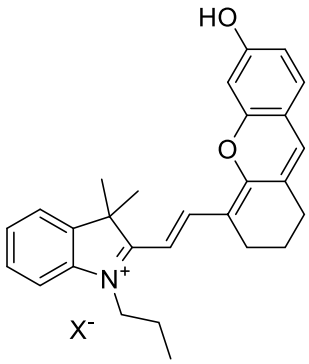	412.6	3.06
XD-BGal	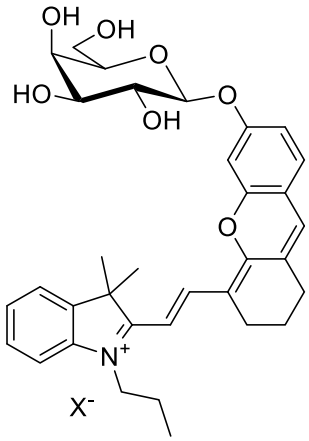	574.7	1.28
XD-Br	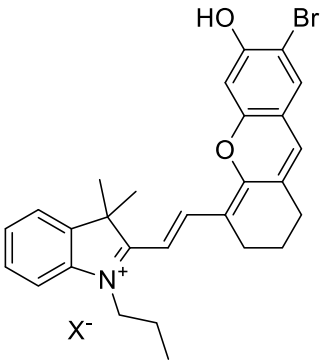	491.5	4.06
XD-BrBGal	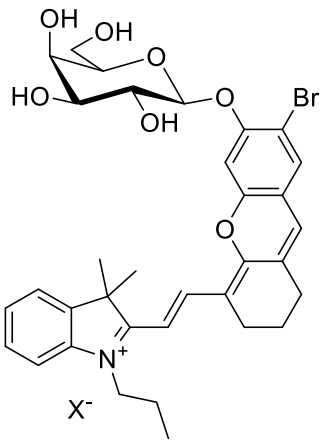	653.6	2.01

The synthesised probes were more hydrophobic than desired and attempting to dissolve these entirely in water or PBS solution resulted in precipitation. Therefore, it was necessary to dissolve the stock solutions in DMSO. It would be desirable to improve the properties of these dyes because the use of solvents such as DMSO are not optimal for human applications. A more soluble probe would be predicted to have a lower logP value.

4.4. Photophysical properties

The photophysical properties of each molecule were characterised by UV-Vis and fluorescence spectroscopy (**Figure 4.6**). A summary of the optical properties (excitation and emission maxima and quantum yield) for the compounds are reported in **Table 4.3**.

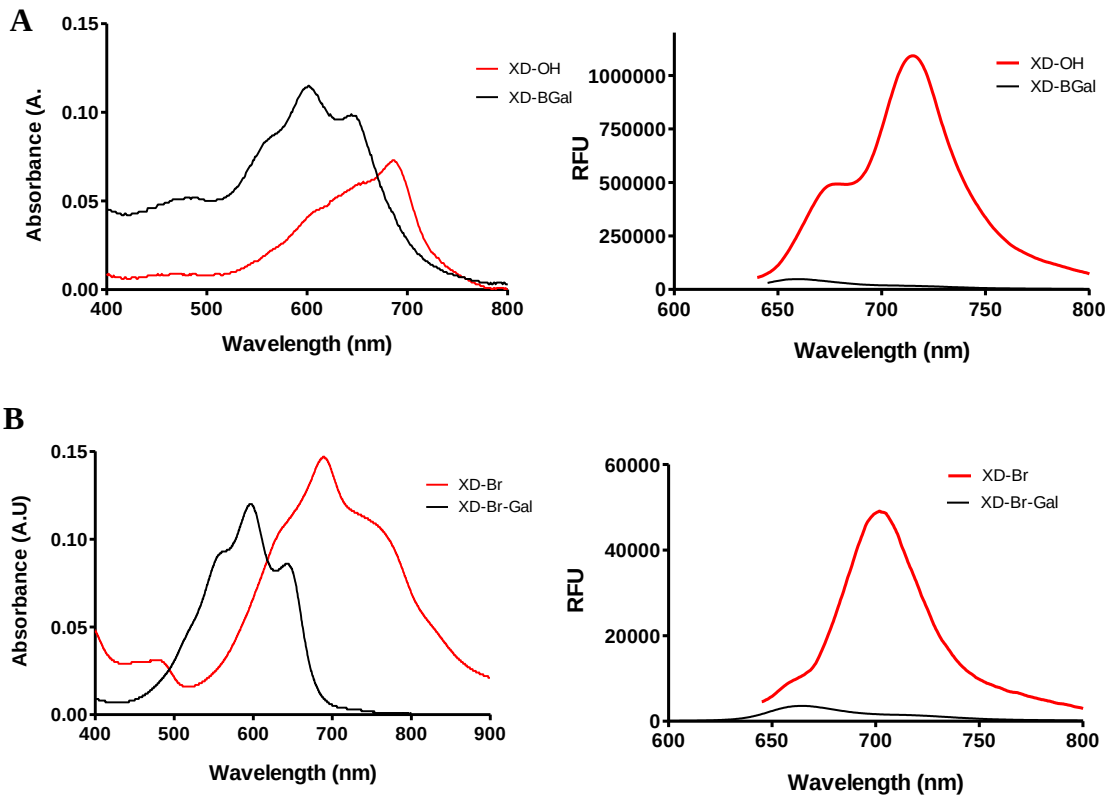

Figure 4.3. Absorbance and emission spectra of A) **XD-OH** and **XD-BGal**, B) **XD-Br** and **XDBr-BGal**. Absorbance spectra recorded using a microplate reader with 10 µM probe in PBS + 5% DMSO. Fluorescence spectra recorded using a spectrofluorometer with 1 µM compounds in PBS + 5% DMSO.

The quantum yields of the galactose probes were calculated using **Equation 3**.

$$\Phi_x = \Phi_{ST}(f_{ST}/f_x)(F_x/F_{ST})(\eta_x/\eta_{ST})^2$$

Where:
f is the absorption factor ($f = 1\text{-}10^{-A}$, where A = absorbance)
F is the area under the emission curve, η is the refractive index of the solvents
Φ_{ST} is the quantum yield of the standard
ST = standard, x = sample

Equation 3. Formula for the calculation of the quantum yield using the comparative method with the reference dye indocyanine green (ICG) in DMSO ($\Phi_F = 0.106$)

Table 4.3. Quantum yields (Φ_F) were recorded with freshly prepared solutions (water + 0.01% DMSO) compared to ICG.

Code	λex max (nm)	λem max (nm)	Φ_F (620nm)
XD-OH	680	714	0.118
XD-BGal	596	661	0.003
XD-Br	685	703	0.016
XD-BrBGal	592	664	0.001

There was little difference between the absorption and emission maxima for both sets of compounds, except for **XD-Br** having a broader absorbance extending over 800 nm compared to **XD-OH** (**Figure 4.3**). As expected, the galactose probe emitted very weakly in the 660 nm region, while the fluorophores emitted at 700-715 nm. The change in absorbance was also noticeable in their visual appearance in solution (**Figure 4.4**). Attaching galactose to **XD-OH** decreased the quantum yield by 40-fold, while **XD-Br** showed a 16-fold fluorescence quenching.

The low quantum yield of **XD-Br** (Φ_F = 0.016) suggested that the bromine heavily quenched the fluorescence of this molecule. It is surprising that Liu was able to use this molecule for fluorescent microscopy.[126] This result meant the **XD-Br** compounds were not used for further imaging based studies due to their inferior fluorescent properties.

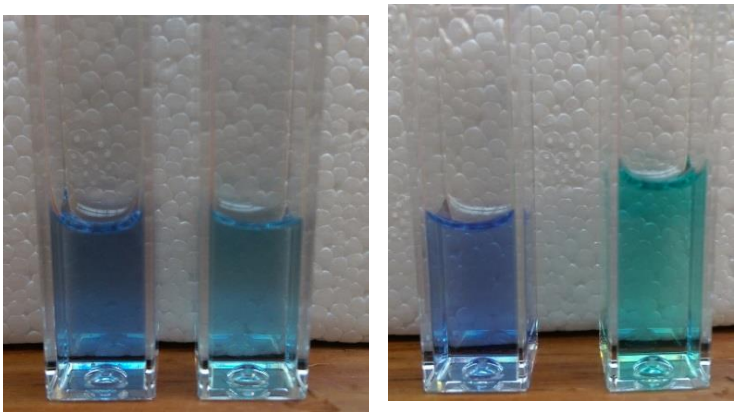

Figure 4.4: Colour change of **XD-BGal** and **XD-BrBGal** before and after β–gal enzymatic cleavage (1 μM, PBS).

4.4.1. Effect of pH

The intensity of fluorescence of **XD-OH** was dependent on the pH of the local environment due to the pH dependent equilibrium between the phenol and phenolate form of the fluorophore (**Scheme 4.6**). This is relevant as beta-galactosidase is a lysosomal enzyme and under the conditions of senescence lysosomal acidity can increase to a pH of 6.[112] Therefore an ideal pro-fluorophore should have sufficient fluorescence intensity at this pH and this would ideally be pH independent. To understand the effect of pH on the probes photophysical properties, the absorbance and emission spectra were measured in different pH buffers (**Figure 4.5**).

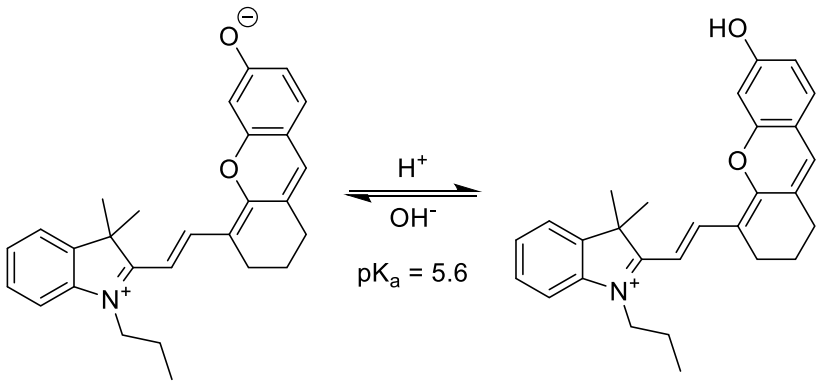

Scheme 4.7. Equilibrium between the phenol and phenolate forms of the **XD-OH** fluorophore.

Previously, Yuan found that the phenol group of **XD-OH** had a pK_a of 5.6.[123] In our hands, with the change of pH from 4.5 to 7.4 the absorbance spectrum undergoes a red-shift from two maxima (600 and 660 nm) to a maxima at 690 nm, presumably due to the phenolate form of the dye (**Figure 4.5A**). With **XD-BGal** the phenolate cannot be formed due to *O*-alkylation with galactose, therefore the absorbance profiles of this probe were insensitive across the range from 4.5 to 7.4 (**Figure 4.5B**).

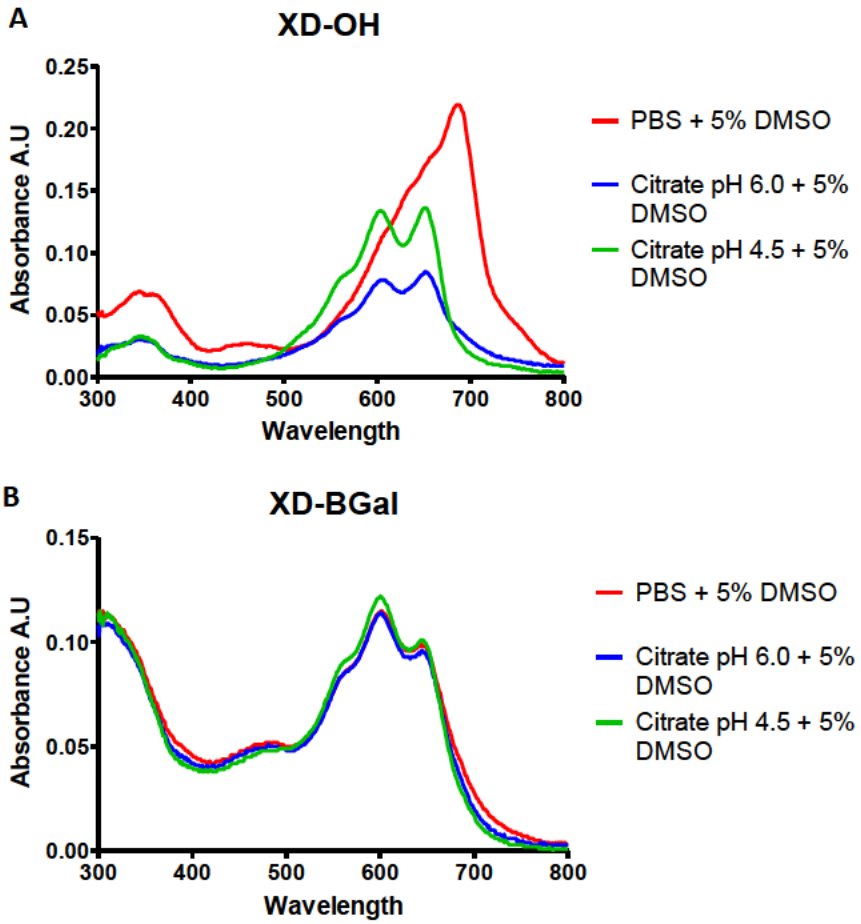

Figure 4.5. pH-dependence of absorbance spectra for A) **XD-OH** and B) **XD-BGal**. 5% DMSO was used to ensure complete solubility. Spectra were recorded as 10 µM solutions in PBS and citrate buffers (pH 7.4, 6.0 and 4.5) + 5% DMSO. Data from Philip Emanuel.

The emission profile of **XD-OH** was measured with excitation at 633 nm. Changing the pH from 4.5 to 7.4 gave a 4.9-fold increase in fluorescence, with an emission maximum (λ_{max}) of 709 nm (**Figure 4.6**). The increase of fluorescence at higher pH can be explained by the formation of the phenolate form that had brighter fluorescent properties. In conclusion, the reduced emission seen at pH 4.5 could help to distinguish endogenous beta-galactosidase from SA-βGal in lysosomes at pH 6.

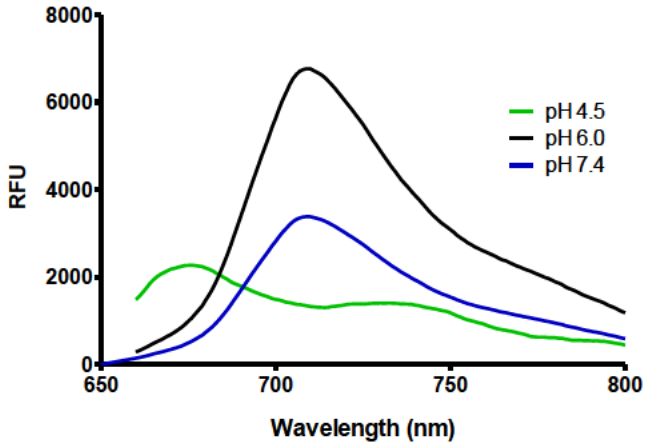

Figure 4.6. pH-dependence of fluorescence of **XD-OH** measured at different pH's. Fluorescence spectra were recorded with excitation at 633 nm, 10 μM solutions in PBS and citrate buffers (pH 7.4, 6.0 and 4.5) + 5% DMSO.

4.5. Biochemical assays

4.5.1. HPLC assays

To determine that the probe was cleaved by β-galactosidase, **XD-BGal** (100 μM) was incubated at 37 °C with β-galactosidase (40 nM). After 1 hour the reaction was stopped, filtered to remove the enzyme and reaction progress determined by HPLC. Standards for the starting material (**XD-BGal**, t_R = 3.7 min) and product (**XD-OH**, t_R = 4.4 min) were also prepared for comparison. HPLC analysis showed that 40 nM enzyme was sufficient to fully cleave the probe over 1 hour (**Figure 4.7**) with confirmation of the identity of the product determined by LC-MS.

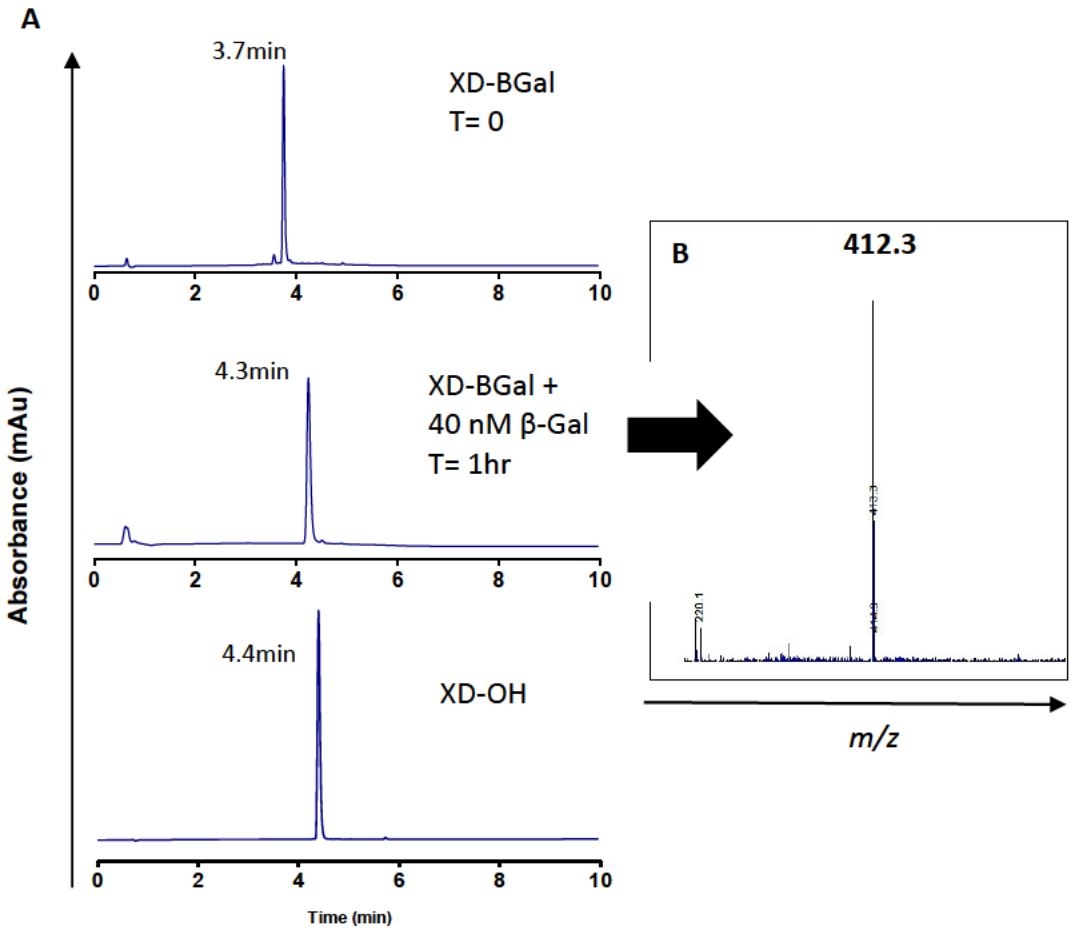

Figure 4.7: A) HPLC analysis of the reaction of **XD-BGal** with recombinant β-Gal. Top: **XD-BGal**, T= 0 hr, Middle: **XD-BGal** reacted with β-Gal for 1 hr, Bottom: a sample of **XD-OH**. HPLC analysis with detection at 650 nm. **B)** ESI-MS analysis of the reaction sample after 1 hr confirmed that the probe (HRMS: $[M]^+ = 574.2755$, see Chapter 6.5 for complete characterisation) was cleaved by the enzyme ($[M+H]^+ = 412.3$).

It was important to determine the stability of the probe to understand if the storage conditions were suitable. To determine the stability of **XD-BGal** a solution of the probe was stored at -20°C for 6 months in DMSO and analysed by HPLC (**Figure 4.8)**, this demonstrated that the probe was stable under these storage conditions.

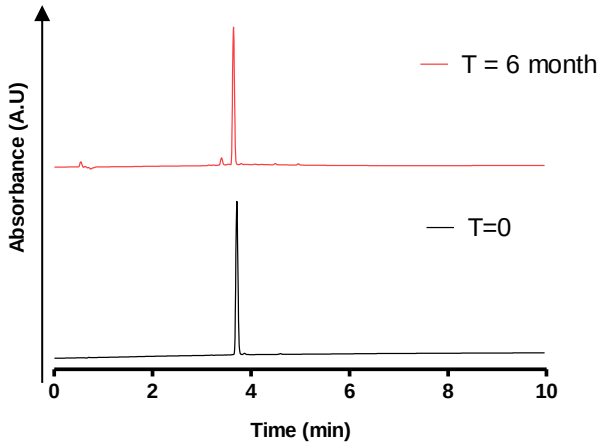

Figure 4.8. HPLC stability study showing both the homogeneity of the initial sample and after storage at -20°C for 6 months (red). t_R = 3.8 min. Detection by absorbance at 650 nm.

4.5.2. Kinetics

To monitor the fluorescence generated by the probe in the presence of β-galactosidase, a microplate assay was used. **XD-BGal** was incubated with β-gal for 10 minutes giving a clear fluorescence increase with an emission maxima at 709 nm and reaching maximum intensity with 25 nM of enzyme (**Figure 4.9**).

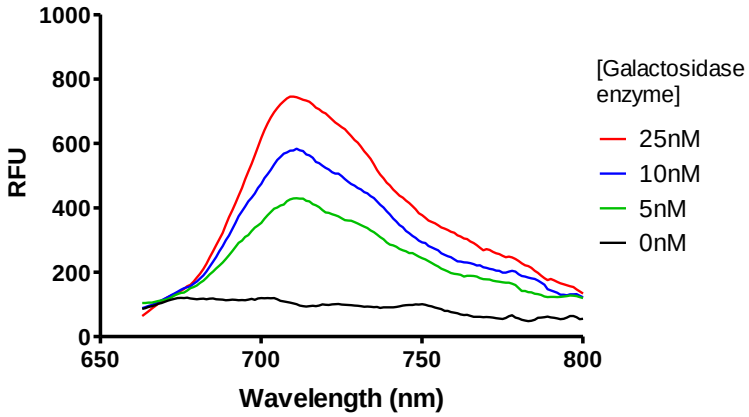

Figure 4.9. Fluorescence spectra of **XD-BGal** (100 µM) after incubation with the indicated concentrations of recombinant β-Gal for 10 minutes as measured by microplate reader with excitation at 633 nm. Data from Philip Emanuel.

The probe was characterised by steady-state kinetics with the fluorescence generated by incubating different concentrations of the probe (1 to 20 µM) with 5 nM β-Gal over 30 minutes and the initial velocity calculated. Plots of initial reaction rate against concentration were generated and non-linear regression used to find the Michaelis constant (K_m), according to the Michaelis-Menten equation ($v = V_{max}[S]/K_m + [S]$). We measured a K_m of 1.5 µM and a maximum rate, V_{max} of 3.2 nM s^{-1}, showing that **XD-BGal** was efficiently cleaved by the enzyme.

4.5.3. Competition with other endogenous glycans

In the cellular environment numerous glycans are present and would decrease the fluorescence signal by competing with the fluorescent probe at the active site of enzymes. Two glycans were investigated, D-glucose which is a common component of cell culture media, and D-galactose which may be found after the hydrolysis of lactose and is a competitive inhibitor of β-gal. (**Figure 4.10**). In the presence of galactose

(100 nM), the fold change of fluorescence was 2-fold reduced as expected. However, glucose had no significant effect on the fluorescence increase, as expected as it is not a competitive inhibitor of β-gal.

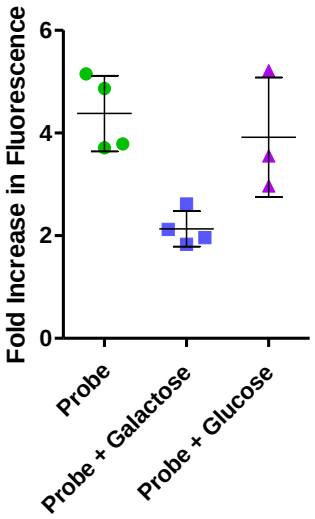

Figure 4.10. Quantification of fold change in fluorescence of **XD-BGal** in the presence of the sugars galactose and glucose. (n=3), Probe (50 μM), D-galactose (100 nM), D-glucose (100 nM). Data from Philip Emanuel.

4.6. **Epithelial cellular senescence**

Senescent cells with SA-βGal expression can be induced in culture by several different treatments including oxidative stress, cytokines and DNA damaging agents. In this work we required an *in vitro* model of epithelial senescence and this has previously been carried out by treating epithelial cells with bleomycin.[127, 128]

Bleomycin was discovered in the 1960's as a fungal natural product with antitumor activity and has been used as a chemotherapy drug.[129, 130] Although its exact mode of action is still not fully understood, bleomycin is known to cause DNA strand breaks in the presence of Fe(II) and Cu(I) triggering the DNA damage response.[130, 131] However, common side effects of bleomycin include lung toxicity which can be life

threatening,[130] thus bleomycin has been used in lung injury models as its administration leads to pulmonary fibrosis.[132]

A549 cells were used to represent the type II alveolar cells that have been seen to undergo senescence in pulmonary fibrosis. For this, the lung adenocarcinoma cell line A549 was treated with bleomycin sulfate for 24 hours to induce stress-induced senescence. Initially, β-galactosidase activity after bleomycin treatment was confirmed by the classic blue precipitation of the X-gal colorimetric stain, as well as changes in cell morphology to enlarged and flattened structures. A549 cells that were not treated were used as a control group and showed no X-gal staining.

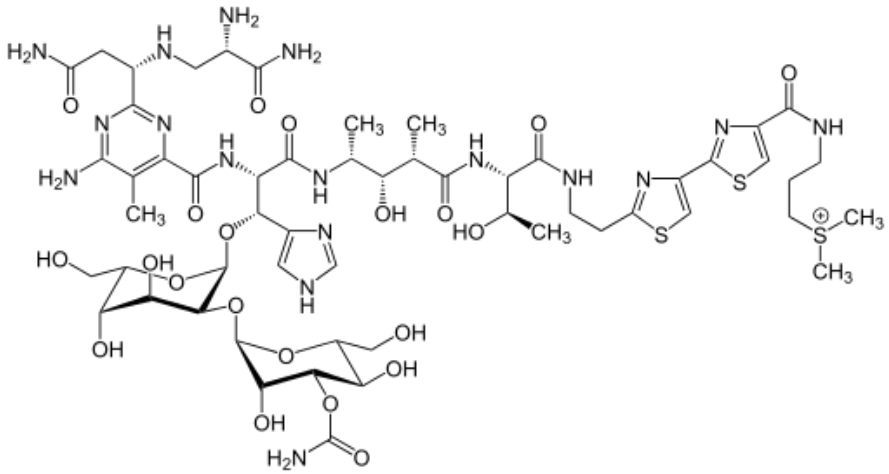

Figure 4.11. Bleomycin, an anti-cancer drug that can be used to trigger cellular senescence.

The **XD-BGal** probe was used to fluorescently stain cells to see if the fluorescence was specific to senescent cells. By fluorescence microscopy, the senescent cells showed clear NIR fluorescence after 30 minutes staining (**Figure 4.12B**). Observation under higher magnification showed the fluorescence was intracellular and appeared to be brighter in certain cellular components (**Figure 4.12D**). This localisation of

fluorescence inside cells allowed the unusual morphology associated with senescent cells to also be seen. In contrast, untreated A549 cells showed only weak fluorescence (**Figure 4.12C**) suggesting they did not have sufficient levels of enzyme to activate the probe. This shows there is selectivity for SA-βGal expressing cells.

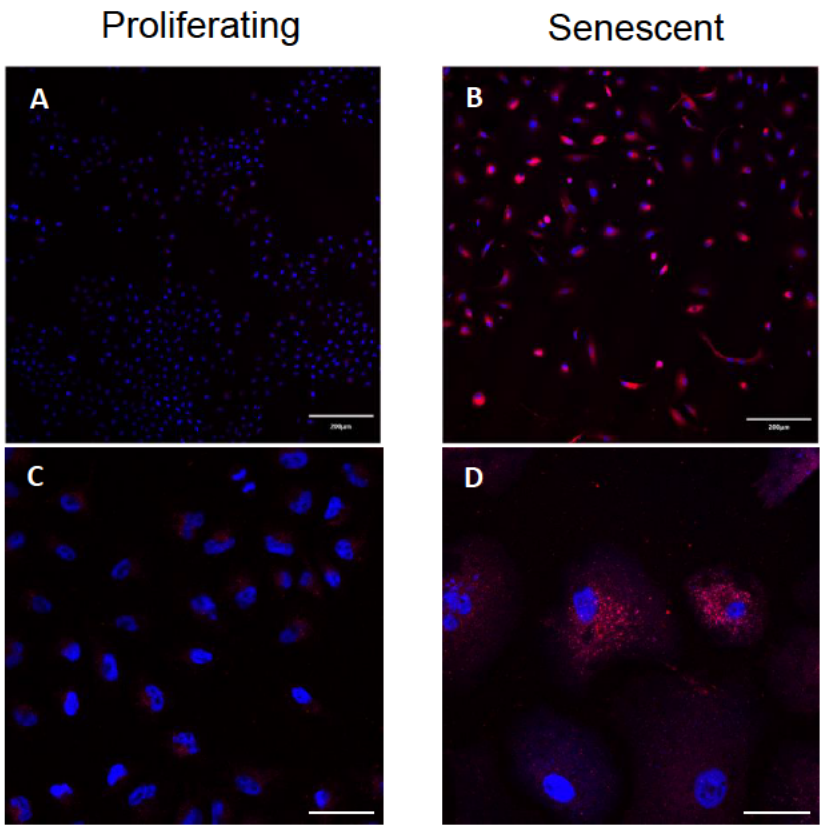

Figure 4.12: Fluorescence microscopy of A549 cells (untreated and senescent bleomycin treatment) and incubated with **XD-BGal**, **A** and **B)** x10, **C** and **D)** x40 magnifications. Cells were incubated with Hoechst 33342 (1 µg/mL and the probe (10 µM) in serum free media for 30 minutes. Hoechst (blue) and Cy5 (magenta). Scale bar = 200 µm for **A** and **B**, 50 µm for **C** and **D**. Data from Philip Emanuel.

Intrinsic galactosidase enzymes are present in cells and to be a suitable turn-on fluorescent probe it is necessary that the probe can sensitively determine SA-βGal expression. One method of distinguishing the mechanism of enzyme activation is to take exploit SA-βGal activity at increased pH. This could be explored by

experimentally comparing the lysosomal accumulation of fluorophore at the regular lysosomal pH ~ 4.5 to pH 6. Future work would look at imaging after lysosomal alkalisation using bafilomycin A1, an inhibitor of VTP-ase that is responsible for inhibiting acidification of lysosomes.

The use of A549 cells has some limitations as a model, mainly the concern that treating cancer cells which have abnormal proliferation with an anti-cancer drug does not replicate normal alveolar epithelium function. In addition it is not clear whether bleomycin itself increases βGal activity. However, the selectivity seen by the probe for senescence epithelial cells gave promise to investigating its use further.

4.6.1. Fibrotic lung slice imaging

A common functional *ex vivo* assay is to use tissue slices. The precision cut lung slice model is an *ex vivo* model for examining lung structure and function whereby lung tissues are inflated and cryosectioned on a microtome. It provides an ideal model for validating lung imaging agents since these slices can be maintained in cell media for a time. The ability to prepare murine and human tissue sections using this technique, giving optically thin and viable cells, has been demonstrated.

Using the precision cut lung slice model with murine lung we tested whether our probe could detect beta-galactosidase activity as *in vivo* exposure of mice to bleomycin has been shown to generate SA-βGal activity. By confocal microscopy, a murine lung tissue slice was stained with the probe and imaged (**Figure 4.13**). A large proportion of cells activated the probe and morphologically some of these appeared to be

macrophages due to their larger size (see highlighted merge image, **Figure 4.13**). Further confirmation of the presence of senescent cells with other techniques is necessary to show the target specificity of the probe, but if the probe is sensitive to lower levels of beta-galactosidase in other cells types then it may be necessary to use image analysis methods to identify senescent cells using this probe.

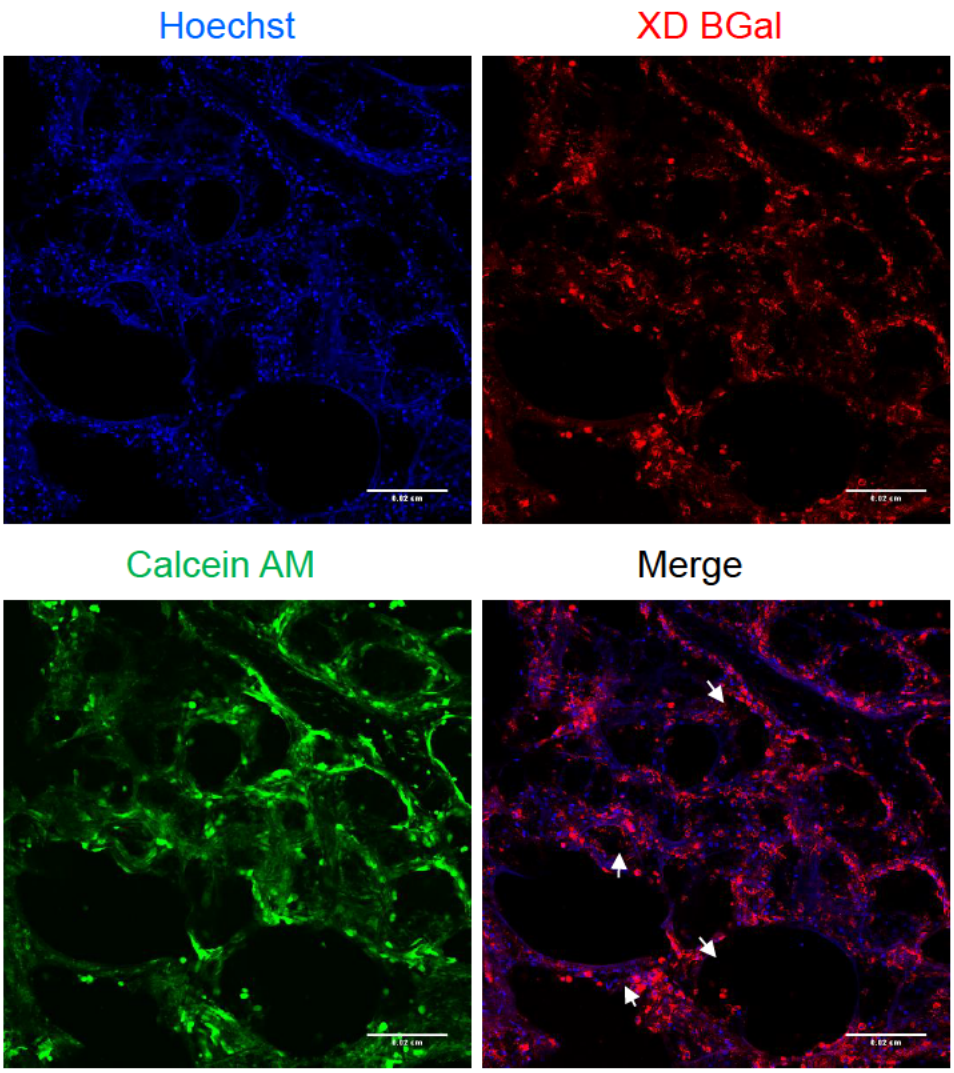

Figure 4.13. Confocal imaging of murine lung slices showing individual fluorescent channel and the merged image. Mice were treated for 7 days with bleomycin to cause lung fibrosis, post-treatment lung slices were cryosectioned using the precision cut lung slice model and stained with **XD-BGal** (10 µM, red), Hoechst (1 µg/mL, blue) and Calcein AM (0.2 µM, a live cell marker in green). A large number of cells were stained for βGal activity (red). Suspected macrophages are highlighted in the merge image. Scale = 20 µm. Data from Philip Emanuel.

4.7. **Conclusions**

In conclusion, the application of **XD-BGal** in cellular models of senescence showed its feasibility for future studies in more advanced models. Each probe and fluorophore were characterised to understand their photophysical properties, stability and kinetics. **XD-BGal** showed selectivity for A549 cells that were treated with a chemotherapy agent (bleomycin) to cause SA-βGal expression**.** Initial imaging of murine lung slices showed that a number of cell types expressing galactosidase activity could be detected. In future, these positive staining cell types should be classified in more detail by immunohistochemical or other techniques. While the brominated analogue (**XD-BrBGal**) was not used for microscopy studies, in an attempt to understand the fluorescent properties of this probe the singlet oxygen quantum yield was calculated.

4.7.1. Singlet oxygen generation

The **XD-Br** probe had a low quantum yield (0.016) probably due to the presence of the bromide group. It is also known that fluorophores can generate singlet oxygen through the heavy atom effect, however the efficiency of singlet oxygen generation is often a trade-off with the fluorescence quantum yield.[133] Common photosensitisers such as methylene blue (MB) and Chlorin E6 (Ce6) exhibit high singlet oxygen generating capacity (0.55 and 0.66, respectively), but MB has a low fluorescence quantum yield (0.02).[133] It was suggested that **XD-Br** could be capable of generating singlet oxygen with a potential application as a photosensitiser.

XD-BrBGal could be used to detect cells that express high levels of β-gal and act as a beta-galactosidase activatable photosensitiser (aPS). Ideally, this would require high

singlet oxygen generating capabilities and allow cell specific ablation based on enzyme expression. A combination of 'imaging' and 'killing' agents could allow a theranostic approach to treating cells overexpressing this disease biomarker.

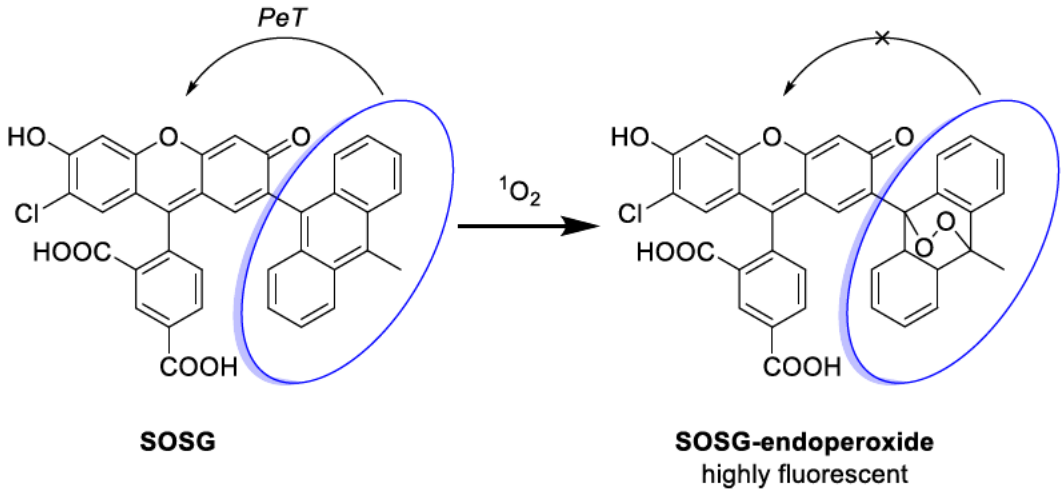

Scheme 4.8. SOSG (which has quenched fluorescence by a PeT mechanism) reacts with singlet oxygen and generates SOSG-endoperoxide resulting in dequenching.

The singlet oxygen ($^1O_2$) generation was determined using the Singlet Oxygen Sensor Green (SOSG) fluorescent assay (**Scheme 4.7**).[134] SOSG is based a fluorescein structure with an "anthracene trap" that quenches fluorescence by a PeT mechanism. In the presence of singlet oxygen, the anthracene reacts with $^1O_2$ to form SOSG-endoperoxide which removes the quenching effect. However, it is unclear whether the method used for determination of the singlet oxygen quantum yield could be susceptible to interference. The fluorescent emission of SOSG-endoperoxide could be quenched in the presence of fluorophores such as **XD-OH** and **XD-Br** that have overlapping excitation spectra (possibly causing a FRET phenomenon). Nevertheless, the relative singlet oxygen quantum yield (Φ_Δ) was determined using SOSG in comparison to the standard methylene blue.

Table 4.4. Properties of the fluorophore singlet oxygen generation capabilities were determine according to procedure by Lin.[134] Samples of each fluorophore in oxygen-bubbled methanol solutions were irradiated under a 650 nm LED lamp for 30 minutes. N.D. = not determined.

Compound	Excitation maximum (nm)	Fluorescence quantum yield (Φ_F)	Singlet oxygen quantum yield (Φ_Δ)
MB	668	0.02	0.55
Cy5	640	N.D.	0.065
XD-OH	680	0.118	0.062
XD-Br	685	0.016	0.119
XD-BrBGal	592	0.001	0.055

XD-Br was capable of generating singlet oxygen and although the efficiency was low (compared to MB) it was similar to the efficiency of HiPorfin, a Chinese clinically approved PDT agent.[134] Additionally, there was a 2.2-fold reduction in $^1O_2$ generation when the galactosyl moiety was present, suggesting **XD-BrBGal** could be used as an activatable photosensitiser for killing cells.

4.8. Further work

Modifications to the fluorophore chemical structures were attempted to improve the solubility of the probes as they required dissolution in DMSO. However, these efforts were not successful during this project. Several analogues were proposed in order to improve on the properties of the dye structure. For example a sulfonate dye would have better solubility (**Figure 4.14**), but it was unclear whether this would make the final probe too polar to diffuse through cell membranes.

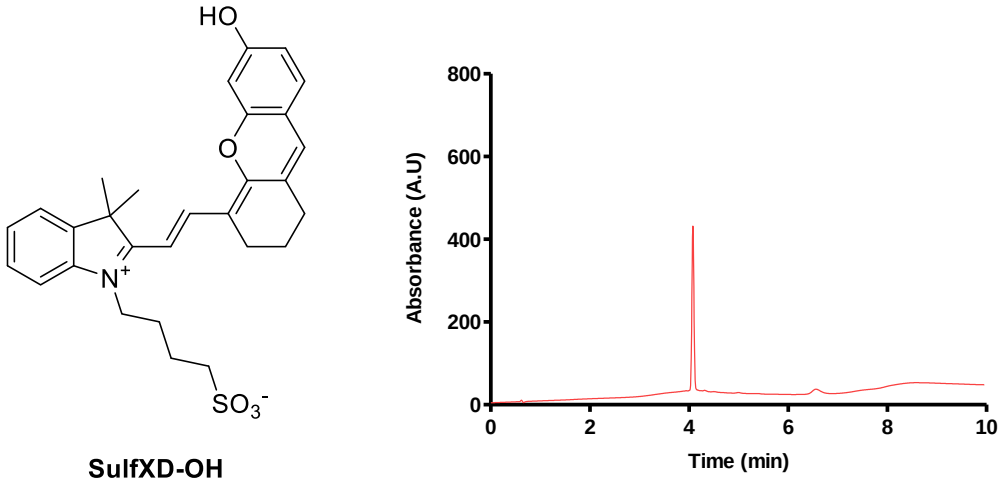

Figure 4.14. Left: A hemicyanine fluorophore with a sulfonate group used to increase hydrophilicity. The clogP of SulfXD-OH was calculated as -0.19 (molinspiration). Right: HPLC chromatogram of the isolated **SulfXD-OH** fluorophore with detection at 650 nm. The retention time (t_R) of 4.1 min, compared to **XD-OH** which has a t_R of 4.4 min.

A probe could be synthesised in three steps starting from the sulfonated Cy7 dye (**Scheme 4.8**). However, several unsuccessful attempts were made to attach the galactosyl unit to the sulfonated dye.

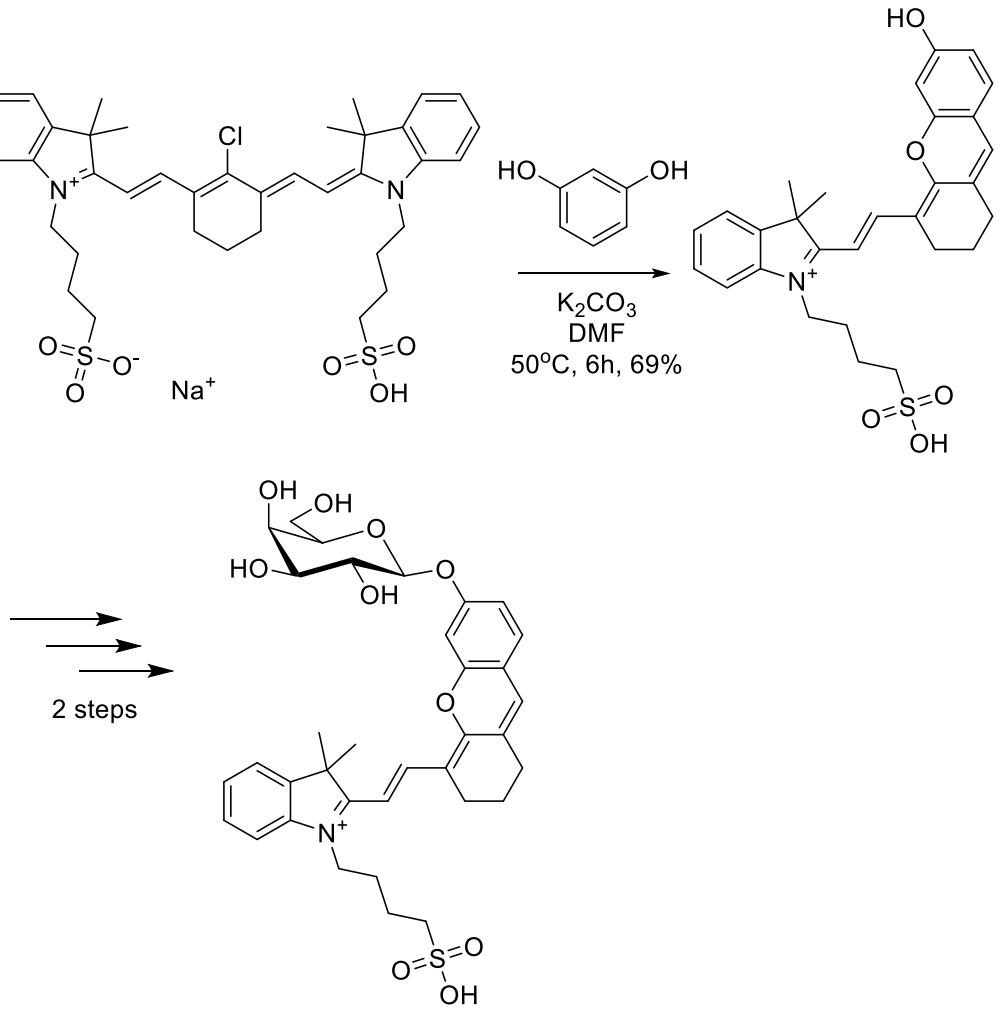

Scheme 4.9. Proposed synthetic route to sulfonated XD-BGal analogue.

An alternative structure involved a cleavable galactosyl moiety connected to a Cy7 aminocyanine (**Scheme 4.9**), this would have ratiometric fluorescent properties based on the unique properties of aminocyanines.[135] Following on from the synthesis of an esterase sensitive Cy7 dye, the galactose analogue was targeted (**Scheme 4.10**). with the reaction of the mixed carbonate (**Gal-Bn-PNP**) with the secondary aminocyanine (**Bn-Cy7**) (**Scheme 4.10**). However, the carbamate product could not be isolated and only trace product was detected by LC-MS.

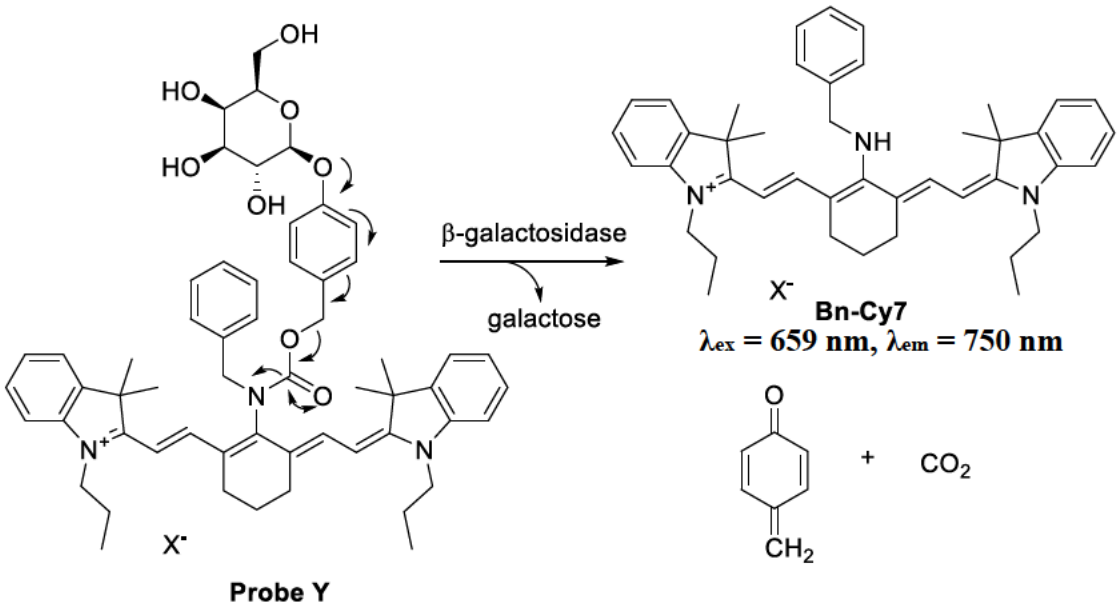

Scheme 4.10. Proposed structure of a probe based on a galactosyl-Cy7 fluorophore with a *para*-benzyl alcohol (safety catch) linker. Following enzymatic cleavage, a quinone methide and carbon dioxide would be liberated along with the cyanine dye (**Bn-Cy7**).

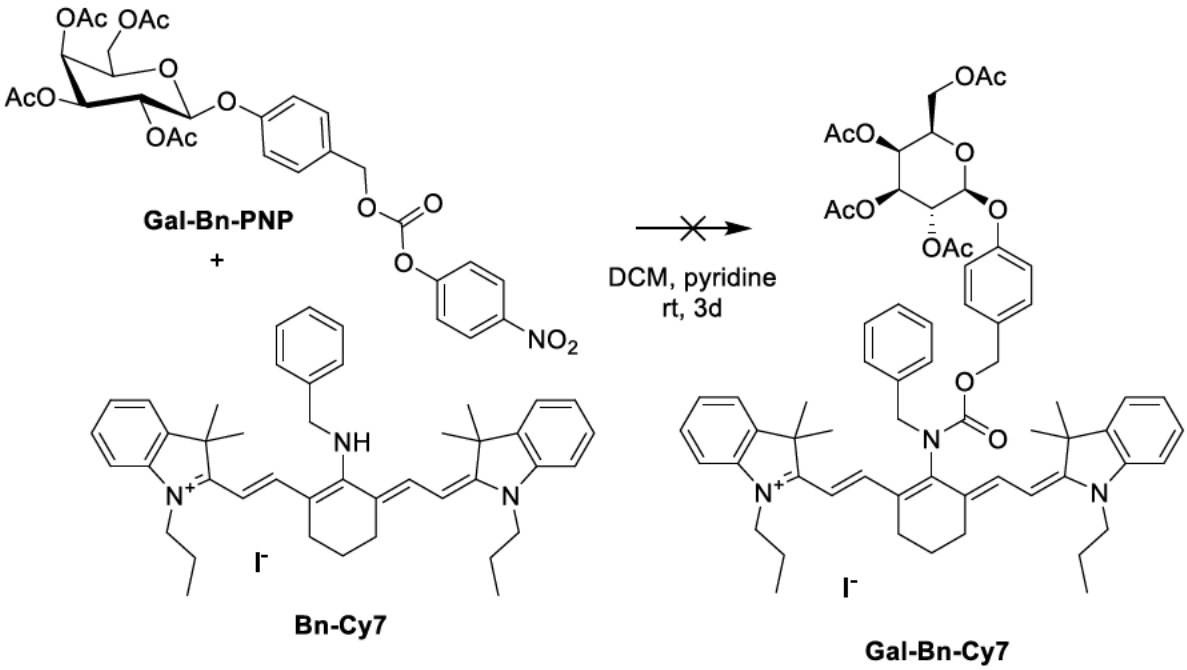

Scheme 4.11. Proposed synthesis of the galactosyl carbamate-Cy7 probe for ratiometric measurements (**Gal-Bn-Cy7**).

There are many potential ways of designing new beta-galactosidase Smartprobes. It has been previously shown that fluorophores can leach from the site of activation, leading to false positive results in regions without galactosidase activity. This could be solved by incorporating a group to covalently link the fluorophore **XD-OH** to proteins at the site of activation.[122]

As well as optimising the probe, additional analysis in *ex vivo* precision cut lung slice models are needed to understand the labelling performance of **XD-BGal**, whether it is truly selective for lysosomal β-gal and the potential for application a clinical setting where other cells may activate the probe (e.g. macrophages).

5. Conclusions and outlook

5.1. Introduction

The prospect of an optical biopsy to interrogate human lung diseases offers the potential to improve both the diagnosis and treatment of such diseases. Optical molecular imaging by endomicroscopy, in combination with SmartProbes, has been previously validated as a way of analysing lung pathologies in humans.[15] The ability to extend this technology to other cell types was a key aim of this research.

The innate immune system plays a major role in the body's response to disease, more specifically, understanding the functions of macrophages is a major focus of biomedical research. For example, macrophages are known to respond to inflammatory stimuli through the release of various cytokines and chemokines, the phagocytosis of opsonized targets and cellular signalling. Macrophage activity in the lung has been associated with pathologies such as asthma, where alveolar macrophages produce higher IL-13 levels and impaired IL-12 production[144, 145]; in COPD where a bias towards M2 macrophages was reported[37]; and in IPF patients where CD163 is highly expressed by M2-like macrophages.[146]

Folate receptors have been identified on macrophages in several inflammatory diseases such as rheumatoid arthritis, osteoarthritis and IPF. A previous study reported uptake of a folate conjugate by pulmonary macrophages in a rodent model of acute lung inflammation, however this work has yet to be translated to human studies of lung

inflammation. As folate-based imaging conjugates accumulate in multiple different inflammatory diseases, investigating this type of conjugate would provide valuable information on the role of folate receptors in lung inflammation. Secondly, macrophage mannose receptors (MMR) are another target for lung macrophage imaging. In addition to work reporting mannose receptors on tumour-associated macrophages in lung cancers,[78] Bazzan used MMR as a biomarker of M2 polarised macrophages in lung sections and this positively correlated with increased COPD severity.[81] More recently, a variety of MMR avid peptides, glycopolymers and antibody fragments have emerged as methods of labelling MMR positive macrophages.[85, 86]

Tissue remodelling is a feature of chronic airway diseases and can lead to the accumulation of senescent cells in tissues. The role of senescent cells expressing the senescence-associated beta-galactosidase enzyme has previously been investigated in alveolar epithelial cells exposed to cigarette smoke.[108] The prospect of validating a fluorescent probe to detect this enzyme would help our understanding of the integrity of the epithelium in lung diseases such as fibrosis.

Overall, the ability to image macrophage activity and epithelial cells *in vivo* would help give a better understanding of the role of these cells in the lung during disease. Thus, to gain an understanding of macrophage activity and alveolar epithelial integrity, a number of families of SmartProbes were synthesised and their abilities to selectively identify biomarkers of inflammation in lung were validated.

5.2. Conclusions and future experiments

5.2.1. Folate receptor probes

In Chapter 2, the folate receptor was utilised as a method for imaging macrophages. Initially a reported folic acid probe was synthesised, however optimisation of later probe structures was difficult using solution-phase chemistry due to the polarity of folic acid. This led to the development of a new solid-phase methodology (FolateTag) for the efficient construction of folate conjugates and provided a terminal amine for fluorophore conjugation. The FolateTag method allowed the synthesis of a spectrum of fluorescent Smartprobes that were evaluated for folate receptor imaging.

With cancer cell cultures, these probes were able to identify folate receptor-alpha expressed on the cells surface and this was demonstrated to be a target-specific event through competition and control experiments measured by flow cytometry and confocal microscopy. With this data giving confidence that these probes bound to folate receptors, attempts were made to identify an *in vitro* model of folate receptor-beta expressing macrophages. The Cy5-folate probe (probe **7** at 50 nM) could detect folate receptor-beta on monocyte-derived macrophages differentiated with monocyte colony stimulating factor (M-CSF), in contrast non-specific binding was seen by the non-expressing NR8383 alveolar macrophage cell line by flow cytometry. Imaging data showed that probe **7** was selective for M2 (M-CSF differentiated) over M1 macrophages (granulocyte-macrophage colony-stimulating factor differentiated). This work supports the conclusion of work by Puig-Kröger that M-CSF stimulated macrophages uptake folate conjugates, however the work presented was not

conclusive in showing a lung macrophage population could be detected by these conjugates.

In collaboration with another academic group interested in investigating the function of the folate receptor, the Cy5-folate probe was further validated with macrophages from the peritoneal cavity of aged mice, showing that folate receptor-beta (FRβ) could be detected by flow cytometry on 20 % of macrophages (gated on $CD11b^{+}$/ $F4/80^{high}$/ MHC class II^{low} status). While the presence of $FR\beta^{+}$ macrophages in the peritoneal cavity has been reported previously,[50] further work would be needed to determine the function of these cells, particularly in an inflammatory model. With the Phase II and III trials of the folate agent OTL38 in ovarian and lung cancer, the agent developed here would be interesting to develop further for diagnosis of diseases where folate receptor expressing macrophages are relevant.[147]

5.2.2. Macrophage nanobody probe

Fluorescently labelled nanobodies are an emerging imaging modality and an alternative to antibody imaging conjugates. In Chapter 3, this modality was explored for the optical imaging of macrophages with the aim of labelling a nanobody with a far-red fluorophore. After scouting for conjugation conditions using the model small protein lysozyme, the sulfoCy5 dye was successfully conjugated to a nanobody targeting the macrophage mannose receptor. The identity of the final conjugate was determined with SDS-PAGE, LC-MS, UV-Vis and RP-HPLC techniques.

The labelled nanobody (**Cy5-Nb**) was progressed to *in vitro* assays with monocyte-derived macrophages from healthy volunteers to show that the probe had high affinity and specificity to macrophages versus a panel of other common cells found in the lung: neutrophils, monocytes and control cancer cells. In the course of this work the probe showed intracellular labelling in macrophages suggesting that it had been actively processed by the cells. Despite attempting chemical blocking methods, we could not determine if this was a phagocytotic or endocytic mechanism. The probe showed benefit as a macrophage imaging agent as it labelled positively with *ex vivo* lavage samples from patients with chronic lung diseases (COPD and IPF patient samples).

Future work with this probe would focus on testing it in a whole lung model to show that probe signal can be detected from labelled macrophages against other cells. In addition, studies would be needed to see if the nanobody causes an adverse immunogenic response when used *in vivo*. Given its applicability to macrophage imaging, this nanobody probe could see rapid advancement into preclinical models and represents the first fluorescent nanobody developed for macrophage imaging. While nanobodies are still in their infancy, the FDA approval of the nanobody Caplacizumab in 2019 gives confidence in the clinical progression of nanobody imaging agents.[94]

5.2.3. Beta-galactosidase probes

In Chapter 4, activity-sensing fluorophores were developed for detecting senescent epithelial cells in the lung. While a number of existing probes are reported to visualise the enzyme beta-galactosidase these have either not been applied to senescent cell

models, or their fluorescent properties would not be ideal for use *in vivo*. A near-infrared (NIR) galactosidase probe (**XD-BGal)** was evaluated for detecting senescent cells that expressed senescence-associated beta-galactosidase (SA-βGal) enzyme. **XD-BGal** was successfully enzymatically activated by beta-galactosidase enzyme in a HPLC-based assay and confirmation that this turned-on its fluorescence was detected by spectroscopy. *In vitro* senescent cell assays were carried out with A549 cancer cells that were induced to be senescent with bleomycin and bright intracellular fluorescence was detected specifically in the senescent group and only weak fluorescence in the control group of untreated, healthy cells. An animal model of bleomycin induced senescence was carried out and *ex vivo* examination of murine lung tissue slices was used to validate the probe. By microscopy, a large number of cells stained positively for beta-galactosidase, although in these preliminary results it was not confirmed that these cells were all senescent epithelial cells, and some might be macrophages. Further validation of lung slices with immunohistochemistry would be needed to show that the probes activation was specific to senescent cells.

An analogue of the galactosidase probe was developed called **XD-BrBGal**, but the fluorophore after cleavage had a poorer fluorescent quantum yield (Φ_F = 0.016) than the non-brominated fluorophore **XD-OH**, limiting its uses for fluorescence imaging. However, a solution-based fluorescence assay for determining singlet oxygen generation showed the fluorophore (**XD-Br**) was able to generate singlet oxygen (Φ_Δ = 0.12). With further work, it was hypothesised that this probe could find an application as an activatable photosensitiser probe for specifically targeting beta-galactosidase positive cells.

While the ability to image senescence-associated beta-galactosidase positive cells with a SmartProbe was carried out in a number of assays, further experiments would be needed to show that senescent cells can be imaged in the human lung with optical endomicroscopy. This work should be placed in the context of other targeting techniques for senescence such as the work by Muñoz-Espín who developed a therapeutic delivery system directed to senescent cells based on their high β-galactosidase activity and this showed the ability to treat pulmonary fibrosis in mice.[148] This gives hope that a SmartProbe approach to imaging senescent cells could be possible in preclinical models.

5.3. Outlook

Together, these sets of probes advance the collection of imaging agents for examining inflammatory processes in the lung, while greatly encouraging their use with *in vivo* models of lung inflammation. New ways to validate these probes in more lung relevant models were explored, such as using patient lung lavages in *ex vivo* assays and tissue precision cut lung slices. While lung slices were taken from an animal for this work, similar experiments could be performed with tissue from human donors to give more information on human immune responses.

In vivo optical imaging is still an emerging field with many challenges ahead. A key problem is that the tissue penetration depth for molecular imaging is limited by light scattering, yet techniques such as fluorescence guided surgery and optical fibre endomicroscopy can overcome this challenge. A further barrier is the lack of clinically

approved targeted imaging agents to use with molecular imaging systems. For more widespread use of optical molecular imaging, further imaging agents will need to be taken into clinical trials. From this work, there are several avenues of future work to advance each Smartprobe towards clinical use. The use of Smartprobes *in vivo* firstly requires an understanding of the biocompatibility and toxicology of each probe. Similar work was carried out in the development of Smartprobes in clinical trials presently; for example, the c-Met targeting probe GE-137[19] and the folate receptor probe OTL-38.[47] While each probe showed target specificity, the ability to detect their target biomarkers of inflammation in a whole lung model would need to be confirmed. Future work should also include the development of the physiochemical properties of each probe as needed for a biocompatible formulation.

Ongoing developments in the field of optical imaging include the validation of new probe targets, new imaging systems and better designed SmartProbes requiring low background signals.[149, 150] Future opportunities to develop the field of optical molecular imaging from this work can be imagined. While this work focused on cellular identification by targeting inflammatory cells, simple modifications to the structure of these probes could allow them to be used in alternative modalities of optical imaging. These include the development of SmartProbes using photosensitisers for photodynamic therapy, Raman tags for stimulated Raman scattering, or labels that generate photoacoustic or photothermal imaging signatures.

6. Experimental

6.1. General section: Chemistry

All solvents and reagents were obtained from commercial suppliers and used without further purification, unless otherwise stated. Evaporation of solvents was performed at reduced pressure, using a Büchi rotary evaporator. All solution phase reactions were stirred magnetically unless otherwise stated and followed to completion by thin layer chromatography (TLC), where appropriate using TLC aluminium sheets coated with silica gel 60 F254 plates (Merck) or RP-18 silica gel (Macherey Nagel). TLC visualisation was performed using short wave UV light (254 nm) and/or TLC staining solutions where stated.

Reactions involving moisture sensitive reagents were performed under nitrogen and reactions involving light sensitive compounds were kept under aluminium foil at all times. Compounds were dried under vacuum at 40^{o}C in a Heraeus vacuum oven.

Fourier-transform infrared spectroscopy were recorded on a Bruker Tensor 27 spectrophotometer with Specac single reflection diamond attenuated total reflexion (ATR) Golden Gate accessory. Fluorescence spectra were recorded on a Horiba FluoroMax fluorospectrometer, using 1 cm path length with fused silica cuvettes. UV/Visible absorbance spectra were recorded on a BioTek SynergyHT or Synergy H1 plate reader in well plates, or Shimadzu UV1800 spectrophotometer using a 1 cm path length with fused silica cuvettes.

^{1}H and ^{13}C NMR spectroscopy were recorded on automated Bruker AV400 or AV500 spectrometer in the deuterated solvents indicated at 298 K. Chemical shifts are reported on the δ scale in ppm. Resonances were characterised as singlet (s), broad singlet (bs), doublet (d), doublet of doublet (dd), triplet (t) or multiplet (m) with coupling constants given in hertz (Hz). Data was processed using the MestReNova software version 10 (Mestrelab Research S.L.)

Microwave heating was carried out by irradiating the reaction mixture in a Biotage Initiator at 2.45 GHz. Experiments were carried out in Biotage sealed tubes. Microwave irradiation was conducted at a defined temperature and time, with pressure and power monitored by the systems software.

Reverse-phase high-performance liquid chromatography (RP–HPLC)

Analytical HPLC was performed on an Agilent Technologies 1100 modular HPLC system coupled to a Polymer Lab 1000 Evaporative Light Scattering Detector (ELSD), with simultaneous detection at 220, 254, 260, 282 and 495, 650 nm. Column: Phenomenex Kinetex® 5µm XB-C18 100 Å, LC Column (50 x 4.6 mm), with a flow rate of 1 mL/min. All solvents used were HPLC grade.

A: MeCN + 0.1% formic acid

B: H2O + 0.1% formic acid

Method 1: 5 to 95 % A in B over 6 min; Isocratic for 3 min; 95 % to 5% A over 1 min; 2 min isocratic.

Method 2 (5PCTMIN): 5% to 95 % A in B over 18 min; Isocratic for 3 min; 95% to 5% A over 1 min; 2 min isocratic.

Preparative RP–HPLC (system 1) was performed on an Agilent Technologies 1100 modular HPLC system equipped with a Agilent Zorbax Eclipse® 5µm XDB-C18 column (250 x 10 mm) with a flow rate of 2.0 mL/min.

Preparative RP–HPLC (system 2) was performed on an Agilent Technologies 1100 modular HPLC system equipped with a Phenomenex Kinetex Axia 5µm XDB-C18 column (150 x 21.2 mm) with a flow rate of 10.0 mL/min.

Elution was using one of the following methods.

Method 1: eluting with A in B, with a gradient of 5 to 95% B over 18 min and an initial isocratic period of 5 min and a final isocratic period of 2 min.

Method 2: eluting with C in D, with a gradient of 5 to 95% D over 22 min and an initial isocratic period of 7 min and a final isocratic period of 2 min.

Method 3: eluting with E in F, with a gradient of 5 to 95% F over 18 min and an initial isocratic period of 5 min and a final isocratic period of 2 min.

A: H2O + 0.1% formic acid

B: MeCN + 0.1% formic acid

C: H_2O + 0.1% trifluoroacetic acid

D: MeCN + 0.1% trifluoroacetic acid

E: 10mM ammonium bicarbonate H_2O solution

F: MeCN (no additives)

Mass spectrometry

Electrospray ionization mass spectrometry (ESI–MS) analyses were carried out on an Agilent Technologies LC/MSD Series 1100 quadrupole mass spectrometer (QMS) in the ESI mode. Column: Phenomenex Kinetex® 5µm XB-C18 100 Å, LC Column (50 x 4.6 mm), with a flow rate of 1 mL/min.

High Resolution Mass Spectra (HRMS) were performed on a Bruker microTOF2 spectrometer by direct infusion. MALDI-TOF mass spectra were obtained with a Bruker UltrafleXtreme MALDI TOF/TOF instrument and analysed with the Bruker Daltonics flexAnalysis software.

6.2. General section: Biology

The following reagents and materials were purchased; DMEM cell culture media (Gibco, 21969-035), L-Glutamine 200mM (Gibco 25030081), Foetal Bovine Serum (Gibco 10500064), Penicillin-Streptomycin 10,000 U/mL (Gibco 15140122), Amphotericin B (Gibco 15290018).

Phosphate buffered saline (PBS) buffer was prepared as follows: 0.01 M phosphate buffer, 2.7 mM potassium chloride and 0.137 M sodium chloride, pH 7.4, at 25 °C.

Flow cytometry analysis was carried out on a BD FACScan or FACS Canto II cytometer. Data was analysed using FlowJo software v10. Protein gels were imaged on a BioRad Laboratories Molecular Imager and processed with BioRad Laboratories Image Lab Software 3.0. Microplate reader assays (absorbance, fluorescence and luminescence) were performed on a BioTek Synergy H1 or SynergyHT plate reader with GEN5 software. Confocal microscopy files were processed in the Fiji distribution

of ImageJ.[140] UV-Vis measurements of proteins were made using a Nanodrop 1000 spectrometer with Nanodrop 100 software version 3.8.1 (ThermoScientific). Cell counting and viability testing was performed with Vial1 cartridges on a Nucleocounter (Chemometec).

Biological data was analysed with GraphPad Prism (v5) software and generally results are presented as mean ± standard error of the mean (SEM).

Whole blood from healthy volunteers was collected according to Research Ethics Committee approval under the AMREC 15-HV-013 project at the Centre for Inflammation Research, University of Edinburgh. Healthy volunteers provided written informed consent prior to collection of blood.

6.3. Chapter 2

6.3.1. Synthesis

***N*-Boc-ethylenediamine-folate (12)**

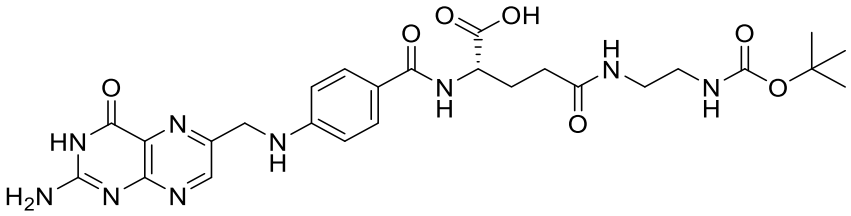

Compound **12** was prepared according to a reported procedure.[58] In a round-bottomed flask was dissolved folic acid (640 mg, 1 eq.) in DMSO (25 mL). After dissolution was complete (about 30 minutes with mild heating), N-hydroxysuccinimide (NHS, 308 mg, 2 eq.) and dicyclohexylcarbodiimide (DCC, 552 mg, 2 eq.) were added successively. The reaction mixture was stirred for 18 hours at room temperature, after which the white urea precipitate was filtered off. Triethylamine (TEA, 0.376 mL, 2 eq.) was added to the filtrate, followed by N-Boc-ethylenediamine (429 mg, 2 eq.) dissolved in DMSO (5 mL). The mixture was again stirred overnight before a mixture of 20% acetone in diethyl ether was added. The thin yellow precipitate was carefully centrifuged and washed four times with acetone and two times with diethyl ether and dried under vacuum (770 mg, 91%). Data in agreement with the literature.[58] MS (ESI) calculated for $C_{26}H_{33}N_9O_7$ $[M+H]^+$ m/z 584.3. Found 584.3 (100%). ^{1}H NMR (500 MHz, DMSO-d_6) δ 8.64 (s, 1H), 8.18 – 7.75 (m, 2H), 7.73 – 7.56 (m, 2H), 7.00 – 6.74 (m, 3H), 6.69 – 6.57 (m, 2H), 4.48 (br, 2H), 4.28 (m, 1H), 3.12 – 2.88 (m, 4H), 2.33 – 1.79 (m, 4H), 1.35 (s, 9H). ^{13}C NMR (126 MHz, DMSO-d_6) δ 174.14, 173.96, 171.87, 171.83, 171.73, 166.13, 161.03, 155.56, 153.86, 150.71, 148.54, 129.06, 128.89, 127.93, 121.44, 111.19, 77.63, 77.57, 52.17, 52.02, 45.91, 45.65, 31.97, 28.21, 9.65.

Ethylenediamine-folate (13)

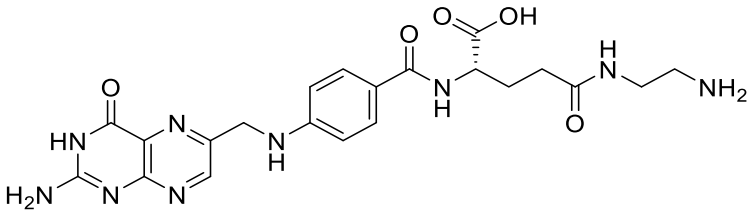

Compound **13** was prepared according to a reported procedure.[58] Compound **12** (100 mg, 0.17 mmol), was dissolved in trifluoroacetic acid (0.66 mL) and stirred for two hours at room temperature. The solvent was removed under vacuum, adding DCM to aid TFA removal. The resulting residue was dissolved in the minimal amount of dry DMF, triethylamine (300 µL) was added to give a yellow precipitate. This was filtered, centrifuged and washed four times with acetone and twice with diethyl ether. Resulting in the final compound as a yellow powder (66 mg, 80%). Data in agreement with the literature.[58] ^{1}H NMR (500 MHz, DMSO-d_6) δ 8.67 – 8.59 (m, 1H), 7.84 – 7.73 (m, 1H), 7.72 – 7.54 (m, 2H,), 7.00 – 6.72 (m, 3H), 6.69 – 6.57 (m, 2H), 4.48 (br, 2H), 4.36 – 4.01 (m, 1H), 2.88 – 2.74 (m, 2H), 2.30 – 2.12 (m, 2H), 2.06 – 1.96 (m, 2H). CH_2 obscured by H_2O peak

FITC Folate (1)

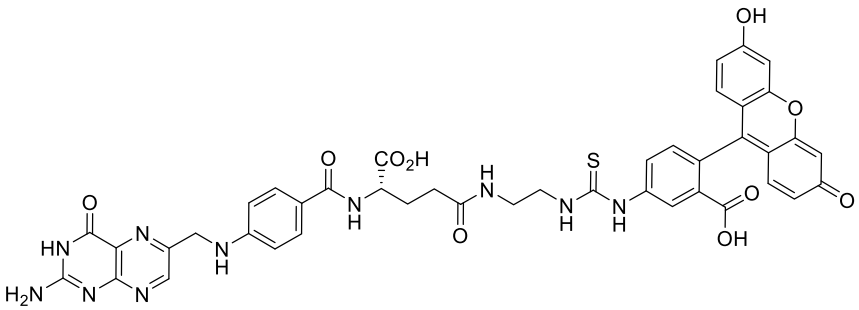

FITC Folate was prepared according to a reported procedure.[41] To a solution of ethylenediamine-folate **13** (12.4 mg, 0.025 mmol) in DMSO (0.2 mL) was added

fluorescein isothiocyanate (FITC, 20 mg, 0.051 mmol) and DIPEA (13 µL, 0.075 mmol). The reaction was stirred under nitrogen for 4 hr in the dark. The product was precipitated by adding water and sonicating. The filtrate was collected and washed with diethyl ether. The pure product was obtained by prep-HPLC purification as an orange solid (4 mg, 18 %). All data was in agreement with the literature.[41] MS (MALDI-TOF matrix: CHCA): calculated for $C_{42}H_{36}N_{10}O_{10}S$ $[M+H]^+$ m/z 873.2. Found 873.3 (100%). HRMS (ESI) m/z: $[M+H]^+$ calcd for $C_{42}H_{36}N_{10}O_{10}S$ 873.2409. Found 873.2394. ^{1}H NMR (500 MHz, DMSO-d_6) δ 10.18 (s, 1H), 8.67 – 8.58 (m, 1H), 8.38 – 8.26 (m, 1H), 8.24 – 8.17 (m, 1H), 7.90 – 7.82 (m, 1H), 7.75 – 7.58 (m, 2H), 7.21 – 7.10 (m, 1H), 6.72 – 6.60 (m, 2H), 6.62 – 6.50 (m, 6H), 4.52 – 4.42 (m, 2H), 4.40 – 4.20 (m, **1**H), 3.56 (s, 2H), 3.34 – 3.23 (m, 2H), 2.29 – 2.14 (m, 2H), 2.13 – 1.85 (m, 2H).

Potassium 2,3,3-trimethyl-3H-indole-5-sulfonate (14)

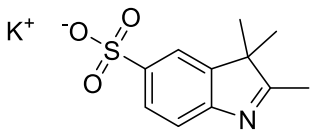

Compound **14** was prepared according to a reported procedure.[136] 4-hydrazinobenzenesulfonic acid (5 g, 26.6 mmol) and 3-methylbutan-2-one (6.86 g, 79.8 mmol) were dissolved in acetic acid (15 mL) and stirred at reflux for 3 hours. The solvent was removed under vacuum. The residue was then dissolved in methanol and stirred with a saturated solution of potassium hydroxide (1.5 g) in 2-propanol (50 mL). The solution turned yellow and the potassium salt was collected by filtration, washing with diethyl ether and the solid dried under vacuum overnight yielding a pale-yellow solid (7.54 g, quantitative yield). All data was in agreement with the literature.[136]

HPLC (Method 1) t_R = 1.22 min. Purity 100% (ELSD). MS (ESI): calculated for $C_{11}H_{12}KNO_3S$ $[M+H]^+$ m/z 278.0. Found 278.1 (100%). ^{1}H NMR (500 MHz, DMSO-d_6) δ 7.62 (d, *J* = 1.6 Hz, 1H), 7.53 (dd, *J* = 7.9, 1.7 Hz, 1H), 7.33 (d, *J* = 7.9 Hz, 1H), 2.21 (s, 3H), 1.24 (s, 6H).

1-(5-carboxypentyl)-2,3,3-trimethyl-3*H*-indolium-5-sulfonate (15)

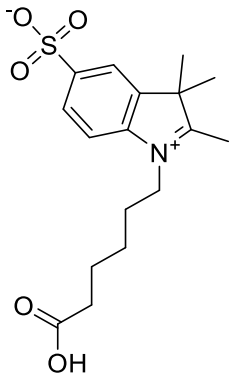

Compound **15** was prepared according to a reported procedure.[136] Potassium 2,3,3-trimethyl-3H-indole-5-sulfonate **14** (250 mg, 0.90 mmol), 6-bromohexanoic acid (176 mg, 0.90 mmol) were dissolved in toluene (2 mL) and refluxed for 24 hours. The reaction mixture was cooled to ambient temperature and further toluene added. The thick precipitate was filtered and washed with toluene and diethyl ether. Dried under vacuum to give a brown solid (251 mg, 79%). All data was in agreement with the literature.[136] HPLC (Method 1) t_R = 2.33 min. Purity 90% (ELSD). MS (ESI): calculated for $C_{17}H_{22}NO_5S$ $[M-H]^-$ m/z 352.1. Found 352.1 (100%). ^{1}H NMR (500 MHz, DMSO-d_6) δ 8.03 (s, 1H), 7.91 (d, *J* = 8.4 Hz, 1H), 7.83 (dd, *J* = 8.4, 1.6 Hz, 1H), 4.44 (t, *J* = 7.7 Hz, 2H), 2.83 (s, 3H), 2.23 (t, *J* = 7.2 Hz, 2H), 1.87 – 1.80 (m, 2H), 1.55 (m, 8H), 1.45 – 1.37 (m, 2H). ^{13}C NMR (126 MHz, DMSO-d_6) δ 197.3, 174.3, 149.5, 141.5, 140.9, 126.4, 120.7, 115.0, 54.3, 47.6, 34.3, 33.4, 26.9, 25.4, 24.0, 21.9, 14.1.

1-(5-carboxypentyl)-2-[(1*E*,3*E*)-4-(acetylanilino)-1,3-butadienyl]-3,3-dimethyl-3*H*-indolium-5-sulfonate (16)

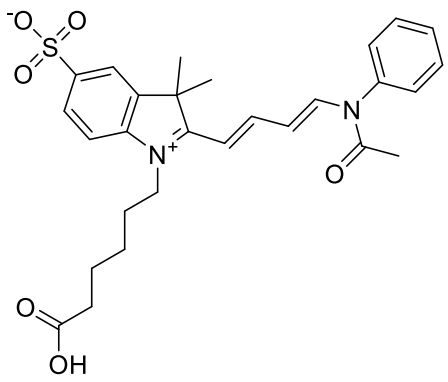

Compound **16** was prepared according to a reported procedure.[137] 1-(5-carboxylpentyl)-2,3,3-trimethylindolium-5-sulfonate **15** (250 mg, 0.57 mmol), malonaldehyde bis(phenylimine) hydrochloride (204 mg, 0.79 mmol) were dissolved in a 1:3 solution of acetic acid (0.8 mL) and acetic anhydride (2.5 mL). The reaction was heated to reflux and monitored by LC-MS until starting indolenine was consumed (~1 hour). The reaction was cooled to room temperature, the solvent was evaporated and a solid precipitated by addition of ethyl acetate. The solution was filtered and washed several times with ethyl acetate and finally with diethyl ether. After drying under vacuum the brown solid (271 mg, 90%) was used directly without purification. All data was in agreement with the literature.[137] MS (ESI): calculated for $C_{28}H_{33}N_2O_6S$ $[M+H]^+$ m/z 525.2. Found 525.2 (100%). HPLC (Method 1) t_R = 4.57 min. Purity 88% (ELSD). ^{1}H NMR (500 MHz, DMSO-d_6) δ 8.93 (d, *J* = 13.3 Hz, 1H), 8.59 (m, 1H), 7.97 (m, 1H), 7.77 – 7.42 (m, 7H), 6.88 (dd, *J* = 15.0, 3.4 Hz, 1H), 5.58 – 5.50 (m, 1H), 4.31 – 4.22 (m, 2H), 2.15 (t, *J* = 7.3 Hz, 2H), 1.91 (s, 3H), 1.71 (d, *J* = 5.5 Hz, 6H), 1.60 – 1.28 (m, 6H).

Dipotassium 2,3-dimethyl-1,3-di(4-sulfonatobutyl)-3*H*-indolium-5-sulfonate (17)

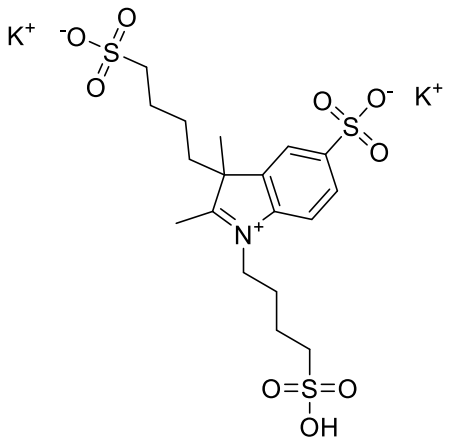

Compound **17** was synthesised by Vikki Evans according to a reported procedure.[137]

1-(5-carboxypentyl)-3,3-dimethyl-2-5-[3-methyl-5-sulfo-1,3-di(4-sulfobutyl)-2,3-dihydro-1*H*-2-indolyliden]-1,3-pentadienyl-3*H*-indolium-5-sulfonate (Cy5)**

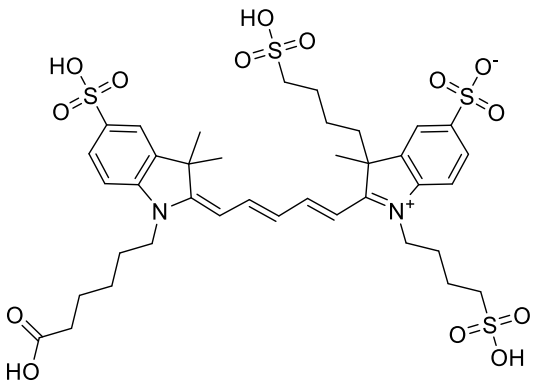

Cy5** was prepared according to a reported procedure.[137] Indolenine phenylacetoamide **3** (800 mg, 1.52 mmol) and trisulfonated indolenine **4** (1.2 g, 2.41 mmol) were dissolved in a solution of acetic acid and acetic anhydride (3:1 v/v, 21 mL) with gentle heating. Potassium acetate (297 mg, 3.04 mmol) in acetic acid (5 mL) was added and the reaction heated to 110°C for 30 minutes. Reaction conversion was determined by HPLC, after 30 minutes starting material **3** was remaining so the reaction was continued for 3 hours at which point only a residual amount of starting

material remained. The reaction mixture was concentrated under vacuum to a viscous solution and ethyl acetate was added before stirring for 1 hour. The product was filtered under nitrogen, washed with ethyl acetate and collected as a dark blue powder. The crude product was suspended in water and stirred for 1 hour and the aqueous layer freeze-dried. Crude mass = 2.65 g.

500 mg batches of crude material, dissolved in 1 M TFA (pH~2), were purified by Biotage flash chromatography (SNAP Ultra C18 30g column, up to 3% loading capacity) using gradient of 5% ACN in H_2O to 35 % ACN in H_2O (both with 0.1% TFA additive). Product fractions were lyophilised to yield a blue tinted powder. All data was in agreement with the literature.[137] λ_{ex} = 656 nm, λ_{em} = 670 nm (PBS). HPLC (Method 1) t_R = 4.66 min. Purity 100% (ELSD). HRMS (ESI) m/z: calc for $C_{38}H_{50}N_2O_{14}S_4$ $[M+H]^+$ 887.2218. Found 887.2258. ^{1}H NMR (500 MHz, DMSO-d_6) δ 8.43 – 8.28 (m, 2H), 7.80 (d, *J* = 1.7 Hz, 1H), 7.77 (d, *J* = 1.6 Hz, 1H), 7.63 (dt, *J* = 8.2, 1.7 Hz, 2H), 7.35 (d, *J* = 8.3 Hz, 1H), 7.31 (d, *J* = 8.3 Hz, 1H), 6.60 (t, *J* = 12.3 Hz, 1H), 6.41 (d, *J* = 13.8 Hz, 1H), 6.30 (d, *J* = 13.8 Hz, 1H), 2.44 – 2.22 (m, 4H), 2.20 (t, *J* = 7.2 Hz, 2H), 1.80 – 1.67 (m, 6H), 1.69 (d, 6H) 1.66 (s, 3H), 1.55 (h, *J* = 8.1, 7.3 Hz, 2H), 1.49 – 1.32 (m, 4H), 0.90 – 0.44 (m, 2H). 13C NMR (126 MHz, DMSO) δ 174.3, 172.9, 171.5, 153.6, 145.1, 142.8, 142.0, 140.5, 138.7, 126.2, 126.0, 119.9, 119.7, 110.1, 104.1, 103.6, 53.3, 51.1, 50.6, 48.9, 43.4, 33.5, 27.2, 27.2, 27.1, 26.6, 25.9, 25.6, 24.8, 24.2, 23.4, 22.3.

Cy5 Folate (3)**

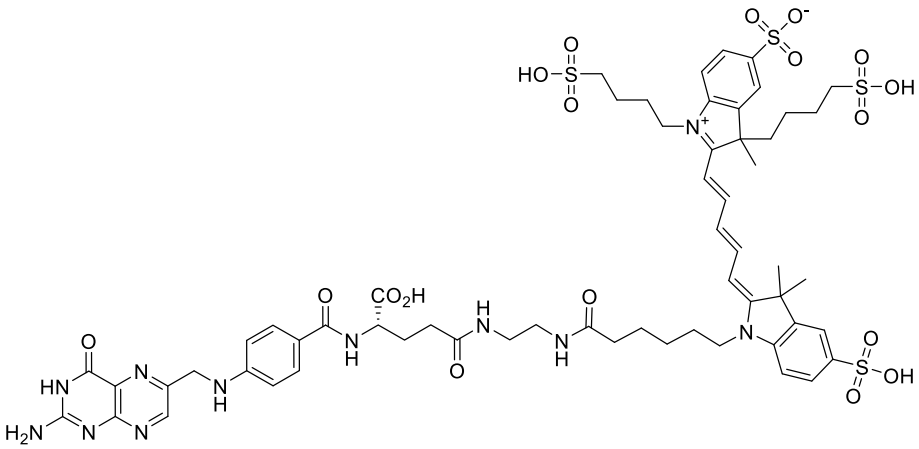

N,N,N′,N′-Tetramethyl-O-(N-succinimidyl)uronium tetrafluoroborate (TSTU, 0.049 mmol), DIPEA (8 µL) in DMF (0.5 mL), after one minute **Cy5**** (10 mg, 0.011 mmol) in DMF (0.5 mL) was added and the reaction shaken for 1 hour. Conversion to the NHS ester was monitored by HPLC. Ethylenediamine folate **2** was dissolved DMF (0.5 mL): NMP (0.1 mL), added to the NHS ester and shaken for 2 hours. Diisopropyl ether (DIPE) was added to the reaction mixture to form a solid and the yellow supernatant removed, further centrifuged and washed with DIPE three times. The green solid was purified by prep HPLC to yield the compound as the ammonium salt. MALDI-TOF (matrix: CHCA), calculated for $C_{59}H_{73}N_{11}O_{18}S_4$ $[M+H]^+$ m/z 1352.4. Found 1352.6. HRMS (ESI) m/z: calc for $C_{59}H_{73}N_{11}O_{18}S_4$ $[M+Na]^+$ 1374.3910. Found 1374.1233.

Poor solubility in deuterated NMR solvents prevented ^{1}H NMR data being acquired.

General procedures for the solid phase synthesis of folate probes

To the Fmoc-amino acid (4 eq) in DMF (0.10 M), Oxyma (4 eq) was added and allowed to stir for 5 min. DIC (4 eq) was added and stirred for a further 5 min. The coupling solution was then added to Fmoc-Rink amide-aminomethyl PS resin (0.20 g,

1 eq) pre-swelled in DCM and the reaction mixture was shaken for 2 h at room temperature. The resin was isolated by filtration, washed with DMF (3 × 10 mL), DCM (3 × 10 mL), and MeOH (3 × 10 mL). Coupling reactions were monitored by the ninhydrin test. Folic acid was coupled by reacting **folic acid-NHS** (prepared as described previously)[58] in DMSO:NMP (1:1) with 1% DIPEA. The reaction mixture was shaken overnight and repeated if not deemed complete by HPLC.

Fmoc deprotection was carried out by suspending the resin (0.20 g) in 20% piperidine in DMF (2 mL) and shaken for 5 min. The resin was filtered and a fresh solution of 20% piperidine in DMF (2 mL) was added and shaken for 15 min. The resin was then filtered and washed with DMF (3 x 10 mL), DCM (3 x 10 mL) and DMF (3 × 10 mL).

Dye couplings were carried out by the following method. The dde protecting group was removed with freshly prepared 2 % hydrazine in DMF solution (5x1 min, then 10 min). The resin was filtered and washed with DMF (3 x 10 mL), DCM (3 x 10 mL) and DMF (3 × 10 mL) and the activated dye-NHS ester, DIPEA (170 μL) was added in DMF (0.1 M). The reaction mixture was shaken for a minimum of 3h at room temperature. The resin was drained and washed with DMF (3 × 10 mL), DCM (3 × 10 mL), and MeOH (3 × 10 mL).

TFA cleavage for Rink Amide resin was carried out by treating the resin with the cleavage cocktail TFA/TIS/H_2O (95:2.5:2.5) (20 mL per gram of resin) and the mixture was shaken for 2-3h. The solution was drained and the resin was washed twice with TFA. The combined filtrates were evaporated until the minimal amount of solvent remained and this was added dropwise to a slowly stirring solution of cold ether (10-15 mL per mL of cleavage cocktail). The precipitate was collected by centrifugation

and washed with cold ether three times, isolated and dried under vacuum. Purification of the probes was performed by RP-HPLC. HPLC method: 95% 10 mM NH_4HCO_3 isocratic for 2 min; 5 to 95 % ACN in 10 mM NH_4HCO_3 over 7 min; Isocratic for 3 min; 95 % to 5% 10 mM NH_4HCO_3 over 1 min. Characterisation was performed by MALDI-TOF and RP-HPLC.

In general, the poor solubility of folate probes in deuterated NMR solvents and limited amounts after HPLC purification prevented NMR data being acquired.

Scheme: folate on resin

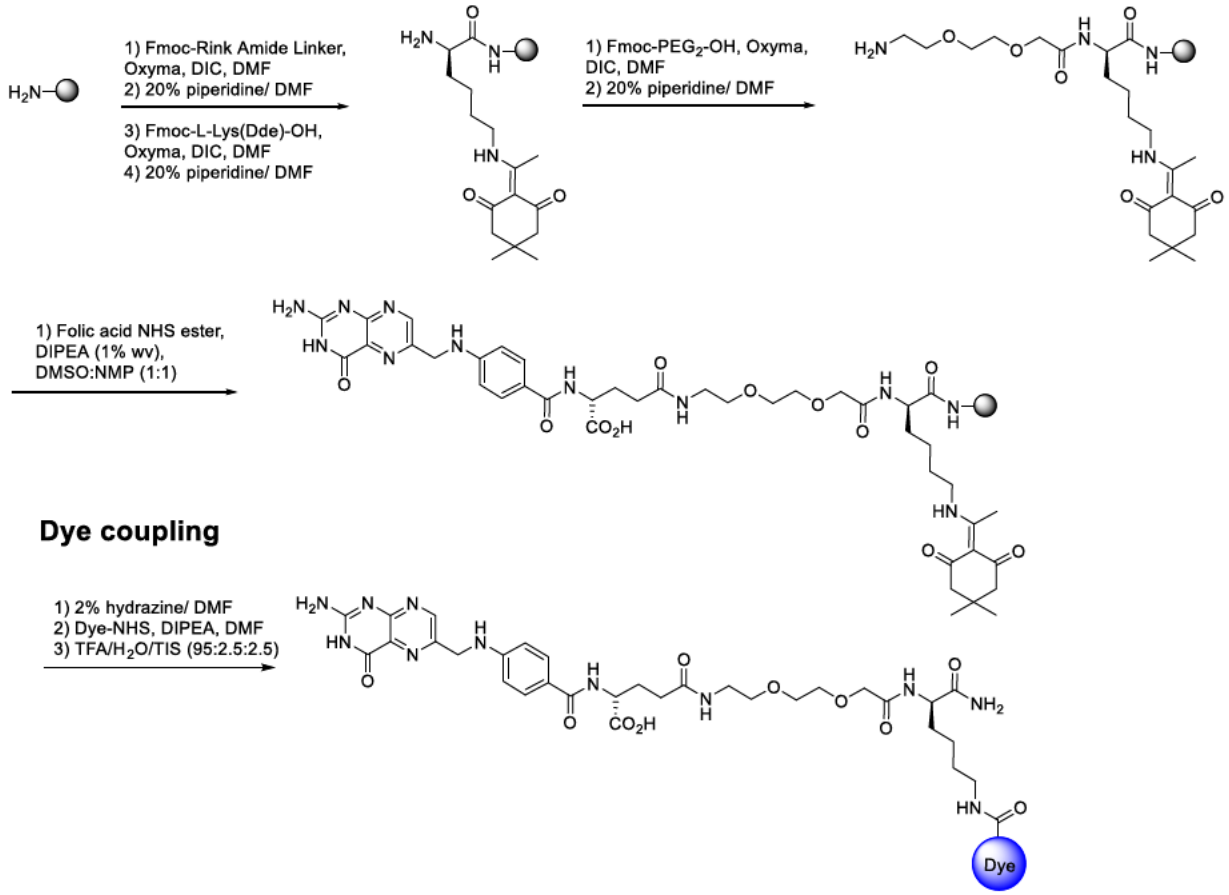

FAM folate (5)

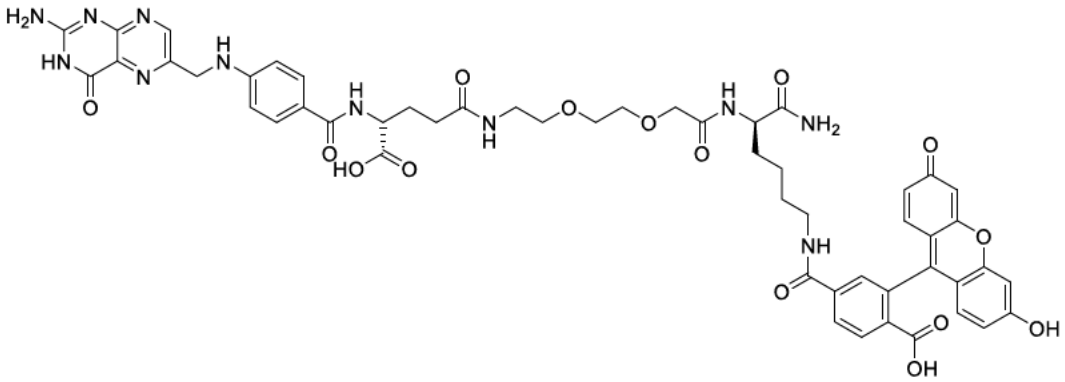

The dye coupling procedure was carried out following the general procedure. 6-carboxyfluorescein diacetate N-hydroxysuccinimide ester was prepared using a reported procedure.[138] Dye (1.2 equiv.) was reacted with the resin for 3h at room temperature. After the reaction, an additional washing step with 20% piperidine in

DMF was used to entirely remove the acetyl protecting groups on fluorescein. The crude product was cleaved from the resin and purified by RP-HPLC.

HPLC (Method 1) t_R = 5.5 min. Purity 85% (495 nm). HRMS (MALDI) m/z: calc for $C_{52}H_{53}N_{11}O_{15}$ $[M+H]^+$ 1072.3805. Found 1072.3848.

NBD folate (6)

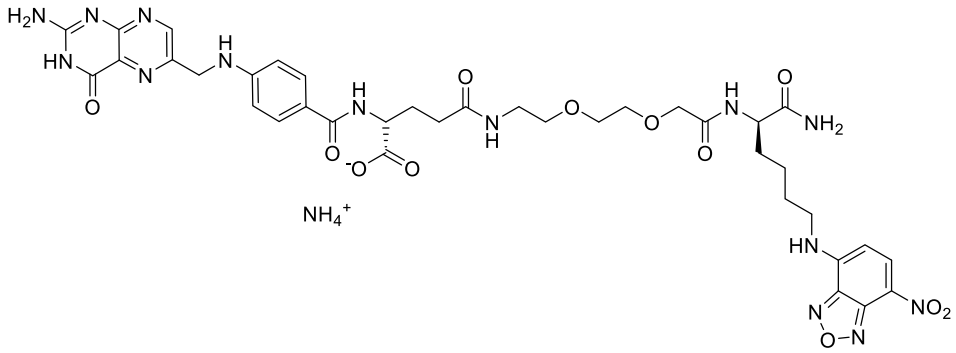

The dye coupling procedure was carried out following the general procedure. NBD-Cl (3 equiv.) was coupled with the resin for 2h at room temperature. The crude product was cleaved from the resin and purified by RP-HPLC.

HPLC (Method 1) t_R = 5.9 min. Purity 100% (650 nm). MALDI: found $[M+Na]^+$ 899.2, $[M+Na+NH_4]^+$ 915.1, expected $[M+Na]^+$ 899.3. HRMS (MALDI) m/z: calc for $C_{37}H_{44}N_{14}O_{12}$ $[M+Na]^+$ 899.3155. Found 899.3116.

Cy5 folate (7)**

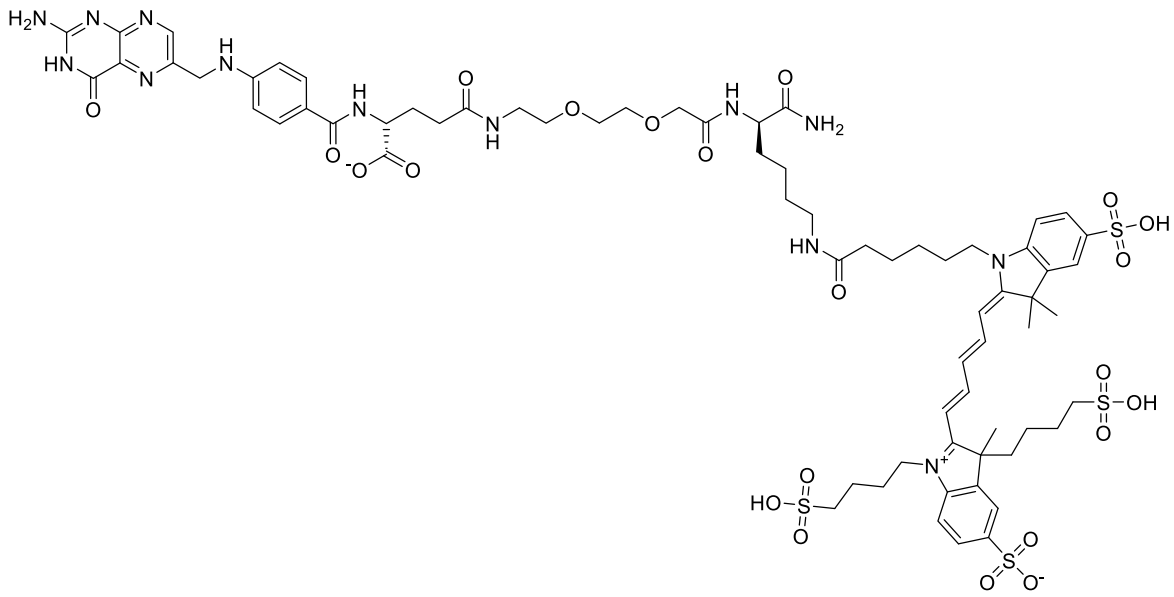

The dye coupling procedure was carried out following the general procedure, 2.5 equiv. of Cy5**-NHS was reacted with the resin overnight at room temperature. The crude product was cleaved from the resin and purified by RP-HPLC.

HPLC (Method 1) t_R = 5.6 min. Purity 96 % (650 nm). MS (ESI): calculated for $C_{69}H_{90}N_{13}O_{22}S_4$ $[½M+Na]^+$ m/z 812.4. Found $[½M+Na]^+$= 812.4 (100%). HRMS (MALDI) m/z: calcd for $C_{69}H_{90}N_{13}O_{22}S_4$ $[½M+Na]^+$ 812.2420. Found 812.4059.

Benzothiophene enol ether (10)

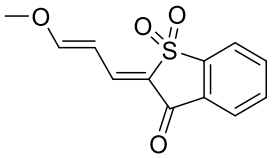

Compound **8** was prepared according to a reported procedure.[139] 1-benzothiophen-3(2H)-one 1,1-dioxide (600 mg, 3.3 mmol) was added to a microwave vial with 1,1,3,3-tetramethoxypropane (2.7 mL, 16.5 mmol), followed by the addition of trifluoroacetic acid (25 µL, 0.33 mmol). The vial was capped and heated to 150 °C for 15 min. The reaction was cooled and the precipitate was filtered and rinsed with cold

hexane/Et_2O (3:1). The product was dried under vacuum and obtained as an orange solid (600 mg, 73%). Data in agreement with the literature.[139] ^{1}H NMR (400 MHz, Chloroform-*d*) δ 8.09 – 8.01 (m, 1H), 7.98 (dq, *J* = 7.7, 0.9 Hz, 1H), 7.86 (tdd, *J* = 7.6, 3.0, 1.3 Hz, 1H), 7.78 (ddd, *J* = 7.5, 6.8, 1.1 Hz, 1H), 7.71 – 7.63 (m, 1H), 7.45 (d, *J* = 11.9 Hz, 1H), 6.46 (dd, *J* = 12.8, 11.9 Hz, 1H), 3.96 (s, 3H). ^{13}C NMR (126 MHz, $CDCl_3$) δ 178.5, 169.0, 162.1, 144.3, 143.3, 136.0, 134.0, 133.1, 126.8, 124.7, 121.3, 101.5, 59.0.

MerocySO (11)

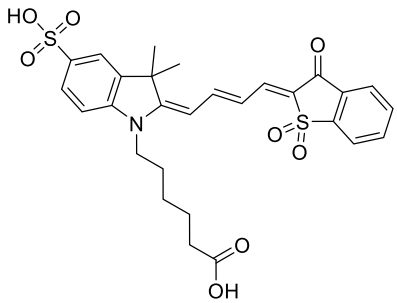

MerocySO was prepared according to a reported procedure.[139] 1-(5-carboxypentyl)-2,3,3-trimethyl-3*H*-indolium-5-sulfonate (184 mg, 0.52 mmol), sodium acetate (43 mg, 0.52 mmol), and benzothiophene enol ether (100 mg, 0.40 mmol) were added to a microwave vial and suspended in 1:1 MeOH/CH_2Cl_2 (1 mL). The vial was capped and heated to 75°C for 30 min. The reaction mixture was cooled and concentrated, then purified by preparative HPLC (system 2). The product was obtained as a dark purple solid (29 mg, 14 %). HPLC (Method 1) t_R = 4.5 min, Purity 100% (ELSD). MS (ESI): calculated for $C_{28}H_{29}NO_8S_2$ $[M+H]^+$ m/z 572.1. Found 572.1 $[M+H]^+$ (100%). ^{1}H NMR (400 MHz, Methanol-*d*$_4$) δ 8.00 (d, J = 7.4 Hz, 1H), 7.94 (d, J = 7.4 Hz, 1H), 7.83 – 7.67 (m, 4H), 7.34 – 7.26 (m, 2H), 7.11 (t, J = 7.5 Hz, 1H), 6.92 (d, J = 7.9 Hz, 1H), 6.86 (t, J = 13.2 Hz, 1H), 5.89 (d, J = 12.8 Hz, 1H), 3.46 – 3.31 (s, 3H), 1.62 (s,

6H). DEPT-135 ^{13}C NMR (126 MHz, MeOD) δ 156.4, 135.9, 134.9, 134.9, 127.9, 124.5, 121.4, 121.2, 110.6, 102.7, 44.6, 34.6, 28.2, 27.9, 27.4, 25.8.

MerocySO folate (9)

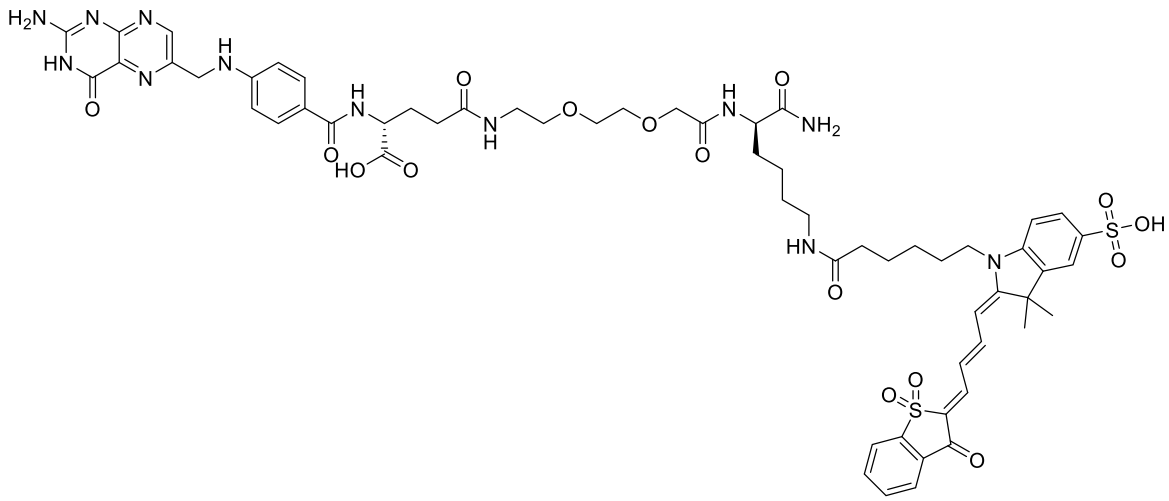

The dye coupling procedure was carried out following the general procedure, with 1.4 equiv. merocyanine SO-NHS was reacted with the resin overnight at room temperature. The crude product was cleaved from the resin and purified by RP-HPLC. HPLC (Method 1) t_R = 6.5 min. Purity = >90% (280, 600 nm). HRMS (MALDI) m/z: calcd for $C_{69}H_{90}N_{13}O_{22}S_4$ $[M+Na+K]^+$ 1327.3925. Found 1327.3712.

6.3.2. Biological studies

Materials

The following reagents and materials were purchased; RPMI-1640 media (Gibco, 21875034), RPMI-1640 media without folic acid (Gibco, 27016021), M-CSF (R&D Systems, 215-GM), M-CSF (R&D Systems, 216-MC), CD14 microbeads for magnetic separation (Miltenyi, 130-050-201), rabbit polyclonal FR-β antibody

(Thermo-Fisher, PA5-45768), folic acid (Sigma, Biochemical grade F8758), 7-AAD (eBioscience, 00-6993-50), CellMask DeepRed (Invitrogen, C10046). Hoechst 33342 (Invitrogen, H3570) and Calcein AM (Invitrogen, C-3100). LPS from *E.coli.* (Sigma Aldrich, L4391), rat IFN-γ (R&D systems, 585-IF), Hoechst 33258 (Invitrogen, H3569), Ham's F12K medium (Gibco, 21127022), mouse anti-rat CD32 (BD Biosciences, 550270, clone D34-485), PE labelled mouse FR-β (Biolegend, 391703, clone 94b), mouse IgG1 isotype control (Biolegend, 400112, clone MOPC-21), RIPA buffer (Sigma, R0278), EDTA-free proteinase inhibitor cocktail (Sigma, P1860), HRP-labelled goat anti-rabbit IgG secondary antibody (ProteinSimple, 040-656), CellTiter Glo 2.0 assay kit (Promega, G9242), Pierce LDH Cytotoxicity Assay Kit (Invitrogen, 88954).

The KB cell line was obtained from ATCC (CCL17), A549 cells were donated by Emma Scholefield (CIR), NR8383 macrophage cells were obtained from the internal GSK cell biobank. Murine peritoneal macrophages were obtained by Pieter Louwe (CIR).

Cancer cell culture

KB and A549 cell lines were cultured in RPMI-1640 media supplemented with 10% fetal bovine serum (FBS), 1% L-glutamine and antibiotics (penicillin/streptomycin, 100 U/mL). Cells were cultured at 37 ^{o}C in a 5 % CO_2 atmosphere in a HeraCell incubator. Cells were harvested with trypsin/EDTA (0.25 % trypsin, 1 mM EDTA) and subcultured by re-suspending in fresh growth medium. For cell experiments with

folate conjugates, cells were cultured in folate-free RPMI-1640 medium (FF-RPMI) for at least 1 week prior.

Live cell confocal microscopy

KB or A549 cells were plated in ibidi μ-slide 8 well chamber slides (5 x 10^4 cells/ mL, 300 μL/well) and cultured for 24 h. Media was removed and cells were treated with the counterstains Hoechst 33342 (1 μg/mL) and/or CellMask DeepRed (5 μg/mL), according to manufacturer's instructions. After incubation, cells were rinsed with PBS and incubated with the folate probe (in FF-RPMI media) for 15 min at 37 ^{o}C. The following concentrations of each probe were used: **1**: 0.5 μM, **3**: 1 μM, **5**: 1 μM, **6**: 1 μM, **7**: 0.5 μM, **9**: 1 μM.

After staining cells were rinsed with PBS once and fresh FF-RPMI media added. Confocal imaging was carried out under environmental control at 37 ^{o}C (5% CO_2 atmosphere) with a Leica SP5 microscope (settings: resolution 1024x1024 pixels; x40 oil or x63 oil objectives; laser lines 405 nm, 488 nm, 633 nm; detection at 435-460 nm (for Hoechst), 500-550 nm (for fluorescein), 640-750 (for Cy5). Images were extracted using the Leica LAS AF software and analysed with the Fiji distribution of ImageJ.[140]

Flow cytometry

KB or A549 cells were plated in 24-well plates (1 x 10^5 cells per well) and cultured for 24 h. Media was removed and cells were treated with the folate conjugate (100 nM) in FF-RPMI for 30 min at 37 ^{o}C, or left untreated as a control. After incubation cells were washed with PBS, harvested with trypsin/EDTA and resuspended in fresh FF-RPMI media. Flow cytometry was performed with a Becton Dickinson (BD) FACScan

cytometer with CellQuest software. Optical settings: Excitation at 488 nm and emission filtered at 525/20 nm (FITC) for probes **1, 5** and **6**, or excitation at 633 nm and emission filtered 666/27 nm (Cy5) for probes **3** and **7**.

For competitive studies the same procedure was used, except cells were first incubated with 1000-fold excess of folic acid (100 mM) for 15 min at 37 ^{o}C to saturated any available folate receptors. The solution was removed and subsequently the folate conjugate (100 nM) in FF-RPMI was added for 15 min at 37 ^{o}C. After incubation cells were washed with PBS, harvested with trypsin/EDTA and resuspended in fresh FF-RPMI media. Flow cytometry was then performed.

Relative binding affinities were calculated from flow cytometry data of serial dilutions of probes **1**, **3**, **5**, **7** (0, 2, 5, 10, 25, 50, 100 nM) to KB cells using the same procedure. Non-linear regression curves were fitted to the MFI values of each probe using Prism. The K_D was determined from the concentration of ligand at which half of the receptors are occupied.

All cytometry measurements were carried out on samples in triplicate, gated on live cells and with 10,000 cells per sample. Data was analysed using FlowJo v10 and the median fluorescence intensity (MFI) for the fluorophore channel was plotted using Prism.

CellTiter Glo cytotoxicity assay

CellTiter Glo 2.0 (Promega): KB cells (2 $x10^4$ cells/well) were cultured in supplemented FF-RPMI medium in a clear bottom 96 well-plate and incubated for 24 h at 37 ^oC. 50, 100 and 500 nM concentrations of probes **1**, **3**, **5**, **7** (in triplicate), or an untreated group, were incubated for 2 h at 37 ^oC. Plates were washed with PBS and fresh medium was added. CellTiter-Glo 2.0 reagent was added according to manufacturers instructions and the plate was shaken for 2 minutes. The solution was transferred to an opaque 96 well-plate and allowed to stand for 10 minutes at room temperature. Luminescence was measured using a Biotek Synergy HT microplate reader. Cell viability was reported as the mean percentage relative to untreated cells.

NR8383 rat macrophages cell culture

NR8383 rat alveolar macrophage cells were cultured in Ham's F12K medium (Kaighns' modification) supplemented with 15% heat inactivated fetal bovine serum (FBS) and penicillin/streptomycin. Cells were cultured at 37 ^oC in a 5% CO_2 atmosphere in a HeraCell incubator. Cells were subcultured twice per week by removal of suspension cells and resuspending these in fresh growth medium.

NR8383 FR-β expression - flow cytometry

NR8383 cells were plated in a flat-bottomed 24 well-plate (2.5 $x10^5$ cells/well). A subset of cells were stimulated with 10 ng/mL LPS + 10 ng/mL IFN-γ diluted in culture media, while the remainder were left untreated. Both groups were incubated for 24h at 37 ^oC. Cells were transferred to FACS tubes and resuspended in FACS buffer (PBS + 0.5% BSA). Fc mediated non-specific binding was blocked by incubating samples with mouse anti-rat CD32 (5 μg/mL) on ice for 5 minutes. PE mouse FR-β antibody

(1:10, 1:20, 1:50 dilutions) or an isotype control (clone MOPC-21) was added and samples incubated on ice for 30 minutes. After washing with FACS buffer, 7-AAD (5 μL/test) was added according to manufacturer's instructions. Samples were analysed by FACSCanto and the data processed with FlowJo. Cells were gated based on viable single cells with FSC/SSC distribution used to remove debris and with negative 7-AAD staining (viable cells). Data was quantified using the geometric mean fluorescence intensity (MFI) of the channel of interest.

NR8383 FR-β expression - Western blot

Cell lysate was prepared from ~10^7 NR8383 and A549 cells. Cells were washed twice with PBS and lysed with freshly prepared RIPA buffer + 1X EDTA-free proteinase inhibitor cocktail (500 μl) for 30 min on ice. After lysis, insoluble material was pelleted by centrifugation at 13,000 g, 15 min at 4 ^{o}C. The supernatant was removed and the total protein content of lysate measured by the colorimetric DC assay (Biorad). 2 μg/mL aliquots of cell lysate were prepared for Western blot.

Western blotting was carried out using the ProteinSimple WES instrument following the manufacturer's instructions and with the following antibodies; rabbit polyclonal FR-β antibody (dilutions of 1:50, 1:100, 1:200, 1:400) and HRP-labelled goat anti-rabbit IgG secondary antibody (ProteinSimple).

NR8383 confocal microscopy

NR8383 cells (1.0 x 10^5 cells/ mL) were plated in ibidi 35mm μ-dish with high walls (2 mL/well). After 1 day the media was removed and replaced with Cy5**-Folate **7**

(250 nM) in fresh FF-RPMI and incubated for 30 min at 37 ºC. Hoechst 33258 (1 µg/mL) was added for the last 10 minutes of incubation. Confocal imaging was carried out on the Yokogawa CQ1 microscope located in GSK Stevenage.

NR8383 flow cytometry

NR8383 cells were prepared as in the receptor expression experiment and transferred to FACS tubes. Cells were washed with acidic sodium acetate saline solution (pH 4.5) for 1 min to remove surface bound folates.[60] Probe **7** was added at 0 – 2.5 µM concentrations and incubated for 30 minutes at 37 ºC. Competitive binding was assessed by incubating probe in the presence of 100 µM folic acid (FA). After incubation, the probe solution was removed, cells were washed with FACS buffer and 7-AAD (5 µL/test) was added according to manufacturer's instructions. Samples were analysed and the data processed with FlowJo. Cells were gated based on viable single cells with FSC/SSC distribution used to remove debris and negative 7-AAD staining. Data was quantified using the geometric mean fluorescence intensity (MFI) of the channel of interest.

Human monocyte derived macrophages

Human monocytes from healthy volunteers were collected by purification of peripheral blood mononuclear cells using CD14 positive magnetic bead separation (Miltenyi) according to manufacturer's instructions. Monocyte-derived macrophages were differentiated with GM-CSF (50 ng/mL) for M1, or M-CSF (100 ng/mL) for M2 macrophages, diluted in RPMI media (with 10% FBS) for 7 days.

Labelling of MDMs – flow cytometry

M-CSF macrophages were plated in round bottom 96-well plates (1 x 10^6 cells/mL, 100 μL/well) and cultured for 7 days to allow differentiation. Media was removed and cells incubated with a range of concentrations of **Cy5**-Folate 7** (0, 10, 50, 100 and 500 nM) for 30 min at 37°C. Competition was performed in the presence of 100-fold molar excess folic acid. After the incubation period the cells were rinsed with PBS once. Cells were transferred to FACS tubes and resuspended in FACS buffer (PBS + 0.5% BSA). 7-AAD (5 μL/test) was added to each sample and put on ice for 5 minutes. Samples were then analysed and the data processed with FlowJo. Cells were gated for viable single cells using FSC/SSC distribution used to remove debris and negative 7-AAD staining to remove dead cells. Data was quantified using the geometric mean fluorescence intensity (MFI) of the channel of interest.

Labelling of MDMs – confocal microscopy

GM-CSF or M-CSF macrophages were plated in ibidi μ-slide 8 well chamber slides (5 x 10^4 cells/ mL, 300 μL/well) and cultured for 7 days to allow differentiation. Media was removed, cells were rinsed with PBS then incubated with **Cy5**-Folate** (250 nM) in FF-RPMI media (in the presence of 100-fold molar excess folic acid for competition assays) for 30 min at 37°C. Hoechst 33342 (1 μg/mL) and Calcein AM (0.5 μM) were added directly to the staining solution as counterstains for the last 10 min. After incubation the cells were rinsed with warm PBS once and fresh RPMI medium was added. Confocal imaging was carried out with a Leica SP5 microscope (settings: resolution 1024x1024 pixels; x63 oil objective; laser lines 405 nm, 488 nm, 633 nm; detection at 435-460 nm (for Hoechst), 500-550 nm (for calcein), 640-750 (for Cy5).

Images were extracted using the Leica LAS AF software and analysed with the Fiji distribution of ImageJ.[140]

Labelling of M-CSF derived MDMs after stimulation – high content imaging

MDMs were plated in black flat-bottom 96-well plates (1 x 10^6 cells/mL, 100 μL/well) and differentiated over 7 days with M-CSF (100 ng/mL). Three conditions were setup; untreated cells, cells that were stimulated with LPS (100 ng/mL) or stimulated with IL-4 (20 ng/mL) for 24 hours. The next day the media was removed and triplicate wells incubated with fresh FF-RPMI containing **Cy5**-Folate** (100 nM) or FolateSense (25 nmol) for 30 min at 37 ^{o}C. Hoechst 33342 (1 μg/mL) was added as a counterstain for the final 10 minutes of incubation. The cells were washed with PBS once (300 μL) and then fresh FF-RPMI medium (100 μL) was added. Imaging was carried out on the CellInsight imaging system (ThermoFisher) and the mean fluorescence per object ± standard deviation was obtained. The data was processed in Prism.

Timelapse imaging of Cy5-Folate labelling – confocal microscopy**

MDMs that had been differentiated over 7 days with M-CSF (100 ng/mL) were plated in ibidi 35mm μ-dish with high walls (1.0 x 10^5 cells/ mL, 2 mL/well). After 7 days the media was removed and replaced with **Cy5**-Folate** (250 nM) in fresh FF-RPMI at 37 ^{o}C. Confocal imaging was carried out on the Yokogawa CQ1 microscope over 15 hours, imaging every 15 minutes over multiple imaging fields. The fluorescence intensity was determined by the software. The video clip was collected in the CQ1 software (Yokogawa).

Labelling of primary BAL macrophages – flow cytometry

Macrophages from BAL fluid were plated in round bottom 96-well plates (1 x 10^6 cells/mL, 100 μL/well) and allowed to attach overnight. Media was removed and cells incubated with **Cy5**-Folate** (100 nM) for 30 min at 37 ^oC. After the incubation period the cells were rinsed with PBS once. Cells were transferred to FACS tubes and resuspended in FACS buffer (PBS + 0.5% BSA). Samples were then analysed and the data processed with FlowJo. Cells were gated for viable single cells using FSC/SSC distribution used to remove debris. Data was quantified using the geometric mean fluorescence intensity (MFI) of the Cy5 channel.

Labelling of murine peritoneal macrophages

Peritoneal macrophages were plated in ibidi μ-slide 8 well chamber slides (1 x 10^6 cells/ well, 300 μL/well) and allowed to adhere overnight before the media was replaced on the next day. The cells were rinsed with PBS then incubated with **Cy5**-Folate** (250 nM) in FF-RPMI media (competition experiments + 2.5 μM folic acid) for 30 min at 37 ^oC. Hoechst 33342 (1 μg/mL) was added as counterstain for the last 10 min. The cells were rinsed with PBS once and fresh RPMI medium added (300 μL). Confocal imaging was performed with a Leica SP5 microscope (settings: resolution 1024x1024 pixels; x63 oil objective; laser lines 405 nm, 633 nm; detection at 435-460 nm (for Hoechst), 640-750 (for Cy5).

Peritoneal macrophage flow cytometry was carried out by Pieter Louwe.

These experiments were performed under Home Office License in compliance with the Animals (Scientific Procedures) Act 1986 and approved by the University of Edinburgh Ethics Committee.

6.4. Chapter 3

This experimental results of this chapter are a collaboration between myself, Edinburgh Molecular Imaging, Tom Speight (CIR) and Vrije Universiteit Brussels. The anti-MMR nanobody was provided by Vrije Universiteit Brussels, the protein conjugation was carried out by myself and Christophe Portal (Edinburgh Molecular Imaging). Characterisation and SDS-PAGE of the labelled nanobody was carried out by myself. All cellular studies were carried out by Tom Speight at the Centre for Inflammation Research.

6.4.1. Bioconjugation

Materials

The following reagents and materials were purchased; Lysozyme from chicken egg white (Sigma, L4919), GE Illustra Nap-5 column (GE Healthcare, 17-0853-01), Amicon Ultra 0.5 mL 10k MWCO centrifugal filter membranes (Merck, UFC501024), Sephadex G-25 PD-10 column (GE Healthcare, 17085101) and PLRP-S 300Å HPLC column (Agilent, 5 µm, 250 x 4 mm).

Validation of lysine labelling conditions - Cy5 labelled lysozyme**

O-(N-Succinimidyl)-1,1,3,3-tetramethyluronium tetrafluoroborate (TSTU, 2.64 mg, 8.8 µmol, 1 equiv.) and N,N-dimethylaminopyridine (DIPEA, 1.2 µL, 12.3 µmol, 1.4 equiv.) were added to N-methyl pyrolidinone (NMP, 50 µL). After one minute, Cy5.0** (7.8 mg, 8.8 µmol, 1 equiv.) in NMP (50 µL) was added. The reaction was monitored by HPLC (C18 5PCTMIN) and maximum conversion was reached after 1 hour. Crude Cy5**-NHS was directly taken to next step without purification.

Lysozyme (4.19 mg, 0.033 equiv.) was dissolved in PBS (1 mL). Borate buffer (0.1 M) was prepared by dissolving sodium borate (0.5 mg) in water and was added to the Lysozyme solution (200 µL). The Cy5**-NHS solution (33 µL) was added to the Lysozyme solution and shaken on an orbital shaker. The reaction was monitored by HPLC (C4 1PCTMIN) and shown to be 90% complete after 30 min. Half of the reaction mixture was quenched by adding hydroxylamine (5 equiv, 1.5 mg) to the mixture and shaken for 15 min. The crude reaction mixture was purified using a Nap-5 column and eluting with PBS.

Labelling of MMR nanobody

The anti-MMR nanobody clone 3.49 (MMR 3.49, provided by Vrije Universiteit Brussels) was provided without a His tag tail. Fluorophore labelling was carried out by a random lysine labelling procedure with a 5-molar excess of reactive dye. Briefly, dye NHS-ester activation was performed by dissolving SulfoCy5 (1.0 mg, 1.50 µmol) in anhydrous *N*-*N*-dimethylformamide (DMF, 80 µL) and *N*,*N*-diisopropylethylamine (0.4 µL, 2.3 µmol) was added. O-(*N*-Succinimidyl)-1,1,3,3-tetramethyluronium tetrafluoroborate (0.46 mg, 1.50 µmol) in DMF (40 µL) was subsequently added and the reaction mixture stirred for 1 hour. Upon complete conversion to the active ester (SulfoCy5-NHS), the nanobody (3.8 mg, 0.3 µmol) in PBS (1 mL, 0.1 M) was added and the mixture incubated for 3 hours. The labelled nanobody was purified by PD-10 gel or centrifugation (15,000 x g, 10k MWCO Amicon centrifugal filters) using PBS (pH 7.4) as buffer.

Nanobody characterisation – HPLC and MS

Fluorophore conjugation was confirmed by RP-HPLC and mass spectrometry. The nanobody was characterised by HPLC (Agilent 1100 series, PLRP-S 300Å, 5 µm, 250x4 mm). The following gradient was used 25% H_2O in acetonitrile for 5 minutes, increase to 34% H_2O in 2 minutes, increase to 100% H_2O over 3 minutes, isocratic elution at 100% H_2O for 15 minutes. All solvents had 0.1% TFA as additive. Detection at 280 nm and 647 nm was used for analysis of protein and dye, respectively, as well as fluorescence detection (λ_{Ex} 647, λ_{Em} 670 nm).

Mass spectrometry was performed using IMS-MS (Waters Synapt Q-ToF, direct infusion). The IMS data was processed and analysed using MassLynx (Waters).

Nanobody characterisation – spectroscopy

The concentration of labelled nanobody and degree of labelling (DOL) was determined by UV/Vis absorbance. UV/Vis absorbance measurements were made on a Nanodrop 1000 spectrometer, measuring the absorbance of the dye and labelled protein at A_{280} and A_{max}.

$$protein\ concentration\ (M) = \frac{[A_{280} - (A_{max} \times CF)] \times dilution\ factor}{\varepsilon}$$

CF correction factor for the dye, adjusting for dye absorbance at 280 nm

ε is molar extinction coefficient of the protein

$$degree\ of\ labelling\ (dye\ per\ protein) = \frac{A_{max} \times dilution\ factor}{\varepsilon' \times protein\ conc.\ (M)}$$

ε' is molar extinction coefficient of the dye

Fluorescence spectra were recorded in polystyrene cuvettes using a FluoroMax spectrofluorometer with solutions having an absorbance less than 0.1 a.u. to avoid inner-filter effects.

6.4.2. Biological studies

Materials

The following reagents and materials were purchased; anti-human PE-CD206 antibody (Biolegend 321105), Precision Plus Protein Kaleidoscope™ Standards (BioRad 161-0375), 4X Laemelli sample buffer (BioRad 161-0747), Colloidal Coomassie gel stain (BioRad 161-0803), Tricine ultrapure (VWR #E170-100G).

Gel electrophoresis

The protein samples (0.5 μg unlabelled MMR, and 0.5 and 1 μg **Cy5-Nb**) were reduced in Laemelli sample buffer at 90 °C for 5 minutes. The reduced sample was loaded onto a handcast SDS-tricine gel (10% separating and 3% stacking gel). SDS-tricine PAGE was performed under reducing conditions according to a published protocol.[141] The Precision Plus Kaleidoscope™ protein ladder was used as a molecular weight standard. Visualisation of protein bands was performed using the colloidal Coomassie staining kit (BioRad) according to the manufacturer's instructions and imaged with the GelDoc system (BioRad).

Further biological studies were carried out by Tom Speight using monocyte-derived macrophages.

6.5. Chapter 4

6.5.1. Synthesis

XD-OH

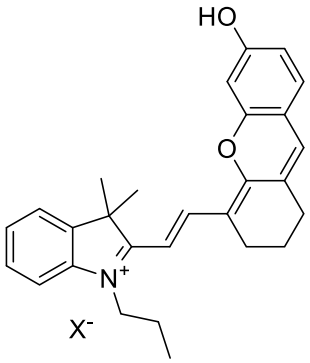

XD-OH was prepared by according to a previously reported procedure.[124] Resorcinol (82 mg, 0.76 mmol), K_2CO_3 (104 mg, 0.76 mmol) were dissolved in MeCN (10 mL) and stirred to room temperature for 15 min. To this a solution of IR780 iodide (200 mg, 0.30 mmol) in MeCN (2.5 mL) was added and the reaction mixture heated to 50 ^oC for 6 h. Conversion was observed by TLC (DCM:MeOH 98:2) and the reaction mixture was concentrated, then separated between DCM/ water. The organics were extracted with DCM and washed with 0.1 M HCl solution, brine and dried over $MgSO_4$. The product was obtained in sufficient purity as a blue solid (176 mg, 100 %). Data in agreement with the literature.[124] HPLC (Method 1) t_R = 4.5 min, Purity = 90 % (ELSD). MS (ESI): calculated for $C_{28}H_{30}NO_2$ $[M]^+$ m/z 412.2. Found 412.3 (100%). ^1H NMR (500 MHz, Chloroform-*d*) δ 8.42 (d, *J* = 13.9 Hz, 1H), 7.40 (dd, *J* = 7.5, 1.2 Hz, 1H), 7.35 (d, *J* = 7.3 Hz, 2H), 7.25 – 7.19 (m, 2H), 7.13 (s, 1H), 7.04 (dd, *J* = 14.6, 8.6 Hz, 2H), 5.91 (d, *J* = 14.0 Hz, 1H), 3.96 (t, *J* = 7.5 Hz, 2H), 2.73 (t, *J* = 6.2 Hz, 2H), 2.63 (t, *J* = 6.4 Hz, 2H), 1.91 (tt, *J* = 14.9, 7.0 Hz, 4H), 1.74 (s, 6H), 1.08 (t, *J* = 7.4 Hz, 3H). ^{13}C NMR (126 MHz, Chloroform-*d*) δ 173.9, 162.6, 156.9, 142.6, 140.9,

139.2, 129.3, 128.6, 124.9, 122.7, 115.4, 115.1, 110.0, 103.5, 98.0, 49.3, 45.8, 28.8, 28.6, 24.4, 21.0, 20.7, 11.8.

XD-BGal

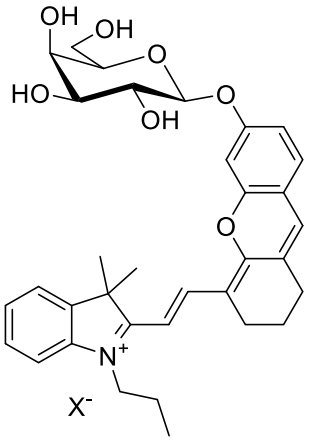

XD-BGal was prepared by according to a previously reported procedure.[124] **XD-OH** (100 mg, 0.19 mmol), Na_2SO_4 (65 mg, 0.46 mmol) and Cs_2CO_3 (155 mg, 0.46 mmol) were dissolved in MeCN (10 mL) and stirred at room temperature under N_2 for 15 mins. α-bromo galactose tetraacetate (124 mg, 0.38 mmol) was added and the reaction stirred for 48 hr. The solvent was evaporated under vacuum and the residue purified by flash column chromatography (DCM:MeOH 0% to 10%) to obtain a blue solid. The acetylated galactose was deprotected with a solution of K_2CO_3 (6.5 mg) in MeOH (1 mL) and stirred for 1 h. HPLC confirmed the complete deprotection of the starting material and the compound was purified by flash column chromatography (DCM:MeOH 0% to 20%) to give a blue solid (30 mg, 30 % over two steps). Data in agreement with the literature.[124] R_f = 0.39 (10% MeOH:DCM). HPLC (Method 1) t_R = 3.8 min, Purity = 100 % (ELSD). HRMS (ESI) m/z: $[M]^+$ Calcd for $C_{34}H_{40}NO_7$ 574.2799. Found 574.2755. ^{1}H NMR (500 MHz, DMSO-d_6) δ 8.61 (d, J = 15.0 Hz, 1H), 7.81 – 7.70 (m, 2H), 7.61 – 7.53 (m,2H), 7.49 (t, J = 7.4 Hz, 1H), 7.45 (s, 1H),

7.17 (d, *J* = 4.8 Hz, 2H), 6.65 (d, *J* = 15.1 Hz, 1H), 5.04 – 4.97 (m, 1H), 4.33 – 4.27 (m, 2H), 4.20 – 4.13 (m, 1H), 3.99 – 3.93 (m, 2H), 3.92 – 3.79 (m, 3H), 2.72 (d, *J* = 6.8 Hz, 2H), 2.68 (t, *J* = 6.2 Hz, 2H), 1.92 – 1.82 (m, 4H), 1.79 – 1.75 (m, 6H), 0.99 (t, *J* = 7.4 Hz, 3H). ^{13}C NMR (126 MHz, DMSO) δ 178.3, 159.6, 158.4, 145.2, 142.3, 141.4, 131.7, 128.9, 128.1, 127.4, 122.7, 117.0, 114.1, 113.4, 106.1, 105.4, 103.9, 96.9, 70.5, 70.1, 69.8, 61.1, 50.7, 30.7, 28.5, 27.4, 27.3, 23.5, 21.0, 20.5, 11.0.

XD-Br

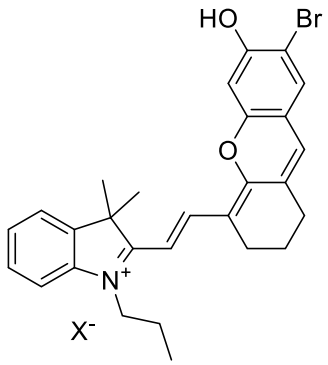

XD-Br was prepared by according to a previously reported procedure.[124] 4-bromoresorcinol (144 mg, 0.76 mmol), K_2CO_3 (104 mg, 0.76 mmol) were dissolved in MeCN (2.5 mL) and stirred to room temperature for 15 min. To this a solution of IR780 iodide (200 mg, 0.30 mmol) in MeCN (2.5 mL) was added and the reaction mixture heated to 50 ^{o}C for 6 h. Conversion was observed by TLC (DCM:MeOH 98:2) and upon completion the reaction mixture was concentrated and diluted with DCM/ water. The organics were extracted with DCM, washed with 0.1 M HCl solution, then brine and dried over $MgSO_4$. The product was concentrated under vacuum to obtain a blue solid (69 mg, 37 %). Data in agreement with the literature.[124] HPLC (Method 1) t_R = 4.7 min, Purity = 100 % (ELSD). ESI-MS: calculated for $C_{28}H_{30}NO_2$ $[M]^+$ m/z 490.1. Found 490.1 (100%). ^{1}H NMR (500 MHz, Chloroform-*d*) δ 8.17 (d, *J* = 13.6

Hz, 1H), 7.58 (s, 1H), 7.34 – 7.27 (m, 2H), (1H obscured by $CDCl_3$), 7.11 (td, *J* = 7.4, 0.9 Hz, 1H), 6.90 (d, *J* = 7.9 Hz, 1H), 6.76 (s, 1H), 5.72 (d, *J* = 13.7 Hz, 1H), 3.83 (t, *J* = 7.4 Hz, 2H), 2.67 (t, *J* = 6.1 Hz, 2H), 2.59 (t, *J* = 6.2 Hz, 2H), 1.92 – 1.77 (m, 4H), 1.64 (s, 6H), 1.03 (t, *J* = 7.4 Hz, 3H). ^{13}C NMR (126 MHz, $CDCl_3$) δ 161.1, 157.7, 153.3, 143.3, 140.2, 139.1, 132.2, 131.0, 128.4, 123.3, 122.4, 115.8, 109.8, 108.8, 103.6, 100.2, 95.6, 48.3, 45.2, 28.8, 28.3, 24.5, 21.3, 20.4, 11.8.

XD-BrBGal protected

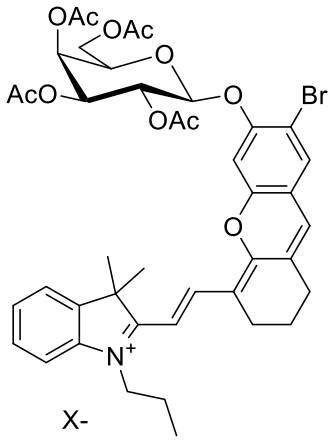

XD-Br (30 mg, 0.056 mmol) and Cs_2CO_3 (56 mg, 0.168 mmol) were dissolved in DCM (3 mL) and stirred at room temperature under N_2 for 15 mins. α-bromo galactose tetraacetate (70 mg, 0.168 mmol) was added and the reaction stirred for 18 hr. The solvent was evaporated under vacuum and the residue purified by flash column chromatography (DCM:MeOH 0% to 8%) to obtain a blue solid (10 mg, 22%). R_f = 0.55 (8% MeOH:DCM). HPLC (Method 1) t_R = 4.8 min, Purity = 92 % (650 nm). MS (ESI): calculated for $C_{42}H_{47}NO_{11}Br$ $[M]^+$ m/z 820.2. Found 822.2 (100%).

^{1}H NMR (500 MHz, Chloroform-*d*) δ 8.78 (d, *J* = 15.1 Hz, 1H), 7.63 – 7.58 (m, 2H), 7.54 – 7.46 (m, 2H), 7.43 (td, *J* = 7.5, 1.0 Hz, 1H), 7.38 (d, *J* = 7.9 Hz, 1H), 7.05 (s, 1H), 6.96 (s, 1H), 6.73 (d, *J* = 15.1 Hz, 1H), 5.65 – 5.61 (m, 2H), 5.59 – 5.56 (m, 1H),

5.29 – 5.26 (m, 1H), 4.71 – 4.65 (m, 1H), 4.59 (t, *J* = 7.5 Hz, 2H), 4.45 (dd, *J* = 10.9, 5.7 Hz, 1H), 4.15 – 4.09 (m, 2H), 2.86 – 2.70 (m, 4H), 2.21 (s, 3H), 2.11 (d, *J* = 5.3 Hz, 3H), 2.08 (d, *J* = 3.7 Hz, 3H), 2.03 (s, 3H), 2.01 (s, 3H), 1.90 (s, 3H), 1.86 (s, 3H), 1.10 (t, *J* = 7.4 Hz, 3H).

XD-BrBGal

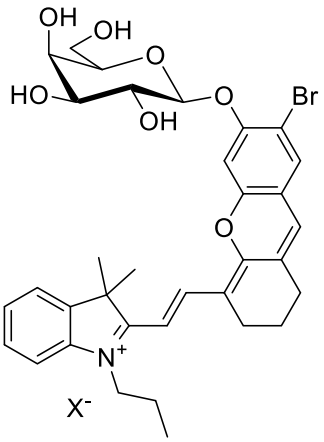

The acetylated protected compound **XD-BrBGal protected** (10 mg) was deprotected with a solution of K_2CO_3 (6.5 mg) in MeOH (1 mL) after stirring at rt for 1 h. HPLC confirms the complete deprotection of the starting material (t_R = 3.9 min) and the compound was purified by RP-HPLC (system 1) to give a blue solid (6 mg, 71 %). R_f = 0.60 (8% MeOH:DCM). HPLC (Method 1) t_R = 3.95 min, Purity = 87 % (650 nm). HRMS (ESI/Q-TOF) m/z: $[M]^+$ Calcd for $C_{34}H_{39}BrNO_7$ 652.1904. Found 652.1904. ^{1}H NMR (500 MHz, D_2O) δ 8.55 – 8.44 (br), 8.47 (d, *J* = 15.1 Hz, 1H), 7.65 (d, *J* = 7.3 Hz, 1H), 7.58 – 7.47 (m, 4H), 7.03 (s, 1H), 6.98 (s, 1H), 6.44 (d, *J* = 15.1 Hz, 1H), 5.04 (d, *J* = 7.7 Hz, 1H), 4.25 (t, *J* = 7.3 Hz, 2H), 4.12 (d, *J* = 3.4 Hz, 1H), 3.99 – 3.93 (m, 2H), 3.92 – 3.79 (m, 3H), 2.72 – 2.59 (m, 2H), 2.56 (t, *J* = 5.7 Hz, 2H), 1.92 – 1.82 (m, 4H), 1.77 (s, 3H), 1.67 (s, 3H), 0.97 (d, *J* = 7.6 Hz, 3H). ^{13}C NMR (126 MHz, DMSO) δ 178.3, 159.6, 158.4, 145.2, 142.3, 141.4, 131.7, 128.9, 128.1, 127.4, 122.7,

117.0, 114.1, 113.4, 106.1, 105.4, 103.9, 96.9, 70.5, 70.1, 69.8, 61.1, 50.7, 30.7, 28.5, 27.4, 27.3, 23.5, 21.0, 20.5, 11.0.

SulfoXD-OH

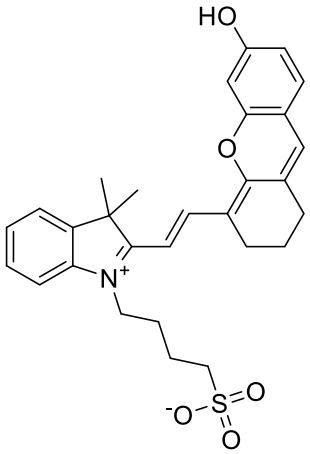

Resorcinol (55 mg, 0.50 mmol), K_2CO_3 (70 mg, 0.50 mmol) were dissolved in DMF (2.5 mL) and stirred at room temperature for 15 min. To this a solution of IR783 iodide (150 mg, 0.20 mmol) in DMF (0.5 mL) was added and the reaction heated to 50°C for 6 h. Conversion was observed by TLC (DCM:MeOH 90:10) and upon completion the reaction mixture was concentrated. The product was isolated by RP-flash chromatography (Biotage C18 Ultra 50g, 10% - 50% ACN in H_2O, with 0.1% formic acid) and the product fractions were lyophilised to give a deep blue powder (70 mg, 69 %). HPLC (Method 1) t_R = 4.1 min, Purity = 100 % (ELSD). HRMS (ESI/Q-TOF) m/z: $[M+H]^+$ Calcd for $C_{29}H_{31}NO_5S$ 506.1996. Found 506.2001. ^{1}H NMR (500 MHz, Methanol-d_4) δ 8.54 (d, *J* = 14.5 Hz, 1H), 7.59 (s, 1H), 7.51 (d, *J* = 7.4 Hz, 1H), 7.44 – 7.37 (m, 2H), 7.32 (d, *J* = 8.4 Hz, 1H), 7.24 (t, *J* = 7.5 Hz, 1H), 6.76 (dd, *J* = 8.8, 2.2 Hz, 1H), 6.65 (s, 1H), 6.20 (d, *J* = 14.0 Hz, 1H), 4.56 (s, 2H), 4.16 (t, *J* = 7.2 Hz, 2H), 2.90 (t, *J* = 7.1 Hz, 2H), 2.78 (t, *J* = 6.1 Hz, 2H), 2.74 (t, *J* = 6.2 Hz, 2H), 2.02 – 1.91 (m, 4H), 1.77 (s, 6H).

SulfoXD-BGal

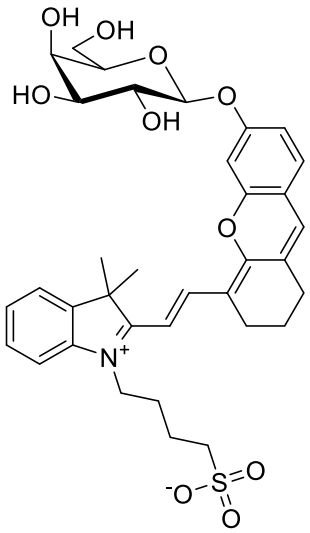

SulfoXD-OH (20 mg, 0.04 mmol) and Cs_2CO_3 (40 mg, 0.12 mmol) were dissolved in DMF (2 mL) and stirred at room temperature under N_2 for 15 mins. α-bromo galactose tetraacetate (50 mg, 0.12 mmol) was added and the reaction stirred for 48 hr at room temperature. No reaction progress was seen and the reaction was abandoned.

4-O-(2,3,4,6-Tetra-O-acetyl-β-D-galactopyranosyl)-4-oxybenzaldehyde (20)

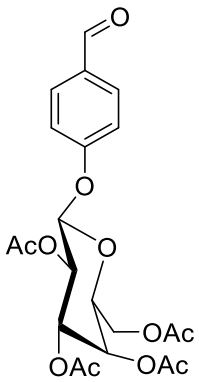

Compound **20** was prepared according to a reported procedure.[142] Silver oxide (464 mg, 2.0 mmol) and 4-hydroxybenzaldehyde (134 mg, 1.1 mmol) were added to a solution of α-D-galactopyranosyl bromide (416 mg, 1.0 mmol) in acetonitrile (10 mL). The mixture was stirred at room temperature for 16h, filtered on celite and the pad washed with EtOAc. The filtrate was concentrated under vacuum and purified by flash column chromatography (1:1 to 7:3 EtOAc-Hexane) to give an oil which was thoroughly dried under high vacuum, giving a white powder (370 mg, 82%). Data in agreement with the literature.[142] R_f = 0.62 (EtOAc/hexane 7:3). HPLC (Method 1) t_R = 4.7 min, Purity = 100 % (ELSD). ESI-MS: calculated for $C_{21}H_{24}O_{11}$ $[M+Na]^+$ m/z 475.1. Found 475.1 (100%). ^{1}H NMR (500 MHz, Chloroform-*d*) δ 9.93 (s, 1H, CHO), 7.86 (d, J = 8.8 Hz, 2H, CHAr), 7.11 (d, J = 8.7 Hz, 2H, CHAr), 5.52 (dd, J = 10.4, 7.9 Hz, 1H), 5.48 (dd, J = 3.4, 1.1 Hz, 1H), 5.17 (d, J = 7.9 Hz, 1H), 5.14 (dd, J = 10.4, 3.4 Hz, 1H), 4.26 – 4.09 (m, 3H), 2.19 (s, 3H), 2.07 (s, 3H), 2.07 (s, 3H), 2.02 (s, 3H). ^{13}C NMR (126 MHz, $CDCl_3$) δ 190.8, 170.4, 170.3, 170.2, 169.4, 161.4, 132.0 (2C), 116.9, 98.8, 71.5, 70.8, 68.6, 66.9, 61.5, 20.9, 20.8, 20.7.

[4-(hydroxymethyl)phenyl]-(2,3,4,6-tetra-O-acetyl-β-D-galactopyranoside) (21)

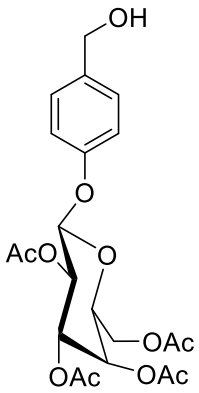

Compound **21** was prepared according to a reported procedure.[142] Sodium borohydride (17.5 mg, 0.46 mmol) was added portion-wise to a cooled solution of aldehyde (100 mg, 0.21 mmol) in $CHCl_3$-*i*PrOH (25 mL: 8 mL) at 0°C. The solution was allowed to reach room temperature and stirred for 3h. An aqueous solution of citric acid (10% (w/w), 25 mL) was added. The organics were extracted and washed with $NaHCO_3$ (10% (w/w), 3x 15 mL) and water (15mL), the organic phase was dried over $MgSO_4$ and filtered. The solvent was evaporated under vacuum and the residue purified by flash column chromatography (EtOAc-hexane 1:1). The product fractions were dried under high vacuum to give a white solid (90 mg, 95 %). Data in agreement with the literature.[142] R_f = 0.30 (EtOAc/hexane 1:1). HPLC (Method 1) t_R = 4.2 min, Purity = 100 % (ELSD). ESI-MS: calculated for $C_{21}H_{24}O_{11}$ $[M+Na]^+$ m/z 477.1. Found 477.1 (100%). ^{1}H NMR (601 MHz, Chloroform-*d*) δ 7.31 (d, *J* = 8.6 Hz, 2H), 7.00 (d, *J* = 8.6 Hz, 2H), 5.49 (dd, *J* = 10.5, 7.9 Hz, 1H), 5.46 (dd, *J* = 3.5, 1.1 Hz, 1H), 5.11 (dd, *J* = 10.5, 3.5 Hz, 1H), 5.03 (d, *J* = 8.0 Hz, 1H), 4.65 (d, *J* = 5.7 Hz, 2H), 4.23 (dd, *J* = 11.4, 6.9 Hz, 1H), 4.16 (dd, *J* = 11.4, 6.4 Hz, 1H), 4.06 (td, *J* = 6.7, 1.2 Hz, 1H), 2.19 (s, 3H), 2.07 (s, 3H), 2.06 (s, 3H), 2.02 (s, 3H). DEPT-135 ^{13}C NMR (151 MHz, Chloroform-*d*) δ 128.49, 117.07, 99.79, 71.06, 70.84, 68.67, 66.88, 64.83, 61.36,

20.73, 20.67, 20.59. ^{13}C NMR (126 MHz, Chloroform-*d*) δ 170.5, 170.4, 170.3, 169.5, 156.7, 136.1, 128.6, 117.2, 99.9, 71.2, 71.0, 68.8, 67.0, 65.0, 61.5, 20.9, 20.8, 20.7.

Gal-Bn-PNP: [4-(4-nitro-phenoxycarbonyloxymethyl)phenyl]-(2,3,4,6-tetra-O-acetyl-β-D-galactopyranoside)

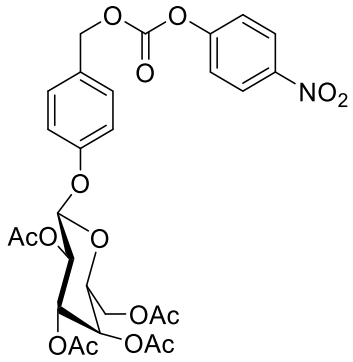

Gal-Bn-PNP was prepared according to a reported procedure.[142] 4-nitrophenyl chloroformate (120 mg, 0.6 mmol) was added at room temperature to a mixture of the alcohol (90 mg, 0.2 mmol) and pyridine (48 μL, 0.6 mmol) in EtOAc (3 mL). The mixture was stirred for 20h at room temperature and diluted with DCM (20 mL). After washing with $NaHCO_3$ solution (5%w/w, 20 mL) and water (20 mL) the organic phase was dried over $MgSO_4$. The solvent was evaporated under vacuum and the residue purified by flash column chromatography (EtOAc-hexane 15:5 then 5:5) to give a yellow oil (60 mg, 48%). Data in agreement with the literature.[142] R_f = 0.53 (3:1 EtOAc:Hexane). HPLC (Method 1) t_R = 5.2 min, Purity = 100 % (ELSD). ESI-MS: calculated for $C_{28}H_{29}NO_{15}$ $[M+Na]^+$ m/z 642.1. Found 642.1 (100%). ^{1}H NMR (500 MHz, Chloroform-*d*) δ 8.30 – 8.24 (m, 2H), 7.40 (d, *J* = 8.6 Hz, 2H), 7.38 – 7.34 (m, 2H), 7.07 – 7.00 (m, 2H), 5.50 (dd, *J* = 10.5, 7.9 Hz, 1H), 5.46 (dd, *J* = 3.4, 1.1 Hz, 1H), 5.25 (s, 2H), 5.12 (dd, *J* = 10.5, 3.4 Hz, 1H), 5.07 (d, *J* = 7.9 Hz, 1H), 4.27 – 4.13 (m, 2H), 4.07 (td, *J* = 6.6, 1.2 Hz, 1H), 2.19 (s, 3H), 2.07 (s, 3H), 2.06 (s, 3H), 2.02 (s,

3H). ^{13}C NMR (126 MHz, Chloroform-*d*) δ 170.5, 170.3, 170.3, 169.5, 157.6, 155.6, 152.6, 145.6, 130.7, 129.2, 125.5, 121.9, 117.2, 99.6, 71.3, 70.9, 70.6, 68.7, 67.0, 61.5, 20.9, 20.8, 20.7, 19.0.

Benzyl-IR780

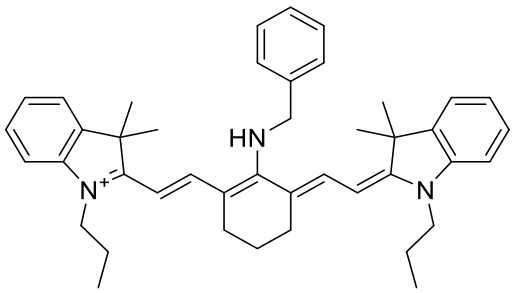

Benzyl-Cy7 was prepared according to a reported procedure.[143] IR780 (50 mg, 93 µmol) and benzylamine (33 µL, 4 eq.) were dissolved in acetonitrile in an oven dried flask and filled with a nitrogen atmosphere. DIPEA (26 µL, 2 eq.) was added and the reaction heated to 80 °C with monitoring by TLC. The reaction mixture was neutralised with 0.1 M HCl, diluted in DCM and dried over $MgSO_4$. The organics were concentrated under vacuum to give a dark metallic coloured solid (140 mg, 100 %). Data in agreement with the literature.[143] R_f = 0.38 (8% MeOH in DCM). ESI-MS: calculated for $C_{43}H_{52}N_3^+$ $[M+H]^+$ m/z 610.4. Found 610.4 (100%). HPLC (Method 1) t_R = 5.6 min, Purity 95% (ELSD). ^{1}H NMR (500 MHz, Chloroform-*d*) δ 7.67 (d, *J* = 12.9 Hz, 2H), 7.46 – 7.30 (m, 5H), 7.24 – 7.19 (m, 4H), 7.03 (t, *J* = 7.5 Hz, 2H), 6.82 (d, *J* = 7.9 Hz, 2H), 5.60 (d, *J* = 12.9 Hz, 2H), 5.11 – 5.03 (m, 2H), 3.82 – 3.70 (m, 4H), 2.48 (t, *J* = 6.3 Hz, 4H), 1.90 – 1.74 (m, 6H), 1.48 (s, 12H), 1.01 (t, *J* = 7.5 Hz, 6H). ^{13}C NMR (126 MHz, Chloroform-*d*) δ 170.1, 143.5, 142.8, 140.6, 137.0, 129.3, 128.2, 128.1, 122.9, 122.2, 108.6, 94.9, 53.6, 53.5, 47.9, 28.9, 28.5, 25.5, 20.3, 11.9.

HSQC: ^{1}H-^{13}C NMR ((500, 126) MHz, Chloroform-*d*) δ (7.7 139.6), (7.5 128.6), (7.4 129.7), (7.3 128.8), (7.3 128.7), (7.2 122.7), (7.1 123.4), (6.9 109.0), (5.6 95.3), (5.1 53.5), (4.9 53.6), (3.8 45.4), (2.5 26.0), (1.9 22.1), (1.8 20.7), (1.5 29.3), (1.0 12.3).

6.5.2. Singlet oxygen generation assay

The SOSG assay was adapted from the reported procedure by Lin.[134] Concentrations of fluorescent dyes (5 μM) and SOSG (5 μM) in aerated methanol solutions were irritated for 30 minutes with a distance of 16 cm. Irradiation was performed using a white LED lamp (ThorLabs) with 610 nm LP filter (power density 1.2 mW cm^{-2}). The fluorescence emission (Ex = 488 nm, Em = 520 nm) was measured (Synergy HT) allowing the singlet oxygen quantum yield to be determined by the comparative method.

6.5.3. Biological studies

Materials

The following reagents and materials were purchased; HBSS (Gibco 14025-050), Senescence detection kit (Abcam ab65351), β-galactosidase from *E. coli* (Sigma G4155), bleomycin sulphate (Apollo Scientific, BI3543), Prolong Gold (Invitrogen, P36934).

HPLC analysis of XD-BGal activation

XD-BGal (100 μM) in PBS+5% DMSO was incubated with recombinant β-galactosidase (40 nM, 1 U/mL) at 37°C for 1 hour. The reaction mixture was filtered

to remove protein and analysed by RP-HPLC. Analysis was performed with HPLC (method 1) monitoring absorbance at 650 nm.

Kinetic analysis of the probe with β-Galactosidase

XD-BGal (100 μM) in PBS+5% DMSO, added to a 96-well plate and incubated with concentrations of recombinant β-galactosidase (0, 5, 10, 25 nM) at 37°C. The fluorescence was measured by plate reader with 633 nm excitation after 0, 10- and 30-minute time points. To calculate the kinetic parameters, 1-20 μM **XD-BGal** was incubated with 5 nM β-Gal at 37°C for 30 minutes. The fluorescence was measured over time.

Inducing cellular senescence in A549 cells

A549 cells were cultured 6-well plates in complete DMEM until 60% confluent. Cells were then treated with PBS (750 μL) containing bleomycin sulphate (50 μg/mL) for 2 hours. Cells were gently washed 2 times in warm PBS and cultured for 7 days in complete DMEM media. Cells were observed for a change in morphology under a microscope.

X-gal staining – fluorescence microscopy

X-gal staining was carried out according to the protocol of the Abcam senescence detection kit. Briefly, senescent A549 cells (groups: untreated and bleomycin treated) were washed twice in warm PBS and incubated in fixative solution for 10 mins at room temperature. Cells were then incubated overnight in X-gal staining solution buffered

at pH 6.0 at 37 °C (without CO_2). Cells were then bright field imaged for colour development on the Z1 profiler microscope (Charles Zeiss). Positively stained cells were counted using Image-J cell counter plugin.

Imaging galactosidase activity – confocal microscopy

Acid-washed coverslips were placed in the bottom of a 6-well plate and treated with 0.1 mg/mL poly-D-lysine solution for 5 mins at room temperature, then washed twice in PBS. A549 cells (4×10^4 cells/mL) were cultured on coverslips in complete DMEM until 60% confluent. Cells were treated with 50 μg/mL bleomycin sulphate (750 μL PBS) for 12 hours. Cells were gently washed 2X in warm PBS and cultured for 5 days in complete DMEM media. Proliferating cells were seeded on the lower row of wells containing coverslips and cultured overnight until ~80% confluent. Cells were then washed three-times in warm PBS before 1 hour incubation in serum-free DMEM containing 10 μM **XD-BGal** and 0.1 μg/mL Hoechst. Cells were washed in warm PBS (2X) and mounted in Prolong Gold aqueous mountant and imaged on a Leica SP8 confocal microscope (laser lines: 405 nm (Hoechst) and 633nm (XD-BGal). Images were extracted using the Leica LAS AF software and analysed with the Fiji distribution of ImageJ.[140]

Lung tissue slices were prepared by Philip Emmanuel and confocal microscopy was carried out by the procedure above.

7. References

1. L. Thiberville, S. Moreno-Swirc, T. Vercauteren, E. Peltier, C. Cavé and G. Bourg Heckly, *Am. J. Respir. Crit. Care Med.*, 2007, **175**, 22-31.
2. I. J. Hildebrandt and S. S. Gambhir, *Clin. Immunol.*, 2004, **111**, 210-224.
3. A. L. Vahrmeijer, M. Hutteman, J. R. van der Vorst, C. J. H. van de Velde and J. V. Frangioni, *Nat. Rev. Clin. Oncol.*, 2013, **10**, 507-518.
4. S. M. Ametamey, M. Honer and P. A. Schubiger, *Chem. Rev.*, 2008, **108**, 1501-1516.
5. J. Chen, C. H. Tung, J. R. Allport, S. Chen, R. Weissleder and P. L. Huang, *Circulation*, 2005, **111**, 1800-1805.
6. F. Zheng, S. Put, L. Bouwens, T. Lahoutte, P. Matthys, S. Muyldermans, P. De Baetselier, N. Devoogdt, G. Raes and S. Schoonooghe, *J. Nucl. Med.*, 2014, **55**, 824-829.
7. C.-H. Tung, Y. Lin, W. K. Moon and R. Weissleder, *ChemBioChem*, 2002, **3**, 784-786.
8. Fluorescein angiography, https://medlineplus.gov/ency/article/003846.htm, (accessed 29 Aug 2019).
9. H. Kobayashi, M. Ogawa, R. Alford, P. L. Choyke and Y. Urano, *Chem. Rev.*, 2010, **110**, 2620-2640.
10. J. R. Lakowicz, in *Principles of Fluorescence Spectroscopy*, ed. J. R. Lakowicz, Springer, Boston, MA, 3 edn., 2006, ch. 1, pp. 1-26.
11. S. A. Hilderbrand and R. Weissleder, *Curr. Opin. Chem. Biol.*, 2010, **14**, 71-79.
12. R. Weissleder and V. Ntziachristos, *Nat. Med.*, 2003, **9**, 123-128.
13. R. R. Zhang, A. B. Schroeder, J. J. Grudzinski, E. L. Rosenthal, J. M. Warram, A. N. Pinchuk, K. W. Eliceiri, J. S. Kuo and J. P. Weichert, *Nat. Rev. Clin. Oncol.*, 2017, **14**, 347-364.
14. O. T. Okusanya, E. M. DeJesus, J. X. Jiang, R. P. Judy, O. G. Venegas, C. G. Deshpande, D. F. Heitjan, S. Nie, P. S. Low and S. Singhal, *J. Thorac. Cardiovasc. Surg.*, 2015, **150**, 28-35.
15. N. Krstajić, A. R. Akram, T. R. Choudhary, N. McDonald, M. G. Tanner, E. Pedretti, P. A. Dalgarno, E. Scholefield, J. M. Girkin, A. Moore, M. Bradley and K. Dhaliwal, *J. Biomed. Opt.*, 2016, **21**, 46009.
16. J. E. East, J. L. Vleugels, P. Roelandt, P. Bhandari, R. Bisschops, E. Dekker, C. Hassan, G. Horgan, R. Kiesslich, G. Longcroft-Wheaton, A. Wilson and J.-M. Dumonceau, *Endoscopy*, 2016, **48**, 1029-1045.
17. M. Koch, P. Symvoulidis and V. Ntziachristos, *Nat. Photonics*, 2018, **12**, 505-515.
18. Y. Urano, *Curr. Opin. Chem. Biol.*, 2012, **16**, 602-608.
19. J. Burggraaf, I. M. C. Kamerling, P. B. Gordon, L. Schrier, M. L. de Kam, A. J. Kales, R. Bendiksen, B. Indrevoll, R. M. Bjerke, S. A. Moestue, S. Yazdanfar, A. M. J. Langers, M. Swaerd-Nordmo, G. Torheim, M. V. Warren, H. Morreau, P. W. Voorneveld, T. Buckle, F. W. B. van Leeuwen, L.-I.

Odegardstuen, G. T. Dalsgaard, A. Healey and J. C. H. Hardwick, *Nat. Med.*, 2015, **21**, 955-961.
20. M. Sakabe, D. Asanuma, M. Kamiya, R. J. Iwatate, K. Hanaoka, T. Terai, T. Nagano and Y. Urano, *J. Am. Chem. Soc.*, 2013, **135**, 409-414.
21. M. Yoshida, M. Kamiya, T. Yamasoba and Y. Urano, *Bioorg. Med. Chem. Lett.*, 2014, **24**, 4363-4366.
22. Y. Koide, Y. Urano, K. Hanaoka, T. Terai and T. Nagano, *J. Am. Chem. Soc.*, 2011, **133**, 5680-5682.
23. N. Narayanaswamy, S. Narra, R. R. Nair, D. K. Saini, P. Kondaiah and T. Govindaraju, *Chem. Sci.*, 2016, **7**, 2832-2841.
24. M. Staderini, A. Megia-Fernandez, K. Dhaliwal and M. Bradley, *Biorg. Med. Chem.*, 2018, **26**, 2816-2826.
25. L. D. Lavis and R. T. Raines, *ACS Chem. Biol.*, 2014, **9**, 855-866.
26. F. M. Hamer, *The Cyanine Dyes and Related Compounds*, John Wiley & Sons, New Jersey, 2009.
27. A. Bunschoten, D. M. van Willigen, T. Buckle, N. S. van den Berg, M. M. Welling, S. J. Spa, H.-J. Wester and F. W. B. van Leeuwen, *Bioconj. Chem.*, 2016, **27**, 1253-1258.
28. R. B. Mujumdar, L. A. Ernst, S. R. Mujumdar, C. J. Lewis and A. S. Waggoner, *Bioconj. Chem.*, 1993, **4**, 105-111.
29. A. R. Akram, N. Avlonitis, A. Lilienkampf, A. M. Perez-Lopez, N. McDonald, S. V. Chankeshwara, E. Scholefield, C. Haslett, M. Bradley and K. Dhaliwal, *Chem. Sci.*, 2015, **6**, 6971-6979.
30. R. B. Sekar and A. Periasamy, *J. Cell Biol.*, 2003, **160**, 629-633.
31. A. P. de Silva, T. S. Moody and G. D. Wright, *Analyst*, 2009, **134**, 2385-2393.
32. T. Hussell and T. J. Bell, *Nat. Rev. Immunol.*, 2014, **14**, 81-93.
33. J. W. Pollard, *Nat. Rev. Immunol.*, 2009, **9**, 259.
34. L. D. Shultz, M. A. Brehm, J. V. Garcia-Martinez and D. L. Greiner, *Nat. Rev. Immunol.*, 2012, **12**, 786.
35. S. Michlewska, I. Dransfield, I. L. Megson and A. G. Rossi, *FASEB J.*, 2008, **23**, 844-854.
36. A. Mantovani, A. Sica, S. Sozzani, P. Allavena, A. Vecchi and M. Locati, *Trends Immunol.*, 2004, **25**, 677-686.
37. R. Shaykhiev, A. Krause, J. Salit, Y. Strulovici-Barel, B. G. Harvey, T. P. O'Connor and R. G. Crystal, *J. Immunol.*, 2009, **183**, 2867-2883.
38. A. Fernandez and M. Vendrell, *Chem. Soc. Rev.*, 2016, **45**, 1182-1196.
39. Treatment of Solid Tumor Cancers with the Chemotherapy Drug Methotrexate https://www.cancer.gov/research/progress/discovery/methotrexate, (accessed 1 June 2019).
40. P. S. Low, W. A. Henne and D. D. Doorneweerd, *Acc. Chem. Res.*, 2008, **41**, 120-129.
41. M. D. Kennedy, K. N. Jallad, J. Lu, P. S. Low and D. Ben-Amotz, *Pharm. Res.*, 2003, **20**, 714-719.
42. J. Kim, C. H. Tung and Y. Choi, *Chem. Commun.*, 2014, **50**, 10600-10603.
43. G. König Sandra and R. Krämer, *Chem. Eur. J.*, 2017, **23**, 9306-9312.
44. L. E. Kelderhouse, V. Chelvam, C. Wayua, S. Mahalingam, S. Poh, S. A. Kularatne and P. S. Low, *Bioconj. Chem.*, 2013, **24**, 1075-1080.

45. G. M. van Dam, G. Themelis, L. M. Crane, N. J. Harlaar, R. G. Pleijhuis, W. Kelder, A. Sarantopoulos, J. S. de Jong, H. J. Arts, A. G. van der Zee, J. Bart, P. S. Low and V. Ntziachristos, *Nat. Med.*, 2011, **17**, 1315-1319.
46. J. Yang, H. Chen, I. R. Vlahov, J. X. Cheng and P. S. Low, *Proc. Natl. Acad. Sci. U. S. A.*, 2006, **103**, 13872-13877.
47. S. M. Mahalingam, S. A. Kularatne, C. H. Myers, P. Gagare, M. Norshi, X. Liu, S. Singhal and P. S. Low, *J. Med. Chem.*, 2018, **61**, 9637-9646.
48. N. Nakashima-Matsushita, T. Homma, S. Yu, T. Matsuda, N. Sunahara, T. Nakamura, M. Tsukano, M. Ratnam and T. Matsuyama, *Arthritis Rheum.*, 2001, **42**, 1609-1616.
49. W. Han, R. Zaynagetdinov, F. E. Yull, V. V. Polosukhin, L. A. Gleaves, H. Tanjore, L. R. Young, T. E. Peterson, H. C. Manning, L. S. Prince and T. S. Blackwell, *Am. J. Respir. Cell Mol. Biol.*, 2015, **53**, 50-59.
50. W. Xia, A. R. Hilgenbrink, E. L. Matteson, M. B. Lockwood, J. X. Cheng and P. S. Low, *Blood*, 2009, **113**, 438-446.
51. J. Shen, V. Chelvam, G. Cresswell and P. S. Low, *Mol. Pharm.*, 2013, **10**, 1918-1927.
52. J. A. Reddy, L. S. Haneline, E. F. Srour, A. C. Antony, D. W. Clapp and P. S. Low, *Blood*, 1999, **93**, 3940.
53. J. F. Ross, H. Wang, F. G. Behm, P. Mathew, M. Wu, R. Booth and M. Ratnam, *Cancer*, 1999, **85**, 348-357.
54. A. Puig-Kröger, E. Sierra-Filardi, A. Domínguez-Soto, R. Samaniego, M. T. Corcuera, F. Gómez-Aguado, M. Ratnam, P. Sánchez-Mateos and A. L. Corbí, *Cancer Res.*, 2009, **69**, 9395-9403.
55. Y. Tsuneyoshi, M. Tanaka, T. Nagai, N. Sunahara, T. Matsuda, T. Sonoda, K. Ijiri, S. Komiya and T. Matsuyama, *Scand. J. Rheumatol.*, 2012, **41**, 132-140.
56. J. Shen, A. R. Hilgenbrink, W. Xia, Y. Feng, D. S. Dimitrov, M. B. Lockwood, R. J. Amato and P. S. Low, *J. Leukocyte Biol.*, 2014, **96**, 563-570.
57. S. Poh, V. Chelvam, W. Ayala-López, K. S. Putt and P. S. Low, *Nanomedicine*, 2018, **14**, 1033-1043.
58. A. F. Trindade, R. F. Frade, E. M. Macoas, C. Graca, C. A. Rodrigues, J. M. Martinho and C. A. Afonso, *Org. Biomol. Chem.*, 2014, **12**, 3181-3190.
59. J. Luo, M. D. Smith, D. A. Lantrip, S. Wang and P. L. Fuchs, *J. Am. Chem. Soc.*, 1997, **119**, 10004-10013.
60. J. F. Ross, P. K. Chaudhuri and M. Ratnam, *Cancer*, 1994, **73**, 2432-2443.
61. S. A. Kularatne and P. S. Low, *Methods in Molecular Biology (Methods and Protocols)*, 2010, **624**, 249-265.
62. D. J. O'Shannessy, G. Yu, R. Smale, Y.-S. Fu, S. Singhal, R. P. Thiel, E. B. Somers and A. Vachani, *Oncotarget*, 2012, **3**, 414-425.
63. N. Parker, M. J. Turk, E. Westrick, J. D. Lewis, P. S. Low and C. P. Leamon, *Anal. Biochem.*, 2005, **338**, 284-293.
64. R. Samaniego, B. S. Palacios, Á. Domiguez-Soto, C. Vidal, A. Salas, T. Matsuyama, C. Sánchez-Torres, I. de la Torre, M. E. Miranda-Carús, P. Sánchez-Mateos and A. Puig-Kröger, *J. Leukocyte Biol.*, 2014, **95**, 797-808.
65. E. Juarez, C. Nuñez, E. Sada, J. J. Ellner, S. K. Schwander and M. Torres, *Respir. Res.*, 2010, **11**, 2.
66. A. R. Pons, A. Noguera, D. Blanquer, J. Sauleda, J. Pons and A. G. Agustí, *Eur. Respir. J.*, 2005, **25**, 647-652.

67. R. J. Helmke, R. L. Boyd, V. F. German and J. A. Mangos, *In Vitro Cell. Dev. Biol.*, 1987, **23**, 567-574.
68. M. Toda, S. Mizuguchi, Y. Minamiyama, H. Yamamoto-Oka, T. Aota, S. Kubo, N. Nishiyama, T. Shibata and S. Takemura, *J. Clin. Biochem. Nutr.*, 2018, **63**, 58-65.
69. C. Machacek, V. Supper, V. Leksa, G. Mitulovic, A. Spittler, K. Drbal, M. Suchanek, A. Ohradanova-Repic and H. Stockinger, *J. Immunol.*, 2016, **197**, 2229-2238.
70. B. Forbes, R. O'Lone, P. P. Allen, A. Cahn, C. Clarke, M. Collinge, L. A. Dailey, L. E. Donnelly, J. Dybowski, D. Hassall, D. Hildebrand, R. Jones, J. Kilgour, J. Klapwijk, C. C. Maier, T. McGovern, K. Nikula, J. D. Parry, M. D. Reed, I. Robinson, L. Tomlinson and A. Wolfreys, *Adv. Drug Del. Rev.*, 2014, **71**, 15-33.
71. S. Gordon, *Nat. Rev. Immunol.*, 2003, **3**, 23-35.
72. C. Leteux, W. Chai, R. W. Loveless, C. T. Yuen, L. Uhlin-Hansen, Y. Combarnous, M. Jankovic, S. C. Maric, Z. Misulovin, M. C. Nussenzweig and T. Feizi, *The Journal of experimental medicine*, 2000, **191**, 1117-1126.
73. L. Martinez-Pomares, *J. Leukocyte Biol.*, 2012, **92**, 1177-1186.
74. P. Stahl, P. H. Schlesinger, E. Sigardson, J. S. Rodman and Y. C. Lee, *Cell*, 1980, **19**, 207-215.
75. S. E. M. Heinsbroek, P. R. Taylor, F. O. Martinez, L. Martinez-Pomares, G. D. Brown and S. Gordon, *PLoS Path.*, 2008, **4**, e1000218.
76. U. Gazi, M. Rosas, S. Singh, S. Heinsbroek, I. Haq, S. Johnson, G. D. Brown, D. L. Williams, P. R. Taylor and L. Martinez-Pomares, *J. Biol. Chem.*, 2011, **286**, 7822-7829.
77. K.-M. Chavele, L. Martinez-Pomares, J. Domin, S. Pemberton, S. M. Haslam, A. Dell, H. T. Cook, C. D. Pusey, S. Gordon and A. D. Salama, *J. Clin. Invest.*, 2010, **120**, 1469-1478.
78. K. Movahedi, D. Laoui, C. Gysemans, M. Baeten, G. Stangé, J. Van den Bossche, M. Mack, D. Pipeleers, P. In't Veld, P. De Baetselier and J. A. Van Ginderachter, *Cancer Res.*, 2010, **70**, 5728-5739.
79. C. E. Lewis and J. W. Pollard, *Cancer Res.*, 2006, **66**, 605-612.
80. S. K. Biswas and A. Mantovani, *Nat. Immunol.*, 2010, **11**, 889-896.
81. E. Bazzan, G. Turato, M. Tinè, C. M. Radu, E. Balestro, C. Rigobello, D. Biondini, M. Schiavon, F. Lunardi, S. Baraldo, F. Rea, P. Simioni, F. Calabrese, M. Saetta and M. G. Cosio, *Respir. Res.*, 2017, **18**, 40.
82. A. K. Azad, M. V. S. Rajaram, W. L. Metz, F. O. Cope, M. S. Blue, D. R. Vera and L. S. Schlesinger, *J. Immunol.*, 2015, **195**, 2019-2029.
83. J. B. Kim, K. Park, J. Ryu, J. J. Lee, M. W. Lee, H. S. Cho, H. S. Nam, O. K. Park, J. W. Song, T. S. Kim, D. J. Oh, D. Gweon, W. Y. Oh, H. Yoo and J. W. Kim, *Sci. Rep.*, 2016, **6**, 22608.
84. T. B. H. Geijtenbeek, R. Torensma, S. J. van Vliet, G. C. F. van Duijnhoven, G. J. Adema, Y. van Kooyk and C. G. Figdor, *Cell*, 2000, **100**, 575-585.
85. A. Blykers, S. Schoonooghe, C. Xavier, K. D'Hoe, D. Laoui, M. D'Huyvetter, I. Vaneycken, F. Cleeren, G. Bormans, J. Heemskerk, G. Raes, P. De Baetselier, T. Lahoutte, N. Devoogdt, J. A. Van Ginderachter and V. Caveliers, *J. Nucl. Med.*, 2015, **56**, 1265-1271.

86. P. Scodeller, L. Simón-Gracia, S. Kopanchuk, A. Tobi, K. Kilk, P. Säälik, K. Kurm, M. L. Squadrito, V. R. Kotamraju, A. Rinken, M. De Palma, E. Ruoslahti and T. Teesalu, *Sci. Rep.*, 2017, **7**, 14655.
87. C. Hamers-Casterman, T. Atarhouch, S. Muyldermans, G. Robinson, C. Hamers, E. B. Songa, N. Bendahman and R. Hamers, *Nature*, 1993, **363**, 446-448.
88. M. Kijanka, F.-J. Warnders, M. El Khattabi, M. Lub-de Hooge, G. M. van Dam, V. Ntziachristos, L. de Vries, S. Oliveira and P. M. P. van Bergen en Henegouwen, *Eur. J. Nucl. Med. Mol. Imag.*, 2013, **40**, 1718-1729.
89. K. De Groeve, N. Deschacht, C. De Koninck, V. Caveliers, T. Lahoutte, N. Devoogdt, S. Muyldermans, P. De Baetselier and G. Raes, *J. Nucl. Med.*, 2010, **51**, 782-789.
90. M. Evazalipour, M. D'Huyvetter, B. S. Tehrani, M. Abolhassani, K. Omidfar, S. Abdoli, R. Arezumand, H. Morovvati, T. Lahoutte, S. Muyldermans and N. Devoogdt, *Contrast Media Mol. Imaging*, 2014, **9**, 211-220.
91. K. Movahedi, S. Schoonooghe, D. Laoui, I. Houbracken, W. Waelput, K. Breckpot, L. Bouwens, T. Lahoutte, P. De Baetselier, G. Raes, N. Devoogdt and J. A. Van Ginderachter, *Cancer Res.*, 2012, **72**, 4165-4177.
92. N. Devoogdt, C. Xavier, S. Hernot, I. Vaneycken, M. D'Huyvetter, J. De Vos, S. Massa, P. De Baetselier, V. Caveliers and T. Lahoutte, in *Single Domain Antibodies*, eds. D. Saerens and S. Muyldermans, Humana Press, Totowa, NJ, Methods in Molecular Biology, 2012, vol. 911, pp. 559-567.
93. N. Deschacht, K. De Groeve, C. Vincke, G. Raes, P. De Baetselier and S. Muyldermans, *J. Immunol.*, 2010, **184**, 5696-5704.
94. C. Morrison, *Nat. Rev. Drug Discovery*, 2019, **18**, 485-487.
95. S. Schoonooghe, D. Laoui, J. A. Van Ginderachter, N. Devoogdt, T. Lahoutte, P. De Baetselier and G. Raes, *Immunobiology*, 2012, **217**, 1266-1272.
96. D. Zabetakis, G. P. Anderson, N. Bayya and E. R. Goldman, *PLOS ONE*, 2013, **8**, e77678.
97. R. Chakravarty, S. Goel and W. Cai, *Theranostics*, 2014, **4**, 386-398.
98. P. Debie, J. Van Quathem, I. Hansen, G. Bala, S. Massa, N. Devoogdt, C. Xavier and S. Hernot, *Mol. Pharm.*, 2017, **14**, 1145-1153.
99. US2016101150, 2016.
100. EP2855526B1, 2012.
101. S. Nagarajan, N. H. Fifadara and P. Selvaraj, *J. Immunol.*, 2005, **174**, 5423.
102. A. Blicher, K. Wodzinska, M. Fidorra, M. Winterhalter and T. Heimburg, *Biophys. J.*, 2009, **96**, 4581-4591.
103. J. R. Peterson and T. J. Mitchison, *Chem. Biol.*, 2002, **9**, 1275-1285.
104. E. Macia, M. Ehrlich, R. Massol, E. Boucrot, C. Brunner and T. Kirchhausen, *Dev. Cell*, 2006, **10**, 839-850.
105. M. Sverdlov, A. N. Shajahan and R. D. Minshall, *J. Cell. Mol. Med.*, 2007, **11**, 1239-1250.
106. B. G. Childs, M. Durik, D. J. Baker and J. M. van Deursen, *Nat. Med.*, 2015, **21**, 1424-1435.
107. L. M. Salazar and A. M. Herrera, *Lung*, 2011, **189**, 101-109.
108. T. Tsuji, K. Aoshiba and A. Nagai, *Am. J. Respir. Cell Mol. Biol.*, 2004, **31**, 643-649.

109. B. Kuźnar-Kamińska, J. Mikuła-Pietrasik, A. Witucka, A. Romaniuk, N. Konieczna, B. Rubiś, K. Książek, A. Tykarski and H. Batura-Gabryel, *Sci. Rep.*, 2018, **8**, 12940.
110. M. Lehmann, M. Korfei, K. Mutze, S. Klee, W. Skronska-Wasek, H. N. Alsafadi, C. Ota, R. Costa, H. B. Schiller, M. Lindner, D. E. Wagner, A. Günther and M. Königshoff, *Eur. Respir. J.*, 2017, **50**, 1602367.
111. D. Muñoz-Espín and M. Serrano, *Nat. Rev. Mol. Cell Biol.*, 2014, **15**, 482.
112. D. J. Kurz, S. Decary, Y. Hong and J. D. Erusalimsky, *J. Cell Sci.*, 2000, **113**, 3613.
113. F. Debacq-Chainiaux, J. D. Erusalimsky, J. Campisi and O. Toussaint, *Nat. Prot.*, 2009, **4**, 1798-1806.
114. M. D. Skudlarek and R. T. Swank, *J. Biol. Chem.*, 1979, **254**, 9939-9942.
115. X. Qiu, H. Guo, J. Yang, Y. Ji, C. S. Wu and X. Chen, *Sci. Rep.*, 2018, **8**, 1679.
116. D. Asanuma, M. Sakabe, M. Kamiya, K. Yamamoto, J. Hiratake, M. Ogawa, N. Kosaka, P. L. Choyke, T. Nagano, H. Kobayashi and Y. Urano, *Nat. Commun.*, 2015, **6**, 6463.
117. S. K. Chatterjee, M. Bhattacharya and J. J. Barlow, *Cancer Res.*, 1979, **39**, 1943.
118. D. J. Spergel, U. Krüth, D. R. Shimshek, R. Sprengel and P. H. Seeburg, *Prog. Neurobiol.*, 2001, **63**, 673-686.
119. H.-W. Liu, L. Chen, C. Xu, Z. Li, H. Zhang, X.-B. Zhang and W. Tan, *Chem. Soc. Rev.*, 2018, **47**, 7140-7180.
120. K. Gu, Y. Xu, H. Li, Z. Guo, S. Zhu, S. Zhu, P. Shi, T. D. James, H. Tian and W. H. Zhu, *J. Am. Chem. Soc.*, 2016, **138**, 5334-5340.
121. B. Lozano-Torres, I. Galiana, M. Rovira, E. Garrido, S. Chaib, A. Bernardos, D. Munoz-Espin, M. Serrano, R. Martinez-Manez and F. Sancenon, *J. Am. Chem. Soc.*, 2017, **139**, 8808-8811.
122. T. Doura, M. Kamiya, F. Obata, Y. Yamaguchi, T. Y. Hiyama, T. Matsuda, A. Fukamizu, M. Noda, M. Miura and Y. Urano, *Angew. Chem. Int. Ed.*, 2016, **55**, 9620-9624.
123. L. Yuan, W. Lin, S. Zhao, W. Gao, B. Chen, L. He and S. Zhu, *J. Am. Chem. Soc.*, 2012, **134**, 13510-13523.
124. J. Zhang, C. Li, C. Dutta, M. Fang, S. Zhang, A. Tiwari, T. Werner, F. T. Luo and H. Liu, *Anal. Chim. Acta*, 2017, **968**, 97-104.
125. H. W. Lee, C. H. Heo, D. Sen, H.-O. Byun, I. H. Kwak, G. Yoon and H. M. Kim, *Anal. Chem.*, 2014, **86**, 10001-10005.
126. H.-W. Liu, X.-X. Hu, K. Li, Y. Liu, Q. Rong, L. Zhu, L. Yuan, F.-L. Qu, X.-B. Zhang and W. Tan, *Chem. Sci.*, 2017, **8**, 7689-7695.
127. K. Aoshiba, T. Tsuji and A. Nagai, *Eur. Respir. J.*, 2003, **22**, 436-443.
128. K. Aoshiba, T. Tsuji, S. Kameyama, M. Itoh, S. Semba, K. Yamaguchi and H. Nakamura, *Exp. Toxicol. Pathol.*, 2013, **65**, 1053-1062.
129. Bleomycin: MedlinePlus, https://medlineplus.gov/druginfo/meds/a682125.html, (accessed 23 August 2019).
130. J. Chen and J. Stubbe, *Nat. Rev. Cancer*, 2005, **5**, 102-112.
131. S. M. Hecht, *J. Nat. Prod.*, 2000, **63**, 158-168.
132. T. Liu, F. G. De Los Santos and S. H. Phan, in *Fibrosis: Methods and Protocols*, ed. L. Rittié, Springer New York, New York, NY, 2017, pp. 27-42.

133. C. J. H. Ho, G. Balasundaram, W. Driessen, R. McLaren, C. L. Wong, U. S. Dinish, A. B. E. Attia, V. Ntziachristos and M. Olivo, *Sci. Rep.*, 2014, **4**, 5342.
134. H. Lin, Y. Shen, D. Chen, L. Lin, B. Li and S. Xie, *Proc. SPIE* 2010, **7845**, 78451J.
135. K. Kiyose, S. Aizawa, E. Sasaki, H. Kojima, K. Hanaoka, T. Terai, Y. Urano and T. Nagano, *Chem. Eur. J.*, 2009, **15**, 9191-9200.
136. M. Lopalco, E. N. Koini, J. K. Cho and M. Bradley, *Org. Biomol. Chem.*, 2009, **7**, 856-859.
137. WO/2012/001063, 2012.
138. A. Brunet, T. Aslam and M. Bradley, *Bioorg. Med. Chem. Lett.*, 2014, **24**, 3186-3188.
139. C. J. MacNevin, D. Gremyachinskiy, C. W. Hsu, L. Li, M. Rougie, T. T. Davis and K. M. Hahn, *Bioconj. Chem.*, 2013, **24**, 215-223.
140. J. Schindelin, I. Arganda-Carreras, E. Frise, V. Kaynig, M. Longair, T. Pietzsch, S. Preibisch, C. Rueden, S. Saalfeld, B. Schmid, J. Y. Tinevez, D. J. White, V. Hartenstein, K. Eliceiri, P. Tomancak and A. Cardona, *Nat. Methods*, 2012, **9**, 676-682.
141. H. Schägger, *Nat. Prot.*, 2006, **1**, 16-22.
142. T. Chauvin, P. Durand, M. Bernier, H. Meudal, B.-T. Doan, F. Noury, B. Badet, J.-C. Beloeil and É. Tóth, *Angew. Chem. Int. Ed.*, 2008, **47**, 4370-4372.
143. N. Y. Kang, S. J. Park, X. W. Ang, A. Samanta, W. H. Driessen, V. Ntziachristos, K. O. Vasquez, J. D. Peterson, S. W. Yun and Y. T. Chang, *Chem. Commun.*, 2014, **50**, 6589-6591.
144. J. Prieto, C. Lensmar, A. Roquet, I. van der Ploeg, D. Gigliotti, A. Eklund and J. Grunewald, *Respir Med*, 2000, **94**, 806-814.
145. A. Magnan, D. van Pee, P. Bongrand and D. Vervloet, *Allergy*, 1998, **53**, 1092-1095.
146. M. A. Gibbons, A. C. MacKinnon, P. Ramachandran, K. Dhaliwal, R. Duffin, A. T. Phythian-Adams, N. van Rooijen, C. Haslett, S. E. Howie, A. J. Simpson, N. Hirani, J. Gauldie, J. P. Iredale, T. Sethi and S. J. Forbes, *Am J Respir Crit Care Med*, 2011, **184**, 569-581.
147. L. E. Kelderhouse, M. T. Robins, K. E. Rosenbalm, E. K. Hoylman, S. Mahalingam and P. S. Low, *Mol Pharm*, 2015, **12**, 3547-3555.
148. D. Munoz-Espin, M. Rovira, I. Galiana, C. Gimenez, B. Lozano-Torres, M. Paez-Ribes, S. Llanos, S. Chaib, M. Munoz-Martin, A. C. Ucero, G. Garaulet, F. Mulero, S. G. Dann, T. VanArsdale, D. J. Shields, A. Bernardos, J. R. Murguia, R. Martinez-Manez and M. Serrano, EMBO Mol Med, 2018, 10.
149. S. H. Alamudi, R. Satapathy, J. Kim, D. Su, H. Ren, R. Das, L. Hu, E. Alvarado-Martinez, J. Y. Lee, C. Hoppmann, E. Pena-Cabrera, H. H. Ha, H. S. Park, L. Wang and Y. T. Chang, Nat Commun, 2016, 7, 11964.
150. S. H. Alamudi, D. Su, K. J. Lee, J. Y. Lee, J. L. Belmonte-Vázquez, H. S. Park, E. Peña-Cabrera and Y. T. Chang, Chem Sci, 2018, 9, 2376-2383.
151. Molinspiration Cheminformatics, www.molinspiration.com, (accessed 23 August 2019).

8. Appendices

8.1. Video files (on CD)

8.1.1. **Figure 2.38**: Timelapse video showing the uptake of Cy5**-Folate by M2 MDMs

8.1.2. **Figure 3.17**: 3D visualisation of macrophage labelling with **Cy5**-Nb** generated using spinning disk microscopy and analysed in Imaris.

8.1.3. **Figure 3.18**: Timelapse imaging of MDMs labelled with with **Cy5**-Nb** generated with spinning disk microscopy